

ABSTRACT

Title of Dissertation: FABRICATION AND MEASUREMENT OF
REGENERABLE LOW WORK FUNCTION
DISPENSER PHOTOCATHODES

Nathan A. Moody, Doctor of Philosophy, 2006

Dissertation Directed By: Professor & Chair, Patrick G. O'Shea
Department of Electrical and Computer
Engineering

Laser-switched photoemitters are a source of electrons for high current applications such as free electron lasers. Laser-modulated photoemission permits rapid switching of the electron beam, far surpassing what can be achieved using electric-field gated emission. Photoinjector systems consist of a drive laser producing short bunches of photons and an efficient photocathode, which converts photon bunches into electron beam pulses. Development of both technologies is required, but the scope of this project is restricted to improvement of the photocathode. Most high-efficiency photocathodes employ cesium-based surface coatings to reduce work function and enable efficient electron emission in the visible range. Lifetime is severely limited by the loss of this delicate coating, which degrades rapidly in practical vacuum environments. More robust photocathodes exist, but have much lower efficiency, and place unrealistic demands on drive laser power and stability. This research proposes a novel dispenser concept that dramatically extends the

lifetime of high efficiency cesium-based cathodes by continuously or periodically restoring the cesium surface monolayer during an in situ rejuvenation process. Sintered tungsten provides an interface between a cesium reservoir and the photoemitting surface. During temperature-controlled rejuvenation, cesium diffuses through and across the sintered tungsten to create and sustain a low-work function photocathode. The prototype dispenser cathode was fabricated and tested for two modes of operation: continuous and periodic near-room temperature rejuvenation. The data are compared with a photoemission model of partially covered surfaces under design for integration with existing beam simulations. Overall performance suggests that this cesium-delivery mechanism can significantly enhance the efficiency and operational lifetime of a wide variety of present and future cesium-based photocathodes. Also reported are surface characterization, ion beam cleaning, and fabrication techniques used to optimize performance of the dispenser photocathode.

FABRICATION AND MEASUREMENT OF REGENERABLE LOW WORK
FUNCTION DISPENSER PHOTOCATHODES

By

Nathan A. Moody

Dissertation submitted to the Faculty of the Graduate School of the
University of Maryland, College Park, in partial fulfillment
of the requirements for the degree of
Doctor of Philosophy
2006

Advisory Committee:
Professor Patrick G. O'Shea, Chair
Professor Isaak D. Mayergoyz
Professor John Melngailis
Professor Wes Lawson
Professor Gottlieb S. Oehrlein

© Copyright by
Nathan A. Moody
2006

Dedication

To Daniela.

Acknowledgements

I would like to express my gratitude to Professor Patrick O'Shea for his inspiration and example. His mentoring has shaped my outlook and approach to graduate school and beyond. Dr. Don and Renee Feldman were the first to welcome me as a graduate student in IREAP and I am honored by their friendship and daily interaction. Dr. Kevin Jensen has lent enormous help by explaining his theories and that of many others in ways I can understand. His work lends significance and credibility to this project. I would like to thank Jay Pyle, Dr. John Rodgers, Dr. Mark Walter, Doug Cohen, and Bart Hogan for their support and expert advice in helping me set up my experiments. Special thanks to Mr. Cohen for brewing high performance coffee. I would also like to thank past and present graduate students Matt Virgo, Jonathan Neumann, John Harris, Todd Firestone, David Demske, Gang Bai, and Oleks Sinitsyn. I wish to thank Professors Melngailis, Mayergoyz, Lawson, and Oehrlein for serving on my dissertation exam committee. I am especially grateful to Professor Mayergoyz for allowing me to learn alongside him as he taught his exemplary quantum mechanics course and shared valuable insights, both personal and academic in nature. Support for this research program comes from the Joint Technology Office (JTO) and the Office of Naval Research (ONR). I would also like to thank my immediate and Covenant families for their lifelong examples and unwavering support in all my endeavors, academic or otherwise. And most of all, I must express immeasurable gratitude to my wife, colleague, and best friend Daniela for putting up with all that goes along with graduate school and for valuing and supporting my dreams.

Table of Contents

Dedication.....	ii
Acknowledgements.....	iii
Table of Contents.....	iv
List of Tables.....	viii
List of Figures.....	ix
List of Figures.....	ix
1. Introduction.....	1
1.1 Overview.....	1
1.2 Photocathode Characteristics.....	3
1.2.1 Spectral Response.....	3
1.2.2 Lifetime.....	4
1.2.3 Response time.....	5
1.2.4 Damage Threshold.....	6
1.2.5 Transverse Energy Spread.....	6
1.3 Electron Beam Characteristics.....	7
1.3.1 Emittance.....	7
1.3.2 Brightness.....	9
1.4 Basic Photoemission Model.....	10
1.5 Types of Photocathodes.....	13
1.5.1 Metallic Cathodes.....	14
1.5.2 Effect of Surface Films on Metallic Cathodes.....	15
1.5.3 Semiconductor Photocathodes.....	18
1.5.4 Negative Electron Affinity.....	22
1.6 The Dispenser Cathode.....	23
1.7 Project Summary.....	23
2. Historical Landscape.....	25
2.1 History of Photocathodes.....	25
2.2 History of Photoinjection.....	27
2.2.1 Types of Injectors.....	28
2.2.2 Recent Developments.....	31
3. Experimental Setup.....	33
3.1 Introduction.....	33
3.1.1 Phase I: Cesium Metal Substrates.....	34
3.1.2 Phase II: Cesium Sintered Substrates.....	35
3.1.3 Phase III: Controlled Porosity Dispenser Photocathode.....	37
3.2 Vacuum Chamber.....	38
3.2.1 Chamber Geometry and Layout.....	39
3.2.2 Vacuum Characteristics.....	42
3.2.3 UHV Pumping Systems.....	44
3.2.4 Pressure at the Cathode.....	50
3.2.5 Source of Background Gas.....	53
3.2.6 Gas Valve Configuration.....	57

3.2.7 Gauges.....	60
3.3 Lasers	62
3.3.1 Diode Laser Basics	63
3.3.2 Diode Laser vs. Diode Pumped Solid State.....	66
3.3.3 Laser Specifications	67
3.3.4 Laser Safety	71
3.3.5 Robotic Control.....	73
4. Experimental Techniques.....	79
4.1 Data Acquisition and Control	79
4.1.1 Instrumentation	79
4.1.1.1 Cathode and Chamber Temperature	80
4.1.1.2 Coating Coverage.....	80
4.1.1.3 Photocurrent.....	83
4.1.1.4 Laser Power	84
4.1.1.5 Residual Gas Analyzer.....	86
4.1.2 Labview Introduction.....	87
4.2 Experimental Procedures	89
4.2.1 Chamber Pumpdown.....	90
4.2.2 Cathode Preparation.....	92
4.2.3 Cesium and Multi-Alkali Deposition.....	97
4.2.4 QE Measurements	103
4.2.5 Labview Automation	105
4.2.6 Ion Beam Treatments.....	112
4.3 Surface Characterization Techniques	127
4.3.1 Optical Microscopy.....	127
4.3.2 Profilometry	128
4.3.3 Scanning Electron Microscopy	130
4.3.4 Ion Induced Secondary Electron Emission	133
4.3.5 Focused Ion Beam Milling.....	134
5. Theory Overview	135
5.1 Introduction.....	136
5.2 Coating Dependent Work function	137
5.2.1 Gyftopolous-Levine Theory.....	138
5.2.2 Comparison to Literature Data.....	143
5.3 Photoemission Model.....	143
5.3.1 Modified Fowler-Dubridge Model	144
5.3.2 Evaluating Quantum Efficiency.....	146
5.4 Scattering Mechanisms	147
5.4.1 Temperature Dependent Scattering Rates.....	147
5.4.2 Post Absorption Scattering Factor	148
5.5 Application to Experiment.....	150
5.5.1 Bare Metals	150
5.5.2 Coated Surfaces	151
6. Experimental Results	154
6.1 Preliminary Observations.....	154
6.1.1 Background Noise.....	154

6.1.2 Monolayer vs. Multiple-Monolayer Cesium Evaporation	156
6.1.3 Space Charge	162
6.1.4 Calculating Error and Uncertainty	166
6.2 Solid vs. Sintered Tungsten	169
6.3 Surface Metrology of Sintered Tungsten	170
6.3.1 General Observations	170
6.3.2 Surface Pores	173
6.3.3 Crystallographic Orientation	178
6.4 Cs-on-Sintered Tungsten: Anneal Cleaned Only	183
6.4.1 QE vs. Coverage	183
6.4.2 Approximating Work function	185
6.4.3 Cathode Lifetime	189
6.4.4 Surface Diffusion of Cesium	191
6.5 Cs-on-Sintered Tungsten: Argon Ion Beam Treated	193
6.5.1 QE vs. Coverage	194
6.5.2 Approximating Work function	197
6.5.3 Cathode Lifetime	198
6.5.4 Surface Diffusion of Cesium	200
6.6 Cesium-on-Tungsten: Theory vs. Experiment	202
6.6.1 Predicted vs. Measured QE	202
6.6.2 Crystallographic Complications	206
6.7 Cesium-on-Silver Photocathode	208
6.7.1 Theory Validation: QE vs. Coverage	208
6.7.2 Cathode Lifetime	212
6.8 Discussion of Ion Beam Cleaning	214
6.8.1 Summary of Surface Characteristics	214
6.8.2 Surface Morphology	217
6.8.3 Hydrogen Ion Beam Results	220
7. Dispenser Cathode	223
7.1 Design and Fabrication	223
7.1.1 Cesium Chromate Pellets	224
7.1.2 Dispenser Cell	225
7.1.3 Heater Mount	228
7.2 Vacuum Insertion	229
7.2.1 Modified Anode-Cathode Configuration	230
7.2.2 Pump-down Procedure	231
7.2.3 Argon-Ion Cleaning	234
7.3 Dispenser Activation	234
7.3.1 Activation Temperature	235
7.3.2 Chamber Conditions during Activation	236
7.3.3 Post-Activation Performance	239
7.4 Rejuvenation Process	244
7.4.1 QE Recovery	244
7.4.2 Indirect Coverage Measurement	246
7.4.3 Chamber Conditions	247
7.5 Modes of Operation	248

7.5.1 Periodic Rejuvenation	249
7.5.2 Continuous Rejuvenation	251
8. Conclusion and Discussion	252
8.1 Precursor Studies	252
8.1.2 Coated Metals	252
8.1.2 Coated Metals	253
8.1.3 Surface Metrology	254
8.1.4 Cleaning Techniques.....	254
8.1.5 Theory Validation	255
8.2 Dispenser Studies.....	256
8.2.1 General Remarks.....	256
8.2.2 Operating Parameters.....	257
8.2.3 Literature Representation.....	258
8.3 Future Studies	259
8.3.1 Application to High QE Photocathodes	259
8.3.2 Conventional vs. Controlled Porosity	260
8.3.3 Alternative Forms of Cesium.....	261
8.3.4 Related Studies.....	261
8.4 Closing Remarks.....	262
Bibliography	264

List of Tables

Table 1: Characteristics of various photocathodes	7
Table 2: Work functions of Various Metals.	13
Table 3: Ionization energies for selected alkali metals	17
Table 4: Comparison Between Photo- and Thermionic Emission.....	30
Table 5: Drive Laser State of the Art.....	31
Table 6: Chamber Information.....	39
Table 7: Temperature Required for nTorr Vapor Pressures	55
Table 8: Task-Specific State of Gas Valves (Open=1, Closed=0)	59
Table 9: Bandgap Energies of Various Semiconductors	66
Table 10: Laser Specifications.....	68
Table 11: List of Labview Instrument Interface VIs	89
Table 12: Argon gas discharge cleaning parameters	96
Table 13: Labview Process Control Programs and Subroutines.....	106
Table 14: Characteristic Lengths for Cesium Atoms.....	151
Table 15: Surface Densities and Cesium Thickness for Various Crystal Planes.....	152
Table 16: Work function of Various Metals	155
Table 17: Uncertainty in Measurements Used to Calculate QE	167
Table 18: Surface Characteristics of Annealed and Ion Beam Cleaned Substrates..	217

List of Figures

Figure 1.1: Band structure for semiconductors and metals.....	4
Figure 3.1: Cesium Deposition Process.....	34
Figure 3.2: Side view of sintered tungsten cathode.....	36
Figure 3.3: Dispenser Cathode with Heater Mount.....	37
Figure 3.4: Cesium Evaporation from External Source.....	38
Figure 3.5: Front View of Chamber Model.....	39
Figure 3.6: Front View of Fabrication Chamber.....	40
Figure 3.7: Rear View of Chamber Model.....	40
Figure 3.8: Side View of Anode-Cathode Assembly.....	41
Figure 3.9: Electrical Standoffs.....	42
Figure 3.10: Front-view of Anode and Cathode.....	42
Figure 3.11: Pressure vs. Time for Isolated Roughing Station.....	43
Figure 3.12: Gas Evolution with No Ion Pumping.....	50
Figure 3.13: Calculated Pressure Profile across Chamber Vertical Axis.....	52
Figure 3.14: Measured Pressure Profile along Chamber Vertical Axis.....	53
Figure 3.15: Pressure vs. Time During System Bakeout.....	56
Figure 3.16: Network of Gas Valves Connected to Chamber.....	57
Figure 3.17: Network of Gas Valves Connected to Chamber.....	59
Figure 3.18: GPIB-Controlled Gas Valve.....	60
Figure 3.19: Occupancy of Allowed Energy Bands.....	64
Figure 3.20: Laser Diode Module - Three Terminal Device.....	69
Figure 3.21: Lasers used to Measure QE.....	69
Figure 3.22: Effect of Temperature Stabilization on Laser Output Power.....	70
Figure 3.23: Optical Power Stability of Lasers.....	71
Figure 3.24: Coated Plexiglas Laser Safety Enclosure.....	72
Figure 3.25: Hole in Optical Enclosure for Laser Viewport.....	72
Figure 3.26: Single Axis Robot for Sequential Laser Positioning.....	73
Figure 3.27: Lasers Mounted on Single Axis Robot.....	74
Figure 3.28: Velocity Profile of Linear Actuator & Laser Shuttle.....	77
Figure 4.1: Illustrations of Deposition Monitor Sensor Head.....	81
Figure 4.2: Relative Positions of Cathode and Deposition Monitor.....	83
Figure 4.3: Wavelength-Dependent Transmission of Quartz Viewport.....	85
Figure 4.4: SRS Residual Gas Analyzer.....	87
Figure 4.5: Example Labview Instrument Interface VI.....	88
Figure 4.6: High Voltage Electrical Vacuum Feedthrough.....	91
Figure 4.7: Paschen Discharge Curve: Field vs. Pressure.....	91
Figure 4.8: Cathode Bakeout Profile: Pressure and Temperature vs. Time.....	94
Figure 4.9: Cathode Cooling via Conduction and Radiation.....	95
Figure 4.10: DC Argon Discharge Cleaning of Cathode Surface.....	95
Figure 4.11: Cesium Sources mounted on 2.75" Flange.....	98
Figure 4.12: Early Stage of Cesium Outgassing.....	99
Figure 4.13: Later Stage of Cesium Source Outgassing: Activation.....	100
Figure 4.14: Background Gas Composition During Cesium Deposition.....	101
Figure 4.15: Constant Deposition Rate of Cesium Source.....	102

Figure 4.16: Custom Fabricated Antimony Evaporation Source.....	103
Figure 4.17: QE Measurement Circuit.....	104
Figure 4.18: Isolated Voltage Source for QE Circuit	104
Figure 4.19: Labview Programming Hierarchy	106
Figure 4.20: Schematic Diagram of Multiple Wavelength QE Measurement VI.....	108
Figure 4.21: Front Panel Labview Interface for QE Measurements.....	109
Figure 4.22: Interdependency of VIs in Multiple Wavelength QE Measurement....	110
Figure 4.23: Flow Chart of QE Experimental Process	111
Figure 4.24: Saddle Field Ion Source	115
Figure 4.25: Ion Beam Port Alignment Bellows	115
Figure 4.26: Ion Beam Alignment Scheme.....	117
Figure 4.27: Gas Composition during Argon Ion Beam Treatment	121
Figure 4.28: Gas Composition during Hydrogen Ion Beam Treatment.....	122
Figure 4.29: Ion Beam Characteristics as a Function of Working Distance.....	124
Figure 4.30: Test Pattern for Optical Microscope Calibration	128
Figure 4.31: Profilometry of Polished Tungsten.....	129
Figure 4.32: Scanning Electron Microscope and Focused Ion Beam System	131
Figure 5.1: Comparison of Modified Gyftopoulos Levine to Work function Data..	143
Figure 5.2: Geometry of Photoelectron Path Length To Barrier	149
Figure 5.3: Theory Comparison to QE Data from Cu [59].....	150
Figure 6.1: Photocurrent Background Noise	155
Figure 6.2: Picoammeter Open-circuit Noise	156
Figure 6.3: Characteristic QE vs. Cesium Coverage Curve.....	157
Figure 6.4: QE vs. Time - Desorption of Various Cesium Layer Thicknesses	160
Figure 6.5: Desorption Heating Profile.....	161
Figure 6.6: Evaporation Rate of Multiple Monolayers of Cesium	161
Figure 6.7: Photocurrent vs. Laser Power Outside of Space Charge Regime	163
Figure 6.8: Saturated Current in the Space Charge Limited Regime	164
Figure 6.9: Defining Space Charge Regime: Photocurrent vs. Voltage	165
Figure 6.10: Constant QE with respect to Laser Power.....	165
Figure 6.11: QE vs. Coverage with Noisy Photocurrent	168
Figure 6.12: QE vs. Coverage with Reduced Uncertainty in Photocurrent.....	168
Figure 6.13: Sintered Surface at 50x Magnification.....	170
Figure 6.14: Images (500x) Top and Bottom Surfaces of Sintered Tungsten	171
Figure 6.15: Top Sintered Tungsten Surface at 1500x Optical Magnification.....	172
Figure 6.16: Bottom Sintered Tungsten Surface at 1500x Optical Magnification ...	172
Figure 6.17: Representative Sub-micron Pores in Sintered Tungsten	174
Figure 6.18: Measure Pore Size Using FIB Milling	174
Figure 6.19: Spatial Distribution of Pores on Dispenser Surface	176
Figure 6.20: Log-Normal Fit for Pore-Pore Separation Distance.....	176
Figure 6.21: Voronoi Diagram for Pores on Dispenser Cathode Surface.....	177
Figure 6.22: Distribution of Areas Surrounding Dispenser Pores	178
Figure 6.23: FIB Image Revealing Crystallographic Map.....	179
Figure 6.24: FIB Milling - Wide Angle View (top) & Back Wall (bottom)	181
Figure 6.25: 3D Image of a Sintered Tungsten Grain.....	182
Figure 6.26: Multi- λ QE vs. Coverage for Annealed Sintered Tungsten	184

Figure 6.27: Normalized QE vs. Coverage (Heat Anneal Only)	185
Figure 6.28: Peak QE vs. Wavelength (Heat Anneal Only)	187
Figure 6.29: Inverse Quadratic Relationship between QE and Wavelength	188
Figure 6.30: Work function of Monolayer Cs on W - Heat Anneal Only	188
Figure 6.31: Lifetime of Cesium Sintered Tungsten - Heat Anneal Only	190
Figure 6.32: Background Gas Composition During Lifetime Measurement.....	190
Figure 6.33: Cesium Desorption from Anneal Cleaned Sintered Tungsten	191
Figure 6.34: QE vs. Time for Deposition Followed By Desorption.....	192
Figure 6.35: Heat Anneal vs. Ion Beam Treatment Using QE Measurements	196
Figure 6.36: Repeatability of Argon Ion Cleaning Process	196
Figure 6.37: Effect of Annealed vs. Ion Beam Treatment on Work function	197
Figure 6.38: Cathode Lifetime for Ar-Ion Cleaned Sintered Substrate	199
Figure 6.39: QE Peaks from Cesium Deposition and Desorption	200
Figure 6.40: QE vs. Coverage - Comparison of Theory to Experiment	203
Figure 6.41: QE vs. Coverage - Linear Comparison with Exp Uncertainty	203
Figure 6.42: Distinguishing Crystal Faces with FIB Image	207
Figure 6.43: Approx. Distribution of Crystal Faces on Sintered Tungsten	207
Figure 6.44: Cesium-on-Silver Photocathode: Theory vs. Experiment.....	210
Figure 6.45: Optical Micrograph Showing Roughness of Silver Substrate.....	210
Figure 6.46: Surface Profilometry of Polished Silver Substrate.....	211
Figure 6.47: Cesium-on-Silver Lifetime.....	213
Figure 6.48: Cesium Desorption from Silver at Elevated Temperature	213
Figure 6.49: Plausible Conclusions from Ion Beam Treatment Data	216
Figure 6.50: Tungsten Before (top) and After (middle, bottom) Ar Beam Cleaning	219
Figure 6.51: QE vs. Cesium Coverage after Hydrogen Ion Beam Cleaning	221
Figure 7.1: Cesium Chromate Powder Pellet, and Fabrication Press	224
Figure 7.2: Schematic Diagram of the Dispenser Cathode Cell	225
Figure 7.3: Top Surface of Dispenser Cathode Showing Pin Hole Leak	227
Figure 7.4: Dispenser Hermetic Seal (left); Ready for Vacuum Insertion (right)	228
Figure 7.5: Schematic Diagram of Copper Cathode Heater Mount.....	229
Figure 7.6: Cathode Holder (Top)	229
Figure 7.7: Cathode Holder (Bottom).....	229
Figure 7.8: Dispenser Cathode Mounted on Button Heater.....	230
Figure 7.9: Completed Anode-Cathode Assembly	231
Figure 7.10: Front Face of Anode-Cathode Assembly Showing Mutual Alignment	231
Figure 7.11: Background Gas Composition During Dispenser Outgassing	233
Figure 7.12: Critical Temperatures Observed During Dispenser Activation	235
Figure 7.13: Onset of Photoemission for Different Wavelengths.....	237
Figure 7.14: Persistent Outgassing During Activation Procedure	237
Figure 7.15: Cesium Deposition in Chamber During Dispenser Activation	239
Figure 7.16: Total Cathode Current and Thermionic Current After Activation	240
Figure 7.17: Chamber Deposition Immediately Following Dispenser Activation ...	241
Figure 7.18: QE of Dispenser Cell During Post-Activation Cooling Phase	243
Figure 7.19: Total Cathode Current during Post-Activation Cooling Phase	243
Figure 7.20: Cathode Regeneration Shown By QE Recovery	245
Figure 7.21: Determining Optimal Rejuvenation Temperature	246

Figure 7.22: Cesium Coverage Measured Indirectly Using QE	247
Figure 7.23: Chamber Conditions During Dispenser Rejuvenation Process	248
Figure 7.24: Lifetime of Dispenser Cathode at Room Temperature	250
Figure 7.25: Background Gas Composition during Lifetime Test	250
Figure 7.26: Dispenser Cathode Lifetime in Continuous Rejuvenation Mode.....	251

1. Introduction

1.1 Overview

Photocathodes have a long history of use in photomultiplier tubes and single photon detectors [1], but have only recently been proposed as a source of high brightness electrons for use in free electron lasers (FELs), energy-recovery linacs (ERL), advanced x-ray sources, high energy linear colliders, and pump-probe experiments [2],[3]. A photoinjector for these applications consists of a photocathode illuminated by short, picosecond-scale drive laser pulses which are in synchronism with the accelerating phase of an RF field [4]. Present drive laser technology can produce pulses that have fast rise time, fast fall time, a flat top, and short duration. If the response time of the cathode is sufficiently prompt, the electron beam preserves this pulse format as it is accelerated to relativistic energies, yielding a high current, high quality beam [5].

Traditional thermionic injectors produce electrons by electronically gating a thermionic cathode to produce long electron beam pulses at low energy. While simple and robust, these sources are not capable of producing beams of requisite quality for the applications listed above [3]. Because the goal is to obtain very short pulses, thermionic emission requires longitudinal compression in sub-harmonic bunching cavities prior to being accelerated to relativistic energies. This compression process degrades the initial beam quality because nonlinear forces from space-charge and bunching fields lead to emittance growth [6]. A photoinjector avoids this difficulty altogether by producing the desired high current pulse directly at the cathode [4].

The quest has been to find the optimum photocathode for use in a practical photoinjector. An ideal photocathode should have high quantum efficiency (defined as the ratio of emitted electrons to incident photons), fast temporal response, long lifetime, and minimal complexity [7]. Such cathodes do not currently exist, and the accelerator community has struggled to find a compromise among these factors. In order to preserve practical drive laser requirements, a photocathode with fast temporal response and good quantum efficiency ($>1\%$) in the visible or soft ultraviolet is desired [8],[9]. Metal photocathodes such as copper exhibit long lifetime and fast response, but have low quantum efficiency ($<10^{-4}$) due to their high optical reflectivity and high work function [10]. Semiconductor photocathodes have much better QE (on the order of several percent) but are slower emitters and typically exhibit very short lifetimes in nano-Torr vacuum situations because of their chemical reactivity [11]. Many of the highest QE cathodes include cesium either as a surface layer or as a chemical compound, such as Cs_3Sb . Lifetime is limited in the case of cesium based metallic and semiconductor photocathodes by the loss of cesium from the photosensitive surface layer and by contamination from background gases.

This project focuses on developing methods to extend the effective lifetime of cesium-based high QE photocathodes. Cesium and other alkali metals are known to reduce the work function of the substrate onto which they are evaporated [12]. Qualitatively, this is due to the fact that the cesium atoms give up their single valence electron and reside on the surface as a positive charge. The effective dipole moment set up by these charges at the surface assists a photo-excited electron in crossing the barrier potential, leading to a lowered work function. The reduction in work function

is sufficient to allow some metals to perform reasonably well as photoemitters in the UV portion of the optical spectrum. Desorption (and chemical reactivity) of the photosensitive cesium layer, however, causes QE to decrease with time because the layer is both leaving the surface and being poisoned by contaminants. If this layer could be replenished *in situ*, then lifetime would be less of a problem because periodic or continuous rejuvenation could restore the cathode's photosensitive layer.

This research program is divided into two parts: the first is to develop experimental methods and a photoemission theory [7],[13] that permits multi-wavelength characterization of cesium-based photocathodes; the second is to develop the dispenser concept [14] into a working near-room temperature prototype with a demonstrated ability for either periodic or continuous *in situ* rejuvenation.

1.2 Photocathode Characteristics

The relevant properties that characterize a photocathode are spectral response, operational lifetime, temporal response, damage threshold, and transverse energy spread (of emitted electrons). Each of these is discussed in turn.

1.2.1 Spectral Response

Spectral response refers to the manner in which quantum efficiency varies with the frequency of incident light. Some photocathodes may operate over an entire range of frequencies, while others perform best in the UV, for example. Copper and cesium telluride respond only to ultraviolet, while potassium cesium antimonide and cesiated metals can be operated in the visible spectrum. The best photoemitters have quantum efficiencies approaching 50%, while typical values range from 0.001-10%.

The wide variation in quantum efficiencies is due to the events that occur as the electron migrates to the surface of a photocathode. The threshold wavelength corresponds to the lowest frequency of incoming light with sufficient energy to overcome either the work function (in a metal) or the bandgap plus the electron affinity (in a semiconductor), as shown in Figure 1.1.

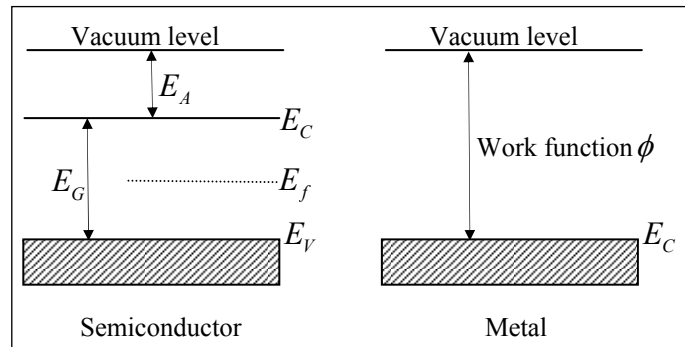


Figure 1.1: Band structure for semiconductors and metals

1.2.2 Lifetime

The operational lifetime of a photocathode depends largely on the vacuum in which it operates. Several factors may contribute to limited lifetime, depending on the type of cathode in question. For semiconductors, adsorbed surface films and surface oxides tend to decrease quantum efficiency (with the exception of coatings used to activate NEA surfaces). The rate at which these films form depends on the background pressure and composition. Ion back bombardment in DC guns damages the cathode surface and degrades performance. For alkali-metal systems such as cesiated tungsten, the photosensitive layer can desorb because of localized heating or be damaged by the mechanisms described above. Certain compounds such as water and carbon monoxide can “poison” the cathode, further reducing its operational

lifetime. Dispenser cathodes have an extended operational lifetime because their photosensitive surface films can be rejuvenated to some extent during a periodic reconditioning period.

1.2.3 Response time

The response time of a photocathode depends upon the penetration depth of incident photons. If photoelectrons are created deep within the bulk and have sufficient energy to escape to vacuum upon arriving at the surface, then their transit time determines the promptness of emission. Because the penetration depth for photons in metals is shallow, photoelectrons are created only very near the surface. Because they have only a miniscule distance to travel to the surface, they result in prompt emission and can closely follow the short pulses (picoseconds) of a drive laser. Semiconductor photocathodes, however, have longer penetration depths, so photoelectrons will be created deep within the bulk and their transit time to the surface leads to a delay in emission. Optical penetration depths in semiconductors can approach hundreds of nanometers, as evidenced by the fact that typical response times are on the order of several picoseconds. If a photoelectron has energy equal to 1eV, then it travels about 1 micron in 2 picoseconds. Its trajectory from the point of excitation to the surface is very likely convoluted because of multiple phonon interactions with the crystal lattice. This added path length, together with the longer optical penetration depth, leads to characteristically longer response times for semiconductors.

It is worth noting that just as long response times are undesirable, so too are those that are extremely short. Drive lasers systems in the visible range use

frequency-doubled or tripled mode-locked fundamental wavelengths of approximately 1 micron. The frequency multiplication is a non-linear process that introduces inherent jitter and noise on the laser pulse. These undesired time variations can be replicated on the electron beam if the photocathode exhibits an extremely short response time. A response time of about 1 picosecond washes out drive laser noise and still preserves the phase relationship between electron emission and the accelerating electric field.

1.2.4 Damage Threshold

Damage threshold refers to the maximum laser intensity a photocathode can withstand without suffering damage to its surface. Cathodes that utilize surface films to reduce work function are more delicate and will have lower damage thresholds than bare metals. The damage mechanisms are usually localized heating or plasma formation at the surface. Damage threshold is not considered a critical cathode parameter because the intensity of most drive lasers is well beneath it.

1.2.5 Transverse Energy Spread

Cathodes with low work functions permit the generation of photoelectrons with energies well above that required to escape to vacuum. Consequently, some of these can suffer collisions and still escape, although with lower energy than those that do not suffer collision. Because emitted electrons have a range of energies, a transverse energy spread is imparted to the resulting beam. The variation, however, is on the order of an electron volt, so when the beam is accelerated to much higher

energies these small differences become less important. Only in applications with low beam energy is transverse energy spread of the emitted electrons considered critical.

Characteristics of some commonly used cathodes, including metals and semiconductors, are listed in Table 1. Notice that semiconductor-based cathodes exhibit very high QE with respect to metals, but require a nano-Torr vacuum and last in some cases only a few hours. A method for extending lifetime while preserving high QE is a main objective of this program and is detailed in subsequent chapters.

Material	λ (nm)	QE at λ	Lifetime	Response Time	Vacuum (Torr)	Max Field (MV/m)
Cs ₃ Sb	527	4%	$T_{1/2} < 4$ h	~1 ps	10^{-9}	> 20
Cs ₂ Te	263	13%	$T_{1/e} > 100$ h	~3 ps	10^{-9}	> 20
K ₂ CsSb	527	8%	$T_{1/2} < 4$ h	~1 ps	10^{-9}	> 20
Cu	266	1.4×10^{-4}	very long	< ps	10^{-7}	> 100
Y	266	5×10^{-4}	long	< ps	$< 10^{-7}$	~100
Mg	266	6×10^{-4}	> 5000 h	< ps	10^{-7}	~20
Ba	337	0.1%	2 hr	< ps	$< 10^{-7}$	~50

Table 1: Characteristics of various photocathodes

1.3 Electron Beam Characteristics

The “quality” of an electron beam launched by a photocathode is frequently mentioned in the literature [15] and throughout this dissertation. It is useful to clarify such terminology by introducing the formal definitions of emittance and brightness.

1.3.1 Emittance

A useful figure of merit for electron beams in accelerator applications is that of *emittance*, defined essentially as the produce of the size of the beam and its divergence. No single definition of emittance is used consistently throughout the

literature, although all references are related [16]. The particles comprising a beam occupy a volume in six dimensional phase space defined by position and momentum, so that emittance is closely related to the two dimensional projection of this volume in the trace space of a given coordinate (i.e. x - x'). Some researchers use the area of this projection as a definition for emittance, but as Reiser points out, this definition does not distinguish between a well-behaved beam and one that is distorted due to nonlinear forces. In describing the quality of a beam, it is more appropriate to define an *rms emittance* $\tilde{\epsilon}_x$, defined by using the moments of the electron distribution in trace space $\langle x^2 \rangle$, $\langle x'^2 \rangle$, and $\langle xx'^2 \rangle$:

$$\tilde{\epsilon}_x = \left[\langle x^2 \rangle \langle x'^2 \rangle - \langle xx'^2 \rangle \right]^{1/2} \quad (1.1)$$

Each point within the emission area of a cathode emits electrons with a slightly different initial energy and direction. The resulting velocity spread is due not only to the intrinsic (thermal) randomness of emission but also to localized differences in temperature, laser intensity, and work function. Regardless of its origin, the velocity spread remains with the emitted beam as it propagates downstream from the source. As defined above, emittance depends upon the kinetic energy of the beam. Thus, in order to correctly compare beams of different energy, it is necessary to introduce a *normalized emittance* ϵ_n by using the Lorentz factor $\gamma = [1 - \beta^2]^{-1/2}$, where $\beta = v/c$ is the ratio of particle velocity v to the speed of light c in vacuum [16]:

$$\epsilon_n = \beta \gamma \tilde{\epsilon} \quad (1.2)$$

This value of beam quality is typically used when comparing the performance of different photoinjectors. The normalized emittance of the LANL gun mentioned

earlier, for example, is reported to be 40 mm-mrad [23]. A lower bound exists for normalized rms emittance, determined by cathode radius r_c and temperature T [16]:

$$\varepsilon_n = 2r_c \left(\frac{k_B T}{mc^2} \right)^{1/2} \quad (1.3)$$

1.3.2 Brightness

Emittance is not comprehensive in its description of electron beam quality, because it can be reduced simply by passing the beam through collimating slits that reduce velocity spread by removing divergent particles. While this improves beam quality, it obviously reduces beam current. A more appropriate figure of merit is *brightness*, defined typically as the current density J per solid angle $d\Omega$: $B = J / d\Omega$. Following the definition of brightness developed for electron microscopy [17], the normalized peak brightness B_n is given by [15]:

$$B_n = \frac{2I}{\sqrt{\pi} \varepsilon_{nx} \varepsilon_{ny}} \quad (1.4)$$

where ε_{nx} and ε_{ny} are the normalized phase space areas of the beam in the transverse directions and I is the peak current. Using $r_c = (I / J\pi)^{1/2}$ in (1.3), the above expression shows that peak brightness is directly proportional to current density and inversely proportional to cathode temperature. This relationship illustrates why photoemission has advantages over thermionic emission: cathode temperature is lower while current density is several orders of magnitude higher, resulting in higher normalized peak brightness [15].

1.4 Basic Photoemission Model

The process of photoemission can be viewed as a three-step process consisting of 1.) photon absorption, 2.) electron migration to the surface, and 3.) overcoming the barrier potential [18]. This perspective allows photoemission to be related to characteristics of the material, such as scattering coefficient, optical reflectivity, and potential barrier height. Using this theory, the response times of existing cathodes has been estimated and found to cover a range of six orders of magnitude [18]. In general, there is an inverse relationship between the response time of a photocathode and its quantum efficiency.

Metals make very prompt emitters because electrons which can escape the barrier are found very close to the surface, but the high optical reflectivity of metals greatly limits their quantum efficiency because few photons are actually absorbed. Semiconductors, however, are less reflective and less conductive, so more photons are absorbed and are capable of escaping upon arriving at the surface. Because more electrons can overcome the surface barrier in semiconductors, they tend to have higher quantum efficiencies than metals [18]. Since many electrons come from within the bulk, however, their transit time to the surface lengthens the response time. For accelerator applications, a fast temporal response is required so that the electron pulse occupies only a small fraction of the RF phase. If this is not the case, then electrons throughout the bunch experience different accelerating gradients and end up having a spread of energies.

During the first fifty years of study on photoemission, it was considered a surface, rather than bulk effect [19],[20]. But the first monolayer can absorb at best

10% of the incoming light [21] and if this were to account for the entire process, the quantum efficiency could not exceed 0.001 for any material [1]. This is clearly not the case, so photoemission in general must be considered an event involving both the surface and the bulk. In modern literature, the term ‘surface’ is reserved for the literal monomolecular layer of a material. A primary distinction between the various types of photocathodes is the degree to which they can be considered metallic versus semiconducting. It is useful to distinguish between these two cases. Using band theory, metals are distinguished from insulators and semiconductors by the fact that, at absolute zero, their conduction band remains partially full. Semiconductors, at absolute zero, will have an empty conduction band separated by gap E_g from a full valence band. Thus, ideal semiconductors are perfect insulators at absolute zero, but as temperature is increased some electrons are promoted to the conduction band and give rise to conductivity. In context of photoemission, in order for an electron to escape to vacuum, it must overcome not only the band gap but also the surface potential barrier, given by the electron affinity E_A .

Returning to the three-step Spicer model [18], recall that the sequence consists of photon absorption, migration to the surface, and crossing the barrier into the vacuum. A more rigorous treatment is given later during theory discussion, but it is useful to consider each of these three processes in turn before moving forward.

Because of the characteristically high optical reflectivity in metals, the process of photon absorption is inherently limited. Semiconductors are less reflective than metals and consequently more incident photons are absorbed if their energy exceeds the bandgap [22].

After absorption, a photoelectron could be traveling in any given direction within the metal. Only electrons whose energy was augmented by photon absorption above the vacuum barrier are capable of being photoemitted. Furthermore, those traveling away from the photoemitting surface will certainly not escape, regardless of their absorbed energy. An electron which has absorbed a photon is considered a *hot* electron because its energy is higher than that of other electrons in thermal equilibrium. Any interactions between this photoelectron and other electrons or the lattice will reduce the chances of it arriving at the surface with sufficient energy to cross the barrier. Because of the abundance of free electrons in metals, a photoelectron will undergo many collisions with other electrons and rapidly thermalize. Only electrons excited within a few atomic layers of the surface will arrive with sufficient energy to escape and contribute to photoemission. In semiconductors, the dominant scattering mechanism is electron-phonon interaction. The energy loss per lattice interaction is much less than the energy loss per electron-electron interaction, so photoelectrons in semiconductors can travel much further distances (compared to electrons in a metal) before reaching thermal equilibrium [18]. This means that for a given number of incident photons, more photoelectrons will reach the surface with sufficient energy to cross the barrier potential.

The third step in Spicer's model involves the surface barrier. For metals, the surface barrier is simply the work function. Photoelectrons excited within the metal can only escape to vacuum if their energy upon arrival at the surface exceeds the work function. The work function of most metals is rather high, as seen in Table 2.

Metal	ϕ (eV)
Silver	4.26
Copper	4.65
Molybdenum	4.37
Tungsten	4.65
Cesium	2.14

Table 2: Work functions of Various Metals.

As stated before, a photoelectron in a semiconductor can only cross the surface barrier if it has energy equal to $E_A + E_g$. From this discussion it is obvious that metals will have much lower quantum efficiencies than semiconductors, but will have faster response times.

Because metal cathodes can tolerate high electric fields, an effect analogous to the Schottky effect in thermionic emission can be used to effectively reduce the work function and improve quantum efficiency. In RF guns, fields on the order of 50 MeV/m can be achieved [23]. This can reduce the amount of energy needed by a photoelectron to escape to the vacuum, causing a shift in the threshold wavelength toward the red. It was found that the magnitude of the shift is roughly proportional to the square root of the applied field [13].

1.5 Types of Photocathodes

Metallic photocathodes are of primary focus in this study because their behavior with respect to surface coatings (such as cesium) can be carefully studied and used to measure the delivery of these coatings from a dispenser cathode. Semiconductor cathodes can be built upon the dispenser structure, as detailed in the latter part of this dissertation, so a discussion of both cathode types is justified.

1.5.1 Metallic Cathodes

Work function is a fundamental characteristic of the metallic cathode substrates employed in this research and various experimental methods are used to measure it. There are three ways that are experimentally convenient: thermionic emission, photoemission, and contact potential difference. The energy required for an electron to escape to vacuum from a metal surface can be obtained by making use of the Richardson equation:

$$I = AT^2 e^{\frac{-e\phi}{k_B T}} \quad (1.5)$$

where T is the temperature, I is the current. If $\ln[I/T^2]$ is plotted versus $1/T$, the resulting straight line is called the Richardson line [22] and its slope is ϕ .

Fowler developed a theory in the 1930's that predicts the shape of spectral response curves in the threshold region [24], a so-called Fowler plot. By fitting such a plot to an experimental curve, an exact value for work function can be obtained. DuBridge extended this method such that the wavelength of incident light could be held constant and the cathode temperature varied instead [25]. The work function can then be found by measuring the quantum efficiency as a function of temperature. A third way to utilize photoemission to determine work function is to measure the maximum velocity of emitted electrons using a retarding field and monochromatic light [22].

If two metals with different work functions are brought into contact, electrons from the lower work function metal will migrate to the higher work function metal, leaving the first metal positive and the other negative. This gives rise to a potential difference at the contact surface equal to the difference of the work functions.

Therefore, if the work function of one metal is reliably known, that of another can be found by measuring this contact potential difference. A common arrangement is to direct an electron beam onto both a reference metal and one whose work function is to be determined. If the current from each electrode is plotted with respect to the voltage, the two curves are displaced relative to each other by an amount equal to the difference of work functions [26]. Although this method seems experimentally simple, contamination of the reference metal can easily lead to erroneous results. And because the thermionic method is useful only for metals with sufficiently high melting points, the Fowler method is the most universally applicable method of measuring the work function of a metal [24].

1.5.2 Effect of Surface Films on Metallic Cathodes

Surface films can greatly alter the photoemissive properties of a material and can be used to fabricate more efficient photocathodes [27]. The effect of a surface film on the work function of a material depends upon the film composition and upon the bonding mechanism involved. If the binding forces between the substrate and the film are weak (i.e. Van der Waals bonds), then the effect of this film on the work function is negligibly small [22]. Conversely, if there is a strong ionic character to the bond, the resulting dipoles at the surface, depending on their polarity, either increase or decrease the work function. The precise relationship between the thickness (or, equivalently, coverage) of a surface film and the work function of the substrate is not trivial but can be modeled quite well by considering the adsorbate and substrate atoms to be hard spheres [13],[28]. It is widely observed that the coverage of interest to the properties of photoemission is on the order of monolayers (usually less than a

monolayer). This is because the emission process occurs within a few hundred Angstroms of the surface barrier. If the surface film were to have this same thickness, then the emission properties observed would be those of the film itself, not of the substrate [22].

Except for the noble gases, some degree of ionic bonding will always occur between the metal and a surface layer of atoms. Adsorbed layers of argon, for example, have little or no effect on the metal's work function because a surface dipole moment is not created. Elements on the right hand side of the periodic table are electronegative and (as a surface film) increase the work function of the metal. The opposite is true of films formed from elements on the left of the periodic table: the positive charge assists the escape of electrons from the surface and reduces the work function. Surface films of oxygen on metals, for example, will increase the work function unless the resulting oxide diffuses into the bulk and exposes new atomic layers of the metal [27].

Because alkali and alkali-earth metals form dipoles on the surface of metals that facilitate photoemission, they are the most effective at reducing the work function. This effect was observed by Langmuir [29],[30] in his studies of thermionic emission from coated tungsten. He found that for a cesium surface layer on tungsten, the resulting work function of the two materials was lower than either of them taken individually. The experiments of Langmuir and others, including this work, suggest that the work function reduction is greatest for *less* than a monolayer of adsorbed cesium. The question then becomes how to define a monolayer (i.e. how many atoms associated with a monolayer). This discussion is pursued further in later chapters of

the dissertation. Even if a surface density of atoms is assumed or calculated, the microscopic surface area is difficult to determine for all but single crystals because polycrystalline metals are microscopically irregular. In any case, Langmuir published an optimal coverage factor of Cs on W at about 70%, which agrees with more recent efforts as well as the experimental results described later in this work [13], [30], [31], [32].

In addition to an optimal coverage, another factor is directly correlated to the work function: the *difference* between ionization energy of the alkali metal and the work function of the substrate. If this difference is augmented, the work function is reduced [22]. Minimum work function values for Cs-on-W vary from 1.4 – 1.7 eV. Notice that Cs has ionization energy of 3.87 eV, while W has a work function of 4.65 eV. The difference between the two (0.78 eV) is greater, for example, than the corresponding difference for the case of K and W. Consequently, a surface layer of potassium has less of a work function reduction effect on tungsten than cesium does. Other ionization energies are listed in Table 3.

Metal	Ionization Energy (eV)
Ba	5.19
Ca	6.09
Cs	3.87
K	4.16
Na	5.12

Table 3: Ionization energies for selected alkali metals

It is also reported that for single crystals, the extent to which the work function is reduced depends upon which crystal face the alkali film is formed [22]. On single crystals of tungsten, for example, the (100) face has a lower work function

at $\phi = 1.82\text{eV}$ than the (110) face with $\phi = 2.06\text{eV}$ [33]. Lastly, it is important to realize that because cesium is so electropositive, it will have a work function-reducing effect on many metals [20]. In the case of copper, cesium reduces the work function from 4.54 eV to 1.55 eV and for silver the reduction is from 4.62 eV to 1.55 eV [19].

1.5.3 Semiconductor Photocathodes

Several comments have already been made about semiconductor-based photocathodes, but further discussion is useful in order to appreciate the challenges involved in understanding, modeling, and measuring these complex photoemitters.

In solids, electron energy levels are divided into bands and the occupancy of these levels determines the degree to which the material is metallic or an insulator. To understand the origin of the energy bands, it is useful to imagine a crystal whose lattice constant can be varied. When the separation distance between atoms is very large, then there is little interaction between valence electrons and their energy levels are simply the atomic levels with degeneracy N , the number of atoms in the lattice. As the lattice constant is reduced, the atoms become close enough for outer electrons to interact according to the Pauli Exclusion Principle, causing the formation of N very closely spaced levels (i.e. bands) clustered around the original atomic levels. At absolute zero, the electrons fill the energy levels up to the Fermi energy, whose value relative to band edges determines the electronic properties of the material in question. If the electrons completely fill a given band (and if a significant energy gap exists between the next adjacent band) then the material is considered an insulator. Recall that an electric current is defined by an electron distribution with a non-zero net

average velocity. Such a distribution can be achieved by an electric field only if vacant energy levels exist adjacent to those that are occupied. In the case of an insulator, an energy gap exists between occupied and unoccupied levels and an electric field is unable to impart the energy required to overcome the gap. In a metal, a given band is either partially full or overlaps an adjacent band such that an electric field can induce a net average velocity causing electric conduction in the material. For temperatures above absolute zero, the Fermi level is no longer the highest occupied energy level because (if the gap is not too large) electrons from one band may be thermally excited to the next higher band. This results in a certain number of charge carriers (holes and electrons) in each band, and the material is termed a semiconductor.

Semiconductor-based photocathodes differ significantly from metals and provide an advantage in terms of quantum efficiency, while exhibiting limitations in the form of short lifetime and longer temporal response. Photoemission from a semiconductor involves the same three steps discussed above, with several important differences. First, optical absorption occurs when an electron in the valence band is excited to the conduction band. This electron can be photoemitted only if it has sufficient energy to overcome the surface potential barrier given by the electron affinity, E_A , defined as the energy difference between the vacuum barrier and the bottom of the conduction band. The threshold energy E_T for photoemission (in the absence of impurities) is given by the sum of the band gap E_G and the electron affinity [18]:

$$E_T = E_G + E_A \quad (1.6)$$

Impurities in the semiconductor crystal complicate matters by creating energy states within the band-gap from which photoelectrons can also originate. Donor impurities give rise to photoemission at energies less than E_g because they tend to populate the conduction band and permit photoexcitation of those electrons at longer wavelengths.

As mentioned before, semiconductors have a much smaller number density of conduction electrons, which reduces the electron-electron scattering rate that is partly responsible for the low QE characteristic of metals. Thus, photoelectrons created deep within the bulk have a much better chance of arriving at the surface with sufficient energy to escape the barrier. Furthermore, the optical reflectivity of semiconductors is much less than metals, leading to increased photon absorption. The dominant scattering mechanism in semiconductors is electron-phonon scattering, which alters the direction of electron travel while leaving energy relatively unchanged. Thus, a photoelectron undergoing many such interactions will appear to make a “random walk” to the surface prior to being emitted, leading to the longer response times referenced in the introduction. It is worth noting that the electron-phonon interactions can, under certain conditions, improve QE. Recall that while photoelectrons initially have velocities which are uniformly distributed in all directions, only those with a component perpendicular to the emitting surface will escape [13]. If electron-phonon interactions can alter the velocity distribution of photoelectrons such that the surface normal component is favored, then more electrons will arrive at the surface and contribute to photoemission. For example, if the average loss per collision is 0.01 and the electron is excited 1eV higher than the vacuum level, then it can suffer 100 collisions and still be able to cross the barrier to vacuum [18].

It was mentioned earlier that the reduced electron-electron scattering in semiconductors is responsible for the higher photoemission efficiency. In order to understand this effect, consider a photoelectron excited just above the vacuum barrier. In a metal, unless the electron originates very close to the photoemitting surface, it will undergo an electron-electron scattering event because the number density of electrons is very high. In such an event, the primary electron will lose approximately half its original energy and the secondary electron will gain this same amount, so that neither will escape to contribute to photoemission. Thus, an optically excited electron in a metal can suffer electron-electron scattering, but such is not the case in a semiconductor because not all energies are allowed. A gap separates the states occupied with large numbers of electrons (i.e., valence band) from the lowest energy conduction band states. A photoelectron with energy near the vacuum barrier can scatter off another electron only if its energy is E_G higher than the conduction band minimum. If this condition is not met, then scattering cannot occur because there are no allowed final states available [18]. Thus, the only scattering mechanism for electrons excited near the threshold energy is electron-phonon scattering.

A necessary condition for obtaining high quantum efficiency is an escape depth L that exceeds the optical penetration depth ℓ_a . It should be obvious that if the escape depth is small and the penetration depth is large, few of the photoexcited electrons can contribute to quantum yield. Experimental observation has shown that escape depth $L(\hbar\omega)$ decreases with increased incident photon energy [34],[35]. In summary, the threshold response of a semiconductor is determined by the summing

its bandgap and electron affinity, while efficiency is dictated by the ratio of escape and penetration depths.

1.5.4 Negative Electron Affinity

It can be argued that the departure from empirical techniques in cathode development began with the introduction of negative electron affinity (NEA) emitters [18]. Recall that electron affinity is defined as the difference in energy between the bottom of the conduction band and the vacuum level. If the vacuum level is brought lower than the conduction band minimum, then electron affinity becomes negative. This situation is generally caused by starting with a low- E_A material and applying an external electric field (e.g., in the form of a dipole monolayer) which lowers the vacuum level below its natural value. A common example is cesiated GaAs, where the adsorbed cesium atoms create polarized surface bonds which can reduce the electron affinity by as much as 2-3eV [36],[37]. This situation is highly advantageous for photoemission because electrons photoexcited into the conduction band can diffuse toward the surface (even after thermalizing to the top of the conduction band) and cross the potential barrier to vacuum. Thus, nearly every photoexcitation leads to photoemission and causes the high efficiencies typically achieved with NEA cathodes. Two types of NEA surfaces are possible: *True* NEA occurs when the vacuum level is completely below the conduction band minimum, while *effective* NEA is characterized by a vacuum level *at the surface* that is lower than the conduction band in the bulk [38].

1.6 The Dispenser Cathode

A fundamental limitation for high QE photocathodes (i.e. semiconductors) is the chemical instability of their photoemitting surfaces [30]. The basic concept of the dispenser cathode is to overcome short lifetime by repairing the vulnerable surface layer. This concept has been successfully applied to thermionic emitters for decades, but has not been demonstrated for near-room temperature photoemitters [9]. Using the knowledge obtained in this work on the behavior of coated metallic surfaces, a prototype dispenser cathode was designed and fabricated using commercially available components. It consists of a sintered tungsten disk situated between a cesium reservoir and the photoemitting surface. Upon heating to 140-160°C, cesium diffuses through the tungsten barrier and coats the surface, forming a low-work function emitter. The operating parameters, including activation and rejuvenation temperatures, have been ascertained and an ability to dramatically extend the effective lifetime of cesiated tungsten has been demonstrated. These tests suggest that the room temperature dispenser photocathode developed in this work could serve as a cesium delivery mechanism that could improve the effective lifetime and efficiency of a number of different cesium-based cathodes in use today.

1.7 Project Summary

This dissertation is divided into two parts: a.) precursor work on cesium coated metals, including tungsten and silver, and b.) design, fabrication, and testing of a cesium dispenser photocathode. Chapter 2 provides a historical perspective of photocathode and photoinjector development, continuing the discussions initiated in

the Introduction. Chapters 3 and 4 discuss the experimental procedures involved in setting up the experiment and obtaining reliable data. Chapter 5 discusses the most relevant portions of a recent photoemission theory and Chapter 6 compares this theory to experimental data. Chapter 7 is devoted to the design and performance of the dispenser cathode, while Chapter 8 draws together the research efforts and concludes the work with a discussion of future directions. Highlights of accomplishments in this work include:

- 1) Model-based design and construction of a versatile cathode fabrication facility
- 2) Multi-wavelength characterization of cesiated tungsten and silver photocathodes
- 3) Demonstration of a novel near-room temperature dispenser photocathode prototype that could extend effective lifetime of cesium-based photocathodes
- 4) Cathode substrate cleaning technique using an energetic Ar^+ ion beam that improves lifetime and efficiency
- 5) Advanced cathode surface characterization techniques, including ion beam milling to determine 3D grain structure
- 6) Use of QE measurements as an indirect measurement of cesium coverage on the surface of a dispenser cathode.

2. Historical Landscape

A rich history has led to the present state of photocathode research and it is reviewed here in two parts, photocathodes and photoinjectors, with the goal of providing a perspective for present efforts.

2.1 History of Photocathodes

The photoelectric effect was discovered in 1887 by Hertz when he observed that the distance across which a spark could be induced was increased when ultraviolet light irradiated the negative electrode [39]. Hallwachs observed the same effect by discharging negatively charged zinc electrodes with ultraviolet light (he observed that positively charged electrodes could not be discharged in this manner) [40]. Elster and Geitel then discovered in 1889 that visible light could produce noticeable photoelectric effects in alkali metals [41]. After J. J. Thomson discovered the electron in 1897, the photoelectric effect could be understood as electron emission induced by electromagnetic radiation [42].

Measurements showed that photocurrent was linearly proportional to light intensity and electron energy was proportional to frequency. These relationships could not be explained via classical electromagnetic theory (which would predict that increased intensity would lead to increasingly energetic photoelectrons). Einstein's response in 1905 was that this is a quantum mechanical effect where photons impinging upon a surface are converted to free electrons, earning him the Nobel Prize of 1921. The photoelectric effect, because of its contradiction with classical theory, played a central role in the development of modern quantum mechanics. Einstein

stated that given incident light with frequency ω , the maximum kinetic energy of an ejected electron is given by:

$$\frac{1}{2}mv^2 = \hbar\omega - \phi \quad (2.1)$$

where ϕ is the work function of the material (i.e. the work that must be done to liberate an electron). The energy of emitted electrons can be determined by measuring the stopping potential V_s required to bring them to rest:

$$V_s q = \frac{1}{2}mv^2 \quad (2.2)$$

Much of the work following Einstein was designed more to establish a body of evidence for quantum theory than to actually expand photocathode technology. Photocathodes during this period were mostly metallic and had very low quantum efficiencies. It was not until the discovery of the “silver-oxygen-cesium” cathode in 1929 that interest in photoemission shifted from pure research to practical application [12],[43]. Other complex photosensitive materials besides Ag-O-Cs were discovered during the next decade through a process of intelligent guessing, but the specific mechanism of photoemission in these materials was not understood until much later.

During the 1940's, the emphasis shifted toward explaining photoemission in terms of fundamental concepts and led to the realization that most promising photosensitive compounds were semiconductors. As solid state physics grew rapidly through the 40's, 50's, and '60's, the concept of negative electron affinity (NEA) surfaced and led to cathodes that outperformed those discovered empirically, at least

in terms of quantum efficiency. Prior to 1965, all practical photocathodes were found by Edisonian-style research [44]. The Spicer three-step theory was developed during this period and began to account for the behavior of alkali-antimonide cathodes. Its theoretical framework led to a gradual departure from empirical study to “scientifically engineered” photocathodes, of which NEA surfaces are considered to be the first [44]. The success of the theory and NEA photoemitters in general ushered in a new family of cathodes that continue to be used today [45],[46]. A remaining difficulty with these high efficiency cathodes is their short lifetime. This research program, and the dispenser cathode concept in particular, is designed to address this shortcoming by suggesting a practical method for extending cathode lifetime.

2.2 History of Photoinjection

The motivation for invention and development of photoinjectors began more than two decades ago, when RF accelerating cavities first came into use. Madey and Westenskow at Stanford High Energy Physics Laboratory first proposed in 1983 to use an RF cavity to accelerate an electron beam from a thermionic cathode [47]. This system served as a bright electron source for the Mark III free electron laser (FEL). During this time, photocathode research benefited greatly from the work of Lee, et. al., which established that very high current densities could be extracted from semiconductor-based cathodes [48]. Pioneering work at Los Alamos National Laboratory (LANL) began in 1985, led by Fraser and Sheffield [49], to incorporate such cathodes into an RF photoinjector in support of a high-power FEL program. The first pure RF photoinjector FEL was demonstrated at LANL first in the IR and then in UV [50],[51]. These inaugural experiments paved the way for more than two decades

of continuous development and application of photoinjection, particularly in the form of RF guns. It is fair to say that since the mid-1980's, photoinjection has emerged as an enabling technology for applications requiring high current, high quality electron beams, such as FELs. A renewed interest in high-average power FELs has motivated further efforts toward high average current photoinjectors, as evidenced by the large number of recently completed and on-going projects [23].

2.2.1 Types of Injectors

Before providing further detail in the development of photoinjection technology, it is helpful to review the types of photoinjectors being pursued: normal conducting RF, superconducting RF, and DC photoinjectors.

RF guns offer several advantages over DC injection. The electric fields obtained in an RF cavity are much higher than in a DC gun and this permits more rapid acceleration of the beam. Such a scenario is preferred because at low energy, the emitted beam is subject to strong space charge forces that lead to emittance growth [23]. Furthermore, ion back-bombardment occurs in DC guns because the constant field accelerates gas particles positively ionized by the electron beam back toward the cathode. Depending upon the cathode type, the constant bombardment can severely reduce cathode lifetime. This problem is eliminated by using an RF gun because the accelerating field is periodic and ionized particles cannot move very far (e.g., back toward the cathode) during the accelerating phase of the RF period.

Normal conducting RF guns were the first to be developed and are the most common in use today. They involve synchronizing a drive laser to the accelerating field of the cavity structure, while a solenoid near the cathode is used for beam

focusing and emittance compensation [53]. Superconducting RF guns share many of the same features, with the major difference being that the cathode is not mounted on the back-wall of a cavity, but rather in its own separate structure designed to provide focusing and emittance compensation using the radial RF electric fields [54]. An obvious advantage for superconducting structures is their capability to conduct current without resistance, leading to higher field gradients, longer duty cycles, and higher beam energies. A disadvantage, however, is the increased complexity of cryogenic systems needed to continuously maintain the cavities at 2 K.

DC photoinjectors share design similarities with thermionic guns, except that the accelerating field does not have to be gated since the laser pulse itself acts to switch the beam on and off. These systems tend also to be larger in size than RF injectors because the field gradients permitted by DC fields are limited by dielectric breakdown and so longer accelerating regions are needed to achieve a given beam energy. Despite the limitations of DC injectors, they are still suitable for high average current operation and being used at several facilities [55],[56]. The most celebrated DC gun belongs to the Thomas Jefferson National Accelerator Facility (TJNAF). It drives an FEL which in 1999 achieved a record 1.72kW of average IR output power and is currently being modified to demonstrate an output of over 10kW [57]. In conclusion, photoinjection technology offers many advantages over traditional (i.e., thermionic) methods, but still presents significant challenges. A comparison between photoinjection and thermionic sources from [23] is repeated below in Table 4 to further illustrate this point of view.

Parameter	Thermionic RF Gun	Photoinjector
High Accelerating Field (100MV/m)	+	+
High Current Density (400A/cm ²)	-	+
Short Pulse Format (20 ps)	-	+
Pulse Format Flexibility	-	+
Cathode Lifetime (1000 hr)	+	-
RF System Simplicity	+	+
Compactness	-	+
Timing and Energy Pulse Stability	+	-
Present Development Stage	-	-

Table 4: Comparison Between Photo- and Thermionic Emission

Whether normal conducting, superconducting or DC in nature, all photoinjectors rely on two crucial technologies: photocathodes and drive lasers. An optimal photocathode would have good quantum efficiency (>10%), long lifetime (>100h), ability to withstand high fields (50MV), and be simple to build and rehabilitate or replace. Such cathodes have not been found. The most successful candidates, in terms of efficiency, are the antimonide-based semiconductors (Cs₃Sb, CsK₂Sb) studied extensively at LANL. They exhibit a QE from 2-8% with a lifetime that strongly depends upon vacuum conditions. When operated at 1Hz duty cycle in a vacuum of 2×10^{-9} Torr, the LANL cathodes exhibit a lifetime of about 15 hours [58]. An alternative to the higher QE emitters is to use more robust cathodes with lower QE and increase drive laser power. Depending upon the drive laser system, this may not be practical. Potential candidates for this approach include bare metals such as the copper cathode used at SLAC [59] and samarium cathode at Brookhaven [60], coated metals, photo-assisted thermionic cathodes [9], and low temperature dispenser cathodes introduced in this program [13]. Despite the higher QE of semiconductor-based photocathodes, yttrium holds the current record for the highest current density

from a macroscopic emitter [23]. Another issue with photocathodes is dark current due to field emission. This unwanted emission depends upon the cathode composition and surface microstructure as well as the magnitude of the electric field in the cavity. An example of dark current in a particular application is given by the LANL gun, where a charge of 100fC per RF period was measured when the laser was off [23].

As stated before, the challenge in designing a high performance photoinjector lies not only with the photocathode, but also with the drive laser. The ideal laser should produce very short, defined pulses at a wavelength that corresponds to the optimal spectral response of the chosen photocathode. Depending upon the cathode's QE, the laser pulse should also be of sufficient energy to extract the desired charge per bunch. The laser pulse should be timed to match the accelerating phase of the RF period and this phase relationship should remain constant throughout the pulse train. Drive laser state of the art is summarized in reference [23] as follows:

Micropulse length	10-20 ps
Micropulse energy	10-100 μ J
Repetition Rate	20-100 MHz
Amplitude Jitter	1 %
Timing Jitter	1-2 ps

Table 5: Drive Laser State of the Art

2.2.2 Recent Developments

The important studies at LANL which ushered in the wide-spread use of photoinjectors involved low average current but led to higher average current demonstrations, such as the 32mA gun at Boeing in 1992 [61]. The decade following this work has seen an increased interest in high average current (>100mA) photoinjectors and progress has been reported both in normal conducting and superconducting RF injectors [62] as well as DC systems [63]. The TJNAF DC gun

mentioned earlier is a prominent example of recent progress and promises to lead to a demonstration of higher average FEL output power in the near future. To summarize the history of photoinjector development, highlights are reproduced from references [52] and [64] in chronological order:

- 1977 DC photoinjector used with GaAs at SLAC (producing polarized beam)
- 1985: RF Photoinjector invented and demonstrated at LANL
- 1990: Theory of emittance compensation developed at LANL
- 1991: RF photoinjector linac with emittance compensation at LANL
- 1992: High duty factor RF photoinjector built at Boeing
- 1992: Photocathode first inserted into superconducting cavity
- 1993: LANL photoinjector is used to drive a UV FEL
- 1995: Experimental demonstration of emittance compensation
- 1996: First operation reported of TJNAF DC photoinjector
- 1999: TJNAF sets record average output power for FEL at 1.72 kW
- 2002: First operation of a superconducting RF photoinjector

3. Experimental Setup

Although photocathode technology has benefited from decades of sporadic development, fabrication and measurement of low-work function photocathodes is not routine [41]. Much of the progress, in terms of discovering favorable coating and substrate combinations, has been determined empirically, lacking a systematic study of surface conditions during fabrication [66]. The overarching goal of this research, beyond developing better photocathodes, is to help validate a recent photoemission model [13] that methodically accounts for all parameters (surface conditions, laser characteristics, material properties, etc) significant to photoemission. Improvements in theoretical modeling can potentially yield significant experimental benefits because optimal cathode compositions could be *predicted* and selected for further study in the laboratory.

3.1 Introduction

To correctly compare experiment to theoretical models, the conditions under which data is obtained must be accurately reported and the experimental outcome must be repeatable. This chapter details the experimental techniques used to achieve both these goals. Repeatability was greatly enhanced by implementing nearly all time dependent processes using *Labview*, permitting nearly full automation of the fabrication and measurement steps involved. The apparatus used in this research has undergone three major revisions, progressively enhancing functionality for the three phases of experimentation: cesiated metal substrates, cesiated sintered substrates, and dispenser photocathodes. These are briefly outlined below.

3.1.1 Phase I: Cesium Metal Substrates

The goal of this phase is to study photoemission from metals as a function of surface conditions. Recall that the most important surface condition is the presence of a relatively uniform, sub-monolayer coating of cesium. This photosensitive layer reduces the work function such that photon energies corresponding to visible light can induce electron extraction. To study this effect, cesium is evaporated onto heat-cleaned polycrystalline metal substrates (tungsten and silver) as shown in Figure 3.1.

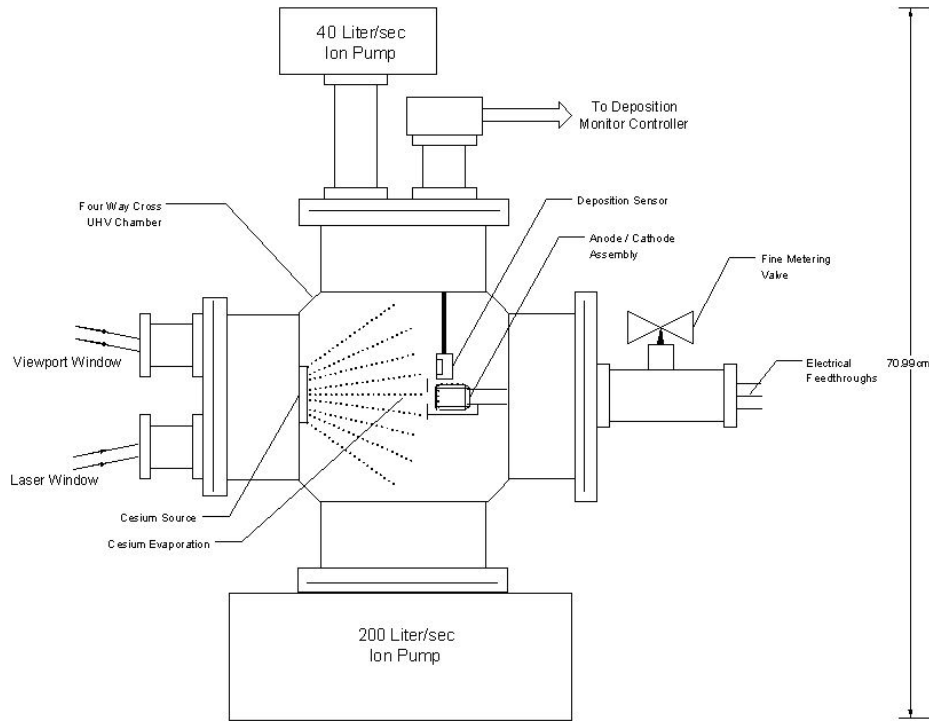


Figure 3.1: Cesium Deposition Process

During evaporation, the resulting cathode is irradiated by a low power laser diode, while photocurrent is measured as a function of cesium thickness (coating thickness is measured using the deposition sensor depicted above). Electrons ejected via photoemission are collected at an anode and register a current on a picoammeter.

Knowing the optical power of the laser together with photocurrent allows calculation of QE. The experimental apparatus consisted of a UHV vacuum chamber built around a four-way cross that accommodated the required electrical feedthroughs and diagnostics to measure cesium coverage, cathode temperature, background pressure, and background gas composition. A major outcome of this effort was obtaining the correlation between quantum efficiency and cesium coverage which allowed measurement of the latter knowing only QE. This is very useful for studying surface conditions in vacuum, where QE can be measured directly but coating thicknesses cannot. A theoretical model was developed that predicted the work function reduction at the surface caused by a coating of cesium and the QE of the resulting cathode as a function of coating thickness. As part of this work, monolayer and bulk evaporation rates of cesium were measured to better understand factors affecting cathode lifetime.

3.1.2 Phase II: Cesium Sintered Substrates

This second phase of research serves as an intermediate step leading toward the controlled porosity dispenser effort. Because the dispenser cathode employs sintered tungsten to allow bulk and surface diffusion to replenish surface coatings, photoemission from sintered materials must be well understood. To this end, the polycrystalline substrates used in the previous phase were replaced with sintered tungsten disks, identical to those used to fabricate the dispenser cell, and the basic measurement process was repeated. A side view of such a disk is shown in Figure 3.2, under 1000x SEM magnification, illustrating the porous nature of the surface. Cesium was evaporated onto a polished face of this surface and five different wavelengths of laser light (275nm, 405nm, 532nm, 655nm, 808nm) were used in rapid sequence to

interrogate the resulting cathode. This allows a more robust understanding of the photoemission process because effects such as quantum mechanical barrier reflections emerge as photon energy approaches that of the work function barrier [13].

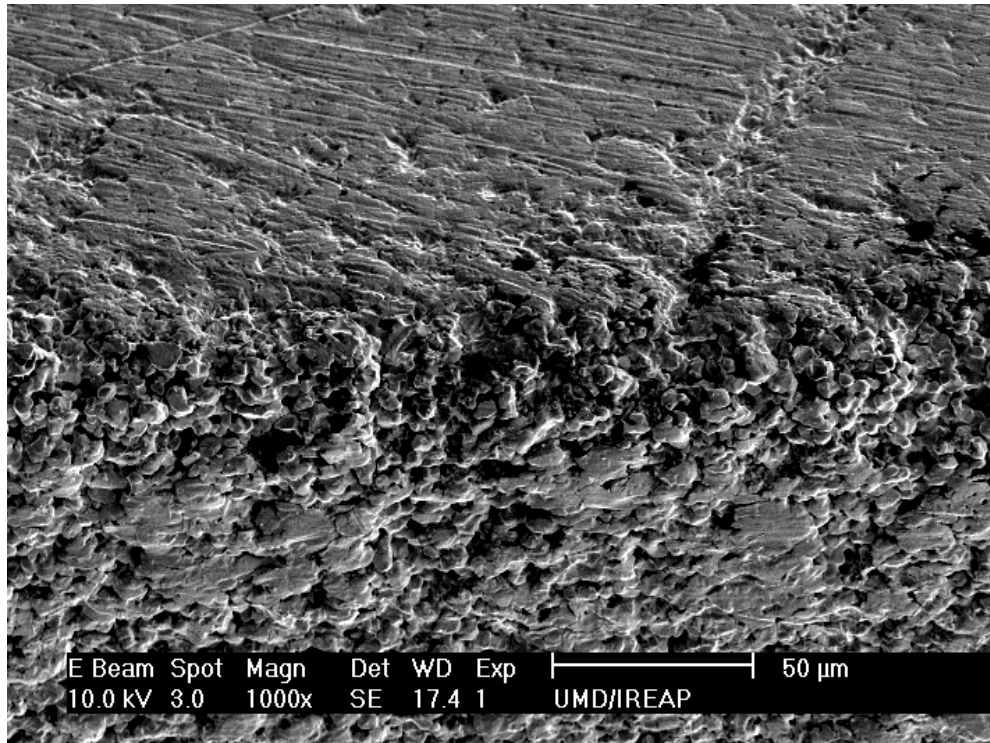


Figure 3.2: Side view of sintered tungsten cathode

QM effects are apparent using IR and red light, but are not apparent at shorter wavelengths (higher photon energy). Other important features were added to the apparatus, including an ion source used to clean the surface of the cathode at room temperature, and a high voltage argon plasma discharge system was installed to clean all surfaces inside the chamber. For dispenser cathodes, diffusion is used to replenish a depleted cesium layer on the surface. Because diffusion depends strongly on temperature, heating the surface for the purpose of cleaning inevitably causes rapid

and unwanted cesium delivery. This is expected, since temperature required for effective heat treatment ($>1000^{\circ}\text{C}$) is much higher than that of cesium diffusion ($<100^{\circ}\text{C}$). In this phase of research, an ion beam is used to clean the surface of sintered tungsten and the relative effectiveness of dose and gas species is explored. Also during this phase, the ability to evaporate antimony is added, allowing fabrication of more complex photocathodes such as Cs_3Sb .

3.1.3 Phase III: Controlled Porosity Dispenser Photocathode

The focus of this final stage is the fabrication and evaluation of a prototype cesium controlled porosity dispenser photocathode. A special heater assembly, shown in Figure 3.3 was used to transfer heat to the cell and a controlled pump-down procedure was followed in order to slowly remove trapped gases inside the dispenser cavity.



Figure 3.3: Dispenser Cathode with Heater Mount

The measurement techniques using QE determined in the previous phases are used to monitor surface conditions of the cathode. This is crucial because cesium arrives at the surface from a reservoir below instead of being evaporated from above by an alkali-metal source, as shown in Figure 3.4. Consequently, coverage can no longer be measured using a deposition monitor. Scanning electron microscopy is used

to determine the distribution of pores on the surface of sintered tungsten, as well as the length scale over which cesium must travel in order to achieve approximately uniform coverage.

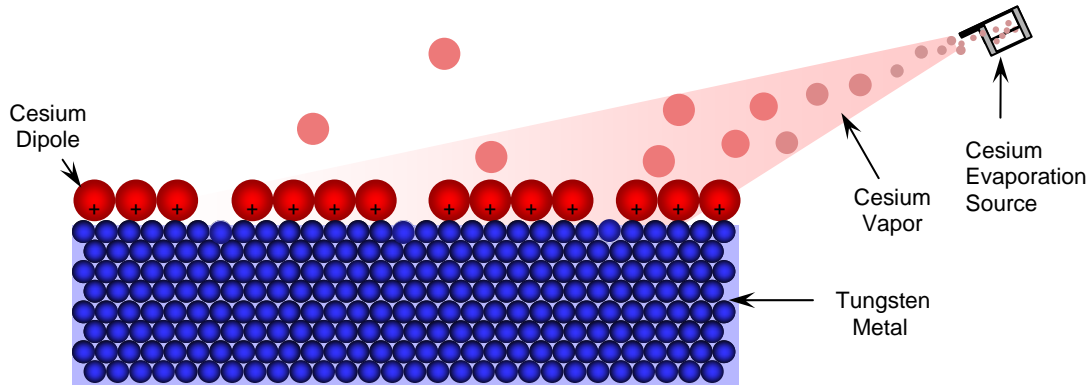


Figure 3.4: Cesium Evaporation from External Source

In this stage, focused ion beam (FIB) milling was used to study the 3D structure of the surface grains and pores, yielding important information about the available diffusion pathways cesium has to the surface. Finally, the performance of the dispenser photocathode is determined in this stage of research and its activation procedure is optimized.

3.2 Vacuum Chamber

The heart of the experimental apparatus used in all three phases described above is an ultra-high vacuum (UHV) chamber built around a central 8" cross. The first generation chamber utilized a four-way, while the latest revision is based on an electro-polished six-way cross. Electro-polishing is preferred because it reduces microscopic roughness that, in turn, reduces outgassing in vacuum. This conditioning step also permits higher bakeout temperatures because it inhibits oxidization of stainless steel in atmosphere. Oxidation normally occurs around 300°C, which

approaches the measured temperature of hotspots (occurring near the heaters) during bakeouts with average temperatures of 250°C. Table 6 shows various statistics about the latest generation chamber.

Total Internal Volume	12.13 L
Total Internal Surface Area	15,212 cm ²
Ion Pump Internal S. A.	2,900 cm ²
Length × Height × Width	89.5 × 97.0 × 74.0 cm
Total Chamber Mass	335.8 kg

Table 6: Chamber Information

3.2.1 Chamber Geometry and Layout

Figure 3.5 shows a front view of a Pro-E engineering drawing of the fabrication chamber and Figure 3.6 shows an actual picture with surrounding apparatus.

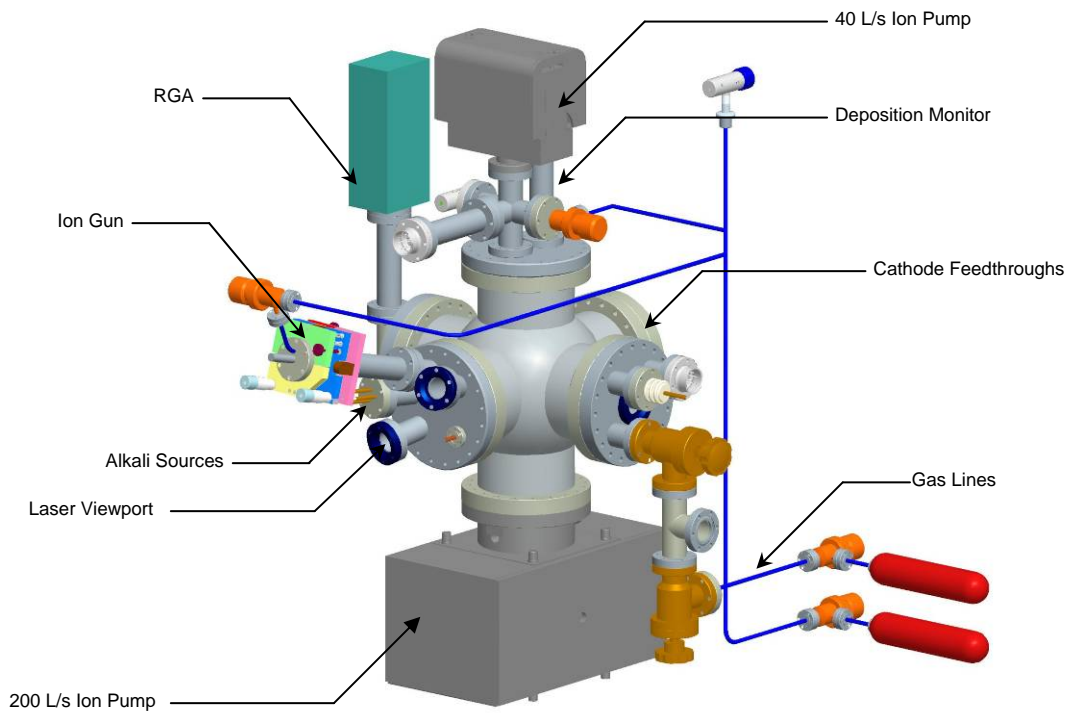


Figure 3.5: Front View of Chamber Model

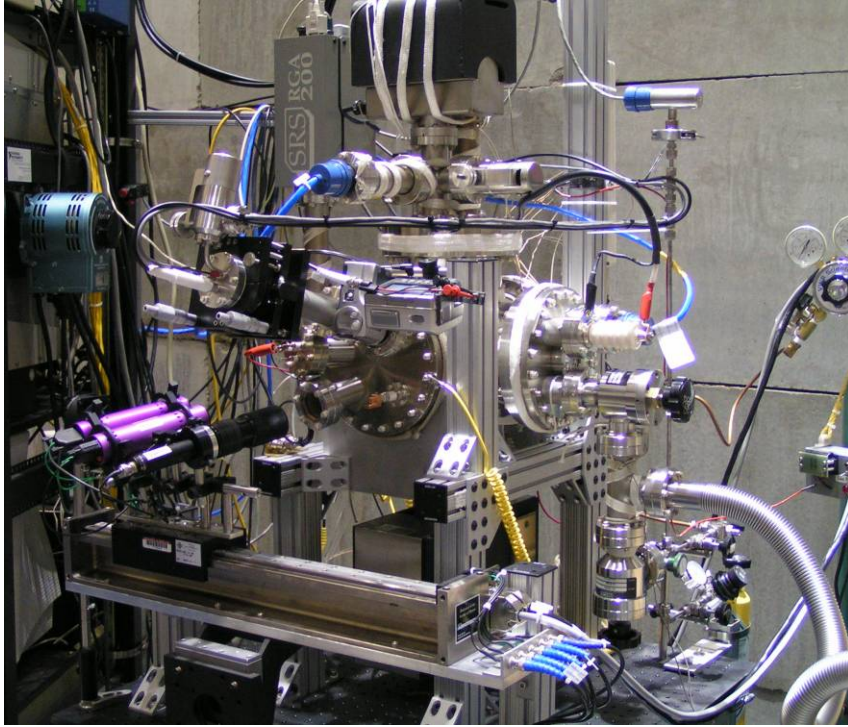


Figure 3.6: Front View of Fabrication Chamber

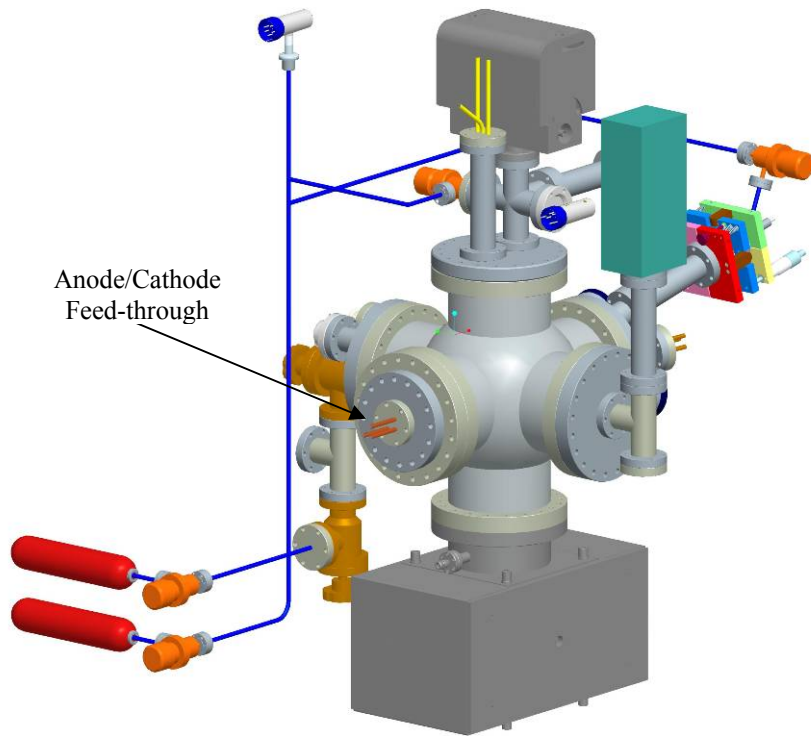


Figure 3.7: Rear View of Chamber Model

Figure 3.8 illustrates the anode-cathode assembly that is mounted on the 8” flange directly opposite the evaporation sources. The annular disk at the bottom-left of the figure is the anode, which serves a dual purpose in the present configuration. Besides collecting photocurrent, the anode serves as a shadow mask to shield other vacuum components from undesired cesium deposition.

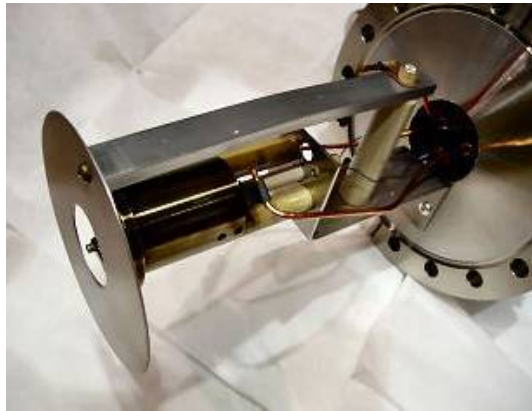


Figure 3.8: Side View of Anode-Cathode Assembly

The cathode is mounted on a button heater 1 cm behind the anode. The heater is mounted within a molybdenum heat shield assembly, which accommodates a thermocouple to monitor cathode temperature. The cathode is held in good thermal contact with the heater by three pointed molybdenum fingers that bolt to the heat shield. The contact area between the finger tip and cathode is small, so that conduction cooling does not occur. The anode and cathode are kept electrically isolated from each other and the chamber by a set of ceramic standoffs that also provide mechanical support, as shown in Figure 3.9. The entire anode/cathode assembly, shown head-on in Figure 3.10, is situated such that the cathode is directly in the center of the six-way cross.

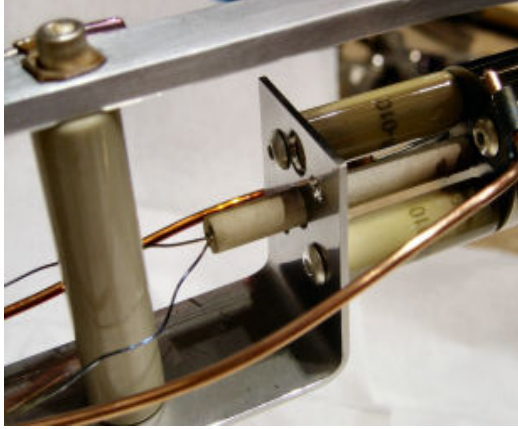


Figure 3.9: Electrical Standoffs



Figure 3.10: Front-view of Anode and Cathode

3.2.2 Vacuum Characteristics

Maintaining a good vacuum is crucial to achieve repeatability in cathode fabrication. Pressures ranging from $1\text{E-}9$ to $1\text{E-}12$ Torr are referred to as ultra-high vacuum (UHV). In this regime, pressure (defined as force per unit area) is not the metric of interest, but rather number density of particles. This is related to the amount of adsorbed gas particles on surfaces in the vacuum and the rate at which they leave the surface. The two obvious requirements for achieving and maintaining a UHV environment are: high pumping speed and low gas evolution or gas load inside the chamber. The number of gas molecules in the chamber is proportional to the gas load and inversely proportional to the pumping speed. The presence of certain gases (such as carbon monoxide, water, and carbon dioxide) poison cesiated photocathodes and lead to short lifetimes. Strict handling procedures were followed during construction or modification of the UHV system, including ultra-pure nitrogen back-fills, single-use gloves and gaskets, double washing of all vacuum components with 100% pure ethanol (residue-free), and Dri-Rite storage of all fabricated components awaiting

incorporation into the chamber. The ethanol wash removes organics and other contaminants that contribute to outgassing and is a convenient solvent because of its residue-free evaporation. After these cleaning procedures, the system is then pumped to the 10^{-6} Torr pressure regime using an integrated scroll and turbo pump. Figure 3.11 shows the pumping performance of the roughing station when connected to a blank flange. This provides a rough estimate of the turbo pump's base pressure, which is taken to be 5×10^{-7} Torr.

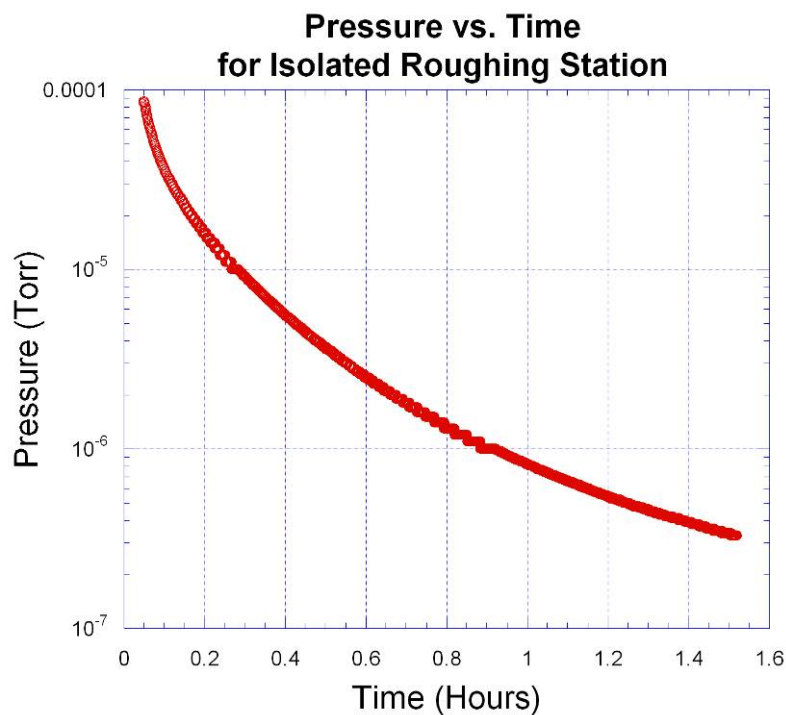


Figure 3.11: Pressure vs. Time for Isolated Roughing Station

A “bakeout” refers to the process of elevating the chamber temperature during initial stages of pumping to increase the rate of gas evolution and rapidly remove the gas from the chamber. In this experiment, heater tape was used to heat the chamber, which in turn imparts energy to adsorbed molecules (mostly water vapor). The

bakeout temperature is usually between 200°C and 400°C, limited by the oxidation temperature of stainless steel (and convection cooling). Effective baking involves chamber heating only after a significant amount of pumping has already occurred, to prevent oxidation of internal vacuum components by the remaining gas. This is especially crucial when outgassing the cathode heater, whose temperature can routinely go above 1200°C. In all experiments, bakeouts occurred only after the roughing station achieved a pressure of less than 5×10^{-6} Torr. The heaters were then turned on and pumping continued until reaching a base pressure of 5×10^{-7} Torr

Depending upon bakeout conditions, approximately 10 hours of pumping is required to reach the base roughing pressure. For a new system, or for a system with a large number of new parts, bakeout with rough pumping can take as long as 72 hours. When the base pressure is reached, the ion-pumps are switched on and allowed to outgas for several minutes. Outgassing occurs as adsorbed atoms are spontaneously knocked off the surface as energetic electrons and ionized atoms impact the active areas of the pumps. Ion pumps work by ionizing residual gases and then electrostatically accelerating them toward a titanium surface where they are permanently embedded and trapped.

3.2.3 UHV Pumping Systems

The background gas composition is of utmost importance when fabricating and characterizing photocathodes, because surface conditions are very sensitive to the presence of specific gases. Since pumping is the dominant mechanism dictating the vacuum environment, a rudimentary background in pumping systems, especially ion pumping, is required in order to diagnose and address myriad vacuum related

problems. As stated earlier, an integrated roughing and turbo-molecular pump is used initially to evacuate the majority of gas from the system, down to a pressure below 1×10^{-6} Torr. The roughing station includes a micro-controller, which monitors performance of the turbo pump and controls its behavior at start-up, shut-down, and in the event of a failure or alarm. A turbo-molecular pump consists of a vertical stack of precisely aligned counter-rotating metal vanes, whose relative angles are such that gas molecules incident on a particular vane will be deflected (regardless of incident angle) out of the chamber and deeper into the pump. When in full operation, these vanes rotate at the rate of 1000 Hz on magnetic bearings. For the most part, this unit can be considered to be an appliance, turned on and off with a single switch and performing as expected unless the micro-controller registers an alarm. It includes two pressure gauges for use over the range of vacuum it is capable of maintaining and connects to the fabrication system via a standard Con-Flat flange. The most important consideration when using the roughing station is protecting the delicate vanes of the turbo-pump from mechanical shock associated with an unexpectedly high gas load. This is especially true for gases with higher atomic or molecular weights. In the case of argon, a sudden increase in pressure dramatically slows the turbo rotation and heats up the rotor, triggering an alarm and shut-down. Such an event could be caused by a leak or gas valve opening during low pressure operation (i.e. when the vanes are rotating at their target speed) either through inadvertent user error or failure.

After achieving base pressure of the roughing pumps, the two ion pumps on the top and bottom of the chamber are switched on. These units have no moving parts and are responsible for continuously maintaining vacuum during experimentation. In

most ion pump designs, an anode and cathode, made of stainless steel and titanium, respectively, are separated by a potential difference of 6kV. Because of this high electric field, electrons are emitted from the cathode and accelerate toward the anode. A strong permanent magnet is situated around the anode-cathode pair such that the magnetic field lines are perpendicular to both surfaces. Ejected electrons then trace helical paths around the field lines as they travel toward the anode. This dramatically increases the path length from cathode to anode and has the effect of increasing the probability of collision with trace gas molecules, which in turn become positively ionized and accelerate back toward the cathode due to the electrostatic field. If the arrival of the ion at the titanium cathode is sufficiently energetic, it can eject titanium atoms from the surface in an effect called sputtering. Sputtering produces a localized, fresh layer of titanium at the surface near the impact site that reacts with gas molecules nearby, effectively removing them from chamber circulation. Titanium is a typical component in ion pumps because it is indeed chemically reactive and forms stable compounds with most common gas molecules. In order for this pumping effect to occur, fresh layers of titanium must be exposed continuously. It should be obvious that the degree to which sputtering occurs depends upon the gas species impinging the surface. Hydrogen, for example, has so little mass that it is unable to induce sputtering, while most other molecules can. Hydrogen is pumped primarily by diffusion into the bulk of the cathode. This process is quite effective, as the pumping speed of hydrogen is roughly twice that of nitrogen [67]. It is interesting to note that the presence of hydrogen in the titanium bulk produces noticeable distortions in the cathode geometry. When the pumps are being baked, audible creaking can be heard

as the titanium cathodes release impregnated hydrogen and physically change their shape. Inert gases, such as argon and neon, cannot be pumped by chemical reactions at the surface. They are trapped only by the sputtering action, and their pumping speeds are noticeably slower than other common gases. This is an important factor when choosing a backfill gas, because the pumpdown time for a system brought to atmospheric pressure with argon is up to 16 times longer than with nitrogen. The pumping rate for noble gases (pumped via sputtering) decreases as pressure drops, because sputtering requires ionized gas atoms, which become increasingly scarce with better vacuum. Ion pumps should not be used at high pressures because their lifetime is closely correlated with the amount of cathode material remaining at the cathode for sputtering. Extended exposure to atmosphere should also be avoided, as it complicates the process of starting the pump. This is because large amounts adsorbed gas molecules initially come off the anode and cathode upon startup and these can lead to an uncontrolled electric discharge. If unchecked, this discharge can heat the active areas of the pump and lead to premature outgassing, which serves only to perpetuate the discharge and potentially induce an avalanche. This ion current amplification situation can cause the formation of “whiskers,” or thin deposits of material that short out the active areas. If a discharge begins upon startup, it was found that a solution is to start the ion pump while the rough pump is still in operation and at its base pressure. This allows gases released during ion pump startup to be dynamically removed from the system and avoid participation in further discharge process. If this procedure is not followed, the ion pump controller typically shuts the pump down completely, as it senses that it is outgassing more material than it is

absorbing. Conversely, starting an ion pump at very low pressure (for example, starting a second ion pump when the vacuum is already well established) can also be problematic because there are so few gas molecules available to be ionized and accelerated to sputter the cathode material.

Pumping speed is not constant over the entire pressure range: it reaches its peak at the 1×10^{-6} Torr range, and falls off by a factor of two at 1×10^{-9} Torr. This is an important consideration when performing processes that lead to gas evolution (such as evaporation of cesium) because it is not difficult to overwhelm the ion pumps at low pressure. While the pumps usually recover quite rapidly, the exposure of cathode surfaces to higher partial pressures during fabrication or measurement can lead to contamination and corrupt the experiment. The pumping speed per unit area can be approximated by the formula:

$$S = 3.64s\sqrt{\frac{T}{M}} \quad (3.1)$$

where T is temperature (Kelvin), M is the molecular weight, and s is the sticking coefficient which varies with pressure and remaining pump lifetime [67]. Two ion pumps are used in this system; the largest (200 l/s) is installed at the very bottom of the chamber, while the smallest (40 l/s) is attached at the very top, as seen in Figure 3.5. Both are effective at pumping most common atmospheric gases but are very slow with the noble gases, for the reasons mentioned earlier. Following the summary given by [67], the sputter-ion pumps rely upon the following actions:

- 1) Entrapment and burial of ions within the metal lattice of the cathode surface
- 2) Gettering of active gases near sputter sites
- 3) Diffusion of hydrogen into the bulk of the active areas.

- 4) Dissociation of complex gas molecules into simpler components, which are then captured via one of the above mechanisms.
- 5) Conversion of background gas ions to neutral atoms (via scattering from cathode surface) with sufficiently high velocity to become lodged in the active areas.

For a clean system (i.e. baked and maintained under UHV conditions for a long time), gas evolution continues due to the processes mentioned earlier, including escape of gas molecules trapped within the titanium electrodes of the ion pump. This fact is established by the fact that pressure increases rapidly after ion pumping ceases, as shown in Figure 3.12, but begins to reach an equilibrium as desorption and adsorption begin to balance one another.

External heaters were installed on both ion pumps so that they could be baked with the rest of the system during appropriate phases of rough pumping. The elevated bakeout temperature forces some of the gas molecules loosely trapped in the electrodes of the pump to be released and pumped out. The molecules that reacted at the surface to form stable compounds remain trapped throughout bakeout. It is important to never bake the ion pumps while they are pumping, because this creates a large gas load at the pumping surface and could lead to excessive sputtering as ionized gases bombard the titanium active areas.

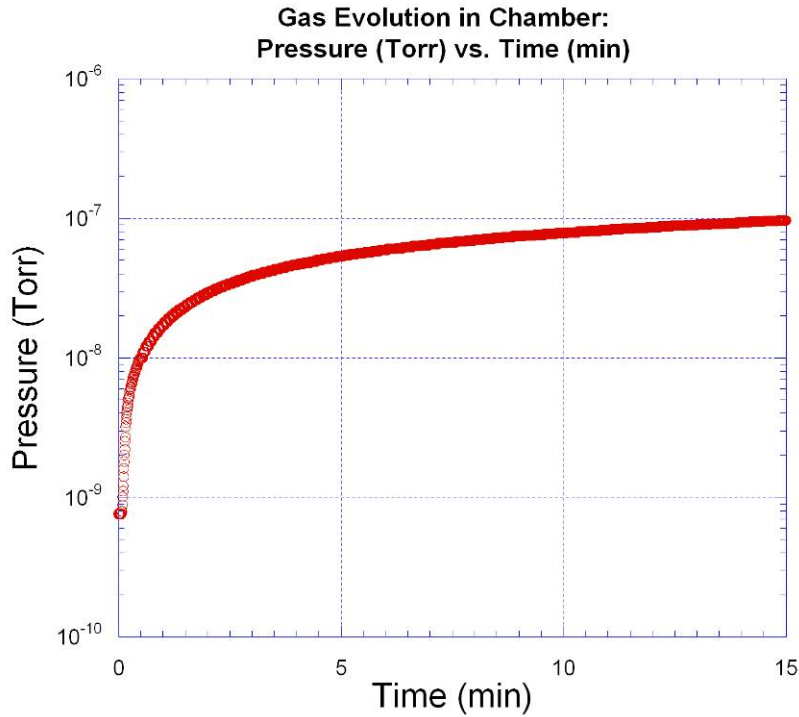


Figure 3.12: Gas Evolution with No Ion Pumping

3.2.4 Pressure at the Cathode

As mentioned before, the background gas composition is an important factor governing surface conditions at the cathode. Pressure throughout the chamber can be measured from five sources: two ion gauges, two ion pumps, and the RGA. The latter provides the partial pressures of constituent gases, while the others simply provide a measure of total pressure. Because each instrument is mounted on a chamber extremity, far from the region of interest, it is useful to calculate the pressure at the cathode. Various methods have been developed to calculate pressure profiles of complex chamber geometries [69],[70]. Pressure in a chamber evacuated such that viscosity can be ignored is described over regions of constant conductance by:

$$c \frac{d^2 P}{dz^2} - sP + Q = 0 \quad (3.2)$$

where P is pressure [nTorr], c is specific molecular conductance [l/s], s is specific linear pumping speed [l/s/m], and Q is specific outgas rate [nTorr · l/s/m]. Solutions to this equation, for $dc/dz = 0$, are given by:

$$P(z) = C_1 e^{\alpha z} + C_2 e^{-\alpha z} + \frac{Q}{c} \quad (3.3)$$

where $\alpha = \sqrt{s/c}$. The reality is that in any practical vacuum chamber, geometry is such that conductance is not constant, $dc/dz \neq 0$. The solution is to segment the chamber along a particular axis (vertical is chosen in this calculation) into small sections of equal length dz and express the derivatives as finite differences. Segment length is chosen such that conductance can be considered constant over that length scale. A more general differential equation now applies to account for changes in conductance from one segment to the next:

$$\frac{d}{dz} \left(c \frac{dP}{dz} \right) - sP + Q = 0 \quad (3.4)$$

This modification guarantees that pressure and flow remain piecewise continuous along the chamber axis. Figure 3.13 shows the calculated pressure profile across the vertical axis of the chamber. The calculation was performed using a vacuum simulation program developed at SLAC called VACCALC, which solves the differential equation using the methods described above [69]. The simulation inputs are the chamber geometry, temperature, and pumping speeds and the output is pressure as a function of position in the vacuum system.

The calculated pressures roughly match the observed pressures after sufficient baking, so the assumption was made that the pressure at the cathode (at room temperature) is about 5×10^{-10} Torr.

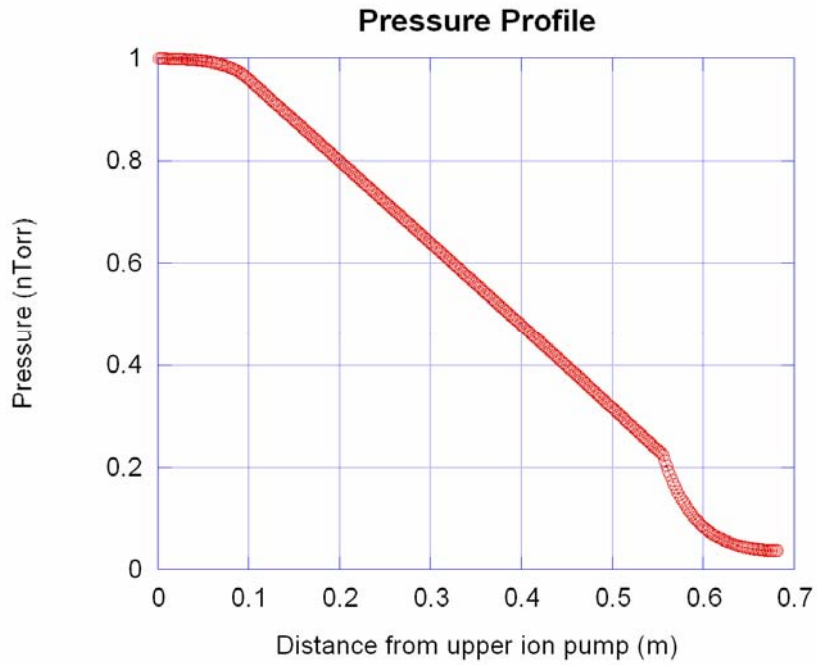


Figure 3.13: Calculated Pressure Profile across Chamber Vertical Axis

Actual pressure is measured using the ion pumps, ion gauges, and a residual gas analyzer. These measured pressures, when plotted as a function of vertical distance from the top ion pump, yield a pressure distribution shown in Figure 3.14. The pressure distribution in the chamber can vary widely depending upon which processes, if any, are in progress. During source evaporation, for example, pressure is locally quite high near the center of the chamber.

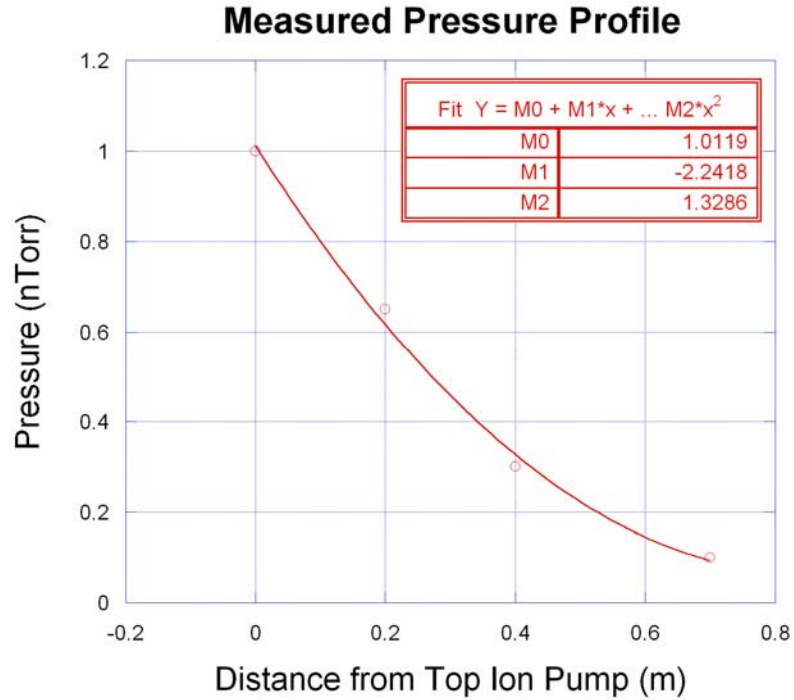


Figure 3.14: Measured Pressure Profile along Chamber Vertical Axis

3.2.5 Source of Background Gas

Sources of gas include leaks, virtual-leaks, materials, and out-gassing. Gas leaks are prevented by UHV quality hardware and checking gaskets and flange knife edges for scratches or defects during installation or maintenance. The so-called “knife edge” of a flange is the most important structure on a mountable vacuum component, for if this edge is compromised, its addition to the system can be costly. These edges mate one to another on opposite sides of a 1/8” thick copper gasket. Flanges and chamber walls are typically made of type-304 stainless steel, because it resists corrosion, has a low outgas rate, and is structurally rigid. Furthermore, it is non-magnetic (important for experiments using charged particles) and can be both welded and brazed. Gaskets used to seal one flange to another must be made of a material

that a.) undergoes plastic deformation, where the applied force can exceed the yield strength of the material, and b.) retains some elastic energy so that the sealing force is maintained over time and during temperature cycles. The standard gaskets used are known under the trade name “Con-Flat” and are oxygen-free high conductivity (OFHC) copper rings whose dimensions match the associated flange. In addition to the elastic properties mentioned above, copper has a nearly identical thermal expansion coefficient as stainless 304, which prevents leaks due to temperature cycling. Con-Flat flanges maintain their seal through temperature cycling at a rate of 10°C per minute in the range of -195°C to 500°C [67].

Leaks are easily detected using the system’s built-in RGA, whose control software includes a specific routine for detecting helium. Leaks as low as 1×10^{-11} Torr-Sec can be detected with the installed RGA, corresponding to a sensitivity of roughly one part in 10 million. Helium is a standard tracer gas because, as the lightest of the inert gases, it penetrates small holes readily. It is also advantageous because it is non-toxic, non-destructive, available in high-purity, and is present in the atmosphere in only very small amounts, roughly 5 ppm. In the event of a suspected leak, helium is systematically sprayed on the outside of the vacuum chamber and components while the resulting changes in partial pressure is detected. To put a leak into perspective, if a pin hole 0.01” in diameter were made in the chamber wall (1/8” thick), a 500,000 L/s pump would be required just to maintain a vacuum of 1×10^{-6} Torr.

Materials are also a source of gas load if they have a significant vapor pressure. Vapor pressure is the gas pressure at which the number of atoms or

molecules leaving the solid phase equals the number returning. A pressure of 1×10^{-9} Torr can be considered a conservative operating pressure for the deposition chamber, and the operating temperature is less than 50°C . Materials present inside the deposition chamber, along with the temperature at which vapor pressure is 1×10^{-9} Torr, are shown in Table 7 [68].

Material	Maximum Operating Temp.	Temp ($^\circ\text{C}$) @ 1 nTorr
Aluminum	630	812
Antimony	~400	343
Cesium	~250	22
Copper	~250	841
Molybdenum	1200	1862
Potassium	250	62
Silver	650	674
Tantalum	700	2222
Titanium	250	1211
Tungsten	1200	2383
Zirconium	250	1690

Table 7: Temperature Required for nTorr Vapor Pressures

It is obvious that the temperatures required for vapor pressures in the nano-Torr range for most materials used in the chamber are exceedingly high. Accordingly, the vapor pressure for these same materials at their stated operating temperature (mostly near room-temperature) is negligibly small. The exceptions are the alkali metals, antimony, and silver. Silver vapor is not a concern unless it is undergoing a heat treatment process, necessary for cesiated silver cathodes, in which case extra pumping is added. For the case of alkali metals, it is important to consider that the chamber is not static, but is being continuously pumped by ion pumps. Thus, the actual vapor pressure of a gas at a given temperature is always less than the published

value because turbo pumping dynamically removes gas that would otherwise contribute to partial pressure.

Outgassing of surfaces and trapped gas volumes is another significant source of gas load, especially during the early stages of chamber pumping. Outgas usually refers to the evaporation of surface layers of adsorbed gas molecules, but can also refer to trapped volumes of gas in defective welds or threaded surfaces, called virtual leaks. Since each of these involve the controlled release of a finite amount of trapped material, the resulting gas load decreases over time. This is usually a slow process, however, and is sped along by heating the chamber and its components during a bakeout. Figure 3.15 shows pressure as a function of time for a system (including the cathode itself) undergoing constant temperature bakeout. Notice that early on, the pressure is high but falls off with time as trapped gases are pumped out of the system.

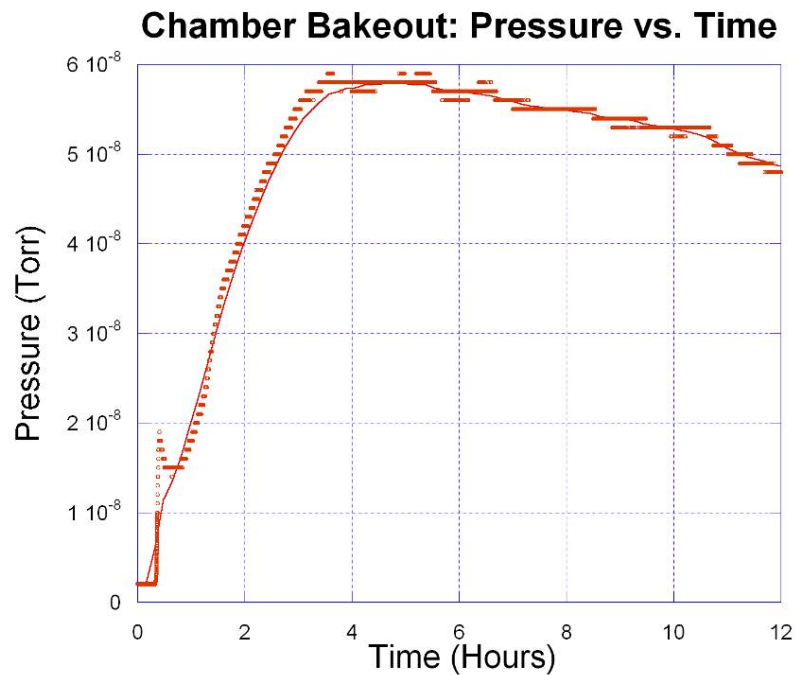


Figure 3.15: Pressure vs. Time During System Bakeout

3.2.6 Gas Valve Configuration

The controlled introduction of select, high purity gases at various stages of cathode development is needed in order to either simulate vacuum conditions or perform specific surface treatment processes. For example, discharge cleaning requires the presence of argon, ion beam surface treatment requires argon and hydrogen, oxygenation requires trace amounts of nitrous oxide or oxygen gas, and chamber backfills require ultra-pure nitrogen. To preserve gas purity (99.99999% in the case of argon and nitrogen) and avoid contamination in the chamber, all components of the gas system are made of stainless steel, including the seamless tubing, and baked out before use. The gas processes involved require pressures that span 12 orders of magnitude, so a network of valves was constructed, to control pressure over this wide range. This arrangement, shown diagrammatically in Figure 3.16 and after construction in Figure 3.17, and includes 3 main types of valves: UHV high conductance bellows valves, UHV precision leak valves, and Swagelok fitting valves for use at milli-Torr range.

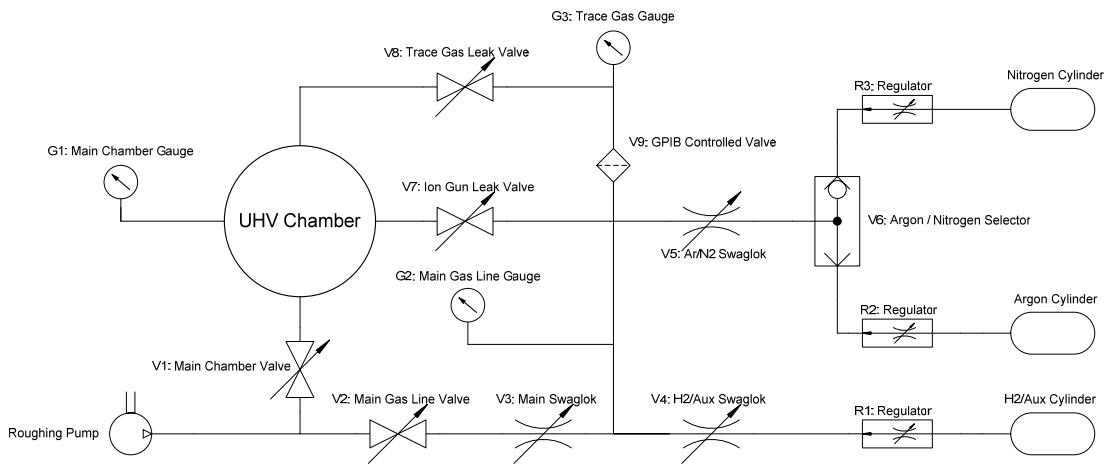


Figure 3.16: Network of Gas Valves Connected to Chamber

Valves labeled V1 & V2 are Vitron-sealed bellows-type for UHV and determine whether the chamber or gas line network is pumped by the roughing pump. Typically, only one of these is open at a time, to prevent contaminants that may enter the gas line network from entering the chamber. This ability to selectively pump the chamber or lines saves considerable time: after the chamber has been roughed down (and its ion pumps energized), it can be isolated and pump-down of the gas lines can begin without restarting or removing the roughing pump. A valuable feature of this network is the ability to vary pumping speed by opening or closing a series of staged valves. This is useful for evacuating a dispenser cathode, whose internal volume contains trapped gases that must slowly pass through the porous cathode surface. If this process happens too rapidly, then the mechanical stress could damage or crack the dispenser cathode structure.

When switching between various gases, all lines must be evacuated, purged (with whichever gas will be introduced), and re-pumped and refilled again before using. Pumping should continue until pressure reaches several milli-Torr. Since Swagelok fittings are not designed for high vacuum, this pressure regime is a nominal target for about 20 minutes of rough pumping. Two pressure gauges give information about the pump-down progress and indicate which valves are opened. The various Swagelok valves (V3-V6) are used to select and isolate a gas source from among connected cylinders, while valves V7-V9 permit the controlled introduction of these gases into the chamber. Seven distinct processes require different valve configurations. Table 8 lists each of these, along with the state of each valve (1=open, 0=closed) and pressure gauge (in units of Torr).

Activity	V1	V2	V3	V4	V5	V6	V7	V8	V9	G1	G2	G3
Chamber Pumpdown	1	0	1	0	0	N ₂	0	0	0	10 ⁻⁶	10 ⁺²	10 ⁺²
Chamber Backfill	0	0	1	0	1	N ₂	0	1	1	10 ⁺²	10 ⁺²	10 ⁺²
Gas Line Pumpdown	0	1	1	1	0	E	0	0	1	10 ⁻¹⁰	10 ⁻⁴	10 ⁻⁴
Gas Line Purge	0	0	1	1	1	N ₂	0	0	1	10 ⁻¹⁰	10 ⁺²	10 ⁺²
Cathode Measurement	0	0	1	0	0	E	0	0	0	10 ⁻¹⁰	10 ⁺²	10 ⁺²
Alkali Evaporation	0	0	1	0	0	E	0	0	0	10 ⁻⁹	10 ⁺²	10 ⁺²
Cathode Oxygenation	0	0	1	1	0	E	0	1	1	10 ⁻⁸	10 ⁺²	10 ⁺²
Argon Plasma Cleaning	1	0	1	0	1	Ar	0	1	1	10 ⁻²	10 ⁺²	10 ⁰
Hydrogen Ion Beam On	1	0	1	1	0	E	1	0	0	10 ⁻⁴	10 ⁺²	10 ⁺²

Table 8: Task-Specific State of Gas Valves (Open=1, Closed=0)

For the case of V6, a dual-port valve, the selected position is shown in terms of gas type, while ‘E’ indicates that either position is acceptable. Notice that when not involved in a particular process, the gas lines are backfilled by default with nitrogen to prevent trace leaks from filling them with atmospheric gases. While all other valves are manually operated, valve V9, shown in Figure 3.18, is a GPIB-controlled valve used to automate processes in Labview.

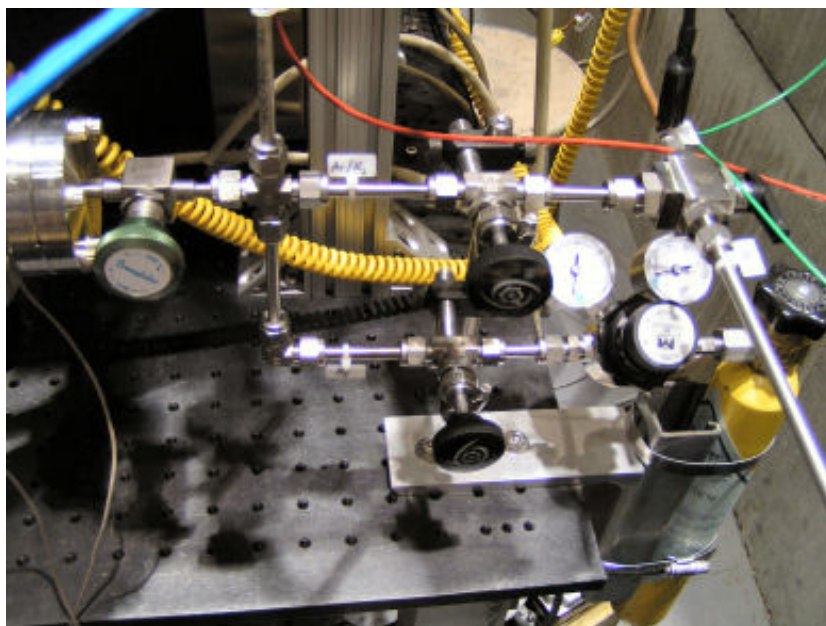


Figure 3.17: Network of Gas Valves Connected to Chamber

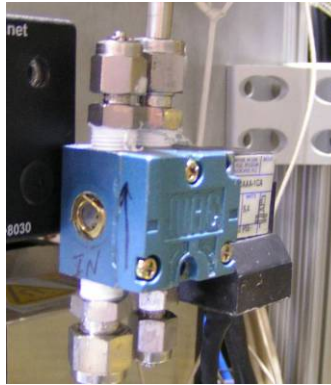


Figure 3.18: GPIB-Controlled Gas Valve

3.2.7 Gauges

Cathode research involves changes in pressure spanning 12 orders of magnitude. No single device is capable of continuous measurement over this enormous range, because detection methods differ depending on whether the system is at high-pressure or high vacuum. As the vacuum improves, measuring pressure becomes increasingly difficult, because the amount of material available for detection becomes vanishingly small. Another differentiation in pressure measurement is whether the devices measure total pressure or partial pressures of gases present in a mixture. The latter is accomplished by a residual gas analyzer (RGA) as discussed earlier. For the high-pressure regime, from 760 to 1×10^{-4} Torr, a thermocouple or “Convectron” gauge is used. This gauge works by measuring the degree to which convection cools a heated filament. In practice, the filament is placed in thermal contact with a thermistor, whose output is used in a feedback loop to control current through the filament such that it is a constant source of heat. The convection cooling of the filament is reflected in the current required to hold temperature constant and

provides a direct measurement of the remaining atmosphere in the chamber. Because convection cooling is involved, the spatial orientation of a thermocouple is crucial: its longitudinal axis must be horizontal. It should also be obvious that any external source of heat, such as human hands, intense lamps, or heater tape corrupt the measurement process. Finally, the thermocouple gauge controller reads pressure based on calibration performed in a standard atmosphere of nitrogen. Unless the chamber atmosphere also contains mostly nitrogen, it is important to properly interpret pressure readings for the gas environment of interest.

In the case of argon, for example, actual pressure will exceed the measured value by a factor of 30, because argon atoms are heavier than nitrogen molecules and interact less frequently with the hot filament. This leads to less convective cooling, which is interpreted erroneously by the gauge controller as a lower pressure. It is extremely important to take this difference in pressure readings into consideration when back-filling the chamber with gases other than nitrogen. If backfilling with argon, for example, a pressure reading of 24 Torr on a nitrogen-calibrated gauge corresponds to atmospheric pressure. Unknowingly backfilling the chamber beyond a pressure reading of 24 Torr for argon could lead to catastrophic over-pressure conditions where viewports or bellows rupture. A final detail to note concerning thermocouple gauges used in this experiment concerns time response. Because the convection gauge relies upon heating and cooling processes, a time delay of up to 10 seconds is observed between actual and measured pressure, especially in the milli-Torr range. For automated Labview processes relying upon this gauge for feedback

information, it is important to adjust the process such that changes in pressure over time can be reasonably tracked by the gauge.

In the low-pressure regime of 1×10^{-4} Torr and below, a Bayard-Alpert ion gauge is used in addition to the ion current of ion pumps. Labview program monitors pressure readings from both the Convectron and ion gauges via a Granville-Phillips 307 controller and interrupts any experimental process if the pressure exceeds a threshold of 1×10^{-7} Torr.

3.3 Lasers

In order to measure the quantum efficiency of a cathode, a light source with sufficient wavelength and intensity is necessary to induce measurable photocurrents. Photocurrent is measured by a Keithly 486 picoammeter, with an advertised resolution of 50 fA. In practice, however, it was observed that photocurrents less than 5pA were too small for reliable detection. At the outset of this experiment, a commercial tungsten filament was used as a broadband light source, and photocurrent was detected from cesiated metals if the filament was glowing white hot. For the theory component of this research, it is important to know QE as a function of wavelength, and such information could not be obtained using such an elementary broadband source. In order to measure QE, the ratio of photoemitted electrons to incident photons, optical intensity must be known. For a hot filament, it is tedious to reliably determine the optical intensity arriving at the cathode, especially when the bare filament is located inside the vacuum chamber. Instead, solid-state diode lasers were chosen to interrogate the cathode during QE measurements: they have narrow bandwidth and allow QE measurements to occur over a small spectrum. Furthermore,

the light is collimated, which allows convenient measurement of optical intensity. Power measured when the laser is focused to a small spot on a detector is assumed to be the same as that arriving at the cathode, multiplied by the transmission coefficient of the vacuum chamber viewport. An alternative method would be to focus a broadband source such as a mercury lamp onto the cathode and use a narrow-band filter to select a desired wavelength. A penalty is paid, however, in available light intensity because so little of the original power is present at a particular wavelength. Yet another option was to use a commercially available tunable laser. These options were deemed either too inconvenient or too costly, and instead lasers of 5 wavelengths in the visible or near-visible spectrum were chosen: UV at 375nm, blue at 405nm, green at 532nm, red at 655nm, and IR at 808nm.

3.3.1 Diode Laser Basics

Laser light in general exhibits three important properties: it is coherent, monochromatic, and collimated. As discussed above, only the latter two properties are advantageous for this experiment, because they simplify the measurement process and allow it to be wavelength-specific. Among the various types of lasers, including diode, diode pumped, gas-discharge, and dye, the first two were chosen for use because they have a conveniently small form factor, are efficient, and require low input power. This allows them to be integrated into a robotic system that allows automatic, sequential selection of wavelengths.

Semiconductor lasers are formed by merging two different types of materials together to form a type of P-N junction, where one material has an excess of electrons (n-type) and the other an excess of holes (p-type). The lasing process occurs at the

interface: when a hole and an electron collide, they annihilate each other and emit recombination radiation. Because electrons in the n-type material exist in the conduction band, they have a higher energy than holes, which exist in the valence band. This energy difference is termed the *bandgap* and ideally it corresponds to the amount of energy released in the form of a photon when a hole and an electron recombine. Different bandgaps, and therefore different photon wavelengths, can be achieved by selecting certain material combinations.

Figure 3.19 shows the energy band diagrams for a conductor, an insulator, and a semiconductor. Notice that in the case of a semiconductor, there exist a number of mobile carriers (either electrons, for the case of a populated conduction band or holes, for the case of a less-than-full valence band).

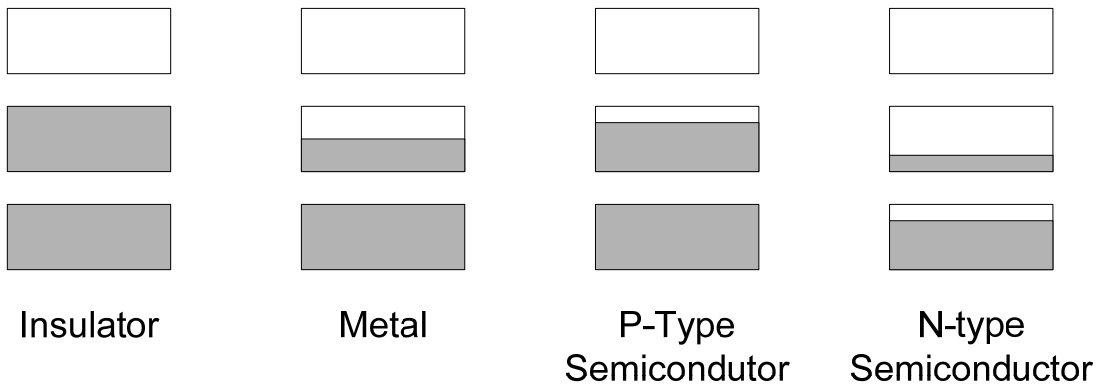


Figure 3.19: Occupancy of Allowed Energy Bands

Excitation of electrons from the valence band to the conduction band occurs when a forward bias is placed across the junction: electrons from the *n*-region are forced near the interface, as are holes from the *p*-type region. Because these have opposite charge, they attract and, upon annihilation, either radiate energy

(electroluminescence) as a photon or give it up in the form of ordered lattice vibrations, known as phonons. The extent to which phonon excitation occurs depends upon whether the semiconductor is made of *direct* or *indirect* bandgap material. These terms refer to whether or not the maxima of the valence band energies coincide with the minima of conduction band energies, in terms of momentum. If they coincide, then the material is considered direct bandgap, meaning that electrons in the conduction band (at its minima) can decay to an eligible position in the valence band (at its maxima) without requiring a change in momentum. This is in contrast to indirect bandgap materials, whose conduction and valence band extrema are offset in terms of momentum. This places additional requirements on the conditions for radiation, because a phonon is required to produce the necessary change in momentum of the electron before radiation can occur. Because phonon interactions reduce the efficiency of the radiative process, it is difficult to maintain a population inversion required for lasing. For this reason, direct bandgap semiconductors are used for diode lasers. There are two distinct types of direct bandgap materials used for diode lasers, depending upon the desired wavelength: III-V and II-VI semiconductors, so named because they are comprised of elements in their indicated columns of the periodic table. These typically include Al, Ga, In, from column III; N, P, As, and Sb from column V; Zn and Cd from column II; and S, Se, and Te from column VI. Table 9 shows the bandgap energies and radiation wavelengths for various diode lasers, including those used in this research (shown in italics).

Material	Bandgap Energy (eV)	Wavelength (nm)
InP	1.35	917.8
GaAs	1.42	872.5
<i>AlGaAs</i>	<i>1.53</i>	<i>808.8</i>
CdTe	1.56	794.2
CdSe	1.70	728.8
<i>GaAlAs</i>	<i>1.89</i>	<i>655.5</i>
GaP	2.26	548.2
ZnSe	2.71	457.2
<i>InGaN</i>	<i>3.06</i>	<i>404.9</i>
<i>GaN</i>	<i>3.30</i>	<i>375.5</i>

Table 9: Bandgap Energies of Various Semiconductors

The relation between output wavelength in nanometers and bandgap energy in electronvolts is given by:

$$\lambda[nm] = \frac{hc}{qE[eV]} \cdot 10^9 \quad (3.5)$$

3.3.2 Diode Laser vs. Diode Pumped Solid State

Because solid-state lasers involve a lasing medium, it obvious that only discrete wavelengths are possible, corresponding to the bandgap of the host material. In the event that a diode laser does not exist for a particular wavelength, an option is to frequency-double a longer wavelength. Such is the case for the 532nm source used in this experiment. It consists of a neodymium-doped yttrium aluminum garnet ($\text{Nd:Y}_3\text{Al}_5\text{O}_{12}$) crystal. The triply ionized neodymium impurity replaces approximately 1% (by weight) of yttrium atoms in the crystal matrix and enables an electronic transition corresponding to a wavelength of 1.064 μm or 1.165eV. Electrons in the lattice are excited to this state through external pumping provided by an 808nm GaAs diode laser. This arrangement is advantageous because the efficient output of the diode laser stores energy in the long-lived upper-level energy states of

the YAG crystal, enhancing population inversion. Frequency doubling, or second-harmonic generation, is accomplished by passing the Nd:YAG output beam at a specific angle and polarization through a non-linear potassium titanyl phosphate crystal (KTiOPO_4) to produce 532nm laser light. The output from the crystal contains both the second harmonic and fundamental wavelengths. The doubling crystal, referred to as KTP, is anisotropic and has a nonzero second order optical susceptibility [71]. When irradiated by sufficiently intense light, the electric field induces nonlinear interactions of dipole moments, whose response includes higher order harmonics. Higher order harmonics are possible by passing the original beam through a series of frequency multipliers, but the output beam quality is vulnerable to fluctuation at higher multiples of the fundamental. This is because the non-linear process depends upon intensity raised to the n^{th} power, where n is the harmonic number. Manufacturing techniques for the common 532nm diode-pumped solid state (DPSS) laser are sufficiently refined such that the optics fit neatly in a compact form factor and exhibit output power fluctuations of less than 2%. Such is the case for the laser used in this program.

3.3.3 Laser Specifications

Figure 3.21 shows the 5 CW lasers used to measure quantum efficiency, and Table 10 provides specifications for each unit. All provide 5-10mW of laser power in circular or elliptical spot sizes that are expanded via focusing to be 4-6mm in diameter to prevent localized heating of the photocathode. The blue and UV lasers use edge-emitting diodes that emit an elliptically shaped beam (4.4mm×1.4mm) with a divergence of 0.4×0.6 mrad. The cylindrical form factors of the lasers are roughly

the same, ranging from 55-165 mm in length, and 13-38mm in diameter, and include control circuitry to optimize power stability and protect the laser diode from temperature and input power fluctuations.

λ (nm)	Type	P_{out} (mW)	V_{op} (VDC)	I_{op} (mA)	Linewidth (nm)	Power Stability	Temp. (°C)
375	GaN	8.0	6.5 ±0.1	500	≤10	≤1%	18-25
405	InGaN	5.0	6.5 ±0.1	500	≤20	≤1%	18-25
532	DPSS	5.0	3.0 ±0.1	300	≤0.1	≤5%	22-24
655	GaAlAs	10.0	5.0 ±0.1	85	≤10	≤2%	18-25
808	AlGaAs	12.5	5.0 ±0.1	80	≤10	≤2%	18-25

Table 10: Laser Specifications

The blue and ultra-violet laser modules listed above have been on the market for less than 4 years, are costly to produce, and have an estimated lifetime of 10,000 hours. For this reason, they are energized before 30 seconds prior to an experimental run, and turned off immediately afterward. The violet and UV lasers include a thermo-electric cooling (TEC) module that helps to regulate diode temperature and stabilize output power. Diodes made from wide bandgap semiconductors (such as GaN) exhibit a strong sensitivity to changes in temperature. In particular, the bandgap is reduced with increasing temperature, causing a shift in the output spectrum (of 0.04nm per °C) and the threshold current needed to achieve lasing [72]. For these reasons, the diode chip is cooled to a constant temperature of 18°C using Peltier junctions, a heat sink, and cooling fan. All laser modules include an integrated photodiode that monitors optical output power, as shown in Figure 3.20, and provides a way of actively adjusting input current to maintain constant output power. When first powered on, the blue and UV lasers operate at 15% of full power to allow the

controller to achieve temperature stabilization. Operation of these lasers outside their desired window of 10-30°C will cause them to shut down and a red diagnostic LED to flash on the control board. The need for temperature stabilization of a laser diode is shown dramatically in Figure 3.22. This plot shows power versus time of lasers with and without active cooling.

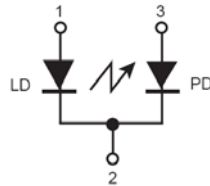


Figure 3.20: Laser Diode Module - Three Terminal Device

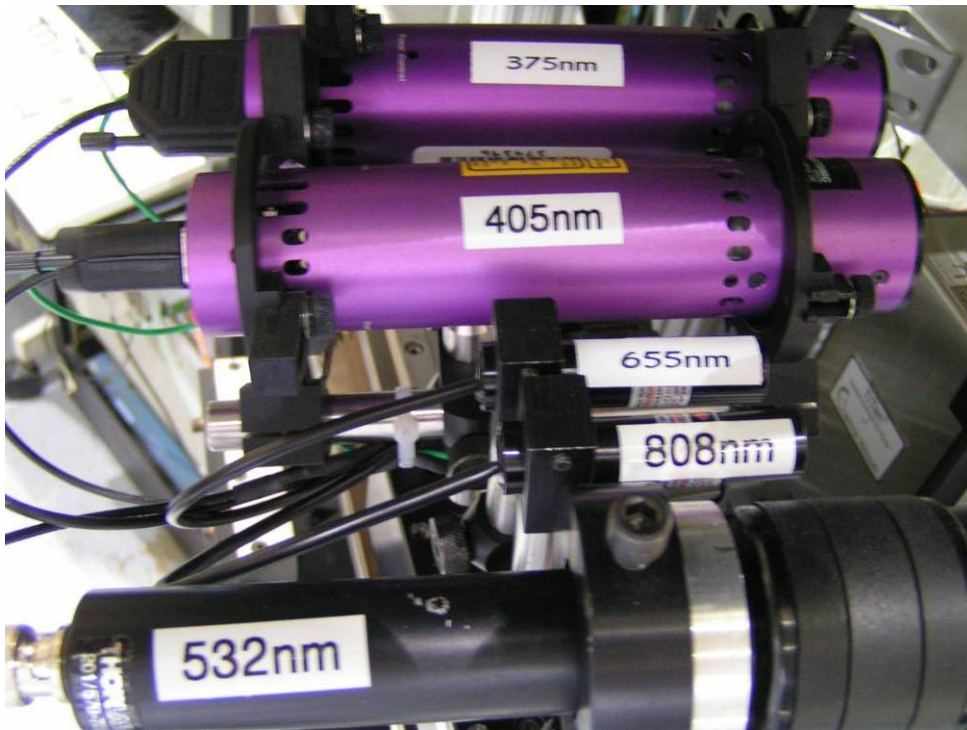


Figure 3.21: Lasers used to Measure QE

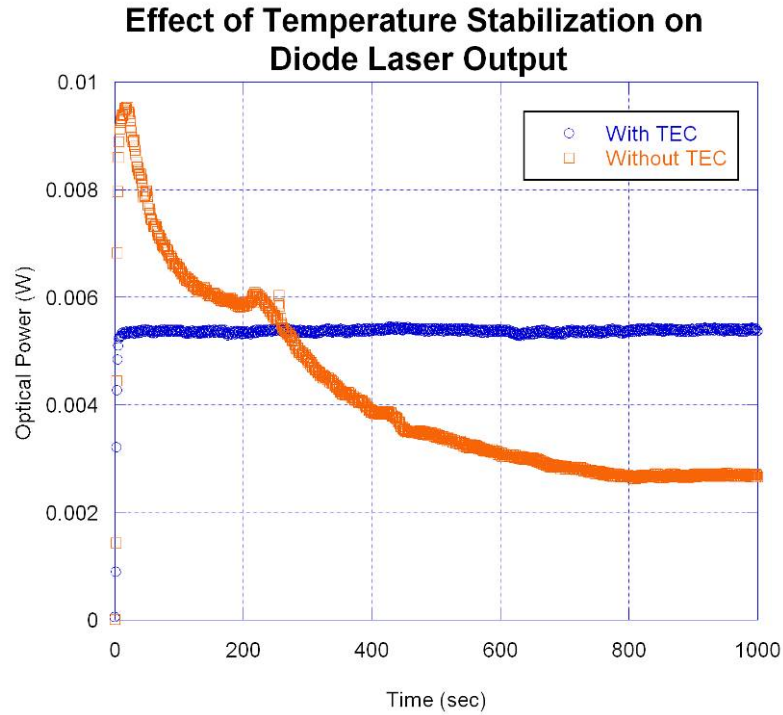


Figure 3.22: Effect of Temperature Stabilization on Laser Output Power

Because optical power is not measured continuously as part of the QE measurements, but rather once beforehand, it is mandatory that the lasers maintain constant output power after being turned on and off. Figure 3.23 shows that on-off keying of the lasers does not change their power output over time. Before QE measurements begin, the lasers are turned on and allowed to “warm-up” (for 30 seconds) to eliminate the possibility of transient behavior as they are powered on. A convenient feature for both the UV and blue lasers is that keying is accomplished using a TTL input which simply turns the diode on and off without shutting the entire module down. This has the effect of keeping junction temperature constant and serves to stabilize output power even as the laser is cycled on and off.

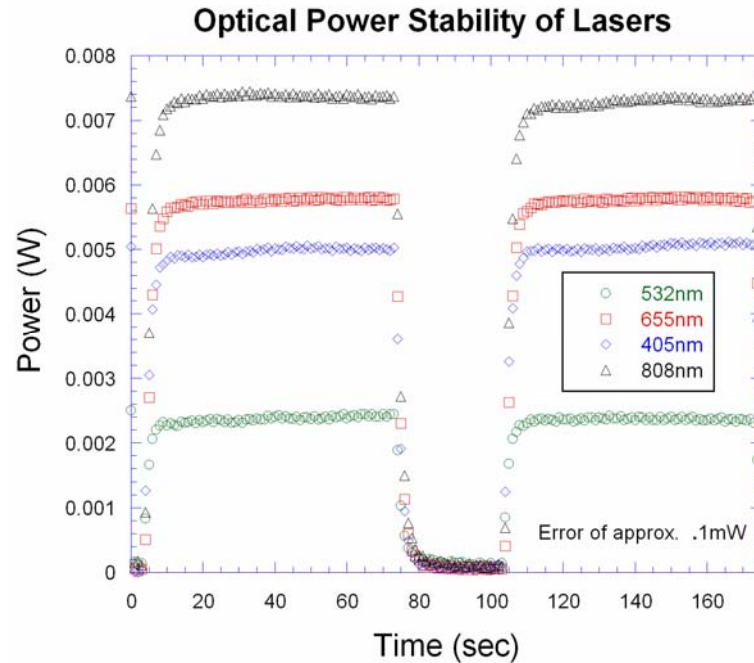


Figure 3.23: Optical Power Stability of Lasers

3.3.4 Laser Safety

Because the lasers used in this experiment have output power in excess of 5mW (Class IIIb) and include invisible wavelengths (IR and UV), safety measures were taken to assure an eye-safe working environment. This was accomplished by enclosing all lasers and optical paths in a black, coated-Plexiglas box and by using a video camera inside this structure to view and position the lasers. The CCD chip of the camera has sufficient sensitivity beyond the visible range to detect both IR and UV, allowing the user to view all lasers within the enclosure. The camera was used, for example, to aim the laser beams at an optical power meter and to align the lasers in preparation for QE measurements. Figure 3.24 shows the front of the optical enclosure, which also serves to protect the optics and robotic actuator from dust.

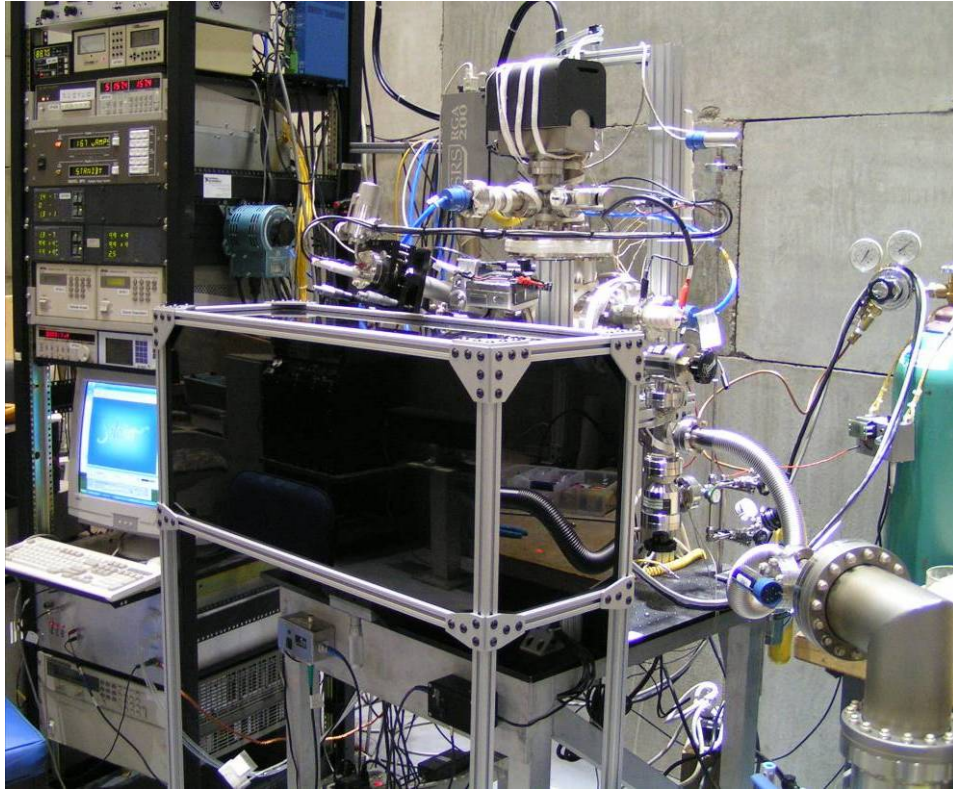


Figure 3.24: Coated Plexiglas Laser Safety Enclosure

Figure 3.25 shows the rear of the optical enclosure, made of double-lined black felt. A hole is situated in this cloth to allow the lasers a line-of-site view into the chamber to the photocathode.



Figure 3.25: Hole in Optical Enclosure for Laser Viewport

Because the lasers were mounted on a mobile stage attached to a computer-controlled robotic actuator, both observation and alignment of all lasers could be performed safely and remotely.

3.3.5 Robotic Control

When measuring QE as a function of cesium coverage, cesium is deposited at a rate of approximately 4.5 Angstroms per 100 seconds. Coverage, therefore, is constantly changing in time and determining QE at various wavelengths requires that such measurements occur nearly simultaneously. The challenge is to minimize the time interval between sequential QE measurements, such that cesium coverage can be considered constant over this period. This is accomplished using a high-speed single-axis robot, manufactured to specification as shown in Figure 3.26. In this arrangement, the lasers are rigidly fixed to a shuttle that is mounted on a linear motor whose motion (speed, acceleration, drift, etc) has been tuned to match the loaded mass of the laser assembly. The laser assembly attached to the linear actuator is shown in Figure 3.27.

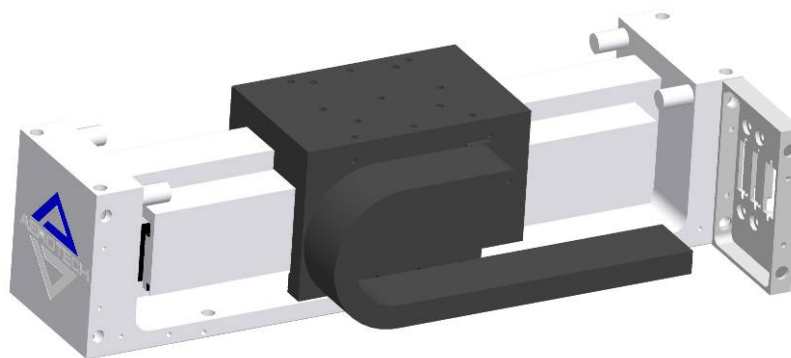


Figure 3.26: Single Axis Robot for Sequential Laser Positioning

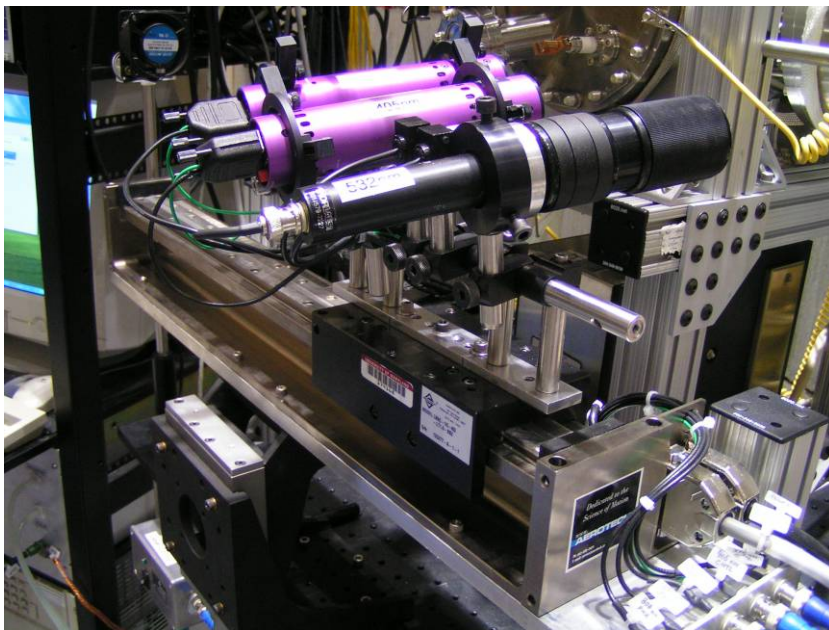


Figure 3.27: Lasers Mounted on Single Axis Robot

Each of the lasers are rigidly mounted and aligned for line-of-sight optical path to the cathode at a particular position along the single axis of motion. Their positions (with $0.1\mu\text{m}$ resolution) are given as inputs to a Labview program. To minimize vibration of optical components, Teflon tape was added to threaded lens mounts and set screws. During an experimental run, Labview controls the actuator, requesting various positions sequentially and collecting data from other instrumentation when the appropriate laser is in place. This allows QE measurements at different wavelengths to occur every 200ms, which is a short enough time interval to consider cesium coverage to be roughly constant.

The linear actuator utilized in this experiment is the LMA-400, shown in Figure 3.26, manufactured by Aerotech Corp. It is driven using the manufacturer's Soloist motor controller, which communicates with control software via Ethernet.

The modern version of a linear motor was invented by the controversial engineer, Eric Laithwaite, in 1944 for the purpose of moving a weaving loom for the textile industry [73]. It can be described as an ordinary rotary motor un-rolled and laid out flat. The circular stator and rotary coil of a rotary motor correspond to the linear track and forcer coil of a linear motor. Certain differences remain, however, as the motion of the linear motor is no longer periodic as in the rotary case, and linear guide rails maintain the airgap instead of rolling mechanical bearings. Whereas torque is the metric of interest [$N\cdot m$] for a rotary motor, force [N] is appropriate in describing a linear motor. Likewise, velocity for a linear motor is expressed as [m/s] instead of angular velocity [rev/min] in rotary motors. The “forcer” consists of coils encapsulated in epoxy and mounted in an aluminum chassis, along with the Hall-effect position sensors, thermistors, and associated connections. Like any brushless motor, the forcer and track (rotor and stator) share no electrical connection. Most applications for linear motors, including this experiment, utilize a mobile forcer and a stationary track containing a linear array of magnets, although a stationary forcer and mobile track is equally feasible. Because the mobile forcer contains the coils, a cable management system is used to accommodate motion of the attached wires. It is important to note that all power connections for the lasers, including ground, are fed through this cable management system.

Advantages of linear motors over other positioning systems include: 1.) very little wear, 2.) no backlash or windup as with rotary systems, 3.) direct positional feedback, and 4.) a resulting high degree of repeatability. Other positioning systems

were considered during experimental setup, including a screw-drive translator, a belt/pulley system, and a rack and pinion system.

The screw-drive option is based on a ball nut attached to a stage that moves uni-axially as a stepper motor rotates the screw. During testing of a candidate system from Zaber Inc., it became obvious that a trade-off exists between speed and positional accuracy of such systems. Unlike a linear motor, where absolute position is measured directly using a linear encoder, screw drives rely upon rotational encoders inside the stepper motor to determine position. The angular position and rotational history of the motor shaft is used to compute position with reasonably good resolution ($<10\mu\text{m}$), so long as linear speed does not exceed about 1 cm/sec. Beyond this velocity, however, the screw begins to slip and positional information of the stage is lost. As discussed earlier, the QE measurement application requires rapid sequential motion and screw drives simply do not provide the acceleration, velocity, or position feedback needed to execute rapid motion. Belt-drive and rack and pinion systems, although not tested for this experiment, were considered and found to have similar draw-backs as screw drives: lack of accuracy, speed, and repeatability. In contrast, the linear motor (actuator) provides unprecedented repeatability, 5 m/s velocity, 4g acceleration, and an accuracy of $\pm 0.1\mu\text{m}$.

Prior to selecting a linear actuator, it was necessary to determine the motor and amplifier requirements. These are dictated by the mass of the lasers and the desired velocity with which they should move. The mass to be moved includes not only the lasers, but the forcer chassis and its attached cable management system. A safe estimate for the combined mass is 10kg. The maximum travel needed in this

experiment is 400mm. The actual motion can be approximated by assuming that the laser stage must travel its furthest distance of 200mm in no less than 100ms, followed by a dwell time of 200ms to allow mechanical vibrations to decay to making a QE measurement. Because the stage must begin and end at rest, the period of motion must consist of an acceleration and deceleration phase, with (possibly) a drift period in between. In this setup, a “trapezoidal” motion profile was chosen where equal time is allocated to the acceleration, drift, and deceleration phases, as shown in Figure 3.28.

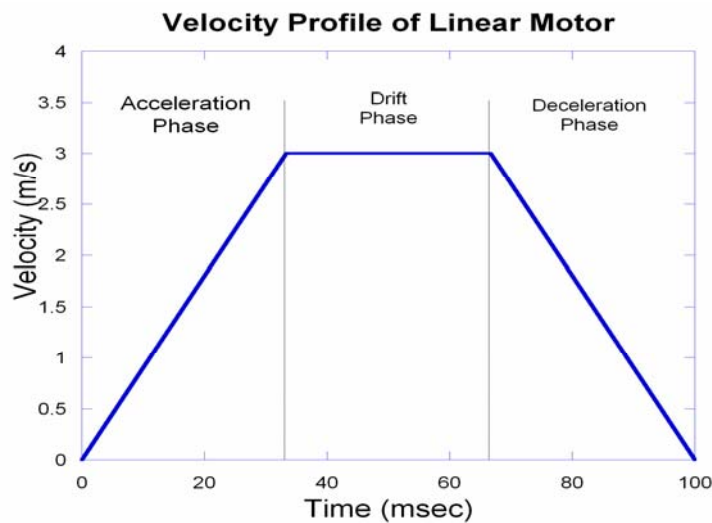


Figure 3.28: Velocity Profile of Linear Actuator & Laser Shuttle

Given this motion profile, a maximum velocity of 3.0 m/s is given by

$$v_{\max} = \frac{s}{2\Delta t}, \text{ where } \Delta t = 100\text{ms}/3, \text{ and total distance } s \text{ is } 0.2\text{m. To attain this velocity in}$$

time Δt , an acceleration of approximately 9g is needed. The motor must therefore apply a peak force of 900N. Friction must also be accounted for: a conservative

estimate for the coefficient of friction of a cross-roller bearing is about 0.003 [73], adding an effective additional loading force of $f_f = mg\mu = 0.294 \text{ N}$. Motor sizes are specified by the manufacturer according to peak and continuous (average) force. RMS force is given by:

$$f_{rms} = \sqrt{\frac{t_1 f_1^2 + t_2 f_2^2 + t_3 f_3^2}{t_1 + t_2 + t_3 + t_{dwell}}} \quad (3.6)$$

where $t_{dwell} = 200 \text{ ms}$. Notice that in order to maintain constant velocity during the drift phase, the motor must still apply sufficient force to overcome friction. Using peak force (900N) and average force (424N), as motor specifications, the LMA-400 linear motor was chosen for this experiment.

4. Experimental Techniques

4.1 Data Acquisition and Control

Emphasis has been placed in previous chapter upon repeatability of fabrication and measurement routines in this experiment. No other feature has greater impact in this regard than automated data acquisition and control. Since the very beginning of this project, priority has been given to automating and recording fabrication procedures and measurement results. As will be seen in the following sections, fabrication of photocathodes involves a complicated sequence of tasks that involve varying vacuum conditions, pumping speed, evaporation rates, temperature, and other factors. In most cases, obtaining a reliable data set is contingent upon executing an exact time sequence of steps. This is an ideal application for computer automation and Labview was used throughout this research program to coordinate and optimize experimental routines. This section outlines the instrumentation used to make measurements and the automation schemes used to collect, save, and analyze the resulting data.

4.1.1 Instrumentation

Instruments for this experiment were selected to have GPIB connectivity, so that a central GPIB bus provides front panel functionality of all instruments through appropriate Labview interfaces.

4.1.1.1 Cathode and Chamber Temperature

Temperature at the cathode is important because in many cases it is critical in achieving desired surface conditions and inducing changes in those conditions for a particular experiment. This includes high temperature cleaning, surface diffusion, evaporation, desorption, and temperature-dependent photoemission effects. It is measured by situating an alumina-potted type-K thermocouple behind the cathode heater, such that the thermocouple junction is in good contact with the rear of the cathode. The thermocouple leads are attached to vacuum feedthroughs that are wired to channel 5 of the SRS SR630 thermocouple monitor. This instrument has 16 thermocouple inputs, all accessible remotely via GPIB. While cathode temperature is the most important, auxiliary thermocouples monitor temperature at various locations on the chamber exterior to ensure uniform heating during bakeout.

4.1.1.2 Coating Coverage

Surface conditions at the cathode depend not only on temperature, but also on the composition and quantity of materials placed there. Composition is carefully controlled by using high quality sources and an RGA to verify the integrity of their emission, while a quartz crystal monitor (QCM) is used to measure quantity, measured in coating thickness and percent monolayer coverage. The instrument chosen for this project is the Inficon XTM/2, based on a quartz crystal sensor unit mounted on a vacuum flange with vacuum feedthroughs to accommodate electrical connections and water-cooling channels. The sensor unit works with a rack-mount micro-controller to interface with GPIB. Figure 4.1 shows an engineering schematic of the unit, along with un-mounted and mounted views of the sensor head.

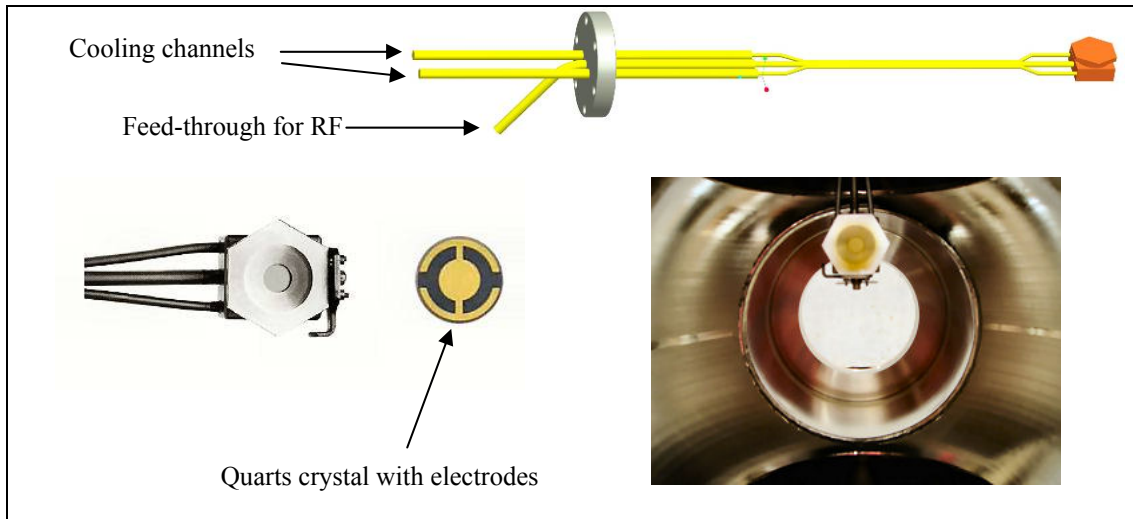


Figure 4.1: Illustrations of Deposition Monitor Sensor Head

The sensor head for Inficon’s deposition monitor XTM/2 consists of a disk-shaped quartz crystal whose piezoelectric resonance is sensitive to added mass. An AC voltage applied to the faces of a piezoelectric crystal cause it to mechanically distort and the change in shape is proportional to the applied voltage. Due to the mass and geometry of the crystal, resonant motion can be established if the frequency of applied voltage matches the natural resonance frequency of the crystal. The resonant frequency is very sensitive to slight changes in mass and can be used to detect the addition of less than an atomic layer of adsorbed material. An RF source sweeps through a range of frequencies and as mass is increased the observed resonant frequency decreases. The Inficon crystals have a starting resonant frequency of 6.0 MHz and register a shift of 2.27 Hz when a 1Å coating of aluminum is deposited. For films less than 2μm thick, the frequency shift is linear and obeys Sauerbrey’s equation:

$$f_c = f_q - \sigma m \quad (4.1)$$

where f_q is the fundamental resonance frequency of an unexposed crystal, f_c is the frequency of the coated crystal, m is the mass and σ is the sensitivity of the resonant frequency to a change in mass [75]. The sensitivity is an intrinsic property of the crystal and is given by $\sigma = f_q^2 / NS\rho_q$, where N is the frequency constant of quartz, S is the film surface area, and ρ_q is the quartz crystal density. The XTM/2 head unit performs the calculations with user-defined parameters describing the film's composition. Its final output is film thickness (in Angstroms), found using the expression:

$$T_f = \frac{N\rho_q(f_c - f_q)}{f_q^2\rho_f} \quad (4.2)$$

where T_f and ρ_f are the film's thickness and density. The sensor is very sensitive to changes in temperature, a water circulation system was installed to minimize temperature fluctuations. When excessively thick films (microns) are deposited on the crystal, its resonant motion becomes unstable and varies between neighboring modes of different frequencies. This is a sign that the crystal sensor has reached the end of its usable life and must be replaced. Cesium coatings are typically measured in this experiment, to determine the effect of coating thickness of photoemissive properties. Inside the chamber, the sensor head is mounted such that it and the cathode are the same distance from the cesium evaporation source, as shown in Figure 4.2.

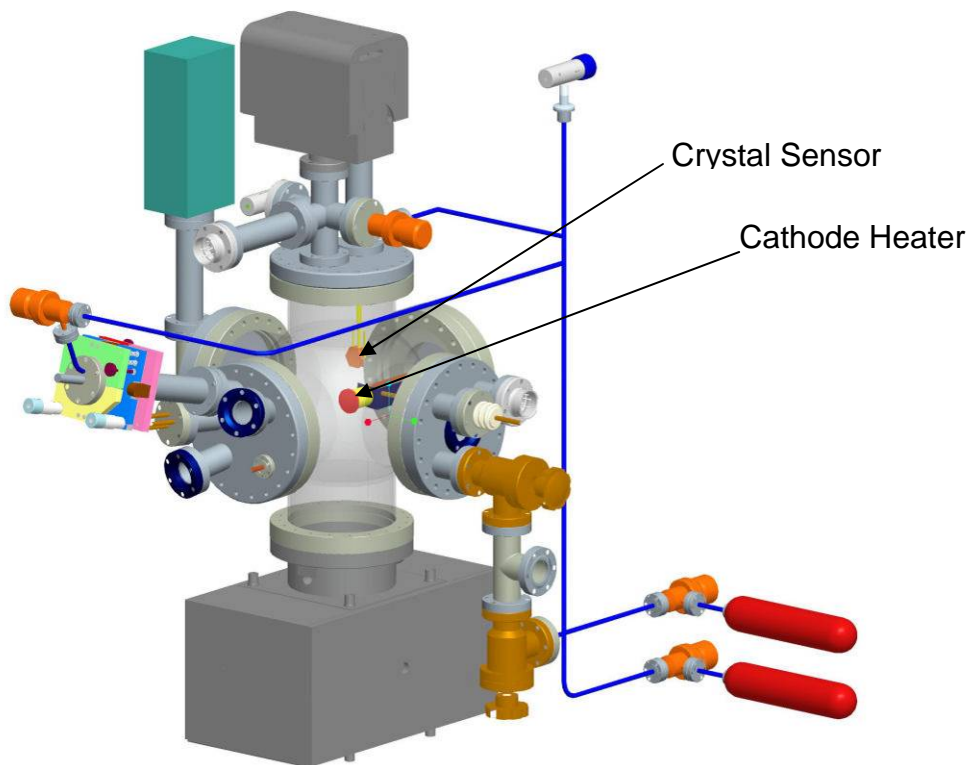


Figure 4.2: Relative Positions of Cathode and Deposition Monitor

4.1.1.3 Photocurrent

Quantum efficiency is defined as the ratio of emitted electrons to incident photons. Measuring this property of a photocathode requires a sensitive current meter, capable of detecting tens of picoamperes of DC current. The instrument chosen for this work was a Keithley 486 pico-ammeter with an advertised current resolution of 0.5 fA. It was calibrated and certified prior to integration with the experimental apparatus. Depending upon QE of a particular cathode and the wavelength of light interrogating it, photocurrent would vary from a few nanoamperes to several microamperes. Unfortunately, the Keithley 486 does not have the ability to seamlessly switch from one measurement range to another, so care must be taken to

select the appropriate resolution prior to experimentation. It does have an auto-range feature, but this proved troublesome because while switching ranges, spurious noise appeared in the metering circuit. It is believed that a brief interruption in the photocurrent causes charge buildup on the cathode with a subsequent in-rush current appears when the interruption is removed. Another problem was that the multi-purpose research building housing the cathode fabrication lab is host to other experiments that generate spurious electrical noise and could overwhelm sensitive photocurrent measurements if only single-shield BNC cables were used. Using triax cable throughout the quantum efficiency measurement circuit eliminated this problem.

4.1.1.4 Laser Power

Measuring QE requires knowledge not only of the quantity of emitted electrons, but also the number of incident photons. A rough estimate of optical power (or number of photons per unit time) is given by the laser specifications outlined in the previous section. These are advertised specifications, however, and the actual power output will differ a few percent. With the exception of the red and IR lasers, fine adjustment of output power is possible by tuning an internal potentiometer. A Molectron EPM1000 light meter using the PM3Q thermopile sensor is used to determine the output power of the lasers. A thermopile is actually a heat sensor consisting of many thermocouple junction pairs connected electrically in series. Absorption of photons causes an increase in temperature of one or more junctions and creates a voltage drop across the series network. The junctions in series are termed *active junctions* while an identical junction held at a known, fixed temperature is

called the *reference junction*. The voltage drop developed across the series network of junctions is in direct proportion to the temperature differential between active and reference junctions. This effect of converting radiant energy into an electrical signal is called a thermoelectric effect. Because heating is involved, it is important to remember that instantaneous measurement of optical power is not possible. Instead, a period of about 0.5 seconds is required for the heating effect of the thermopile to register a change in output voltage. Quartz viewports are used in this experiment to prevent attenuation of the shorter wavelength lasers. Figure 4.3 shows that transmissibility of quartz is constant over the visible range [76].

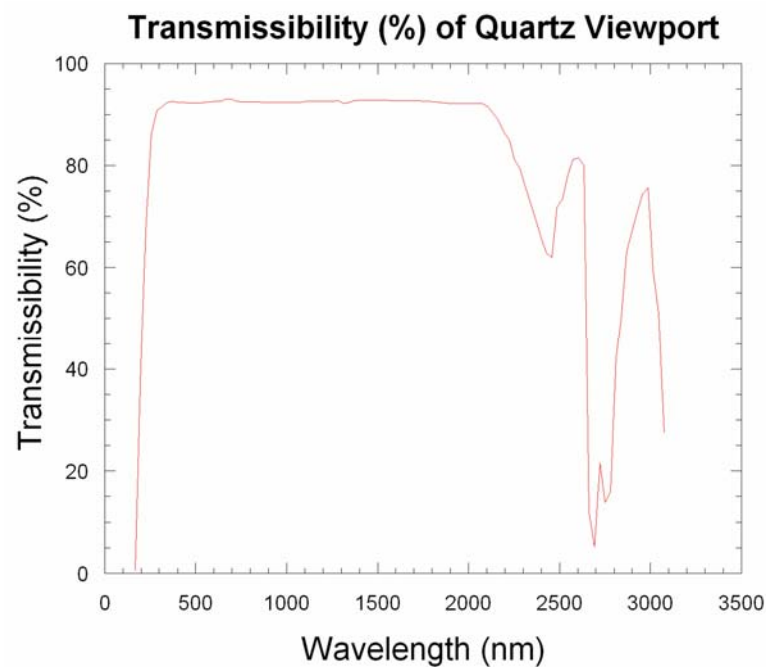


Figure 4.3: Wavelength-Dependent Transmission of Quartz Viewport

When measuring quantum efficiency, it is important to account for reflection of incoming laser light off the viewport surfaces, since this reduces the amount of

light incident at the cathode surface. Approximately 3.5% of light incident on each surface of the quartz window is reflected, so only 93% of the beam arriving at the viewport is transmitted to the cathode. The Labview routine used in this experiment was programmed to automatically accept reflectivity and accept as inputs the output power and wavelength of each laser.

4.1.1.5 Residual Gas Analyzer

While an ideal vacuum system for photoemission experiments should have as low a background pressure as possible, the *composition* of the residual gas in the system is just as critical. Water and carbon monoxide, for example, are highly detrimental to the lifetime and performance of cesiated cathodes. A residual gas analyzer (RGA) was installed on the system to measure not only the total background pressure, but also the gas composition at various stages of the experiment.

An RGA is essentially a mass spectrometer that ionizes gas molecules using a hot filament and separates the resulting positive ions according to mass, while measuring the ion current (which is a direct measure of partial pressure) corresponding to each gas species. The mechanism responsible for separating ions according to their mass is the quadrupole mass-filter, consisting of four long rods, operated by a combination of RF and DC voltages. The RF field's magnitude and frequency determine the mass/charge ratio of ions permitted to pass through without striking the rods, while the RF/DC voltage ratio determines filter selectivity. Ions that pass through the filter constitute a current measured by a sensitive electrometer. The unit, shown in Figure 4.4, is mounted such that cesium ions do not have a direct path

to the detector during fabrication of cesiated photocathodes. Coatings that develop on the active elements of the RGA degrade performance.

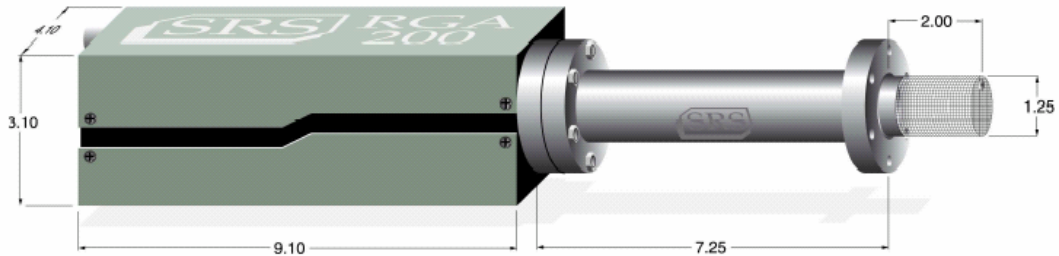


Figure 4.4: SRS Residual Gas Analyzer

The unit is controlled via its RS-232 communication port using a software interface that collects and plots pressure data in a number of different formats. An important feature of this software is the leak-check feature, where detection is intentionally focused on a trace gas, typically helium, that is sprayed by the user over suspicious vacuum components. During all vacuum processes, care must be taken to assure that the filament in the RGA is turned off whenever total pressure rises above 1×10^{-4} Torr.

4.1.2 Labview Introduction

Labview is a graphical programming language that is extremely well suited to laboratory data acquisition and process control. The environment loosely resembles an electrical schematic diagram, showing subroutines as icons that pass data to each other through connecting “wires.” These virtual wires are color-coded depending upon the type of information they carry. Software written in Labview serves one of two distinct purposes: instrument interface or data acquisition. In either case, the

resulting code is called a *virtual instrument (VI)*. A VI designed interface with a piece of physical hardware, such as a thermometer, is usually nothing more than a vendor-specific set of formatted ASCII character commands that are sent to an appropriate destination on the GPIB bus. Typically, diagnostic features are added to instrument interface VI's to enhance troubleshooting. Figure 4.5 shows a simple VI whose purpose is to turn off a set of relays. It accepts an input Boolean (T/F) variable and sends commands to device 26 of the GPIB bus if this variable is true. All instruments listed in the previous section have their own interface VIs, which serve as components in larger VIs that together coordinate the operation of all instruments as part of a specific experiment. Table 11 lists the name and function of each VI.

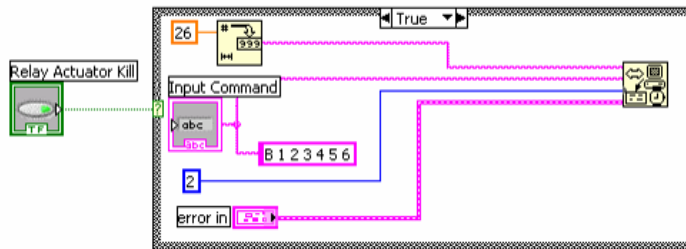


Figure 4.5: Example Labview Instrument Interface VI

Detailed discussions for VI's that coordinate experimental process control and data acquisition are reserved for later in the chapter, when the various experimental processes are outlined in turn. The suite of Labview programs developed in this project offer an advantage not only in experimental repeatability, but also in productivity, since lengthy processes such as bakeout or depositions can be programmed to run for hours or days without user intervention.

VI Name	Instrument	VI Function
gpib_read_convectron.vi	Granville-Phillips 307	Read pressure from thermocouple gauge
gpib_read_inficon.vi	Inficon XTM/2	Read coating deposition thickness
gpib_read_keithley.vi	Keithley 486	Read current from picoammeter
gpib_read_molelectron.vi	Molelectron Power Meter	Read optical power incident on thermopile sensor
gpib_read_pressure.vi	Granville-Phillips 307	Read pressure from ion gauge
gpib_read_therm.vi	SRS SR630	Read temperature at cathode from thermocouple monitor
gpib_supply_adjust.vi	PPS-10710	Control output from DC current source
relay_actuator_off.vi	GPIB Relay Rack	Shut off all relays (used as fail-safe)
laser_relay_control.vi	GPIB Relay Rack	Control relays supplying current to lasers
WaitForAxisStatusBit.vi	Single Axis Robot (SAR)	Position feedback for lasers on SAR
Move.vi	Single Axis Robot (SAR)	Move lasers to absolute position along x -axis
Enable.vi	Single Axis Robot (SAR)	Enable SAR for motion (release brake, etc)
Init.vi	Single Axis Robot (SAR)	Initialize communications link with SAR
Home.vi	Single Axis Robot (SAR)	Bring SAR stage to x -axis origin to recalibrate distance

Table 11: List of Labview Instrument Interface VIs

4.2 Experimental Procedures

The goal of this research is not only to pioneer better photocathodes, but also to advance the theoretical framework explaining cathode behavior with respect to surface conditions, operating environment, and incident drive laser. This is accomplished by validating theoretical predictions for cathode performance. The

quality of such validation obviously rests on a firm knowledge of what physical system is being modeled. Great care was taken throughout this project to understand surface conditions at the cathode and assure that observed behavior can be replicated. Unless otherwise stated, each experiment was repeated at least 3 times and is only mentioned as significant if the resulting data sets coincide within acceptable limits. The procedures developed to accomplish these tasks fall in several distinct categories and are outlined below.

4.2.1 Chamber Pumpdown

After assembly or modification of the vacuum fabrication chamber, various steps must be executed to reliably achieve UHV (0.1 nTorr) conditions. These are: initial pumpdown, argon discharge cleaning, continued pumping, chamber bakeout, and ion pumping. The roughing station is first connected to the main chamber pump port and valve V1, as shown in Figure 3.16, is opened just as the pump is activated. When the Convectron gauges read 1×10^{-4} Torr, the ion gauges (on the pumping station and chamber) can be energized to monitor further pumping progress. Pumping must continue until the roughing station's base pressure of 1×10^{-6} Torr is reached. The next step is to remove adsorbed gas molecules on the chamber walls and components using argon ion bombardment with dynamic pumping. A Variac-driven high voltage source, connected to a high voltage feedthrough shown in Figure 4.6, enables adjustment of the plasma discharge. Figure 4.7 shows the breakdown electric field of argon gas as a function of pressure [77]. The minimum of the Paschen curve occurs at about 0.2 Torr, requiring a field of 200kV/m.

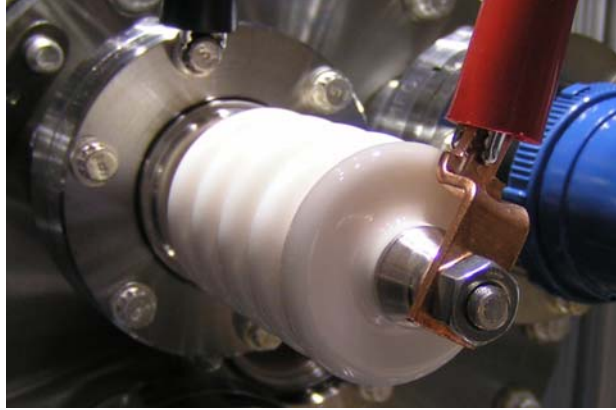


Figure 4.6: High Voltage Electrical Vacuum Feedthrough

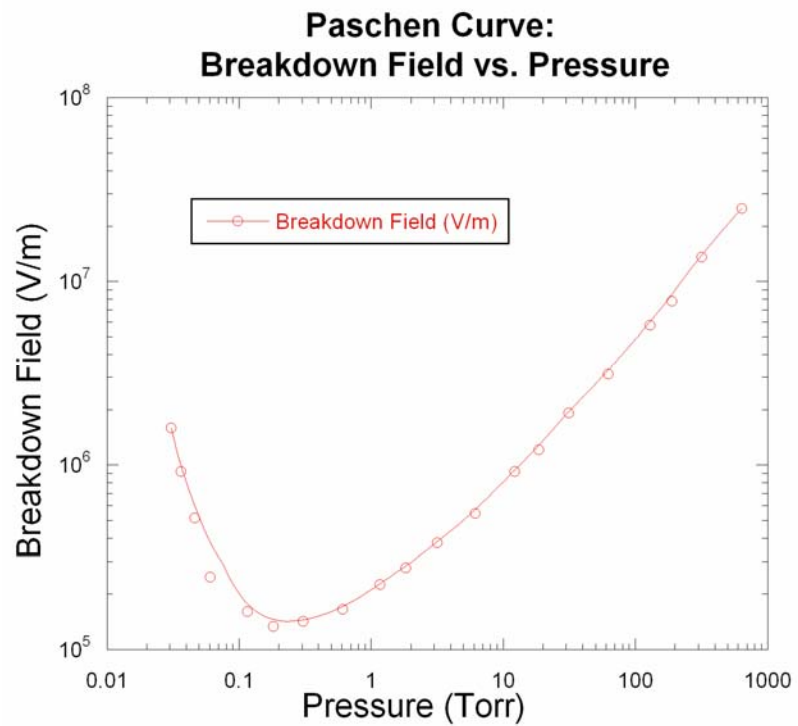


Figure 4.7: Paschen Discharge Curve: Field vs. Pressure

At a Variac setting of 40%, the supply delivers 5kV AC to the high voltage standoff that is internally situated 2.54cm from the chamber wall. This distance and field enables a chamber-wide plasma discharge. Because the goal of this process is to

remove contaminants from the chamber, it is not enough to simply knock them off the walls. Dynamic pumping while discharge cleaning allows the contaminants to be removed and then pumped out of the system. This is accomplished by reducing the pumping speed of the roughing station by completely closing valve V1 and opening it only 3 turns. Then valve V8, a sapphire-sealed fine metering valve, is opened 8 turns to allow argon to slowly enter the chamber. Upstream from valve V8 is a GPIB-enabled valve that is controlled by Labview to maintain a target pressure of 0.2 Torr in the chamber. This process continues for an hour and then the system is once again pumped to base pressure.

The next step is a chamber bakeout, in which the system is heated to 250°C for 4 hours if no new components have been added to the system. If new components were been introduced, then an overnight bakeout is recommended. During this phase, the cathode is also heated to a temperature just above that of the chamber, to prevent contaminants from the walls from “freezing out” on the cathode. It is important to wait until base pressure is reached before heating either the cathode or the chamber and to assure that the chamber temperature is uniform and does not exceed 350°C. Beyond this temperature, the braze sealing the quartz viewports melt, causing catastrophic failure of the vacuum system.

4.2.2 Cathode Preparation

After UHV conditions have been reached, it is necessary to prepare the cathode surface for subsequent fabrication and measurement steps. This is accomplished by outgassing, argon-discharge cleaning, high-temperature anneal, and ion-bombardment. The latter step was found to be so successful in preparing the

surface that it alone would suffice as the cleaning mechanism. This is discussed separately later in this chapter. The outgassing, plasma discharge, and anneal were still performed prior to ion beam treatment to maintain consistency. Outgassing the cathode simply involves controlled heating in order to avoid an instantaneously high gas load on the ion pumps when cathode temperature is later increased as part of an experiment. When pressure is in the nano-Torr range, the current through the cathode heater is slowly incremented if the chamber pressure is less than 3 nTorr using a Labview routine. The cathode heater consists of a nichrome filament alumina-potted inside a molybdenum chassis capable of reaching temperatures in excess of 1200°C. As the cathode temperature increases, trapped gasses and adsorbed material are released and pressure typically exceeds the 3 nTorr threshold. When this occurs, Labview slowly decreases heater current to reduce the outgas rate, bringing the pressure below the threshold once again. Once pressure is again below 3 nTorr, cathode heater current is incremented as before. This process continues until a temperature of about 400-600°C is reached and the trapped gases are released. If Labview is not used to dynamically increment cathode temperature, pressure rises sharply as shown in Figure 4.8. Notice that at elevated temperature, pressure increases as trapped gases are released and then begins to decline even at elevated temperature. This particular cathode sample (rolled tungsten) had been exposed to atmosphere and had only undergone glow discharge cleaning prior to its bakeout. For samples exposed to atmospheric conditions, this sharp increase in pressure during bakeout is expected.

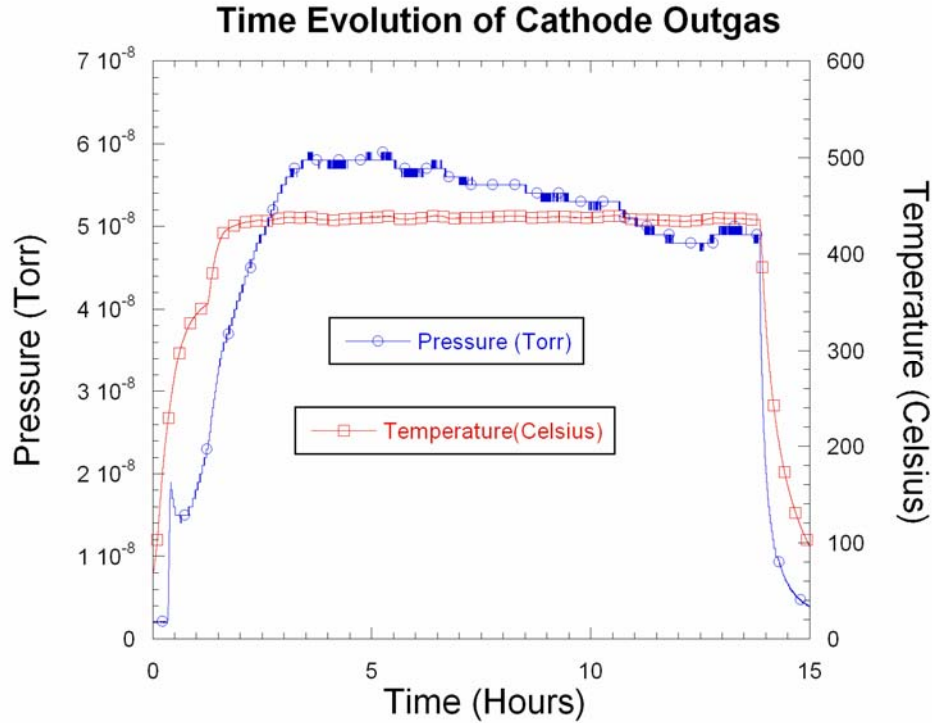


Figure 4.8: Cathode Bakeout Profile: Pressure and Temperature vs. Time

If cleaning the cathode surface using high temperature anneal, the current through the cathode is increased to roughly 8 amps and its temperature rises to 1200°C. At this elevated temperature, almost all contaminants (except perhaps oxides) leave the surface. Because the cathode assembly is connected to the chamber only through thin ceramic standoffs and electrical feedthroughs, it is thermally isolated and takes several hours to cool down, as shown in Figure 4.9. It was found that unless some combination of surface cleaning was performed, photoemission would not occur for any amount of cesium coverage. Presumably, higher work function contaminants uniformly cover the surface and prevent dipole-moment interaction of the adsorbed cesium atoms with the cathode substrate.

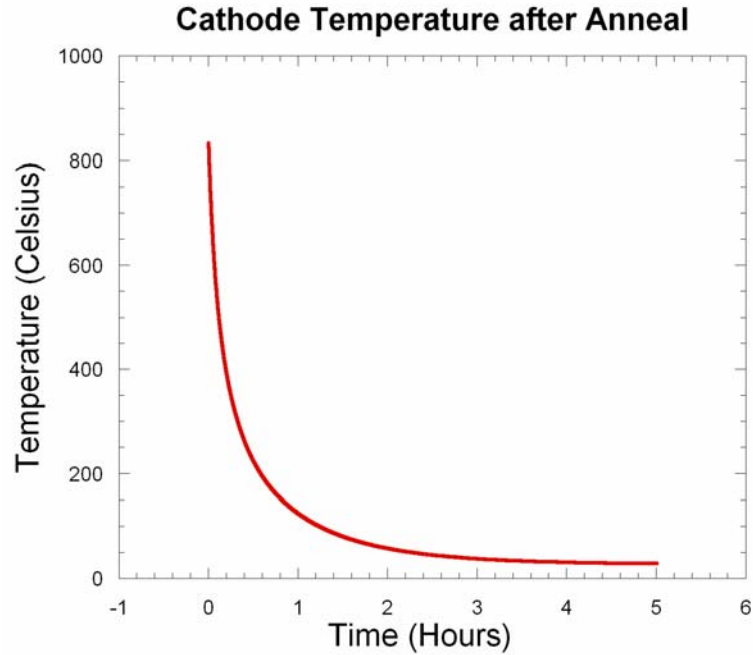


Figure 4.9: Cathode Cooling via Conduction and Radiation

Another surface cleaning technique used is DC argon plasma discharge. Unlike the discharge process outlined earlier, which was intended to clean all surfaces in the chamber, this process is intended to selectively clean only the cathode surface. Figure 4.10 shows the familiar purple glow of argon plasma at the cathode surface.

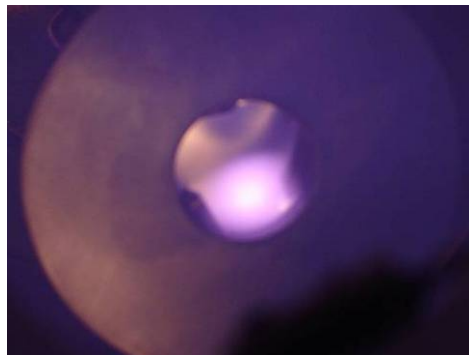


Figure 4.10: DC Argon Discharge Cleaning of Cathode Surface

In this process, a potential of +350V is applied to the chamber relative to the cathode surface and the chamber is held at a temperature above 100°C, to prevent collection of water and other contaminants released from the cathode. Other parameters of the DC glow discharge cleaning process are shown in Table 12. Positively ionized argon atoms accelerate toward the negatively biased cathode and clean the surface via kinetic bombardment. As with the AC fields discussed earlier, the glow discharge is maintained by secondary electron emission, requiring a critical current density of about $1\mu\text{A}/\text{cm}^2$ [78]. When the current density exceeds $100\mu\text{A}/\text{cm}^2$ arcing may occur, causing unwanted deposition of metal due to sputtering. To prevent arcing, a $2\text{k}\Omega$ current limiting resistor was placed in series with the source and electrodes.

Voltage	350VDC
Current	30mA
Pressure	3×10^{-2} Torr
Chamber Temp	180° C
Cathode Temp	< 600° C
Gas Flow	0.2 cc/s

Table 12: Argon gas discharge cleaning parameters

Because the electrode at the lower potential experiences discharge cleaning, it is simple to interchange the polarity of applied voltage such that various surfaces throughout the vacuum chamber are selectively cleaned. It was discovered that it is beneficial to clean the anode along with the cathode, because contaminants on the

anode are released in an undesirable fashion during QE measurements as photoexcited electrons strike the anode surface.

4.2.3 Cesium and Multi-Alkali Deposition

Recall that for the first two phases of experimentation, the goal is to determine the effect of cesium coverage on polished and sintered metallic substrates in preparation for fabrication and measurement of a controlled porosity dispenser photocathode (the third phase). In the dispenser case, cesium originates beneath the cathode surface and diffuses to the top, reducing the work function and enabling photoemission. In such an arrangement, the quantity of cesium arriving at the surface cannot be directly measured. The only quantities conveniently measured are photocurrent and quantum efficiency. If a relationship can be established between these values and surface conditions, then indirect measurement of the dispenser cathode's cesium coverage is possible. To determine the relationship between QE and coverage, cesium was evaporated first onto rolled, polished substrates while QE was measured at various incident laser wavelengths. What follows is an outline of the process for reliably depositing cesium and other alkali-metal coatings.

After the cathode surface is prepared through either heat anneal, glow discharge cleaning, or ion beam treatment, cesium evaporation on the surface can begin. The cesium sources, shown mounted on a standard 2.75" flange in Figure 4.11, are activated with a current of 6.0A when new and 7-8A after about 10 temperature cycles. After this amount of use, the sources are replaced. For new sources, the temperature must be gradually increased prior to activation to outgas the source. The process is similar to outgassing the cathode, discussed earlier.

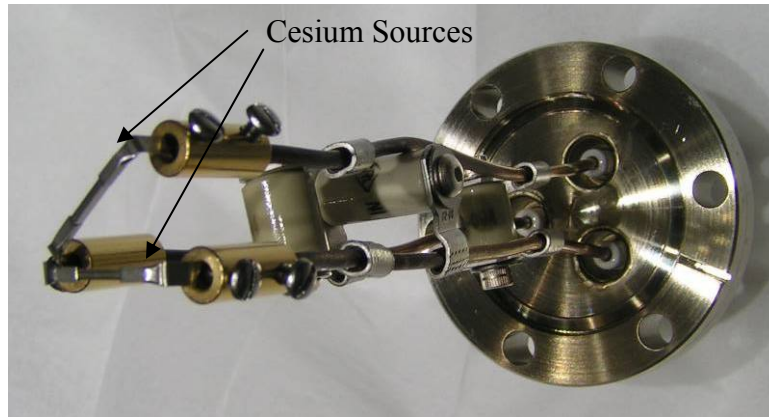


Figure 4.11: Cesium Sources mounted on 2.75" Flange

Labview directs a programmable DC power supply to slowly increment the current passing through the source. Labview prompts the user for a target pressure and then adjusts the rate of increase in source temperature to stay within that pressure limit. If pressure exceeds the given threshold, the temperature is decreased until pressure is sufficiently reduced and the outgassing process continues. The program will shut down the outgas procedure if the deposition monitor registers 20 Angstroms of cesium during this stage, signaling that the source has been activated and is ready to use. Figure 4.12 shows the effect of chamber pressure as current is slowly incremented during the early stages of outgassing a new source. Notice that the target pressure was 5×10^{-8} Torr during outgassing of the source and the magnitude of pressure oscillation is reduced as the process continues. Notice also that the oscillations of cesium source current (temperature) and pressure are not in phase. This is a reflection of the simple fact that an increase in source current does not produce an instantaneous increase in temperature of the source. The lifetime of the cesium sources varied from between 10 to 15 temperature cycles, and it was observed that

each consecutive cycle required a higher activation current than the previous. Unused cesium sources were kept in a desiccator to prevent moisture contamination from being introduced into the system. As the outgas process continues, the source reaches its activation temperature of about 500°C, corresponding to a source current of about 4.5A. Figure 4.13 shows this stage of the process. Notice that as the source begins to emit cesium, chamber pressure begins to drop dramatically, even though source current continues to increase. This is due to the fact that cesium is an effective getter material, reacting with (and trapping) stray gas molecules, leading to lower background pressure. As source current continues to increase, this effect is overwhelmed by the increasing gas load caused by a hot source and pressure begins to increase again beyond ~5.5A.

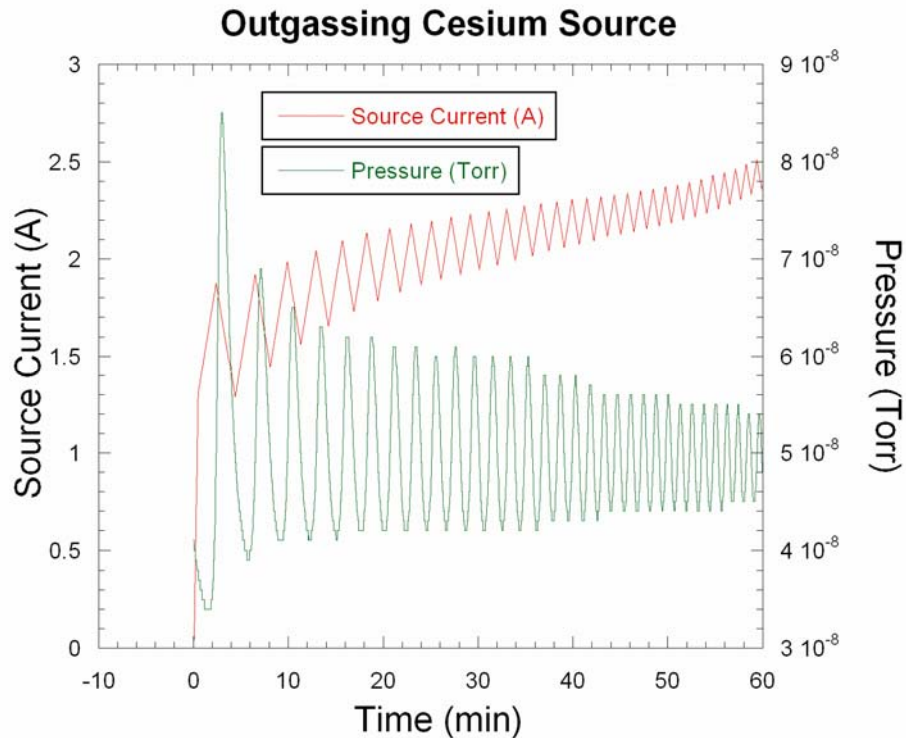


Figure 4.12: Early Stage of Cesium Outgassing

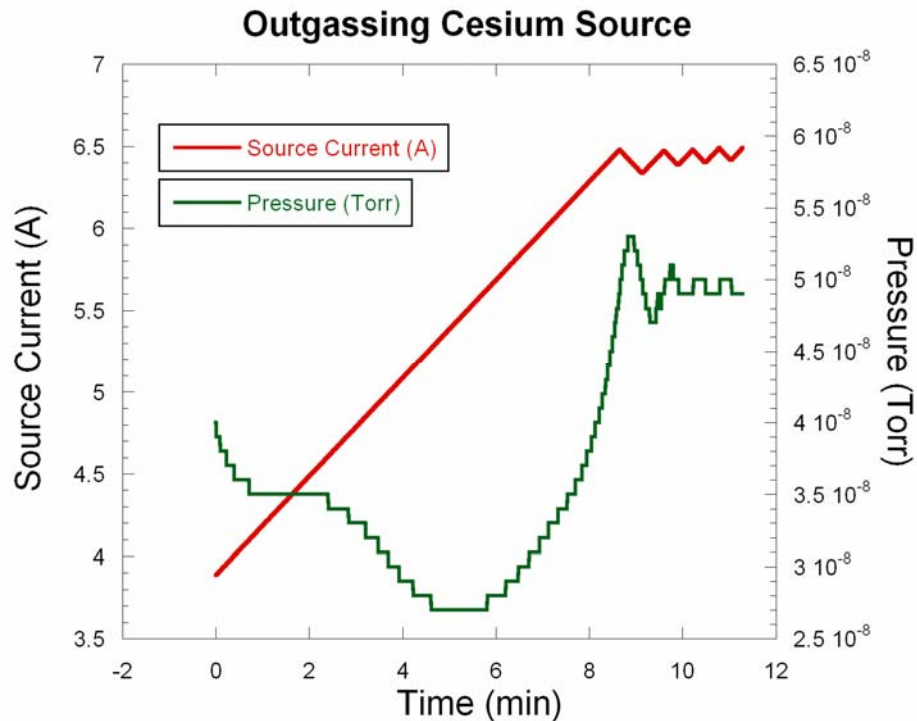
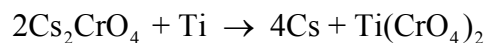


Figure 4.13: Later Stage of Cesium Source Outgassing: Activation

The sources shown in Figure 4.11 are commercially available from SAES, Inc. not only for cesium, but most all of the alkali and alkali-earth metals. In most cesium sources, such as the dispenser cathode discussed in following chapters, cesium chromate reacts with titanium to produce elemental cesium. Titanium metal powder serves as a reducing agent, donating electrons in the chemical reaction:



Each cesium atom gains one electron and titanium loses four. Cesium is released as an atomically neutral vapor and the titanium chromate remains as an inert solid inside the source. SAES has improved upon this reaction slightly by using a composition of reduction agents, zirconium (84%) and aluminum (16%), in an alloy called St101. In addition to producing cesium vapor, this reaction has the added benefit of removing

chemically active gases from the device during operation. Even with these gettering compounds present, however, the SAES cesium source is not without some degree of contamination, as shown by an RGA scan in Figure 4.14. Of particular concern are traces of cathode poisons such as water, carbon monoxide, and carbon dioxide. This may be partly due to the fact that the sources were exposed to atmosphere during insertion into the vacuum system. While the vendor advertises that atmospheric handling is an acceptable practice, it would be better to install the sources in an inert-gas glove-box. This was not available, so the outgas procedures outlined earlier, together with an ion beam treatment, were used to remove these and other contaminants after source outgassing. Figure 4.15 shows a constant deposition rate of about 4.5 Angstroms per 100 seconds. As the source nears the end of its useable life, its deposition rate decays and requires an increase in source current.

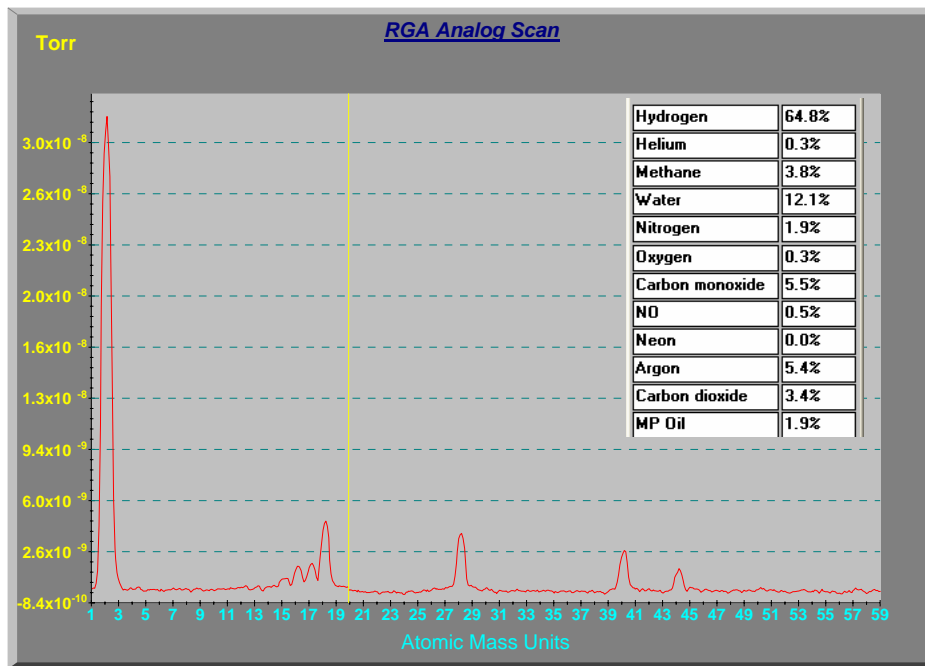


Figure 4.14: Background Gas Composition During Cesium Deposition

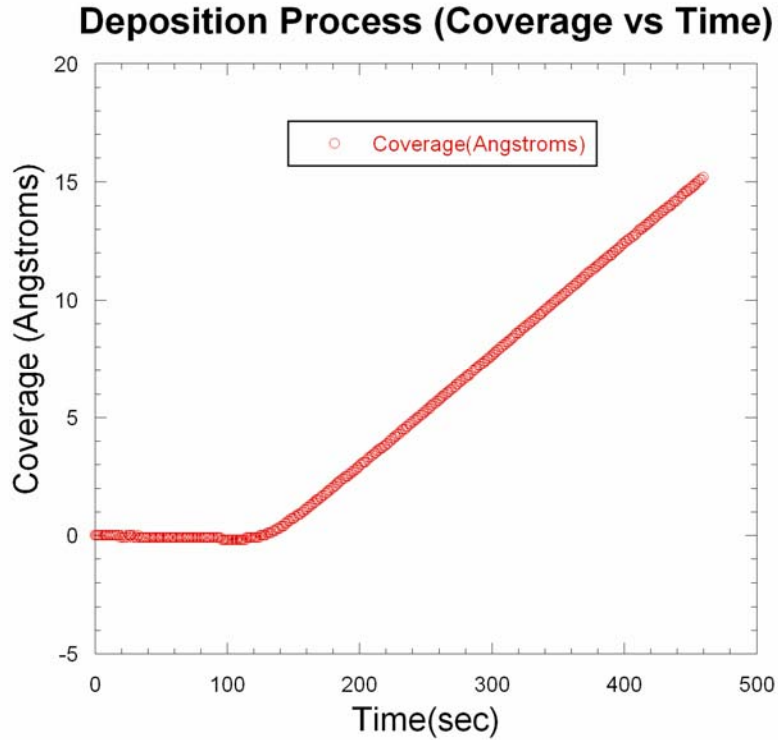


Figure 4.15: Constant Deposition Rate of Cesium Source

Because this project studies progressively complex photoemitting surfaces, provisions were made to study the photoemission effects of coatings that include not only cesium, but also potassium and antimony. A potassium source was purchased from SAES and its operation is identical to that of cesium discussed earlier. An antimony source was not available commercially, however, and had to be custom fabricated. The author's design called for a 2" long tube (5mm diameter) of tantalum to be filled with antimony pellets 1mm in diameter. It is mounted vertically on the vacuum side of an 8" flange and a hole is drilled in the tube facing the cathode. When current is passed through this tube, Joule heating melts the antimony, creating a vapor that is emitted from the hole. Figure 4.16 shows the final assembly of the antimony source. The tube with a hole in the center is visible just behind a heat shield (with a

larger hole in it) designed to minimize the amount of radiant heat emitted by the source during operation. Nearly 100 amperes of DC current are required to achieve the 1177°C melting point of antimony. The high-current copper connections and vacuum feedthrough (top) are also visible. An Agilent 6681A current source, capable of 500A output at 5VDC, allows GPIB control of antimony evaporation. Procedures similar to those involving cesium source outgassing were used to prepare the antimony source for use.

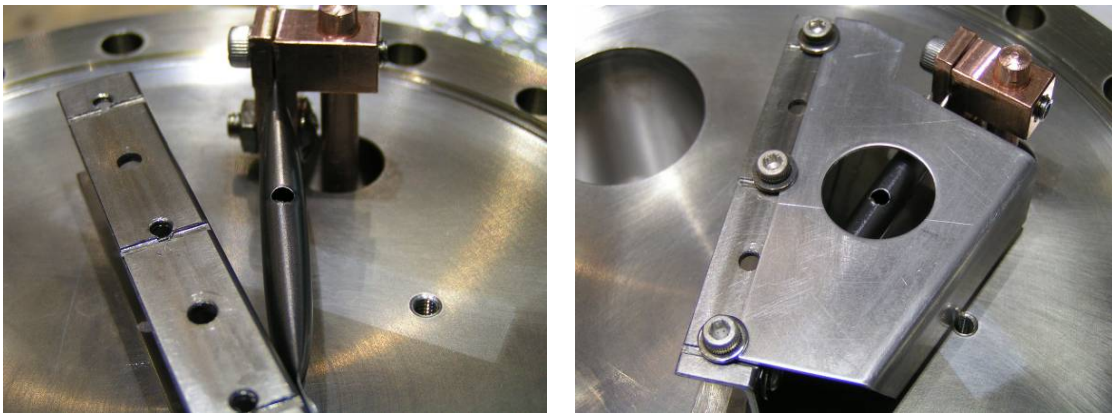


Figure 4.16: Custom Fabricated Antimony Evaporation Source

4.2.4 QE Measurements

A central measurement in this project is that of photocurrent and quantum efficiency. Laser light is directed at the cathode and the resulting photocurrent is extracted at the anode. The anode is held at a potential of +286V relative to the cathode via a shielded battery bank, as shown in Figure 4.17. The battery bank consists of series cells that are periodically tapped by a rotary switch to allow selectable output voltage. This arrangement is shown in Figure 4.18. All connections are electrically isolated from the chamber, which is kept at ground potential.

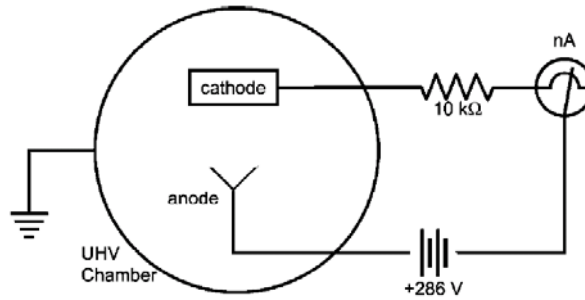


Figure 4.17: QE Measurement Circuit

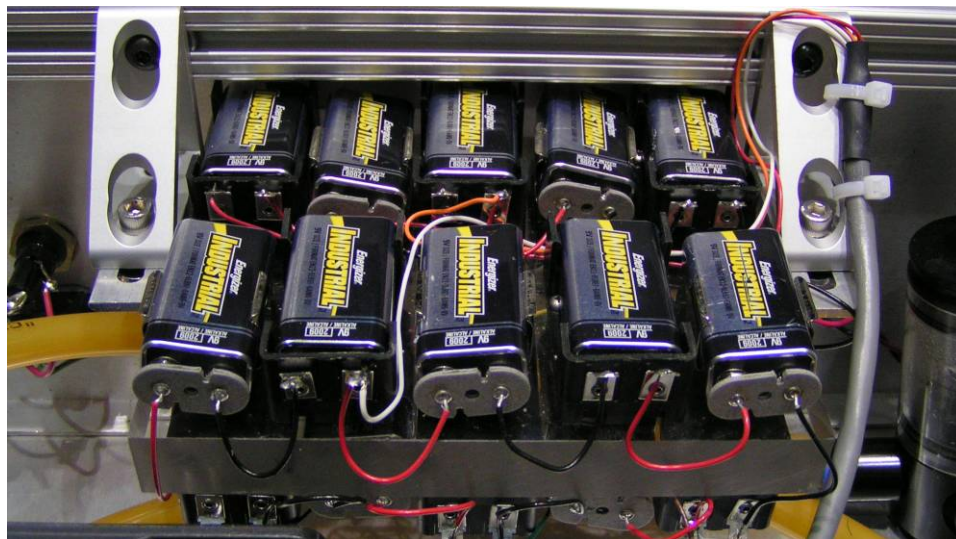


Figure 4.18: Isolated Voltage Source for QE Circuit

Because cesium atoms are deposited throughout the chamber, not just the cathode surface, care must be taken to ensure that the laser impinges only on the cathode to prevent photoemission from other metallic components. As the laser strikes the cathode, electrons are emitted and accelerate toward the anode where they constitute a photocurrent that is detected by the meter.

There are three phases of QE measurement in this project: deposition, desorption, and lifetime. During the deposition phase, QE is measured as cesium is

added to a cleaned cathode substrate, usually tungsten. In the case of the controlled porosity dispenser cathode, cesium diffuses from within the cathode to the surface. As will be shown, there is an optimal amount of cesium that corresponds to a peak QE. When this cesium coverage is reached, cathode temperature can be slightly elevated to reveal the effect of cesium desorption on QE. Finally, starting from optimal cesium coverage, cathode lifetime can be ascertained by observing QE as a function of time during either continuous or periodic laser interrogation.

4.2.5 Labview Automation

Having detailed the experimental steps involved in photocathode fabrication and measurement, this section outlines the process of automating such tasks. A distinction was made earlier between Labview programs dedicated to instrument interface versus process control. A third category consists of sub-programs that simplify programming by combining separate, related tasks, into one logical sub-routine. These three types of programs are then assembled as building blocks to automate experimentation, as illustrated by the programming hierarchy in Figure 4.19. Programs in Table 11 facilitate only instrument control, while those in Table 13 include both process control and sub-routines. Process control programs features a “front-panel” user interface with appropriate indicators, controls, and input fields. Process control programs can be used independently of other programs for specific tasks, while subroutines exist only as a component of more complex programs and are not designed for stand-alone use.

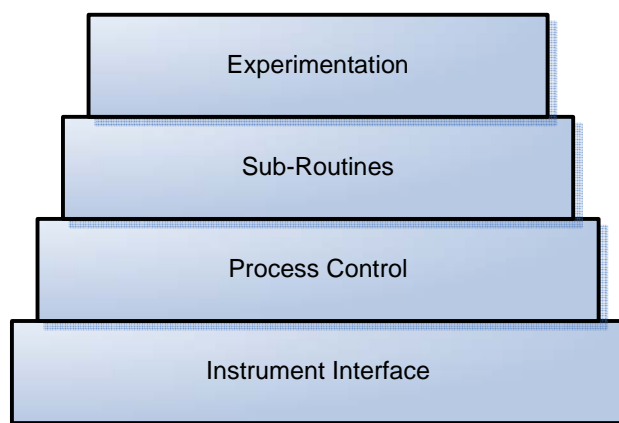


Figure 4.19: Labview Programming Hierarchy

Program Name	Program Type	Program Function
plasma_control.vi	process control	Maintain plasma discharge during dynamic pumping
gpib_cathode_bakeout.vi	process control	Bake cathode while holding pressure constant
gpib_evaporation_control.vi	process control	Outgas alkali source while holding pressure constant
pressure_monitor.vi	process control	Record pump-down progress and history to disk
laser_monitor.vi	process control	Turn on lasers and record power stability
evaporation_module.vi	subroutine	Evaporate cesium while making QE measurements
elapsed_time.vi	subroutine	Solicit user input on duration and update progress bar
signal_bundle.vi	subroutine	Aggregate data into cluster to be saved to disk
motion_then_QE.vi	subroutine	Move lasers into position and make QE measurement
gpib_read_temp_press_thickness.vi	subroutine	Combine several related measurements into one step
MoveToHome.vi	subroutine	Suspend all activity while homing robot
laser_indicator.vi	subroutine	Correlated program loop iteration with wavelength
gpib_read_current_QE.vi	subroutine	Calculate QE after measuring photocurrent

Table 13: Labview Process Control Programs and Subroutines

The central data acquisition program in the project is named “experiment_in_motion.vi” and it is comprised of interconnected process control programs and subroutines as shown in Figure 4.20. Inputs, controls, and indicators map to icons on the front panel user interface displayed in Figure 4.21. It is based upon a master while loop whose iteration variable is used to step through QE measurements using each of the five lasers. Front panel switches allow the user to select which lasers will participate in a given experiment. All measurement data is saved to disk with a user-defined time resolution and the program automatically shuts down all processes when either experiment duration, cesium coverage, or chamber pressure exceed user-defined thresholds. For very long-term experiments, such as lifetime measurements where the time rate of change in QE is very small, time resolution can be quite coarse (10 seconds or more), to save disk space. For QE versus cesium coverage experiments, however, the time resolution was selected to be 200ms so that changes in QE and coverage can be sufficiently observed.

Lasers not selected to participate in a given experiment automatically have all experimental data that relates to them (output laser power, photocurrent, and QE) set to zero. If data is being written to disk, then these null values are saved in place of actual data.

Figure 4.22 shows the interdependency of the various VIs used in this experiment. The logical steps they execute are shown as a flow chart in Figure 4.23.

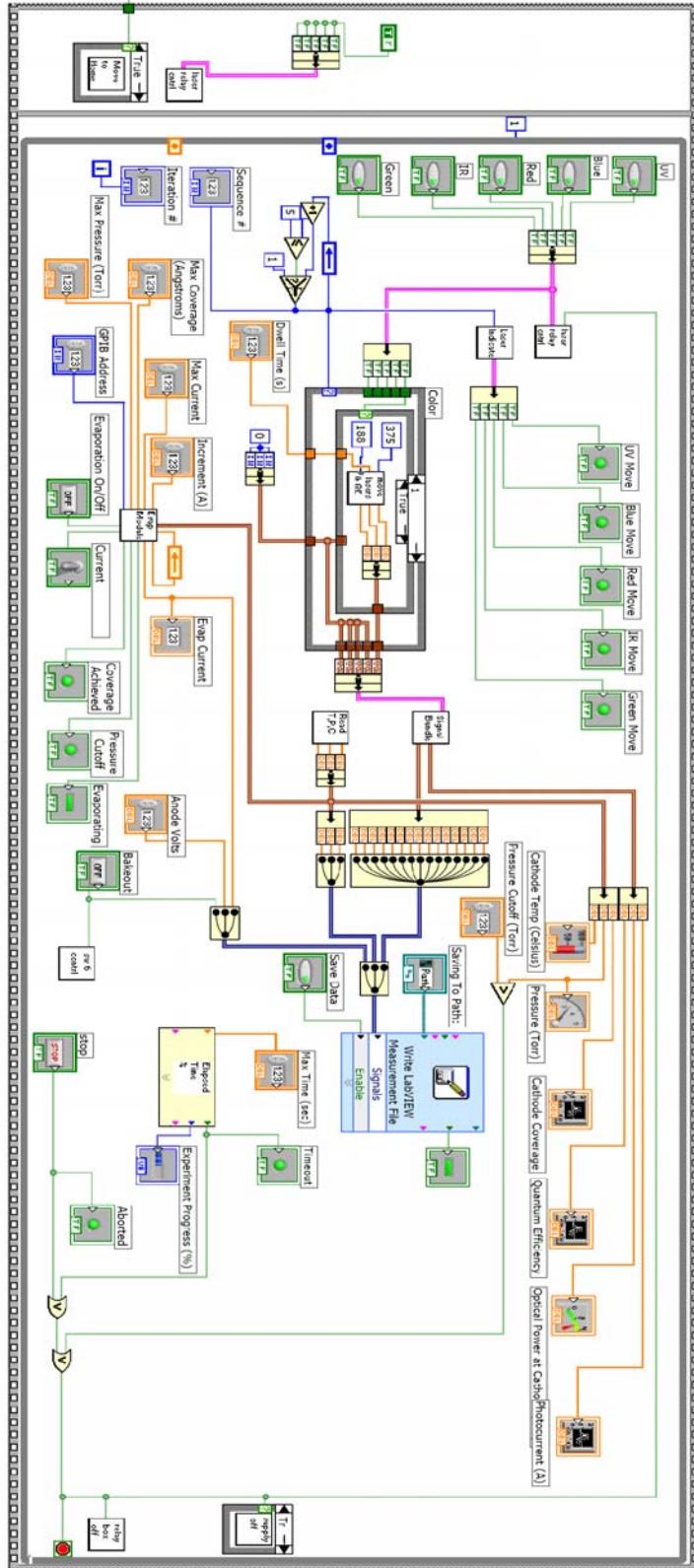


Figure 4.20: Schematic Diagram of Multiple Wavelength QE Measurement VI

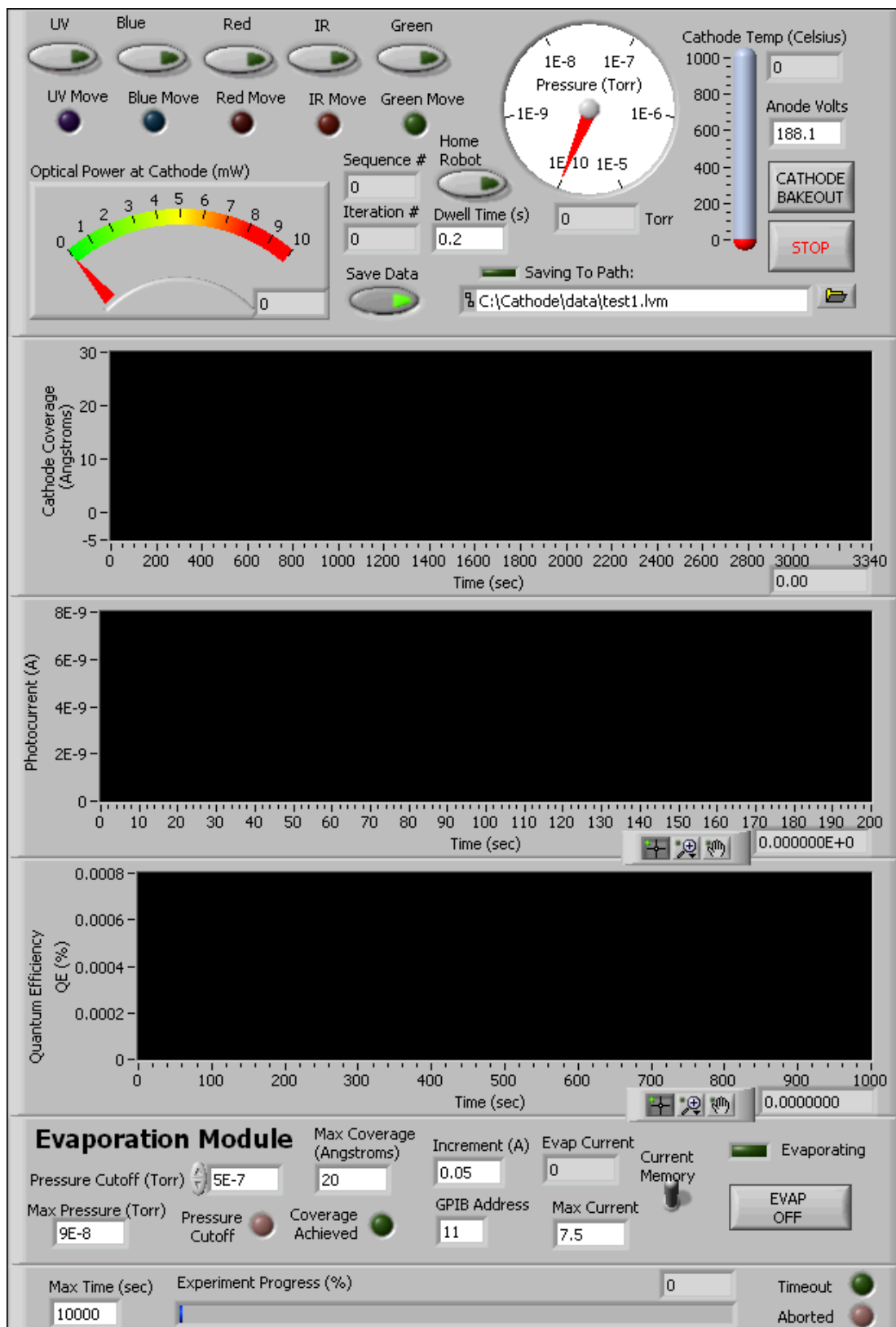


Figure 4.21: Front Panel Labview Interface for QE Measurements

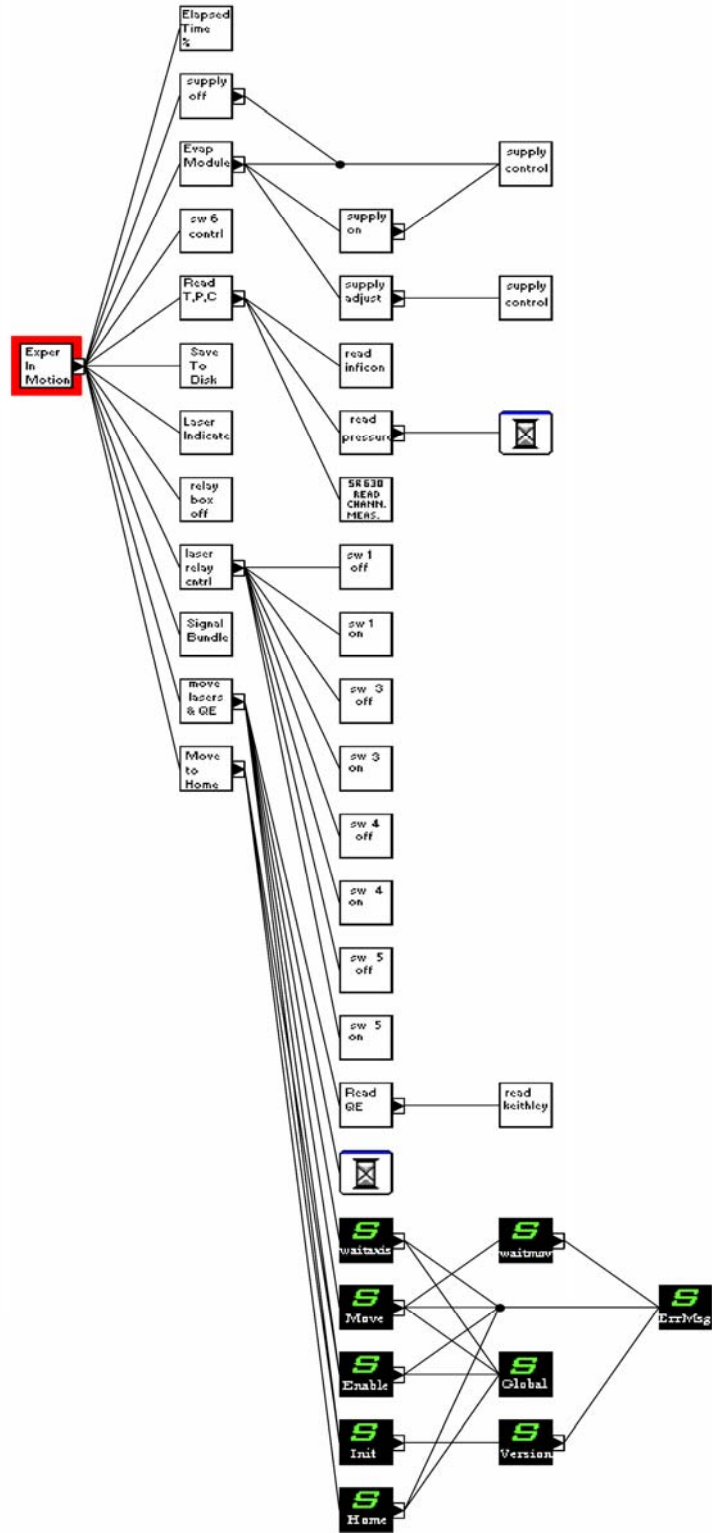


Figure 4.22: Interdependency of VIs in Multiple Wavelength QE Measurement

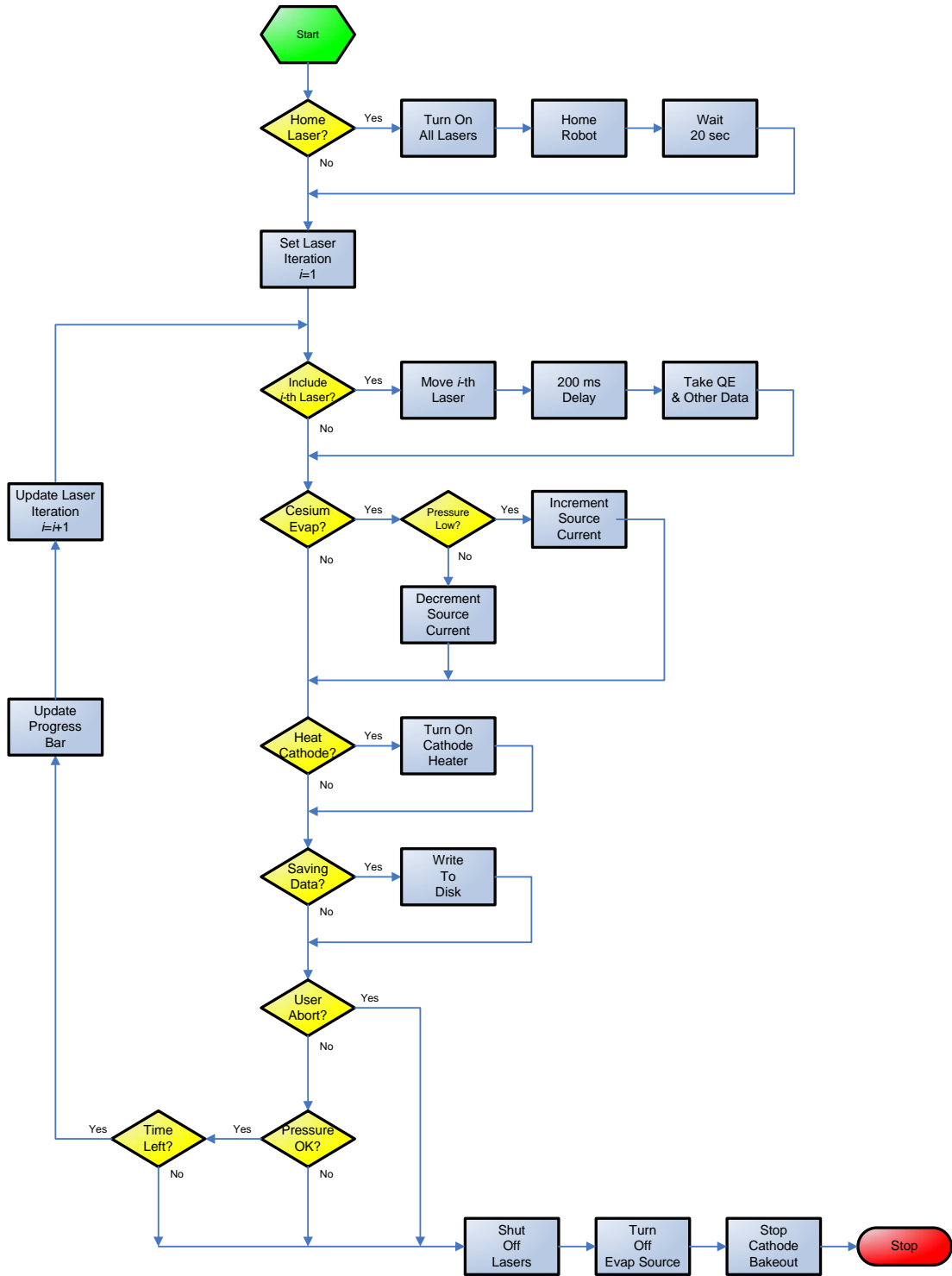


Figure 4.23: Flow Chart of QE Experimental Process

4.2.6 Ion Beam Treatments

An unfortunate reality in most ultra-high vacuum research is that surfaces are rarely “clean” on an atomic scale. An atomically clean surface can be defined as a solid-vacuum interface consisting only of surface atoms of the parent lattice, free of adsorbed, substitutional, or interstitial foreign atoms. Gas molecules are in a constant process of adsorbing and desorbing from surfaces. The rate at which this occurs obviously depends upon temperature and pressure, but even in good vacuum environments, surface coatings and compounds form if given enough time. Langmuir showed [22] that a surface can acquire one monolayer of adsorbate if exposed for just one second to a background gas pressure of 1×10^{-6} Torr. It takes only 1000 seconds for an adsorbate having a partial pressure of 1×10^{-9} Torr to form a monolayer. Such formation assumes that gas molecules incident on a surface contribute to this monolayer formation. In photoemission research, monolayer surface coatings are intentionally used to manipulate work function, so the presence of trace contaminants will prevent, obscure, or distort this effect. Clearly, a reproducible cleaning mechanism is needed to return the cathode surface to some known, initial state prior to (and after) cesium deposition. Heat anneals and low energy plasma discharge processes have already been addressed in this chapter. Experience suggests that while these treatments do indeed clean surfaces, they do not result in atomic cleanliness. The cleaning effect of heat annealing is apparent: if a tungsten cathode substrate is exposed to atmosphere and cesiated without annealing, no photocurrent is detected regardless of cesium coverage.

Other cleaning methods were considered in this project, including laser cleaning, wet chemical etch, and ion beam cleaning. For laser cleaning, a high power laser is tightly focused to produce a small spot size on the cathode such that its intensity falls just below the damage threshold of the material. The spot is then rastered over the surface, resulting in localized heating that removes contaminants. Besides being quite costly, this process suffers from several drawbacks: 1.) it is difficult to tightly focus and raster an intense (usually pulsed invisible IR) laser beam; and 2.) it is highly probable that the surface is altered and perhaps damaged in this process. The resulting changes in surface morphology could lead to emission non-uniformities whose effect on QE is unknown. Wet chemical etching has been used [79] with limited effectiveness to clean semiconductor photocathodes, but this method suffers from a lack of repeatability due to variation in chemical quality and composition.

Another cleaning method considered was ion beam bombardment, following recent demonstrations of hydrogen ion beam cleaning at SLAC [59]. These studies showed that a 1 keV hydrogen ion beam has the effect of reducing the work function of uncleaned copper. It was shown that the reduction was due to removal of stubborn contaminants such as carbon and oxides, so that the final work function matched published and theoretical values.

Recall that the final phase of this research is the fabrication and investigation of a prototype dispenser photocathode. While it was possible to use heat anneal treatments to clean separate sheets or disks of tungsten, such is not the case for a completed dispenser cathode containing cesium. While detailed discussion of the

dispenser concept is deferred to later chapters, it is helpful to remember that it consists of a sub-surface reservoir of cesium that diffuses to the surface after activation and mild heating. The activation temperature for a dispenser cathode is no more than 550°C, and the operating and rejuvenating temperatures are lower still. By contrast, temperatures in excess of 1000°C are necessary to effectively remove most contaminants from tungsten surfaces. Thus, heat anneal is not a viable cleaning mechanism for the dispenser cathode. Ion bombardment, however, is a promising alternative, since it occurs at room temperature, does not alter surface morphology, and is relatively cheap and experimentally convenient. For these reasons, it was selected as a component to this research program.

There are a number of options to consider when preparing to clean surfaces with an energetic ion beam. Common to all, however, is a gun that generates gas plasma and extracts ions to be accelerated as a beam toward a target. One could envision raster-scanning this beam across the cathode surface, but for simplicity, an expanded, static beam was preferred in this work. A commercial saddle field ion source [80] was chosen and installed to have a line-of-site path to the cathode. Figure 4.24 shows the gun chosen for this experiment and Figure 3.5 specifies its location with respect to the cathode and the chamber at large. The beam travels approximately 15 centimeters to reach the cathode surface, which is negatively biased with respect to ground. The source is driven by an accompanying power supply, and affords full control of beam energy and current. Since cathodes of varying dimension (i.e., depth) will be mounted on the button heater, the possibility exists that the ion beam will not be centered on the active area of the photocathode.



Figure 4.24: Saddle Field Ion Source

Adjustment of the beam's direction is accommodated (up to $\pm 20^\circ$) in the x - and y - directions using a port alignment device, shown (in black) mounted together with the gun in Figure 4.25.

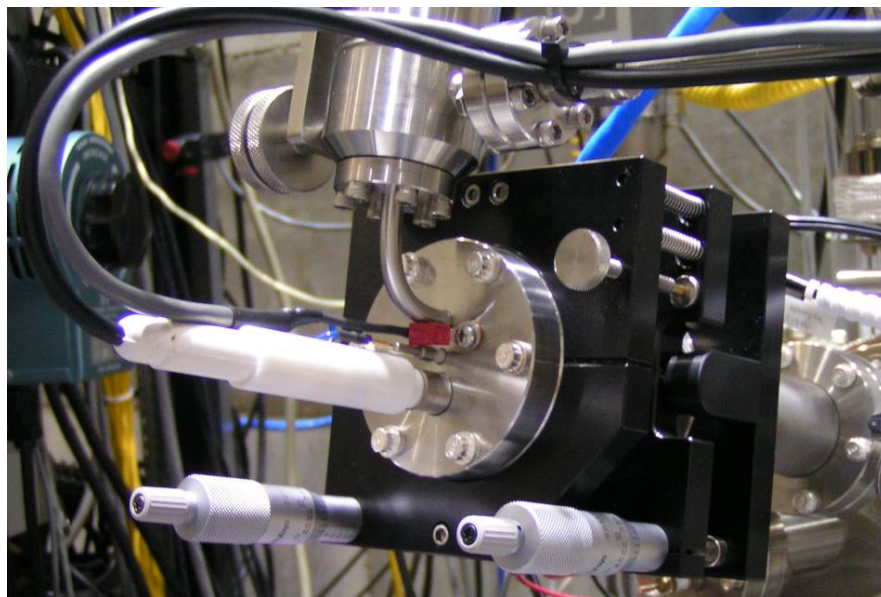


Figure 4.25: Ion Beam Port Alignment Bellows

The micrometers allow fine adjustment of the relative position of one side of a stiff set of bellows while the pivot structure is firmly fixed to the main chamber and provides rigidity of the entire assembly. Several methods were considered in an attempt to align the ion beam with the center of the cathode. One option was to mount a straight rod to the flange where the ion source was to reside and then adjust the port alignment such that this rod intersects the cathode's center. This required a large amount of assembly that lengthened the amount of time the vacuum chamber would be exposed to atmosphere. Another idea was to put either a mirror or phosphor screen in front of the cathode and observe either surface roughness (of the mirror) or phosphorescence (of the screen) to ascertain the position of the beam. These methods were also deemed inconvenient because they required installation of a mechanical actuator to position and manipulate the mirror or screen in vacuum, and this was not compatible with existing chamber geometry. The best solution was to utilize existing vacuum components. Because the anode and cathode are electrically isolated from the chamber, ion current collected on each can be measured separately, as shown in Figure 4.26. Meters M1 and M2 measure ion current extracted from the cathode and anode, respectively. Notice from previous discussions and from Figure 3.10 that the anode is annular in shape, having an outside diameter (OD) of 7.62 cm and an internal diameter (ID) of 2.54 cm. The cathode, together with its button heater, has an overall OD of 3.05 cm. Because the spot size of the ion beam is much smaller than the OD of the anode, it can be presumed that the entirety of ion current will be collected by the anode and cathode (when allowed they are connected to ground). If the beam is centered perfectly on the cathode, then ion current measured from the

anode to ground is minimized because this position is where the annulus' intersection of the beam is least. If the beam is off-center, then this current increases and is accompanied by a similar decrease in ion current collected from the cathode. Using the symmetry of existing anode-cathode geometry, alignment was performed simply by adjusting the beam's position in the transverse directions to maximize current collected by the cathode (M1) and minimize current collected by the anode (M2).

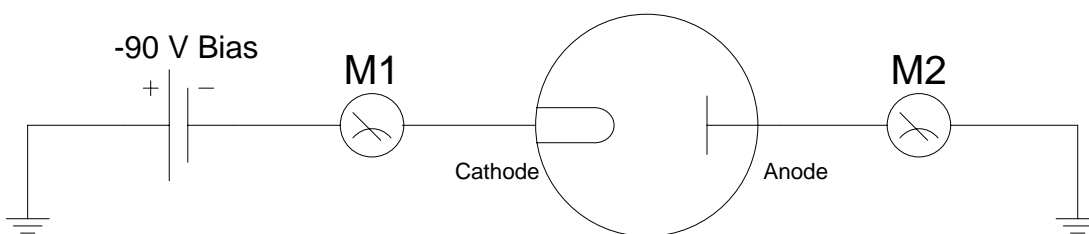


Figure 4.26: Ion Beam Alignment Scheme

The cathode is negatively biased to help direct the positive ions preferentially toward its surface, where cleaning is most required. Negatively biasing the cathode had the effect of doubling the argon ion beam current collected there. The effect was even more pronounced for hydrogen, since it is less massive by a factor of 40. Cumulative ion beam current never exceeded $50\mu\text{A}$ and was typically divided equally between the anode and cathode.

The Microbeam-7 Saddle Field ion gun operates by the basic principle similar to ion back bombardment, where electrons streaming off a cathode collide with and ionize residual gas molecules that accelerate in the opposite direction because of their positive charge. If a small pin-hole is made in the cathode, then some fraction of these backward traveling ions would travel through to constitute an ion beam. This is the

exact arrangement in the cold-cathode ion gun: the anode is centrally located and is completely surrounded by the cathode, which has a pin-hole in the center of the front face. Electrons are extracted from the cathode and collide with gas atoms in the gun, exciting them and causing them to accelerate toward the cathode. Upon collision, they generate a number of secondary electrons, each of which are accelerated and repeat the ionization process. This secondary electron amplification process is what sustains the plasma discharge at such low background pressure (approximately 1×10^{-4} Torr) and provides the positive ions that accelerate and constitute the beam. It is interesting to note that the gun can be a source not only of positive ions, but also of neutral fast atoms. If the region where secondary electron amplification occurs is elongated near the beam extraction pin-hole, then these secondary electrons have the opportunity to neutralize the ionized gas atoms prior to their escape. Ions rather than neutral fast atoms were preferred in this experiment, however, because of literature [59] precedence and experimental convenience. Recall that ion current measurements are used to align the beam on the cathode and these are not possible with fast atoms.

The internal geometry of the gun is designed to cause electrons from the cathode to trace out long, spatially oscillatory trajectories toward the anode. This longer path length increases the probability of its collision with a gas atom during its journey, which in turn, permits a sustained plasma discharge at a reduced background pressure. This feature is extremely important in this experiment, because it allows lower chamber pressure during treatment and shorter pump-down times immediately following. Reducing the time required to prepare the chamber for QE measurements is paramount, because as stated earlier, atomically-clean surfaces do not remain clean

indefinitely. The goal is to apply cesium or other multi-alkali coatings as soon as possible after the ion beam treatments.

The energy of the ion beam depends upon the potential difference between the anode and cathode, typically 5-10kV. The energy of the ion beam is related to the anode-cathode potential difference by:

$$E_{beam} = 0.85V_{AK} \quad (4.3)$$

The potential difference is applied and controlled by a special high voltage power supply, manufactured by AtomTech. It allows for adjustment of plasma current and applied voltage, while a fine metering valve connected to the inlet port of the gun allows adjustment of gas flow. These three adjustments control the final beam current, energy, and spot size. A typical ion beam cleaning procedure in this experiment calls for an applied voltage of 7.5kV, and a plasma current of 1.5mA. It should be obvious that ion beam current is much less than plasma current, since only a small fraction of the ions in the plasma contribute to the actual beam. Ion current is measured in several places in order to understand the behavior and characteristics of the beam. Just outside the extraction pin-hole in the gun is another cathode surface that collects a very small portion of the emitted beam to measure beam current at the gun. As stated earlier, beam current is also measured at the anode and cathode surfaces of the fabrication chamber.

The basic operation of the gun is straightforward and involves evacuating the chamber to better than 1×10^{-4} Torr using dynamic pumping, applying voltage to the gun, and adjusting gas flow to achieve the required ion current. It was observed that continued adjustment of gas flow is required during the first 10 minutes of treatment

in order to maintain constant beam current. This is due to temperature fluctuation of internal gun components and until equilibrium is reached, the changing temperature produces corresponding changes in the plasma and beam.

Because of the high voltages involved, safety is a concern when using the ion gun. The power supply includes a ground-loop interlock circuit, such that the unit will not operate until properly grounded. Also included by the author is a conveniently mounted “kill switch” that disables the high voltage sections of the power supply. While separate switches exist on the supply for both the control and high voltage sections, it is best to completely shut off the supply when not performing cleaning treatments. It was also necessary to ensure that all other instrumentation in the experiment was chassis-grounded in order to prevent damage due to high voltage discharge. Spurious behavior of the thermocouple monitor was observed during treatment and this was attributed to charge buildup on the thermocouple leads. This was eliminated by grounding the thermocouple leads, as well as the outer conductive sheaths on the input cables of the thermocouple monitor. In order to prevent damage or undesired operation, all experimental instrumentation was shut down during ion beam treatments.

Gun performance is tied closely with gas purity. Care was taken to use ultra high purity argon (99.99999% pure) fed into the gas inlet through baked, seamless, stainless steel tubing. As with glow discharge cleaning, the tubing was purged and pumped prior to use. Figure 4.27 shows that only inert gases were present during treatment.

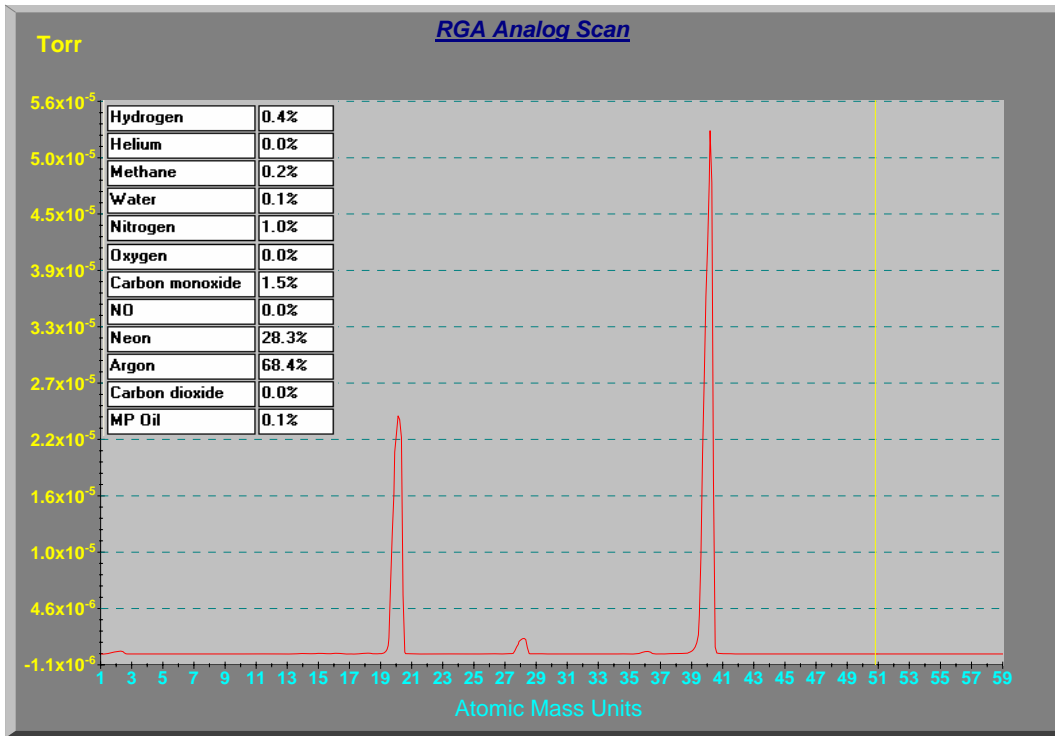


Figure 4.27: Gas Composition during Argon Ion Beam Treatment

Elevated plasma current and decreased beam current was noticed after several treatments using hydrogen gas. This behavior is indicative of conductive buildups on the insulating surfaces inside the ion gun caused by accumulated impurities. These surface films serve as a low-resistance current path between the gun's anode and cathode and sink large amounts of power while producing very little plasma. Buildup of conductive surface films usually signals that the gas being used is dirty or "wet," or was contaminated via leaks in the gas tubing. Upon investigation, it was indeed discovered that the hydrogen gas used in this phase was not "five nines" purity, but rather only 99.999% pure. While the RGA did not detect the presence of other gases in any significant quantity, as shown in Figure 4.28, the observed reduction in gun performance suggests that higher purity gas is necessary.

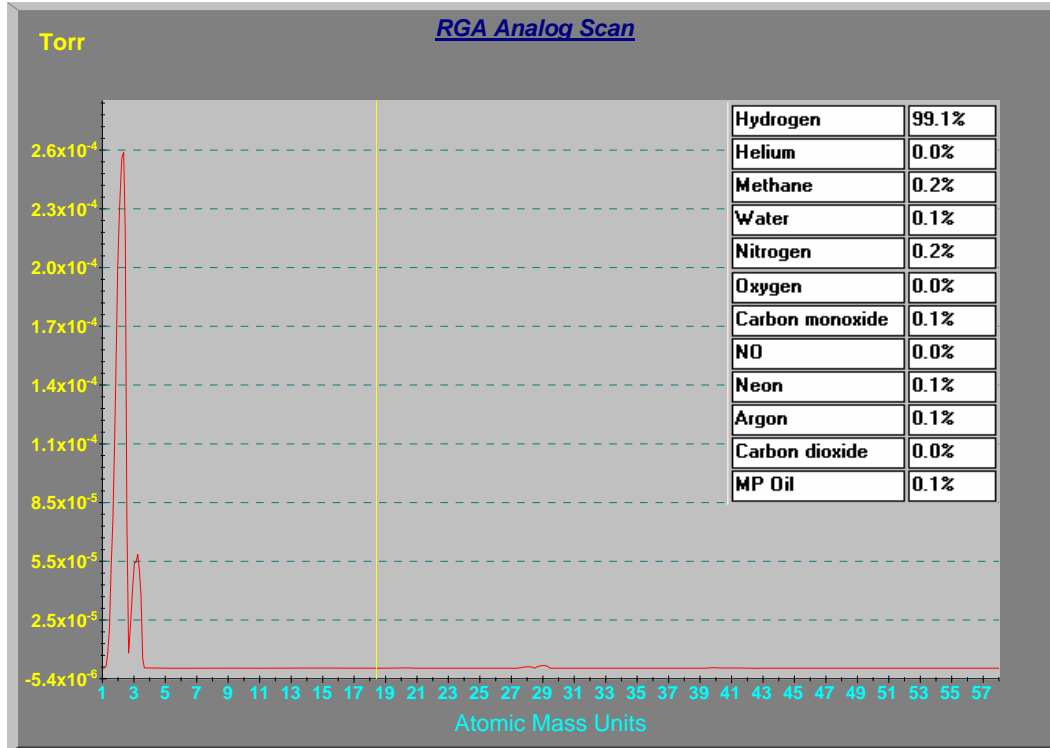


Figure 4.28: Gas Composition during Hydrogen Ion Beam Treatment

When degraded performance of the gun was noticed, as indicated by high plasma current and low beam current, the gas lines were pumped and purged with argon and an argon beam was extracted. Within ten minutes of running the beam with clean argon gas, the performance improved. This shows that argon plasma, as in the case of the fabrication chamber, has the effect of cleaning conductive impurities from vacuum insulators. Another potential problem when using the gun with either gas was plasma formation at pressures higher than 1×10^{-3} Torr. This scenario occurs when either pumping speed is reduced, due to a partially closed main valve, or rapidly opening the fine metering valve regulating flow rate. The plasma that forms at this elevated pressure corresponds to what the manufacturer terms “wide mode” operation

because it involves single electron ionization instead of relying on secondary electrons. The result is distributed plasma throughout the gun that affords very few ions available for extraction as a beam. Wide mode operation, indicated by low applied voltage and high plasma current, should be carefully avoided because it too can contribute to the formation of conductive coatings on vacuum insulators inside the gun.

The fine metering valve used to adjust gas flow into the ion gun is mounted directly to the gun's 1.33" CF mini-flange gas inlet. Care should be taken to avoid any mechanical stress on this valve or its connected tubing, as the gas inlet tube is made of only thin-walled stainless steel. The valve itself is operated by turning a threaded shaft which exerts pressure, through a lever, to a movable piston that presses an optically flat sapphire seal onto a captured metal gasket. The lever's mechanical advantage is 13,000 to one, so it is very important to not over-tighten the shaft because the stress can crack the sapphire and create a slow leak. As part of this experiment, one such valve failed after approximately 250 open-closure cycles.

Figure 4.29 shows how the calculated beam spot size and current density vary as a function of distance traveled. Since no other magnetic or electric fields are present in the chamber to perturb the beam, one expects the linear growth in spot size and inverse-square decrease in current density. Note that the distance from the ion gun to the cathode was restricted by chamber geometry to be no less than 420mm. This arrangement, chosen to accommodate viewport accessibility and port alignment functionality, results in a beam whose RMS spot size is about 30mm in diameter with a current density of $21 \mu\text{A}/\text{cm}^2$.

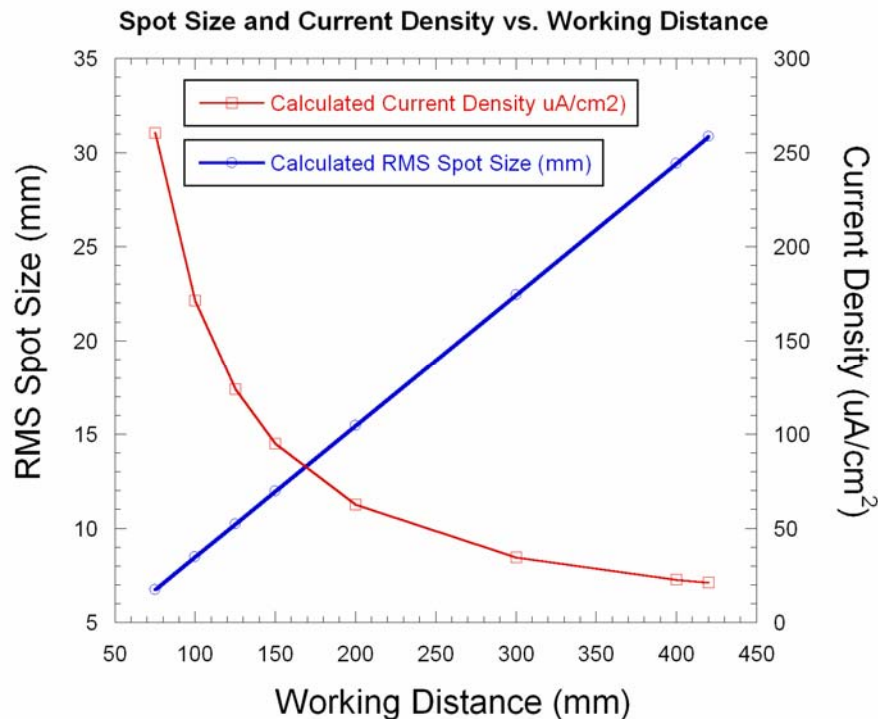


Figure 4.29: Ion Beam Characteristics as a Function of Working Distance

The procedures used repeatedly to atomically clean surfaces using the ion beam are outlined below.

Procedure for Ion Beam Cleaning

1. Pumping Preparation
 - a. Purge, pump, and fill gas lines with either argon or hydrogen gas
 - b. With all UHV valves closed, pump roughing station to its base pressure
 - c. Shut off ion pumps and allow system to come up in pressure on its own
 - d. When pressure of system exceeds base pressure of rough pump, completely open main valve and allow roughing station to pump the system (this prevents contaminants in rough pump from entering the vacuum chamber)
2. Instrumentation Preparation
 - a. Disconnect power to all instruments except for **ion gauge controllers** and **current meters** to prevent HV discharge damage from ion gun source

- i. Turn OFF the “Iso-Bar” power strip under main chamber to power down:
 1. GPIB relay box
 2. UV, Blue, Red, IR lasers
 3. Linear actuator motor control
 4. SRS Thermocouple monitor
 5. Cesium source power supply
 - ii. Turn off Inficon deposition monitor
 - iii. Turn off green laser power switch
 - b. Turn off A-K accelerating voltage switch and disconnect QE circuit
 - c. Connect the cathode to -90V with respect to ground through the Keithley 486 picoammeter (i.e. series circuit from cathode terminal, through Keithley meter, to negative battery terminal, and then connect positive battery terminal to ground).
 - d. Change Keithley 486’s current range to highest possible (1 milliamp resolution) and connect directly to alligator clip cable through triax barrel connector
 - e. Connect the anode annular disk to ground through the Agilent 34401A current meter.
 - f. Disconnect cathode thermocouple cable and connect both pins to ground (prevents charge buildup on thermocouple).
 - g. Stop RGA and turn OFF RGA filament
3. Ion Beam Cleaning
 - a. Turn off chamber ion gauge
 - b. Power ion beam supply on with **HV switch in the OFF (up) position** and the “kill switch” in the ON position.
 - c. Set accelerating voltage to 7.5kV and ion current to 1.5 mA.
 - d. Slowly open fine metering valve (~2.5 turns) until plasma in gun “strikes”
 - e. Allow 10 minutes for thermal equilibrium and adjustment of gas flow to maximize ion current while holding voltage fixed.
 - f. Briefly turn on RGA to determine gas composition and record screenshot if necessary. Immediately turn off filament current.
4. Shut-Down
 - a. Turn off HV switch on ion beam supply
 - b. Close fine metering valve and close gas regulator valve
 - c. Allow rough pump to achieve base pressure and then switch to ion pumping
 - d. Turn on chamber ion gauge
 - e. Turn on RGA (optional)
 - f. Close main chamber valve
5. Preparing for QE measurements
 - a. Reconnect thermocouple to cathode feedthrough
 - b. Turn on instruments by switching ON the “Iso-bar” power strip
 - c. Turn on deposition monitor

- d. Turn on green laser power supply
- e. Re-connect Keithley meter to QE measurement circuit and turn on accelerating bias voltage.
- f. Set Keithley to have 2 digits to the left of the decimal point **in the microampere range.**
- g. Disconnect Agilent meter from anode
- h. Reconnect cathode heater alligator clips to cathode feed-through and set variac to desired heater voltage

4.3 Surface Characterization Techniques

The ability to measure and model interactions of surface coatings with the host substrate requires some knowledge of what the surface is like on a relevant length scale. This applies to all types of cathode substrates investigated in this program: rolled, polished, and sintered metals. Surface conditions can affect many cathode properties such as coating coverage, coating evaporation, surface diffusion, photon absorption, and field enhancement. In the special case of dispenser photocathodes, verification of surface conditions is crucial because microscopic pores are used to deliver cesium to the surface. The distribution of these pores, in terms of size and location, critically determine the operating parameters of the dispenser. The characterization techniques available in this program include: optical microscopy, profilometry, scanning electron microscopy, secondary electron ion microscopy, and focused ion beam milling.

4.3.1 Optical Microscopy

As a first-order attempt to gain information about surface roughness, cathode substrate samples were viewed under a Leitz Ergolux optical microscope with a magnification range of 50x to 1500x. While this magnification is far too small to reveal details about porosity or individual grains, it does afford a wide-area view of several hundred microns that reveals any residual tooling or scratches left during polishing or handling. A digital camera was mounted on the microscope eyepiece to capture images for later analysis. The microscope did not provide a calibrated length scale at each magnification, so a test pattern was obtained to provide calibration. The

pattern consisted of various line-widths etched into silicon and measured using profilometry. This calibration allowed measurement of absolute size of various artifacts on the cathode surface. Figure 4.30 shows a 100 μm line, identified by arrows, at 50, 100, 200, and 500x magnification.

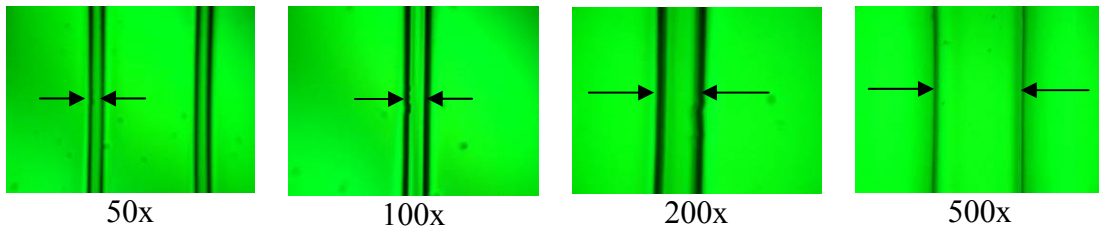


Figure 4.30: Test Pattern for Optical Microscope Calibration

Focusing is accomplished by vertically translating the sample stage using course and fine position adjustment knobs. To simplify focusing, sample investigation began with the 50x objective lens first, and its focal point was found before magnification was increased further. At higher magnification, sample illumination was increased in order to image the sample. This was necessary because higher power lenses have a smaller field of view and reduced light gathering ability. At 1500x magnification, it became apparent that the depth of field was approximately equal to the height of most scratches and ridges on the surface.

4.3.2 Profilometry

Profilometry uses the vertical position of a scanned diamond stylus to measure surface topology. The tip is mounted to a cantilever that is bonded to a piezoelectric quartz crystal transducer that converts force into an output voltage whenever the stylus moves up or down. The voltage is linear with vertical height within a range of

several hundred microns. Depending upon the radius of the diamond tip, step heights as small as a few nanometers can be measured. The instrument used in this work was the Alpha-Step 500 Profiler by Tencor, with a resolution of 5nm. An example profilometry scan of sintered tungsten is shown in Figure 4.31.

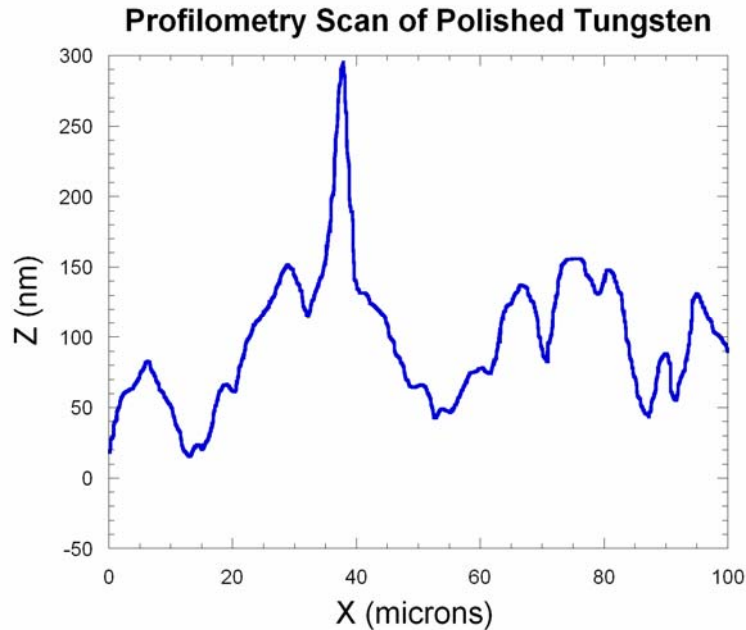


Figure 4.31: Profilometry of Polished Tungsten

Because other people and systems utilize the laboratory housing the profilometry station, care was taken to schedule measurement when other activity was at a minimum. Fume hoods and roughing pumps were either shut down or mechanically isolated prior to measurement to preserve precision and accuracy. Care must be taken to guarantee that the stylus does not encounter step heights greater than 880 microns (such as in a deep groove or the sample edge), as this will permanently damage the diamond tip. A color video camera allowed examination of the sample

surface prior to lowering the tip into measurement position. Scan length was restricted to 200 μm in order to prevent edge run off and maintain good positional resolution.

4.3.3 Scanning Electron Microscopy

Following the work of De Broglie and Davisson-Germer, which revealed the wave-nature of matter in the 1920's, it was realized that electrons have a wavelength about 100,000 times smaller than that of light. Furthermore, the trajectory of an accelerated electron through either an electric or magnetic field is similar to that of light going through a lens. The question was how to use electrons to image small things with greater resolution than optical microscopy. The first use of electron imaging was by Dr. Ernst Ruska at the University of Berlin, where he built a transmission electron microscope (TEM) in 1931. It was for this and related work that he was awarded the 1986 Nobel Prize in physics. Tunneling electron microscopy requires the sample to be no more than a few hundred nanometers thick, corresponding to the typical penetration depth of energetic electrons. This makes sample preparation tedious or even impossible in some cases, especially in the 1930s.

Scanning electron microscopy was a natural technological extension of the TEM and the basic concept was first published in a 1935 paper by another German physicist, Dr. Max Knoll. In 1942, however, it was three Americans (Zworykin, Hillier, Snijder) that conceived an actual SEM design that had a resolving power of 50 nm and 8000x magnification. All modern instruments were derived from this basic design. The system used in this experimental program is the FEI Company's Model 620 Dual-Beam instrument, shown in Figure 4.32, which integrates an SEM with a

focused ion beam (FIB). The role of the FIB functionality is discussed later in this chapter. The entire unit is housed in the Institute for Research in Electronics and Applied Physics (IREAP) and is an integral part of a campus-wide surface characterization laboratory.



Figure 4.32: Scanning Electron Microscope and Focused Ion Beam System

Just as a light microscope is built around an optical column containing glass lenses, so the SEM is centered around a vacuum column containing electromagnetic coils (lenses) that steer and guide the beam. Unlike optical lenses, whose focal point is static for a fixed position, electromagnetic lenses have variable focusing strength, dictated by the field strength of a coil. Sitting atop the vacuum column is the electron gun, consisting of a hair-pin shaped tungsten filament that is heated to approximately 2700°C as a thermionic emitter. Electrons are extracted from the filament by applying a potential of tens of thousands of volts on an adjacent anode that has a small hole in

its center. The electrons emerging from the other side constitute the beam and propagate through the electron optics housed in the column to be focused to a 4nm spot-size at the sample. Using coils in the column, the beam is raster scanned over a rectangular area while secondary electrons are produced and detected by a nearby detector. The image obtained from this detector constitutes the SEM image and it is digitally processed on the platform's PC, displayed on a monitor, and saved to disk (if requested). Increased magnification is achieved by reducing the size of the scanned rectangular area, effectively mapping a smaller portion of the sample to the same image size. A distinct advantage to SEM imaging is the 3D effect with which objects are rendered, providing a depth perspective to the image. This usually helps in characterizing the surface and is caused by the fact that the intensity of secondary electron emission depends upon the relative angle between the incoming beam and the localized surface normal of the specimen. The angular dependence is a result of the interaction of the incident beam with electrons in the sample. If the primary electron beam arrives at normal incidence, absorption of these electrons will be uniform in the transverse plane and the resulting distribution of secondary electrons will be radially symmetric. If the incident beam arrives at a glancing angle, however, electron absorption will be favored in that same direction projected on to the transverse plane and secondary electron emission will likewise have a preferred direction. The end result is that surfaces having steep angles with respect to the incident beam will appear brighter than those perpendicular to it, giving the image higher resolution and a 3-dimensional appearance.

Since the entirety of electron optics are under vacuum ($<1 \times 10^{-5}$ Torr) the sample must be clean and dry to prevent contaminants from evaporating and accumulating on internal SEM components. For a clean sample, washed with acetone, about 15 minutes of pumping is required to reach a low enough pressure to turn on the electron gun. Because samples will quickly charge up under exposure to an electron beam, they must be conductive and have an electrical path to the grounded sample stage. Because metal cathode substrates were used, only a small sliver of conductive tape was required to discharge the sample during imaging.

4.3.4 Ion Induced Secondary Electron Emission

The dual-beam system discussed in the previous section includes not only a scanned electron beam, but also a scanned 30 keV gallium ion beam. The beam is created via field emission using a liquid metal ion source (LMIS) and is very stable up to $1 \mu\text{A}$ of total beam current. Although the spot and scan dimensions are larger, secondary electrons are produced when the ion beam strikes the specimen surface. Because ions are 2000 to half-million times more massive than an electron, they not only cause secondary electron emission, but also dislodge surface particles from the sample. In this manner the ion beam can be intentionally used to modify the surface. Imaging the secondary electrons resulting from the ion beam's interaction with the surface is also very useful because it allows differentiation of features according to crystallographic orientation. This is due to the fact the penetration depth of the ion beam depends on exposed crystal face. Crystal faces with a shallow penetration depth will give rise to more secondary electrons, producing a brighter image. In this manner, individual crystal grains can be distinguished and studied.

4.3.5 Focused Ion Beam Milling

Since an energetic ion beam can dislodge atoms from the surface it interacts with, milling with sub-micron precision is possible using a focused ion beam (FIB). This technique, together with the ability to create a crystallographic map of the surface, is used to study the three dimensional nature (i.e. aspect ratio, shape, etc) of a representative crystal grain. Milling was also used to determine the diameter and depth of several pores in the sintered tungsten dispenser cathode substrate.

5. Theory Overview

While this research program is largely experimental in nature, it benefits from and contributes to a recent photoemission model that shows promising predictive capability, as demonstrated in the next chapter. Most of today's popular photocathodes were identified and improved upon using an empirical approach whose often sporadic success was either initiated or accelerated by fortuitous accident [66]. A stunning example is the ubiquitous barium oxide cathode that has enjoyed nearly a century of continuous application: its first identification in 1904 was the result of accidental contamination by vacuum grease (containing trace amounts of barium oxide) on a platinum thermionic cathode [81]. The photosensitive surface thus discovered is identical, with only minor improvements, to that of today's low-work function barium dispenser cathodes which have been thoroughly investigated and widely used [82],[83]. A large body of experimental data exists for many other photoemitters, including cesium on tungsten and much higher QE cathodes, but a universally applicable model describing photoemission from each has been elusive. Certain models have proven very useful, such as Spicer's "three-step" approach [66], but do not account for the temperature dependence of photoemission and the effects of laser heating. The experimental goal of this work requires such a parametric theory: the dispenser cathode involves operation over a wide temperature range, extreme electric fields, and intense drive lasers. The purpose of this chapter is to introduce the essential components of photoemission theory, and describe its components and their applicability to the experiments in this project.

5.1 Introduction

The ideal photoemission model should account for time-dependent thermal absorption of the laser energy, temperature-dependent thermal conductivity, electron scattering rates, the effect of surface coatings on emission, and possible effects of field enhancement. It should also utilize parameters that are commonly reported by other experiments in the literature to demonstrate universal utility. In this project, the Jensen, et. al. theory is used to analyze data from coated metals and predict performance of other cathode compositions of interest for dispenser studies based on material and laser parameters. Furthermore, the low field and low drive laser intensity used in this project afford a particularly rigorous validation test of the theory because many of the justifications typically used to account for inaccurate prediction (i.e., field enhancement factor, laser-induced desorption of surface coatings, heating of the electron gas, etc.) do not apply.

The theory follows the approach of Spicer by decomposing the problem of photoemission into three parts, corresponding to the three basic steps leading to electron emission: photon absorption, electron transport to the surface, and barrier crossing. A distinguishing factor about this particular theory is that in each of the above processes, an effort has been made to systematically reduce or eliminate unknowns, either by means of models or approximations, which were arbitrarily assigned or used as fit parameters in other treatments. Every experimental arrangement includes unique features that make modeling difficult, including, in this case, the fact that dispenser substrates are porous, granular, polycrystalline, and potentially contaminated. Rather than allow the theory to become “experiment-

specific,” by qualifying each parameter for the details of a material in question, literature parameters were used to obtain an “out-of-the-box” analysis of experimental data. The agreement shown in the next chapter for two different cathodes suggests this approach is justified. Replacing literature parameters with those specific to sintered tungsten would likely improve agreement, but would reduce the theory’s applicability to other materials whose specific parameters might not be known or knowable. Besides data analysis in this particular work and its application to the development of dispenser cathodes, an important outcome of experimental theory validation is its broader utility as an emission model for existing beam codes. These codes currently assume an arbitrary electron distribution at the cathode, and could be greatly enhanced if provided with a more realistic distribution from an experimentally validated emission model. The components of this model relevant to the experiments in this program are detailed in the following sub-sections.

5.2 Coating Dependent Work function

While bare metals offer certain advantages as photocathodes, including long-lifetime, robustness, and simplicity of use, they require UV drive lasers and suffer from low QE. For this reason, the vast majority of cathodes in the visible range utilize work function-reducing coatings, such as cesium or some alkali-based compound [84]. Since work function plays a dominant role in the emission process, a relationship is needed between this parameter and coating coverage, typically described in terms of percent-monolayer, θ .

5.2.1 Gyftopolous-Levine Theory

A relationship based on electronegativity was proposed in 1961 by Gyftopolous and Levine (GL) that relates coverage and work function and serves as the basis for Jensen's treatment of the same. Because cesium surface coverage is crucial to the fabrication of high efficiency cathodes and is central to the experimental efforts in this program, it is worthwhile to explain its theoretical treatment in some detail. Recall that electronegativity describes the energy required to extract a single electron from an atom (or molecule). It is important to note that the effect of adsorbed layers on work function has been known and extensively studied since 1933 [27], with the most extensive treatment being that of Langmuir [30]. He proposed a correlation between coverage, temperature, and adsorbate vapor pressure, which only partially succeeded for small values of coverage [85]. GL theory, which omits the temperature dependence, was the first to provide a theoretical relationship valid for all degrees of coverage. It states that for a coated surface, the effective work function $\phi_e(\theta)$ depends upon the electronegativity barrier $W(\theta)$ and a dipole moment $d(\theta)$ induced by adsorbed atoms, given by:

$$\phi_e(\theta) = W(\theta) + d(\theta) \quad (5.1)$$

where $(0 \leq \theta \leq 1)$ represents fractional monolayer coverage. It should be clear that whatever the form of $W(\theta)$, it must satisfy boundary conditions defined by the surface itself. As coverage goes to zero, for example, the barrier becomes nothing other than the work function of the substrate metal, $W(0) = \phi_m$. At zero coverage, the introduction of a few adsorbate atoms has little effect, so $\left(\frac{dW(\theta)}{d\theta}\right)_{\theta=0} = 0$. Similarly,

at full monolayer coverage, the electronegativity is simply that of the film $W(1) = \phi_f$, with $\left(\frac{dW(\theta)}{d\theta}\right)_{\theta=1} = 0$. The exact expression for $W(\theta)$ is unknown, but it is assumed to be the simplest polynomial that satisfies the stated boundary conditions:

$$W(\theta) = \phi_m - (\phi_m - \phi_f)(3\theta^2 - 2\theta^3) \quad (5.2)$$

It is convenient to cast this in a slightly different form:

$$W(\theta) = \phi_f + (\phi_m - \phi_f)H(\theta) \quad (5.3)$$

with $H(\theta) = 1 - 3\theta^2 + 2\theta^3$. To determine the functional form of the dipole moment, recall Pauling's treatment of molecular electronegativity [86] which states that the dipole moment $M(\theta)$ exhibited by two dissimilar atoms is proportional to the difference in their electronegativities. GL expands upon this by modeling a substrate lattice site and an adsorbed atom as such a molecule. Their collective dipole moment can be expressed as a function of electronegativity: $M(\theta) \propto W(\theta) - W(1)$. If the dipole moment of a *single* adsorbed atom at zero coverage is defined as $M_0 \propto W(0) - W(1)$ then mutual proportionality dictates that:

$$\frac{M(\theta)}{M_0} = \frac{W(\theta) - W(1)}{W(0) - W(1)} = H(\theta) \quad (5.4)$$

so that the coverage dependent moment is given by $M(\theta) = M_0 H(\theta)$. A correction factor is needed, however, to account for dipole-to-dipole interaction at high coverage that tends to reduce the overall effective dipole moment as individual ones begin to cancel each other. Topping [87] showed that the depolarizing field due to other neighboring dipoles depends upon the dipole moment per unit adsorbed atom $M_e(\theta)$, according to:

$$E(\theta) = \frac{9\gamma_f^{3/2}\theta^{3/2}M_e(\theta)}{4\pi\epsilon_0} \quad (5.5)$$

where γ_f is the number of adsorbate atoms per unit area. The effective dipole moment is equal to the original dipole moment minus the effect of the depolarizing field:

$$M_e(\theta) = M(\theta) - \alpha E(\theta) \quad (5.6)$$

where the polarizability of a substrate unit cell and its adsorbed atom is approximated by $\alpha = 4\pi\epsilon_0 n r_f^3$, where r_f is the covalent radius of the adsorbate (film) atom and n is a number which accounts for the number of valence atoms present in the adsorbed atom. For alkali metals, $n = 1$, corresponding to a single valence electron. For alkali earth metals with two outer electrons, $n = 1.65$, where the difference is due to the fact that each valence electron shields the other by an amount approximated by 0.35. Inserting (5.4) and (5.5) into (5.6) and solving for $M_e(\theta)$ gives the effective dipole moment:

$$M_e(\theta) = \frac{M_0 H(\theta)}{1 + 9\alpha\gamma_f^{3/2}\theta^{3/2} / 4\pi\epsilon_0} \quad (5.7)$$

The dipole term is then given by $d(\theta) = -M_e(\theta)\gamma_f\theta / \epsilon_0$ or,

$$d(\theta) = -\frac{M_0 H(\theta)\gamma_f\theta}{\epsilon_0 + 9\alpha\gamma_f^{3/2}\theta^{3/2} / 4\pi} \quad (5.8)$$

All the terms are now available for insertion into a coverage dependent expression for work function:

$$\phi_e(\theta) = \phi_f + (\phi_m - \phi_f)H(\theta) - \frac{M_0 H(\theta)\gamma_f\theta}{\epsilon_0 + 9\alpha\gamma_f^{3/2}\theta^{3/2} / 4\pi} \quad (5.9)$$

Because the substrate and adsorbate are modeled as hard spheres, the value of M_0 can be evaluated using a geometrical arrangement. For cesium on tungsten, it can be assumed that a larger cesium atom rests atop four substrate atoms. The four links between each substrate atom and the central cesium atom can be considered to exhibit a separate dipole moment $M_{fm} \propto \phi_m - \phi_f$ in the method of Pauling [86]. A depolarization effect will also be apparent in this set of clustered dipoles, which can be approximated according to [88] by dividing by the factor $1 + \alpha / (4\pi\epsilon_0 R^3)$ such that:

$$M_{fm} = \frac{K(\phi_m - \phi_f)}{1 + \alpha / (4\pi\epsilon_0 R^3)} \quad (5.10)$$

Jensen shows that the proportionality constant K is given by $\epsilon_0 r_0^2$ where $r_0 = 4.3653 \text{ \AA}$ [13]. The vector sum of the four component moments along the vertical axis of the pentahedron gives the total dipole moment at zero coverage:

$$M_0 = 4M_{fm} \cos \beta \quad (5.11)$$

where the angle β is defined by the surface normal and single link, $\cos \beta = (1 - 1/2\gamma_m R^2)^{1/2}$, and $R = r_f + r_m$ is the sum of the adsorbate and substrate atomic radii. Inserting these expressions into (5.9) yields:

$$\phi_e(\theta) = \phi_f + (\phi_m - \phi_f)H(\theta) \left[1 - \frac{4\epsilon_0 r_0^2 (1 - 1/2\gamma_m R^2)^{1/2} \gamma_f \theta}{[1 + \alpha / (4\pi\epsilon_0 R^3)] [\epsilon_0 + 9\alpha \gamma_f^{3/2} \theta^{3/2} / 4\pi]} \right] \quad (5.12)$$

The full GL coverage-dependent work function expression is then:

$$\phi_e(\theta) = \phi_f + (\phi_m - \phi_f) \left[1 - 3\theta^2 + 2\theta^3 \right] \left[1 - \frac{4r_0^2(1-1/2\gamma_m R^2)^{1/2} \gamma_f \theta}{\left[1 + n(r_f/R)^3 \right] \left[1 + 9nr_f^3(\gamma_f \theta)^{3/2} \right]} \right] \quad (5.13)$$

Notice that effective work function depends only on coverage, atomic radii, and the number of adsorbed atoms per unit substrate area. Jensen [13] uses a parameterization approach to recast (5.13) in an experimentally accessible form by pointing out relationships between atomic radii and the number of atoms per unit substrate cell, namely, that $\gamma_f = f/(2r_f)^2$, $\gamma_m = w/(2r_m)^2$, and $\gamma_f : \gamma_m = 1:4$ for cesium on tungsten. Taken together, these relations state that:

$$\frac{w}{f} \left(\frac{r_f}{r_m} \right)^2 = 4 \quad (5.14)$$

which reduces (5.13) to:

$$\phi_e(\theta) = \phi_f + (\phi_m - \phi_f) \left[1 - 3\theta^2 + 2\theta^3 \right] \left[1 - \frac{(r_0/r_f)^2 (1-2/w(r_m/R)^2) f \theta}{\left[1 + n(r_f/R)^3 \right] \left[1 + \frac{9}{8} n(f\theta)^{3/2} \right]} \right] \quad (5.15)$$

In this form, the work function relationship depends only upon two empirically determined parameters, the number of adsorbate and substrate atoms per unit cell.

These values are related and will depend upon the crystalline orientation of the substrate in question and whether the adsorbate is an alkali or alkali-earth metal.

In summary, Jensen's modifications to the original GL theory include: parameterization of related input variables, minimization of the input data set, updates of empirically determined parameters, and use of modern values for each.

5.2.2 Comparison to Literature Data

The performance of the modified GL theory is demonstrated not only in the next chapter's experimental results, but also by data which figures prominently in the literature [30], [84]. Most of the data concerning coverage dependent work function or QE reports coverage values indirectly via deposition time or change of mass, as measured on a quartz crystal monitor (QCM). Jensen addresses these ambiguities by using a least-squares analysis to determine an appropriate scaling factor for the particular observable in question. For data referenced above, the agreement with the modified GL theory is quite good, as shown in Figure 5.1.

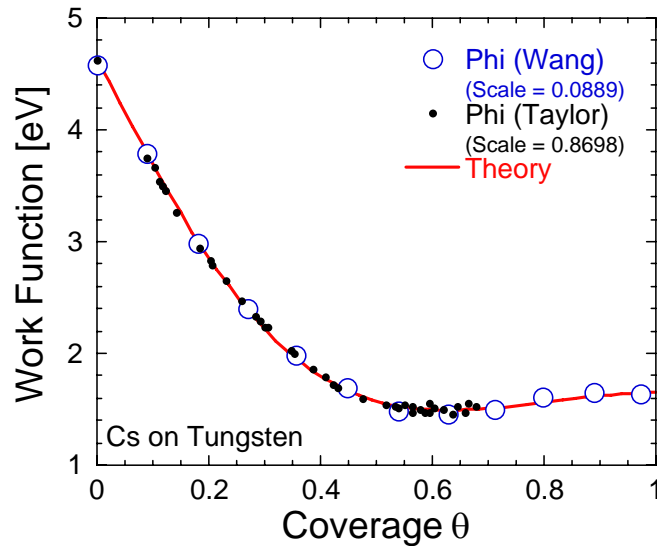


Figure 5.1: Comparison of Modified Gyftopoulos Levine to Work function Data

5.3 Photoemission Model

Any photoemission model for coated metals will take as an input the effective work function of the photoemitting surface. The previous section provides the method

for evaluating this parameter as a function of surface coverage. Discussion is now directed toward the behavior of photo-excited electrons within the material. It can be appreciated that at non-zero temperature, Einstein's famous equation $\hbar\omega - \phi$ provides only an upper bound on the energy of emitted electrons. Electrons are ejected with a distribution of energies ranging from zero to this upper limit, reflecting the fact that photo-excited electrons also have a wide range of energies. Only some portion of this distribution is able to cross the barrier and constitute a beam current. For a photoemission theory, the challenge is to obtain an expression for this energy distribution and relate it to emission probability.

5.3.1 Modified Fowler-Dubridge Model

In the Fowler-Dubridge (FD) model of photoemission, photocurrent depends upon: 1.) the amount of absorbed laser light, which depends upon reflectivity R of the photoemitting surface (assuming its thickness is much larger than photon penetration depth) and the number of incident photons ($I_\lambda / \hbar\omega$), 2.) the probability that a photo-excited electron has energy greater than the vacuum barrier height, and 3.) the probability $f_\lambda < 1$ that an electron some distance from the surface can migrate to the vacuum barrier without collision [24]. Notice that each of these factors address the three steps involved in photoemission: photon absorption, migration to the surface, and escape to vacuum. Modification of FD theory [9],[89] gives photocurrent density J_λ as a product of these factors:

$$J_\lambda[T_e, F, \phi] = f_\lambda(1-R) \left(\frac{q\lambda}{hc} \right) I_\lambda(t) \left\{ \frac{U \left[\beta \left(hc\lambda^{-1} - \phi + \sqrt{4QF} \right) \right]}{U(\beta\mu)} \right\} \quad (5.16)$$

where $\beta = (k_B T_e)^{-1}$, k_B is Boltzmann's constant, T_e is temperature, F is the electron charge multiplied by local electric field at an emission site, $4Q = \alpha_{fs} \hbar c$, α_{fs} is the fine structure constant, and ϕ is the difference in barrier height and chemical potential μ . A simplified expression, applicable to the experimental conditions encountered in this work, is obtained by observing that the field is negligibly small, such that the radical term can be neglected and ϕ can be considered the effective (coverage dependent) work function. The bracketed ratio of (5.16) describes the probability that a photo-excited electron has energy greater than the barrier height. Using the Richardson approximation, which assumes that only electrons with energy higher than the barrier are photoemitted, FD describe this probability by using "Fowler" functions $U(x)$:

$$U(x) = \int_{-\infty}^x \ln(1 + e^y) dy \quad (5.17)$$

Jensen has developed [9] convenient approximations to this integral which are accurate to within 1% for all values of x and help elucidate trends in experimental data:

$$U(x) \approx \begin{cases} e^x (1 - be^{ax}), & x \leq 0 \\ \frac{1}{2}x^2 + \frac{1}{6}\pi^2 - e^{-x}(1 - be^{-ax}), & x > 0 \end{cases} \quad (5.18)$$

Notice that for room temperature and photon energy greater than the effective work function, the argument of the Fowler function in the numerator is about 38. The exponential term in the $x > 0$ approximation of $U(x)$ is therefore vanishingly small and the quadratic term dominates. Applying the same analysis to the denominator allows an approximation for photocurrent:

$$J_{\lambda}(\phi) \approx f_{\lambda}(1-R)I_{\lambda}(t) \frac{q(\hbar\omega - \phi)^2}{(\beta\mu)^2} \quad (5.19)$$

The quadratic dependence on the difference between photon energy and work function is apparent in the experimental data of the next chapter.

5.3.2 Evaluating Quantum Efficiency

Recall that QE is defined as the ratio of the number of photoemitted electrons to incident (i.e., not absorbed) photons. To determine each of these quantities, given current and optical laser intensities, integration over the emission area and laser spot size, respectively, is generally required. This is because for the case of high power drive lasers, variations in light intensity can result in localized fluctuations of electron temperature. These, in turn, alter the photoemission process since the U functions are temperature dependent, along with some properties of the material (e.g., scattering time constants). Because laser heating is negligible for experimental conditions considered herein, the emission area and laser spot size can be considered equal, leading to a simplified approximation of QE:

$$QE \approx \frac{hc}{\lambda q} \frac{J_{\lambda}}{I_{\lambda}} \quad (5.20)$$

Substituting (5.16) for current density yields a coverage-dependent expression for QE:

$$QE[\theta, \phi, T_e] \approx f_{\lambda}(1-R) \left\{ \frac{U \left[\beta \left(hc\lambda^{-1} - \phi + \sqrt{4QF} \right) \right]}{U(\beta\mu)} \right\} \quad (5.21)$$

5.4 Scattering Mechanisms

5.4.1 Temperature Dependent Scattering Rates

In general, two scattering mechanisms prohibit a photo-excited electron with sufficient energy from crossing the vacuum barrier: electron-electron scattering and electron-phonon scattering. The theory component accounting for these effects is valuable for use with high intensity drive lasers, which tend to heat the cathode surface (especially for longer laser pulses or higher repetition rates). As photoexcited (but not photo-emitted) electrons come into thermal equilibrium with the rest of the electron gas, this population achieves thermal equilibrium with the lattice via electron-phonon interaction. Any energy not carried away as photoemitted electrons goes into heating the photocathode, with an absorbed power density at depth z given by [13]:

$$G(z,t) = (1-R)I_{\lambda}(t) \left(\frac{e^{-z/\delta}}{\delta} \right) \left\{ 1 - \frac{U[\beta(hc\lambda^{-1} - \phi)]}{U(\beta\mu)} \right\} \quad (5.22)$$

where δ is the wavelength-dependent penetration depth. While Jensen's theory accounts for the effects of absorbed laser power, this research program involves only low power CW lasers (less than 0.5 W/cm^2), so any effect of laser heating is negligible. Elevated cathode temperatures are encountered, however, during activation and rejuvenation of the dispenser cathode. Electron relaxation time τ is temperature dependent and is related to the electron-electron τ_{ee} and electron-phonon τ_{ep} relaxation times according to Matthiessen's Law [90],[91]:

$$\frac{1}{\tau} = \frac{1}{\tau_{ee}(T_e)} + \frac{1}{\tau_{ep}(T_i)} \quad (5.23)$$

where T_e and T_i are the electron and ion temperatures, respectively. The electron-electron and electron-phonon relaxation times for tungsten at 300°C are 5.26fs and 0.948fs [13]. Jensen uses the fundamental theories of scattering to formulate expressions for these scattering times, capturing not only temperature effects, but also those involving electron density and material properties.

5.4.2 Post Absorption Scattering Factor

The temperature dependent relaxation time dictates how far a photo-excited electron can travel within the cathode before suffering a collision, given by the scattering length $l(k)$:

$$l(k) = \frac{\hbar k}{m} \tau \quad (5.24)$$

If photon absorption occurs at a perpendicular depth x from the surface, the resulting photoelectron could propagate in any given direction with equal probability. Those electrons which propagate directly toward the surface, for example, travel a smaller distance and are less likely to encounter an emission-terminating collision. The angle of propagation θ with respect to the surface normal determines the path length to the surface $z(\theta) = x / \cos(\theta)$, as shown in Figure 5.2.

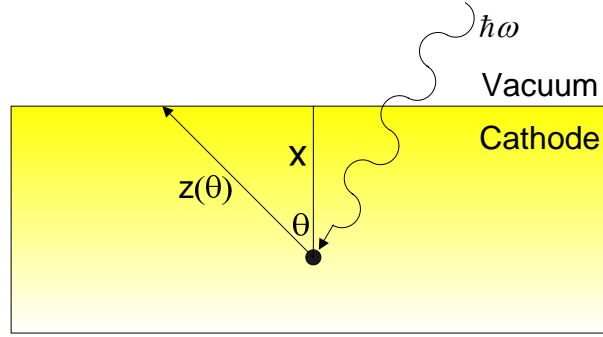


Figure 5.2: Geometry of Photoelectron Path Length To Barrier

Thus, a photoelectron will escape the vacuum barrier if $z(\theta) < l(\theta)$, where the assumption has been made that a single collision event is sufficient to prevent emission. This leads to two probabilities: the probability that an electron at depth x will absorb a photon (determined by the wavelength-dependent penetration depth δ), and the probability that that electron will not suffer a scattering event on the way to the surface. The total probability, introduced as f_λ in (5.16), is found by integrating over all values of momentum that are above the minimum required for photoemission $k_0 = \frac{1}{\hbar} \sqrt{\mu + \phi + \hbar\omega}$:

$$f_\lambda = \frac{\int_{k_0}^{\infty} f(k) \int_0^{\pi/2} \int_0^{\infty} \exp[-x/\delta - z(\theta)/l(k)] dx d\theta dk}{\int_{k_0}^{\infty} f(k) dk \int_0^{\pi} d\theta \int_0^{\infty} \exp(-x/\delta) dx} \quad (5.25)$$

where the angular limits of integration in the numerator $0 \leq \theta \leq \pi/2$ include on those electrons with a momentum component in the direction of the photoemissive surface. This is justified because a photoelectron traveling deeper into the cathode will not escape and should be excluded. The term $f(k)$ is the “supply function,” which determines the fraction of electrons at momentum k that are headed toward the

surface. It is obtained by integrating over the transverse energy components of the Fermi-Dirac distribution and is given by: $f(k) = (m / \pi\beta\hbar^2) \ln[1 + e^{\beta(\mu - E(k))}]$.

5.5 Application to Experiment

5.5.1 Bare Metals

Before comparing experimental data from coated surfaces to Jensen's model, it is useful to first make a comparison with the simplest of all photoemitters: bare metals. Figure 5.3 shows theory prediction along with QE vs. wavelength data from D. Dowell's copper photocathode [59]. This is a useful comparison because the accelerating field and average laser power are roughly equal to those encountered in the experiments of the previous chapter. The agreement is quite good and indicates that the theory's approach to modeling scattering and emission appear to be valid.

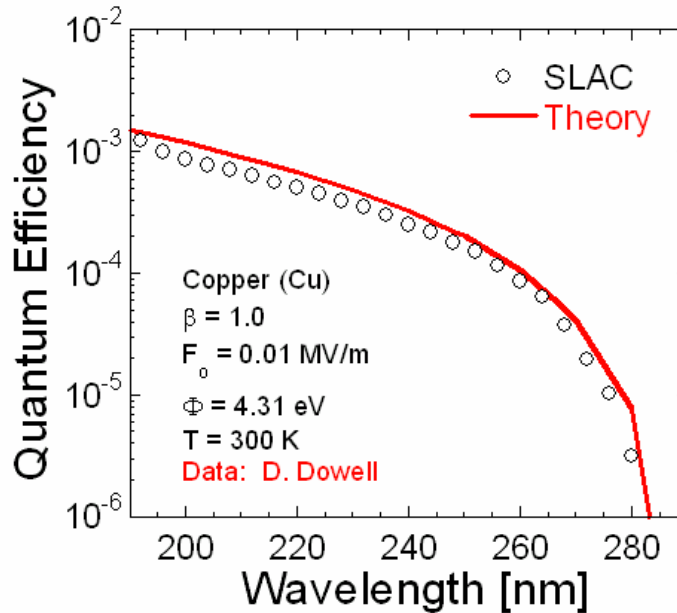


Figure 5.3: Theory Comparison to QE Data from Cu [59]

5.5.2 Coated Surfaces

Recall that Jensen's modified GL theory predicts the work function (and QE) of a photoemitting surface based on the percent monolayer coverage of alkali or alkali-earth metals. Experimentally, cesium coverage is measured indirectly by observing the change in mass apparent on a crystal balance and is reported on an instrument as a coating thickness. Comparison of experimental data to theory requires, therefore, a method for relating these two quantities. The simplest approach is to use a characteristic length scale of a cesium atom, such as atomic diameter, covalent bond length, etc. Various length scales for cesium are listed in Table 14.

Bond Length of CsH	2.494 Å
Bond Length of CsCs	5.309 Å
Atomic Diameter (calculated)	5.96 Å
Atomic Diameter (empirical)	4.50 Å
Avg. Diameter of <i>s</i> -orbital	5.648 Å
Lattice Constant	3.17 Å

Table 14: Characteristic Lengths for Cesium Atoms

While these lengths provide a range of thicknesses that might be interpreted loosely as monolayer thickness, there remains a large degree of uncertainty as to which best applies in the case of adsorbed cesium on tungsten. Following the method of Langmuir, an alternative approach was pursued in this research. It has been observed that upon crystallization, cesium and tungsten atoms both assume the body-centered cubic lattice structures. Furthermore, the lattice constant for cesium, 6.17Å, is nearly twice that of tungsten, 3.15Å [30]. It follows that the atoms comprising a monolayer of cesium on a tungsten lattice form a surface lattice identical to that of tungsten, but with twice the nearest-neighbor spacing. Thus, for every four tungsten

substrate atoms, there is only one cesium atom. Langmuir argues that because the tungsten substrate atoms force the cesium adsorbate atoms to occupy definite elementary spaces, a 4:1 relationship between surface densities of the two is justified [92]. Using this assumption, surface concentration of cesium can be calculated if the crystalline orientation of the tungsten substrate is known. Furthermore, the apparent thickness of one monolayer can be calculated using volume density and atomic mass:

$$t_{Cs} = \frac{\sigma_{Cs} m_{amu}}{N_A \rho_{Cs}} \quad (5.26)$$

Surface concentrations of tungsten γ_W and cesium γ_{Cs} are shown in Table 15, along with apparent monolayer thicknesses for four different substrate crystal planes [93].

Substrate Plane	γ_m related to $\gamma_{m[100]}$	$\sigma_W \times 10^{14}$ atoms/cm ²	$\sigma_{Cs} \times 10^{14}$ atoms/cm ²	t_{Cs} (Å)
[100]	$\gamma_{m[100]}$	10.0	2.5	2.9
[110]	$\sqrt{2}\gamma_{m[100]}$	14.1	3.5	4.2
[112]	$\sqrt{2/3}\gamma_{m[100]}$	8.20	2.05	2.4
[111]	$3/5\gamma_{m[100]}$	5.8	1.45	1.7
[B]	$\sqrt{3}\gamma_{m[100]}$	17.3	4.33	5.1

Table 15: Surface Densities and Cesium Thickness for Various Crystal Planes

If the cathode substrate were made of single crystal tungsten, then cesium thickness would simply be t_{Cs} , and could serve as the conversion factor between measured thickness and cesium coverage. In reality, the dispenser cathode designed and tested in this work utilizes a sintered tungsten surface, which exhibits many different crystal faces and defects. For this reason, the fictitious crystal plane denoted by [B] was devised by Gyftopolous and Levine to account for surface irregularities.

Its assumption in the case of the dispenser cathode leads to a cesium monolayer thickness of 5.1 Å. Even with this calculated value, the actual thickness may deviate slightly because the crystal balance measures cesium that has adsorbed on its sensor, not on the cathode itself. Desorption from the cathode surface can occur during cesium deposition, so that some cesium leaves the cathode surface, but not the monitor. The discrepancy is usually small if the deposition rate is large (i.e., if many more cesium atoms arrive than leave in a given time), but for slower depositions this must be considered. Recall that the coverage at which QE peaks corresponds to that which minimizes the work function. According to GL theory, work function is minimized with a surface density of 11.68×10^{14} atoms/cm², or an apparent thickness of 3.14 Å. The competing effect of desorption during deposition is to cause measured thickness to be higher than actual thickness. This can be corrected for by noting the apparent cesium thickness at which QE peaks and scaling the measurement such that it corresponds to 11.68×10^{14} atoms/cm². All graphs with coverage expressed in percent monolayer θ have been scaled in this fashion to eliminate the effects of desorption.

6. Experimental Results

This chapter systematically details the outcome of experiments designed to provide a fundamental understanding of photoemission from bare and coated metal surfaces in preparation for controlled porosity dispenser studies. Experimental outcome is compared to theoretical predictions outlined in the previous chapter. Before confronting the central measurements, preliminary results which validate those that follow are presented.

6.1 Preliminary Observations

6.1.1 Background Noise

Visible light will not produce photoelectrons from most metals at room temperature, because the work function can be as much as twice the energy of a visible photon. Table 16 lists the work function of several metals used in this experiment. In order to test the integrity of the QE measurement circuit and establish a noise level, IR laser light was shown on a bare tungsten disk and photocurrent was measured using the highest meter resolution possible. The results, in Figure 6.1, show that the background noise level was 0.26 ± 0.1 nA with all equipment (lasers, etc) connected and turned on. If current had been detected, it would have indicated experimental problems consisting perhaps of a conductive path between the anode and cathode or between some point in the QE circuit and ground. Furthermore, no current should be detected if either the incident laser beam or accelerating voltage is off. Figure 6.2 shows that background noise drops by a factor of 2 when the meter is

completely isolated from the QE circuit. The added circuit noise is to be expected, since the circuit includes more than 3m of cable.

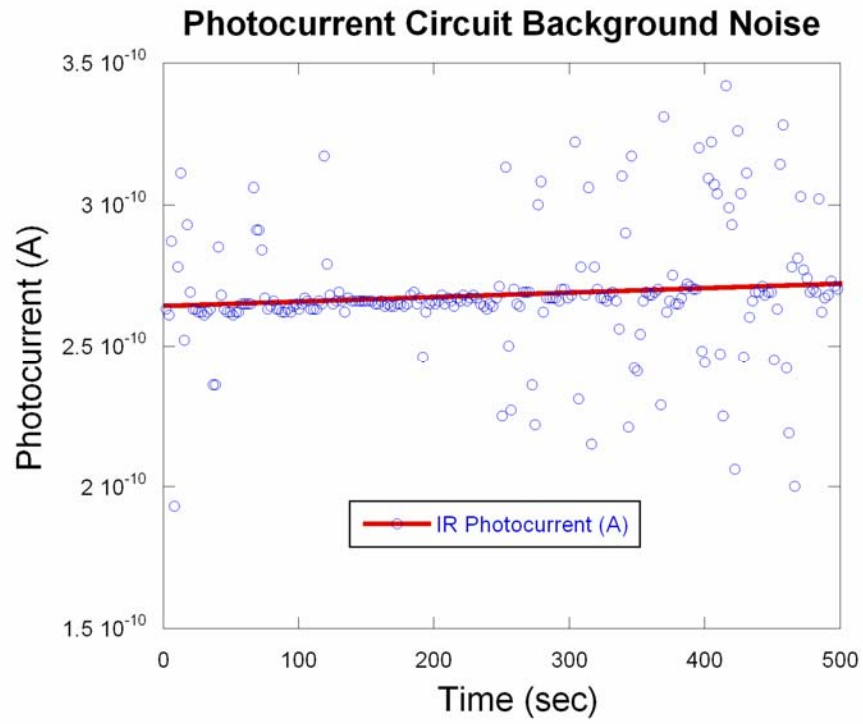


Figure 6.1: Photocurrent Background Noise

Metal	ϕ (eV)
Silver	4.26
Copper	4.65
Molybdenum	4.37
Tungsten	4.65

Table 16: Work function of Various Metals

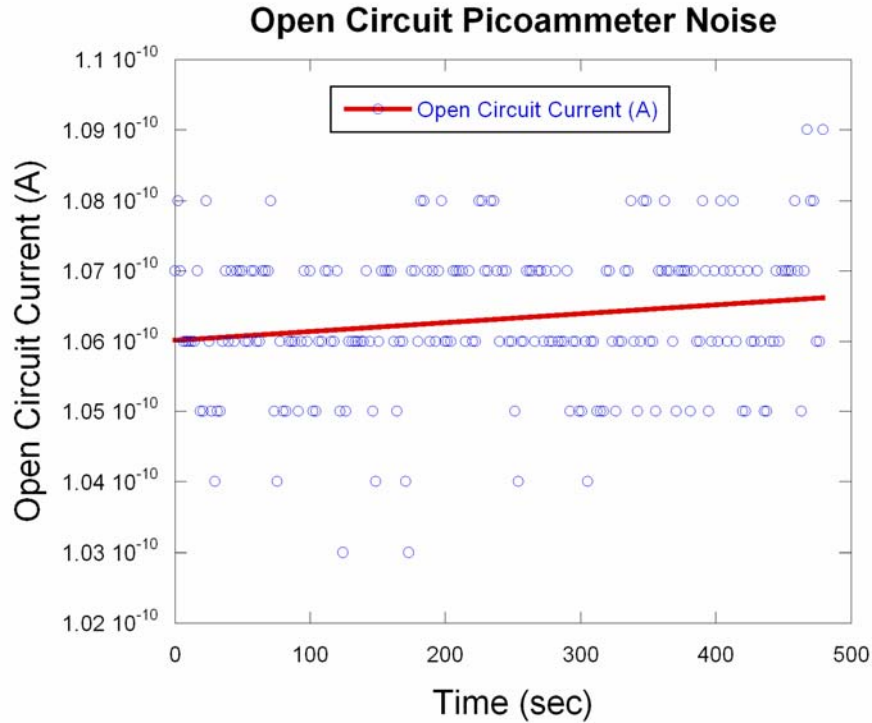


Figure 6.2: Picoammeter Open-circuit Noise

6.1.2 Monolayer vs. Multiple-Monolayer Cesium Evaporation

As previously discussed, the presence of alkali metal coatings is crucial to obtaining an appreciable photocurrent from metals and semiconductors. These coatings should not be arbitrarily applied, however, without some knowledge of their behavior over time and in various thickness regimes. Three thickness regimes can be distinguished for surface coatings: sub-monolayer, multiple-monolayer, and bulk. Coatings that are hundreds or perhaps thousands of monolayers thick can be considered bulk metal for the purposes of this experiment, because any photo-excited electrons originate not from the substrate-coating interface, but from the coating itself. For most of the experiments in this program, sub-monolayer thicknesses are investigated, but in some cases more than one monolayer is intentionally added.

Recall from theoretical prediction that there exists an optimal cesium coverage that permits maximum surface dipole enhancement resulting in a lowered work function and a maximized QE. This effect was seen repeatedly throughout the program at all wavelengths and is a useful mechanism for specifying approximate coverage: the coverage resulting in peak QE corresponds to approximately one single-monolayer coating. A characteristic curve relating QE and coverage using a 405nm laser is shown (with QE normalized to its peak value) in Figure 6.3.

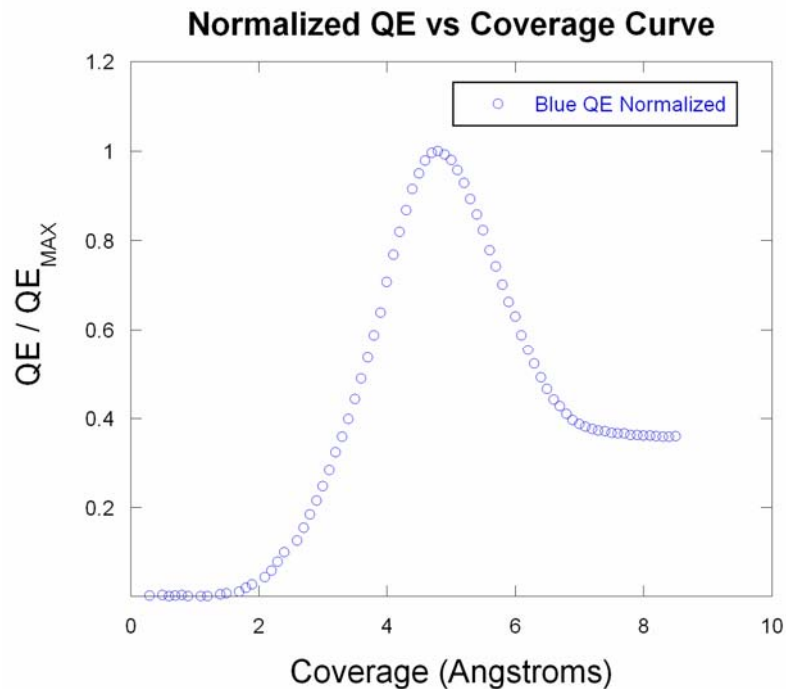


Figure 6.3: Characteristic QE vs. Cesium Coverage Curve

Single-monolayer coatings adhered to the surface longer and at higher temperature than multiple-monolayer coatings. After peak QE had been obtained during cesium deposition, additional application did not result in increased QE. This is reflected in Figure 6.3, and occurred because the number density of cesium atoms on the surface

had exceeded that which provides the best dipole enhancement. Recall that the combined work function of a monolayer coating of cesium on tungsten is less than the work function of either metal alone. Thus, as cesium coverage is increased beyond a single monolayer, the photoemitting surface becomes more like bulk cesium, resulting in a higher work function and lower QE.

Figure 6.4 shows the outcome of six experiments in which cesium was deposited to a known thickness and then removed by heating the cathode for 500 seconds while measuring QE. In each of the QE vs. coverage plots (a – f), cesium was being removed as the cathode temperature was increased according to the profile in Figure 6.5. The initial conditions were the same for all trials. Notice that for the first two trials, the amount of cesium deposited was less than a monolayer, evidenced by the fact that QE decreased monotonically instead of going through a local maximum. In trial *c*, QE does go through a peak as the 5-Å thick layer is removed, an indication that more than one monolayer had been deposited. The time required to reach the peak was noted and the experiment was repeated three more times using 10, 15, and 20 Å cesium coating thicknesses, as shown in trials *d-f*. The time required to reach the peak in each case (i.e. for all but one monolayer to be removed) increased linearly with time, as shown in Figure 6.6. The slope is 0.214 Å/sec and is essentially the multiple-monolayer evaporation rate for cesium at temperatures less than 200°C. Given that the thickness of one monolayer is roughly twice the covalent radius of a cesium atom, this rate can be expressed as 0.04 monolayers/sec. After the peak had been reached, it was observed (in all trials) that about 140 seconds was required for QE to decay to half its maximum value. Using Figure 6.3, it can be seen that a 50%

decrease in QE (from its peak value) corresponds to a loss of approximately 1.2 Å of cesium from the surface. Because this loss occurred over a 140 second time period, the sub-monolayer evaporation rate is approximately 0.009 Å/sec. Thus, the multiple-monolayer evaporation rate is about 23 times *faster* than the sub-monolayer evaporation rate. This fact is strong evidence that cesium atoms adhere more strongly to a tungsten substrate, than to an existing cesium surface layer. Thus, cesium coverage in excess of a single monolayer will evaporate quite rapidly. For the case of a dispenser cathode, this result underscores the importance of preventing over-cesiation during the activation and rejuvenation procedures.

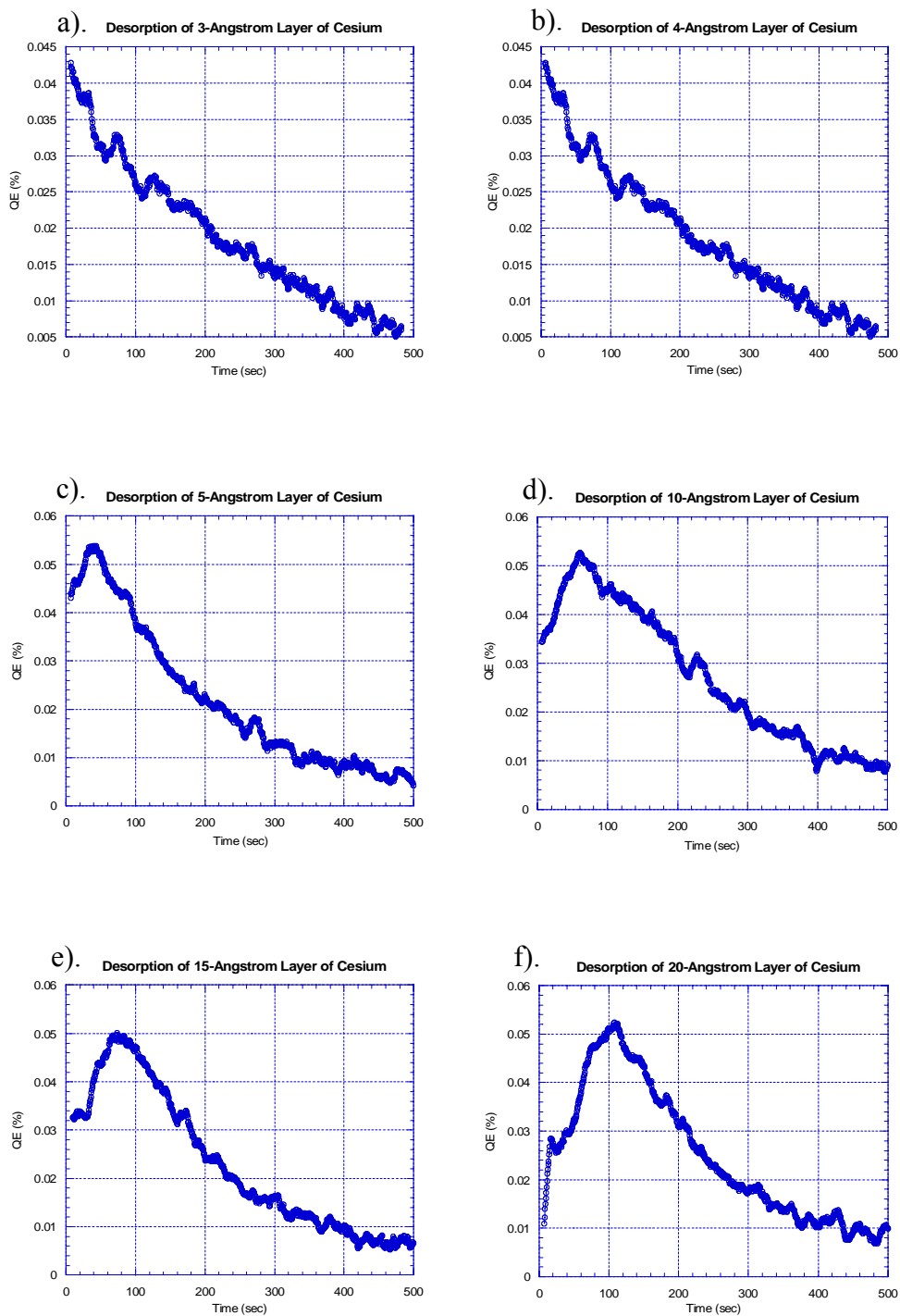


Figure 6.4: QE vs. Time - Desorption of Various Cesium Layer Thicknesses

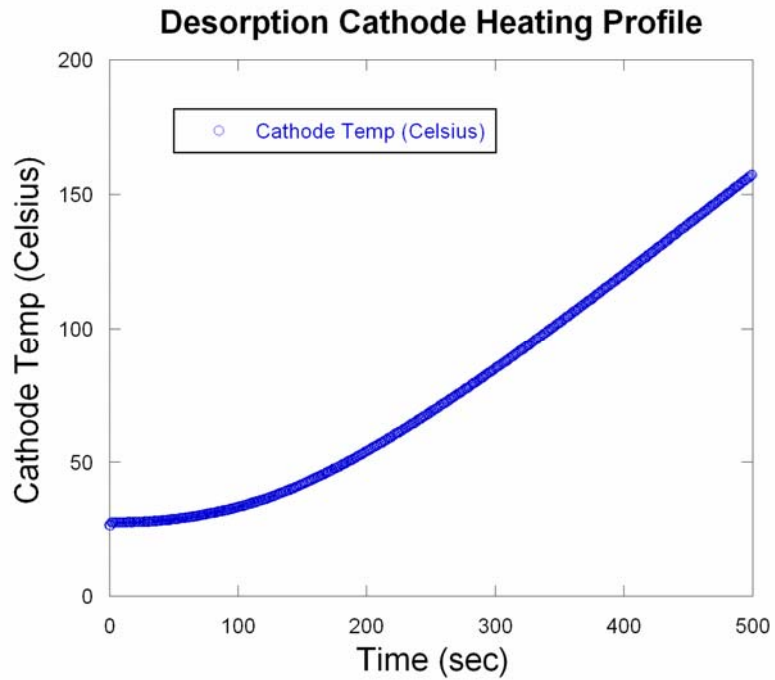


Figure 6.5: Desorption Heating Profile

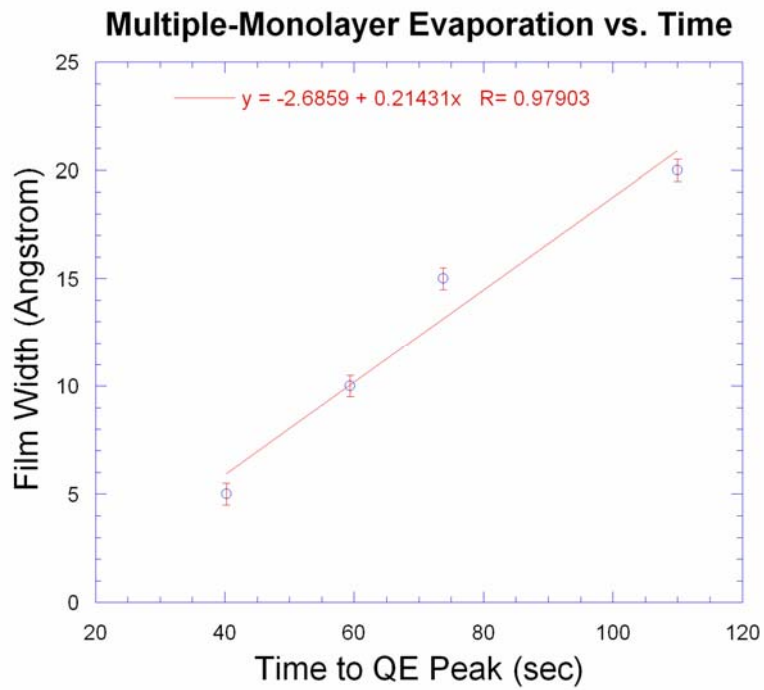


Figure 6.6: Evaporation Rate of Multiple Monolayers of Cesium

A promising consequence to a higher multiple-monolayer evaporation rate is that it suggests that cesium will not form localized “clumps” on the surface but will assume a sparse distribution for sub-monolayer thicknesses. This is highly desirable because work function is very sensitive to changes in coating thickness and “clumps” of cesium would create emission non-uniformity and potentially lead to an increase in beam emittance.

6.1.3 Space Charge

Prior to measuring quantum efficiency, it is crucial to verify that every photo-emitted electron is extracted and contributes to measured photocurrent. If this is not the case, space charge shields the anode from the cathode, limiting the current that can be extracted, and causes QE to appear fictitiously low. Space charge refers to the localized concentration of electrons near the cathode, whose electric field limits the current that can be accelerated using a given extraction voltage. This effect is evident when extracted current J exhibits a 3/2-power dependence on accelerating voltage V and is described by the *Child-Langmuir law* given:

$$J_{\max} = \frac{1}{9\pi d^2} \sqrt{\frac{q}{m_e c^2}} V_0^{3/2} \quad (6.1)$$

where q is the charge of the electron, m is its mass, c is the speed of light, and d is the anode-cathode spacing [16]. Knowing the spot size of the laser and assuming that its entirety constitutes the emission area, the total amount of current that can be extracted at a given voltage can be calculated. If the number of photo-excited electrons arriving at the cathode surface per unit time is *less* than this amount, then the cathode is not space charge limited. If it is found to be the case, then the extraction voltage must be

increased in order to extract the entire population of photo-electrons eligible (in terms of energy) to cross the vacuum barrier. Figure 6.7 shows a photocathode operated outside of the space charge regime, with an extraction voltage of +186V on the anode, and where an increase in incident (405nm) laser power produces a linear increase in photocurrent. In this and subsequent experiments, laser power was controlled not by altering the laser module's output power but rather by placing standard filters in the beam path.

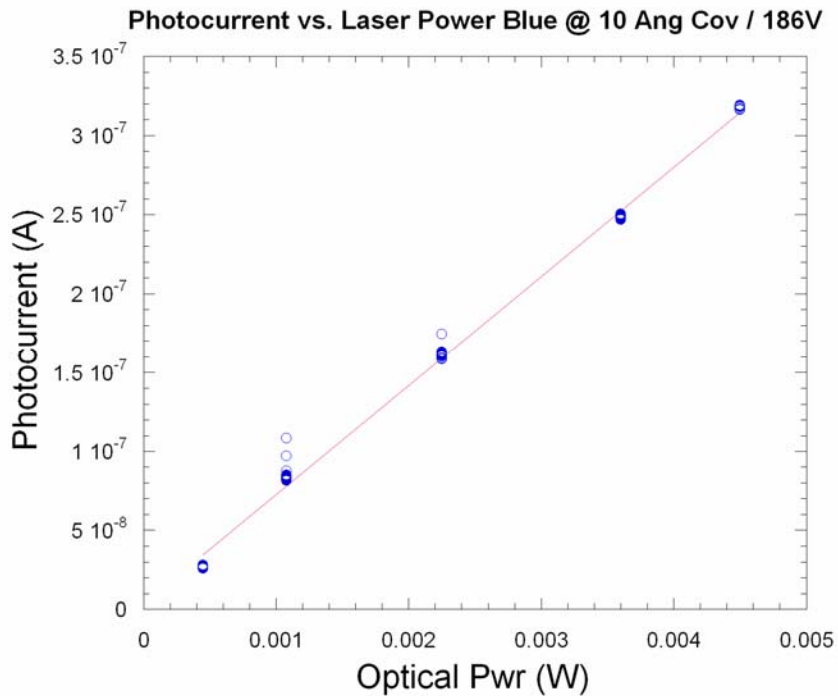


Figure 6.7: Photocurrent vs. Laser Power Outside of Space Charge Regime

If the accelerating voltage is reduced dramatically, the cathode becomes space charge limited and an increase in incident laser power does not result in a corresponding increase in beam current, as shown in Figure 6.8. Current increases linearly initially, but then saturates as space charge prevents the extraction of additional current.

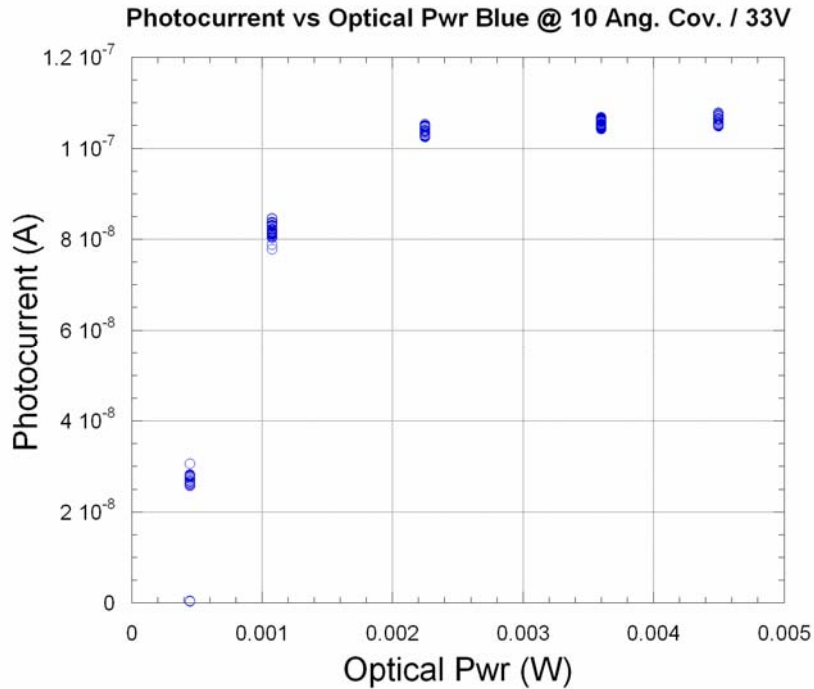


Figure 6.8: Saturated Current in the Space Charge Limited Regime

If full optical power is shown on the cathode and voltage is varied, then the space charge regime can be characterized in terms of accelerating voltage. Figure 6.9 shows that space charge dominates until accelerating voltage is increased to about 100V, at which point further increase in voltage does not allow additional extraction of charge. This is the desired operating regime of photocathodes undergoing QE measurement. To be certain that space charge would not complicate measurements, an accelerating voltage of +186V was placed on the cathode. Under these conditions, QE was constant with respect to incident laser power.

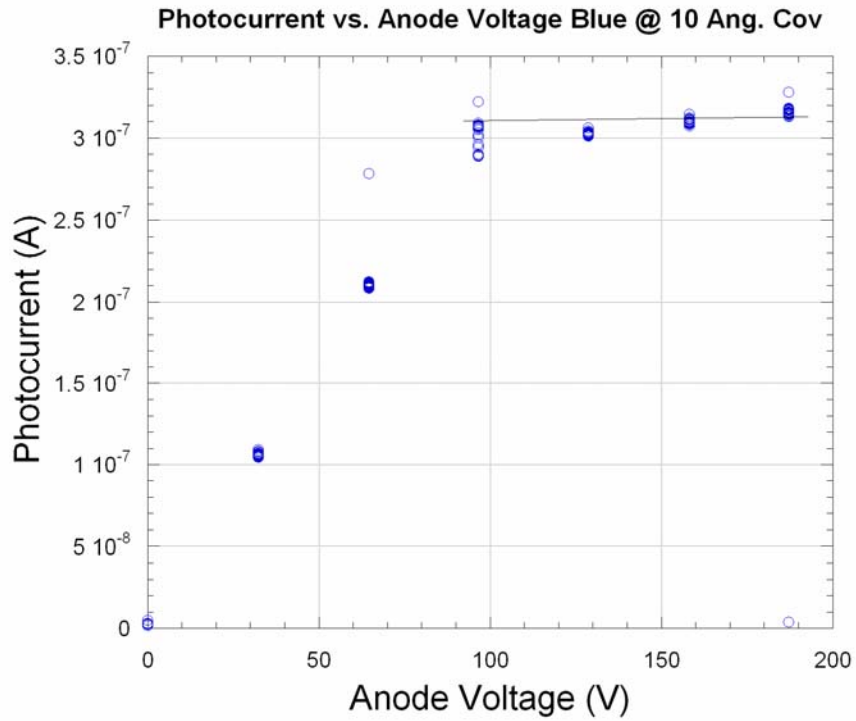


Figure 6.9: Defining Space Charge Regime: Photocurrent vs. Voltage

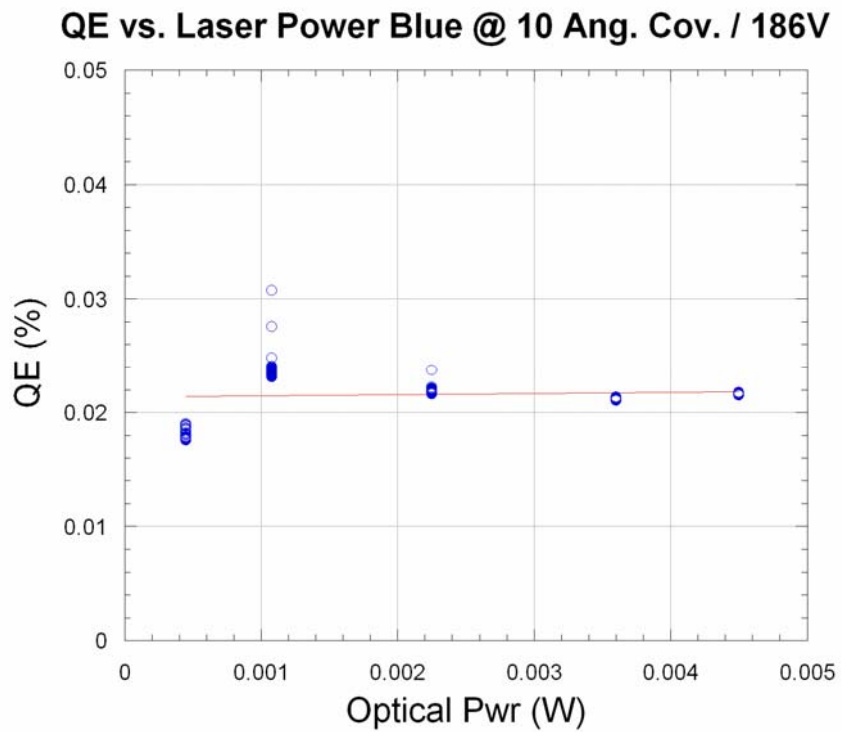


Figure 6.10: Constant QE with respect to Laser Power

6.1.4 Calculating Error and Uncertainty

Significant effort has been made to reduce measurement error in this project. Random errors in photocurrent were reduced by 2 orders of magnitude through improved instrumentation and QE circuit shielding, while systematic errors were lowered by masking vacuum insulators from cesium deposition and separating the ion gauge from the anode-cathode region. In the latter example, ions created on the hot filament of a nearby ion gauge gave rise to a pressure dependent dark current of up to 10nA.

Recall that QE depends upon measured observables in the following manner:

$$QE = \frac{I}{P_\lambda} \frac{2\pi\hbar}{\lambda e} \quad (6.2)$$

where I is photocurrent [A], P_λ is optical power [W], λ is drive laser wavelength, and e is electron charge. Because these measurements are uncorrelated, the total error is calculated using the canonical method of quadrature addition:

$$\Delta QE = QE \sqrt{\left(\frac{\Delta I}{I}\right)^2 + \left(\frac{\Delta P_\lambda}{P_\lambda}\right)^2 + \left(\frac{\Delta \lambda}{\lambda}\right)^2} \quad (6.3)$$

where the differential quantities represent the uncertainty in each of the observables above. The basis for the quadrature addition is the assumption that each measured quantity is actually a Gaussian distribution about a mean (what is read by the instrument) with a width specified by the given uncertainty. The width of error bars shown in any subsequent graphs are calculated using this method. Table 17 shows measured uncertainty for laser power and wavelength. Because different lasers are used for each wavelength, it is to be expected that uncertainty in their power and

spectrum would vary one to another. The green laser, because it is a diode pumped YAG crystal, has a more defined output spectrum than the laser diodes.

λ (nm)	$\frac{\Delta P_\lambda}{P_\lambda}$	$\frac{\Delta \lambda}{\lambda}$	$\left(\frac{\Delta QE}{QE}\right)_{\max}$
375	0.01	2.67×10^{-2}	2.85%
405	0.01	4.94×10^{-2}	5.04%
532	0.05	1.88×10^{-4}	5.00%
655	0.02	1.53×10^{-2}	2.52%
808	0.02	1.24×10^{-2}	2.35%

Table 17: Uncertainty in Measurements Used to Calculate QE

Figure 6.11 and Figure 6.12 show a characteristic QE vs. coverage curve before and after implementing the changes described above to reduce systematic and random errors. Notice that the measurement uncertainty is reduced by more than one order of magnitude. The largest values of uncertainty in QE for each of the wavelengths above are shown in the right-most column of Table 17. All subsequent QE data presented in the remaining chapter share this level of uncertainty, as reflected by the use of error bars in graphs. Error bars are selectively omitted in some figures because their inclusion obfuscates the data, but the inherent uncertainty is still the same as given above.

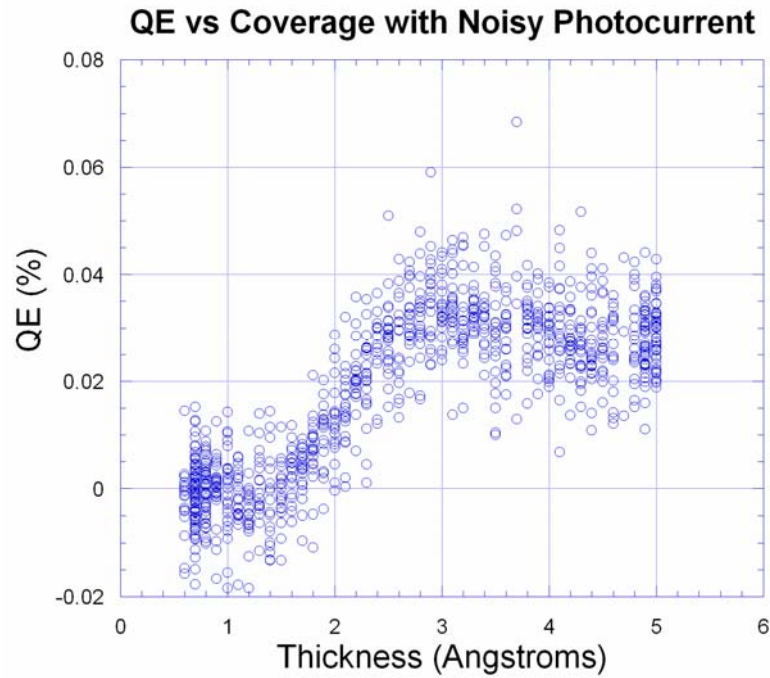


Figure 6.11: QE vs. Coverage with Noisy Photocurrent

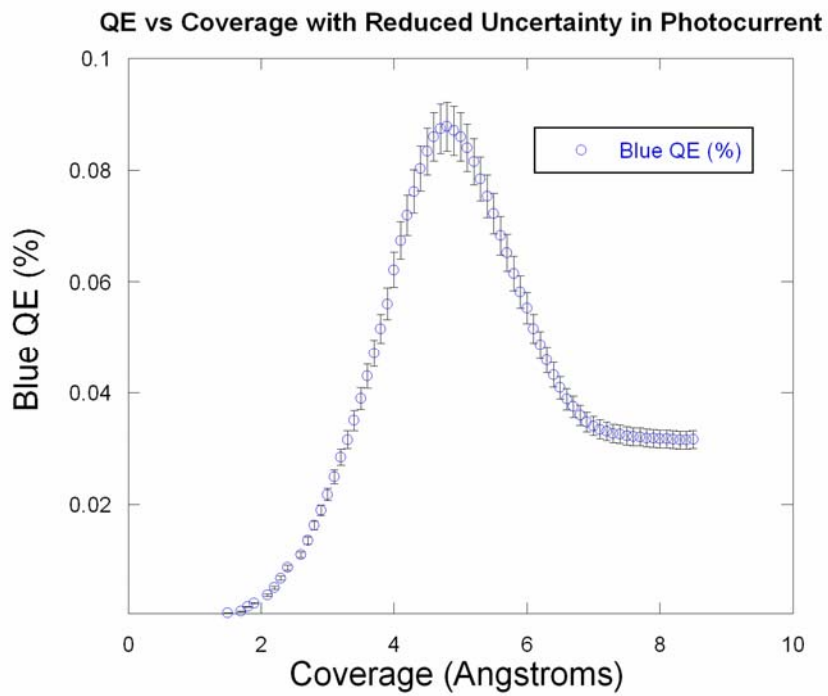


Figure 6.12: QE vs. Coverage with Reduced Uncertainty in Photocurrent

6.2 Solid vs. Sintered Tungsten

Sintered tungsten was chosen as the substrate material for the prototype dispenser photocathode detailed in the next chapter because it is a well-documented (refractory) metal that can be laser welded to stainless steel. As described elsewhere, the goal of the dispenser cell is a controlled, room-temperature release of cesium from within the cathode that results in a replenished surface coating enabling high efficiency and long life. Because the quantity of cesium on the surface critically determines the operating parameters and functionality of the cathode, this coating and its effect on photoemission must be well understood. An underlying theme in this program is to perform modeling and measurement on simpler systems first, increasing complexity as the essential features are understood. To this effect, rolled and polished tungsten was first studied to eliminate possible effects of sintering. Measurements included multi-wavelength QE vs. cesium coverage, QE vs. temperature, duty-cycle dependent cathode lifetime, and sub- and single-monolayer work function. These essential measurements were then compared to those of cesiated sintered tungsten, with no apparent change in behavior. This observation is consistent with theory predictions, since both substrates are polycrystalline and share similar surface roughness. A substantial difference is that the sintered tungsten features surface pores while the solid does not. Since cesium is applied externally in both cases, however, it evidently masks the presence of the sub-micron pores.

6.3 Surface Metrology of Sintered Tungsten

In dispenser cathode studies, performance is critically determined by the size and distribution of pores, grains, and grain boundaries. These features were studied using SEM and FIB imaging as detailed in the previous chapter. This information is extremely relevant when considering a prototype dispenser cathode design: if cesium diffuses to the surface too slowly, for example, then either pore size or pore distribution should be modified to accommodate a faster diffusion rate. This could be modified by using smaller grains in the sintering process or (preferably) a laser drilling fabrication method that allows precise placement and distribution of pores.

6.3.1 General Observations

Because surface characterization is most applicable to dispenser studies, the discussion to follow focuses on a tungsten disk identical to the one used to fabricate the dispenser cell. Figure 6.13 below shows an optical image of the top surface of this disk with surface scratches resulting from the polishing process.

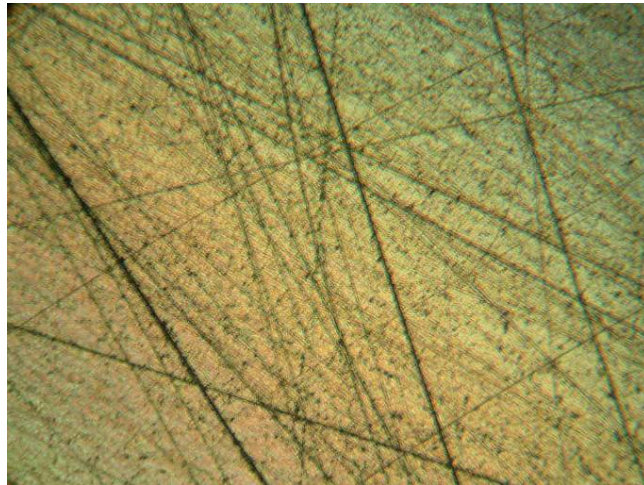


Figure 6.13: Sintered Surface at 50x Magnification

The two most pronounced scratches (near the bottom left) were used to macroscopically locate the area of the cathode to be studied in depth at higher magnification. Both scratches continue nearly the entire width of the cathode, can be easily identified at low magnification, and have one point of intersection. This singular intersection was selected as an area of interest for additional study at high magnification. The ability to relocate this area is important because the sample will be characterized again after ion beam cleaning to determine what effects this has on surface roughness. High magnification reveals voids and artifacts that are 50-100 μ m in diameter. These exist on both the top and bottom surfaces of the disk, as shown in Figure 6.14. Notice also from this image that the number density of surface defects is less on the top surface than on the bottom. This was found to be the case at three other test sites on the cathode and can be attributed to a higher degree of polishing applied to the top surface. The smoothest side was selected to be the photo-emitting surface and the disk was mounted in the appropriate orientation in the dispenser cell. Another significant difference between the top and bottom surfaces is the arrangement of grains and pores. Figure 6.15 shows the top surface at 1500x magnification while Figure 6.16 shows the bottom. The top surface has about 30% more pores whose spacing and size appears more uniform.

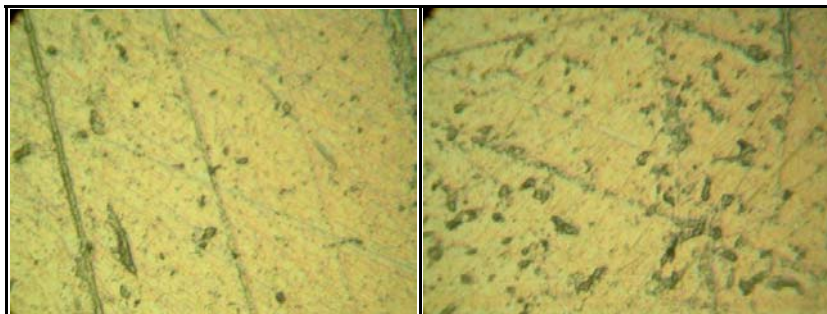


Figure 6.14: Images (500x) Top and Bottom Surfaces of Sintered Tungsten

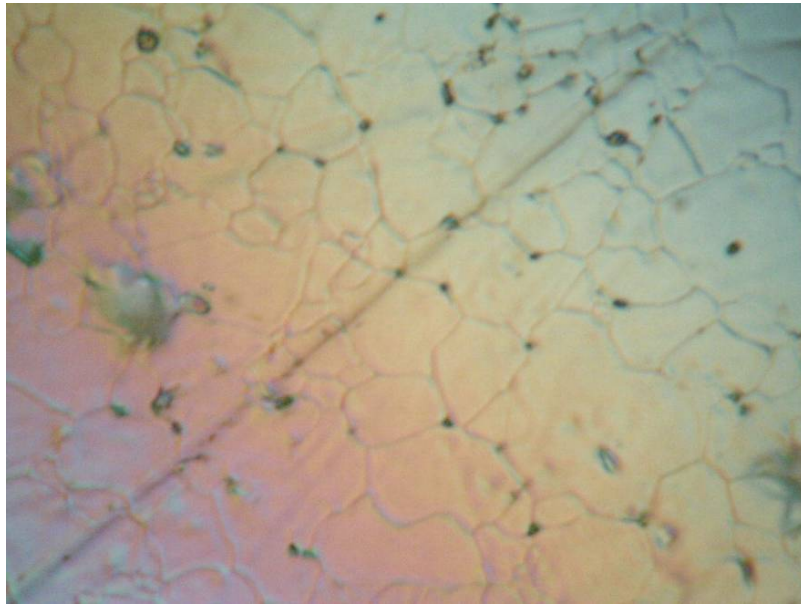


Figure 6.15: Top Sintered Tungsten Surface at 1500x Optical Magnification

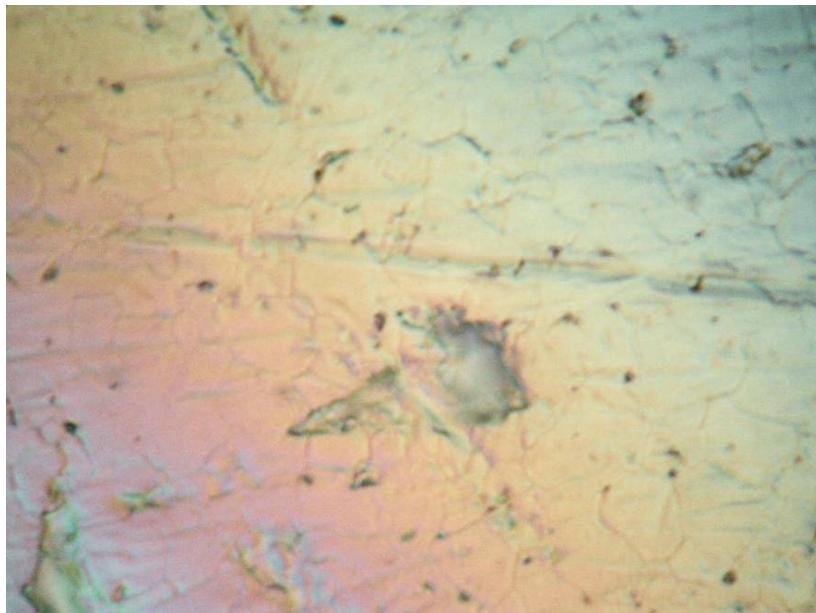


Figure 6.16: Bottom Sintered Tungsten Surface at 1500x Optical Magnification

Because the top side of the disk was selected as the photo-emitting surface, all subsequent discussion applies only to that side.

6.3.2 Surface Pores

If cesium is to be delivered to the surface through a controlled porosity substrate, it will arrive through (in the case of sintered materials) internal, interconnected channels that terminate at the surface as a pore. The surface area it occupies is usually at the intersection of two or more grains boundaries. Figure 6.15 shows that a few pores exist within a single grain, but the vast majority form at the confluence of three grains. In order to quantify the distribution and size of these pores, SEM was used to image individual pores at higher resolution. Figure 6.17 shows a close up of several representative pores, with a zoomed inset, whose surface diameter is about 250nm. Initial observations in this project as well as other studies of pore morphology suggest that diameter increases as the pore reaches an interface, including the surface [94]. Thus, the pore diameter directly at the surface may not reflect the mean size of the entire pore. For dispenser studies, pore diameter both at and below the surface is important. Pore size at the surface can be directly measured using an SEM image. In order to determine sub-surface pore size, a novel approach was taken using a focused ion beam (FIB). Using the methodology described in the previous chapter, a region directly adjacent to a pore was milled to a depth of 2 microns (roughly 10 times the surface diameter of the pore). Milling a material that is homogenous on all sides of the milling area normally results in a symmetric cut where the removed material is ejected uniformly from the resulting hole. In the method used here, however, a pore exists directly adjacent to the milling area and material that would otherwise be sputtered uniformly spills preferentially into the vacant space defined by the pore. This material is pushed upward as the milling

process continues and a finger-like structure is forced out of the pore, as shown in Figure 6.18.

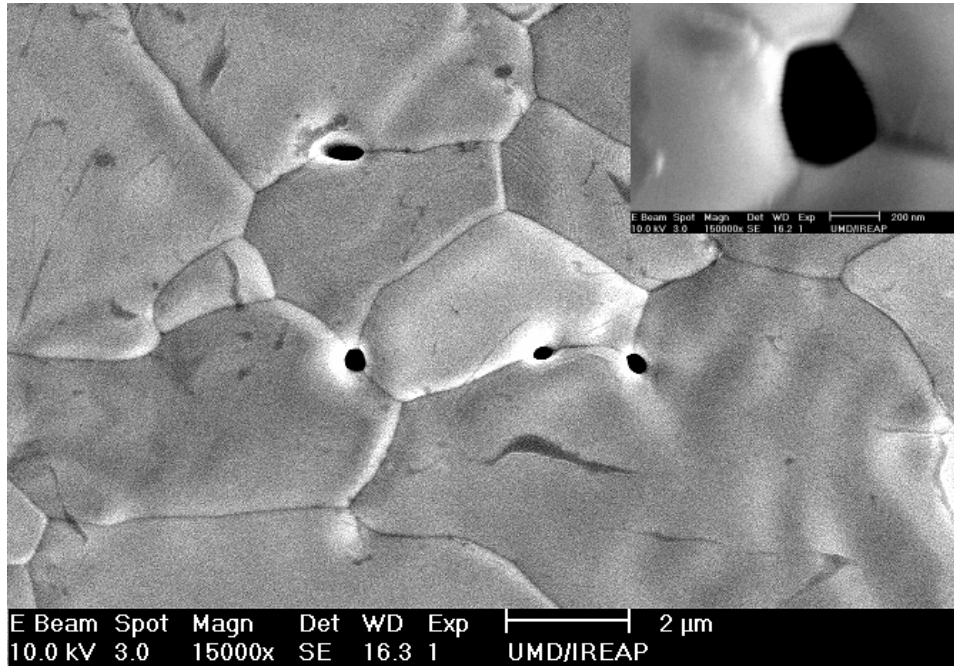


Figure 6.17: Representative Sub-micron Pores in Sintered Tungsten

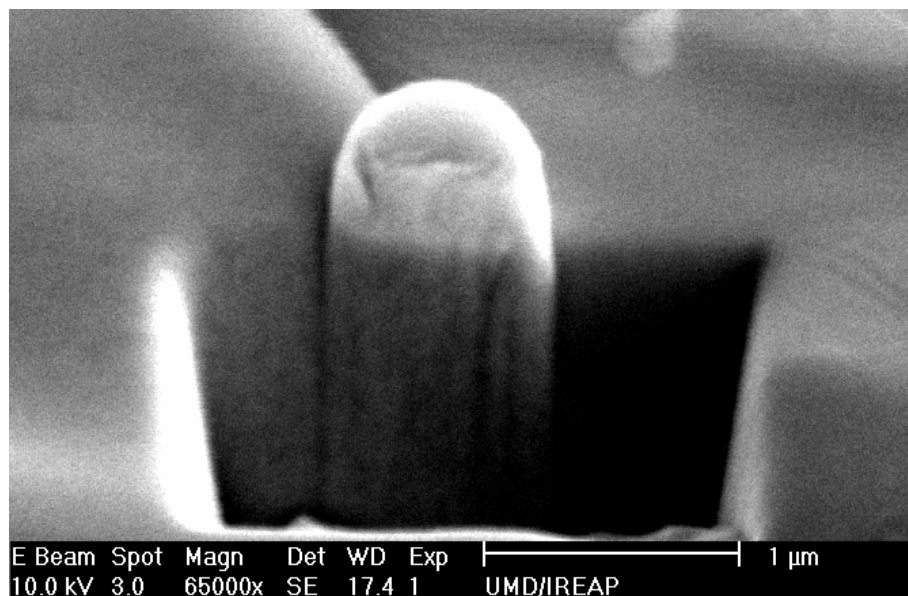


Figure 6.18: Measure Pore Size Using FIB Milling

The dimension of the protrusion closely matches the narrowest diameter of the sub-surface pore. Using several such measurements of pores in various regions across the cathode, it was found that pore diameter varied from 200 to 450nm, with an average of about 350nm. The spatial distribution of surface pores is crucial because it determines the degree to which cesium can be delivered uniformly to the surface. The ideal dispenser would have regularly spaced pores whose size and separation distance are such that cesium atoms can reach all areas via surface diffusion. For a sintered material, pore distribution depends upon manufacturing process and can be characterized by a mean pore-to-pore distance determined through SEM analysis. Figure 6.19 shows highlighted pores (dots) in a representative region of the cathode. The nearest-neighbor distances of these pores appear to follow a log-normal distribution:

$$f(x, \mu, \sigma^2) \equiv \frac{1}{\sqrt{2\pi\sigma x}} \exp\left\{-\frac{1}{2\sigma^2}(\ln(x-\mu))^2\right\} \quad (6.4)$$

as illustrated in Figure 6.20, with a mean pore-pore separation distance μ of 3.14 μm . Also highlighted in Figure 6.19 are some representative grains across the surface. The areas of each were computed and assigned an equivalent diameter $D = \left(\frac{4}{\pi} \int dx dy\right)^{1/2}$ that averaged 4.8 μm . As can be seen below, however, the grains do not necessarily overlap pores, so a better characteristic length for cesium diffusion would be the area between pores.

Location of Pores and Representative Grains

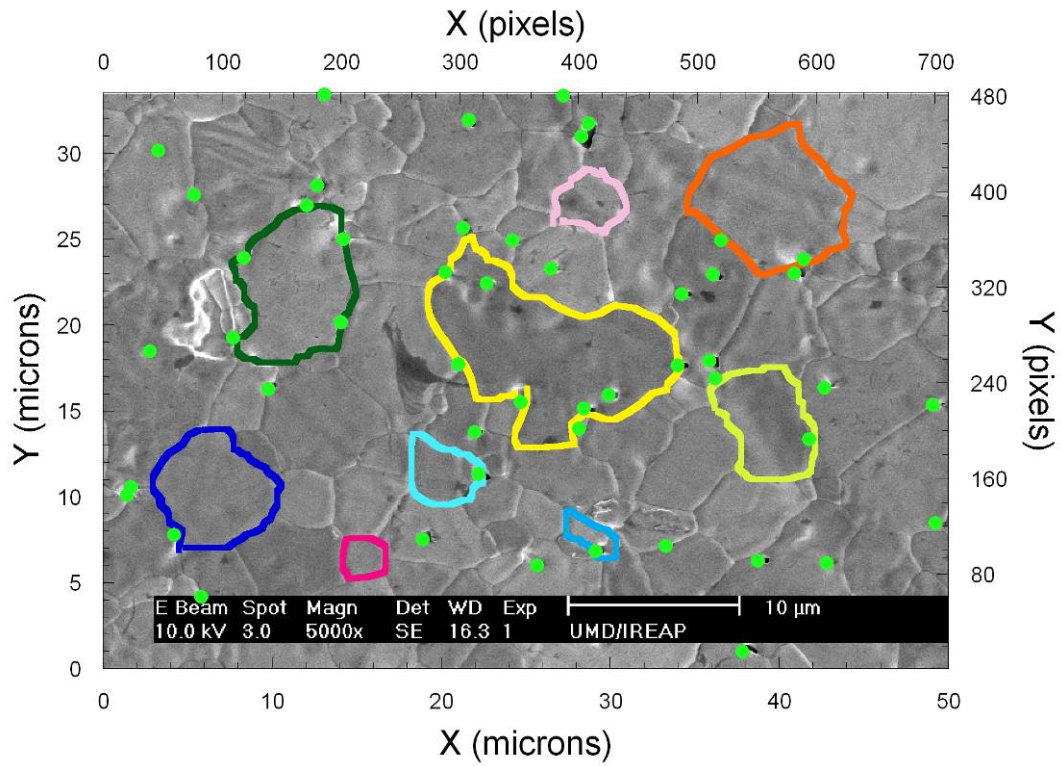


Figure 6.19: Spatial Distribution of Pores on Dispenser Surface

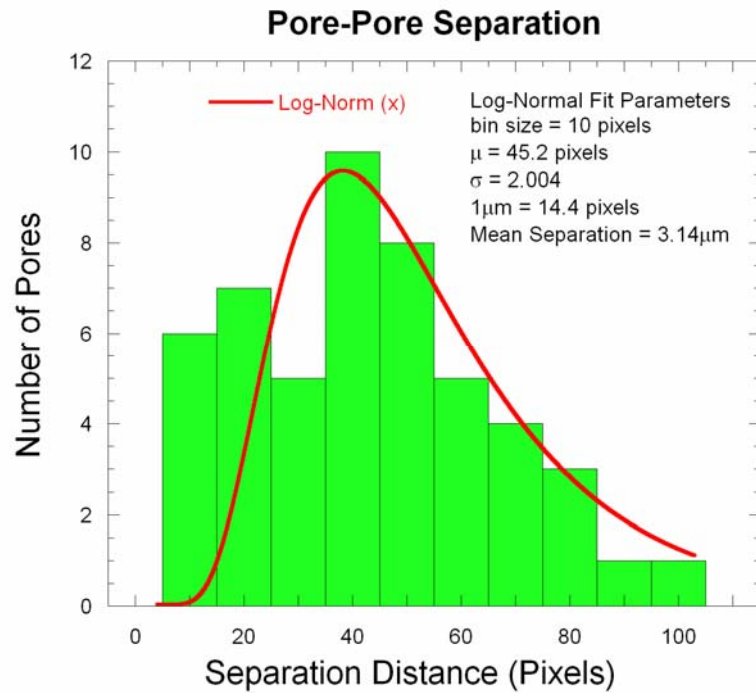


Figure 6.20: Log-Normal Fit for Pore-Pore Separation Distance

The localized area that cesium atoms from each pore would ideally coat can be determined by Voronoi decomposition (also known as Dirichlet tessellation), where perpendicular boundaries bisect each line connecting nearest neighbor pores [95]. The polygon defined by these intersecting boundaries contains just one pore and approximates the local surface area over which cesium atoms must diffuse to achieve uniform coverage. Figure 6.21 illustrates such a construction, where each dot represents a dispenser pore, while Figure 6.22 provides the distribution of the corresponding areas. On average, the localized area surrounding each pore is 30 square microns, roughly 60 times larger than the average pore. It is interesting to note that grain size and Voronoi polygons share roughly the same area and equivalent circular diameters. This diameter, along with pore radius provides two a characteristic length scales that quantitatively describe the sintered tungsten cathode substrate.

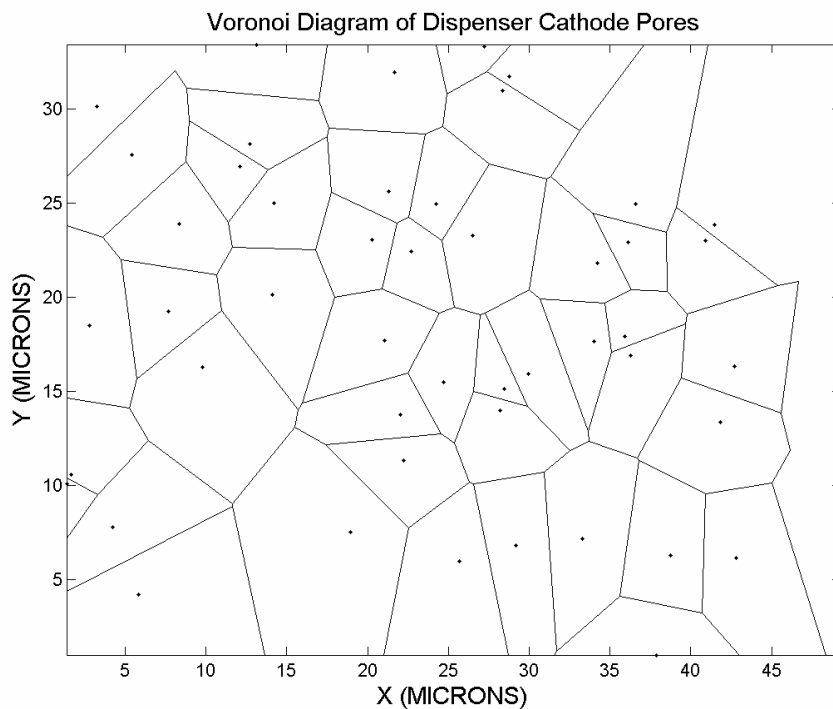


Figure 6.21: Voronoi Diagram for Pores on Dispenser Cathode Surface

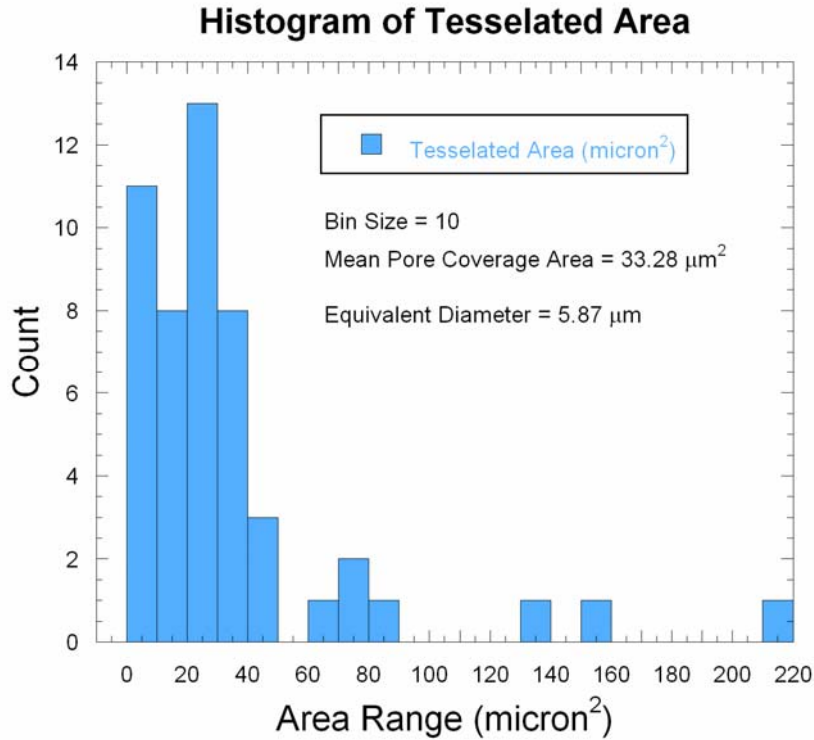


Figure 6.22: Distribution of Areas Surrounding Dispenser Pores

6.3.3 Crystallographic Orientation

If the cathode surface is imaged using a focused ion beam (via secondary electron emission), then a crystallographic map of the surface can be obtained by observing changes in image intensity. Figure 6.23 shows such an image: the patches of varying intensity correspond to different exposed crystal faces. Because the intensity is uniform within a given patch, and because a patch appears to correspond to a grain, it can be assumed that each grain is a single crystal. Crystal orientation is important for photoemission, because each exposed face exhibits a slightly different work function and will accommodate different surface packing densities of cesium atoms. Therefore, electron emission is modified not only by the variation in substrate work function, but also by local changes in the cesium dipole enhancement factor.

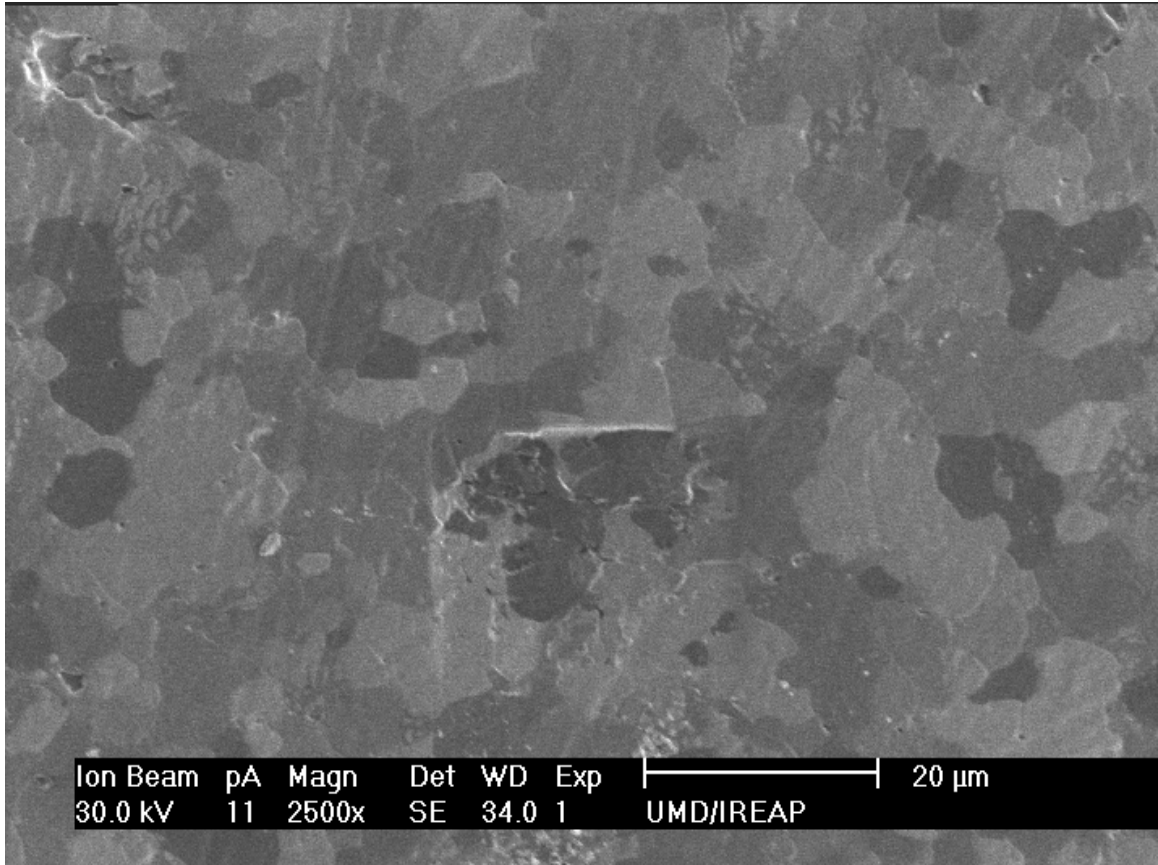


Figure 6.23: FIB Image Revealing Crystallographic Map

During activation of the dispenser cathode, elemental cesium is released when cesium chromate is reduced at elevated temperature. Because cesium's outer electron is not tightly bound, it is easily relinquished to any neighboring metallic surface, including the sintered substrate through which it is diffusing. With its outer electron removed, the cesium ion is much smaller and perhaps capable of traveling not only through interconnected porous channels, but also along grain boundaries. To gain insight into the 3D structure, ion milling was used to examine boundaries of a representative grain. Using FIB imaging, a single grain was identified for study

(through intensity contrast) and its 2D contour was recorded starting at the surface and throughout FIB milling in 1 micron steps. The top half of Figure 6.24 shows the wide angle view of the milled area while the bottom shows the back wall of a partially-milled volume: notice the cross section of grains, diffusion channels and voids. The milling continued until only sub-surface grains were visible and the resulting contours were then assembled as a 3D mesh image, shown from a sub-surface perspective in Figure 6.25. It is interesting that this grain, along with those visible in the back-wall of the milled cross section, has an approximate aspect ratio of unity. This is important because it suggests that length scales measured on the surface are likely to apply to the bulk as well.

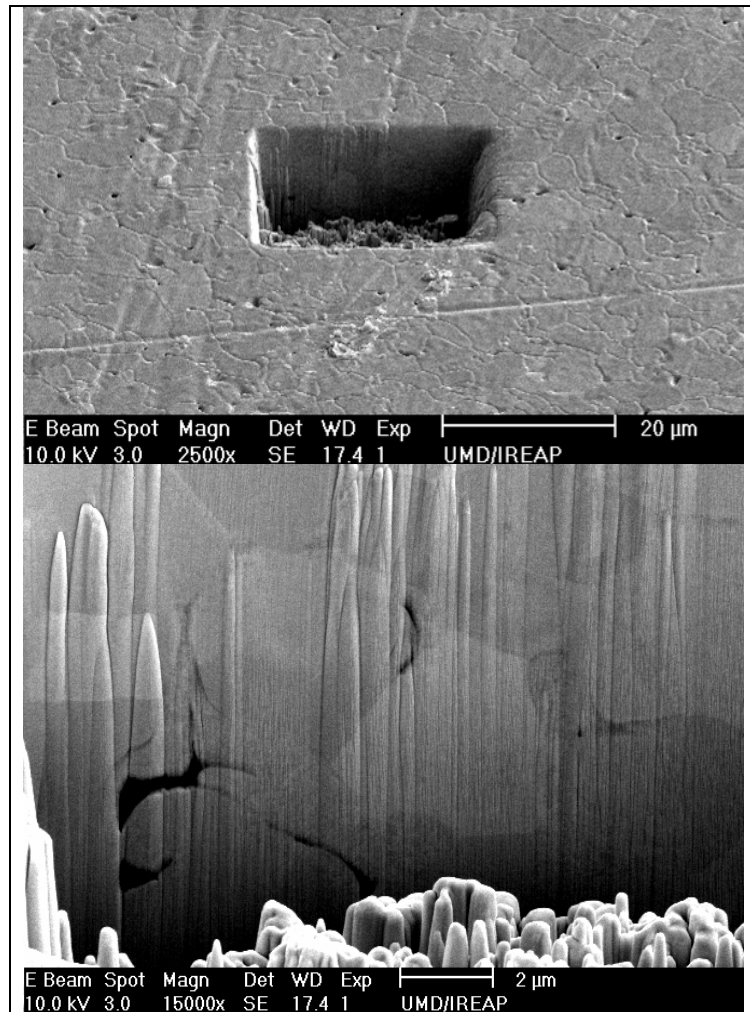


Figure 6.24: FIB Milling - Wide Angle View (top) & Back Wall (bottom)

Grain Contour: Sintered Tungsten

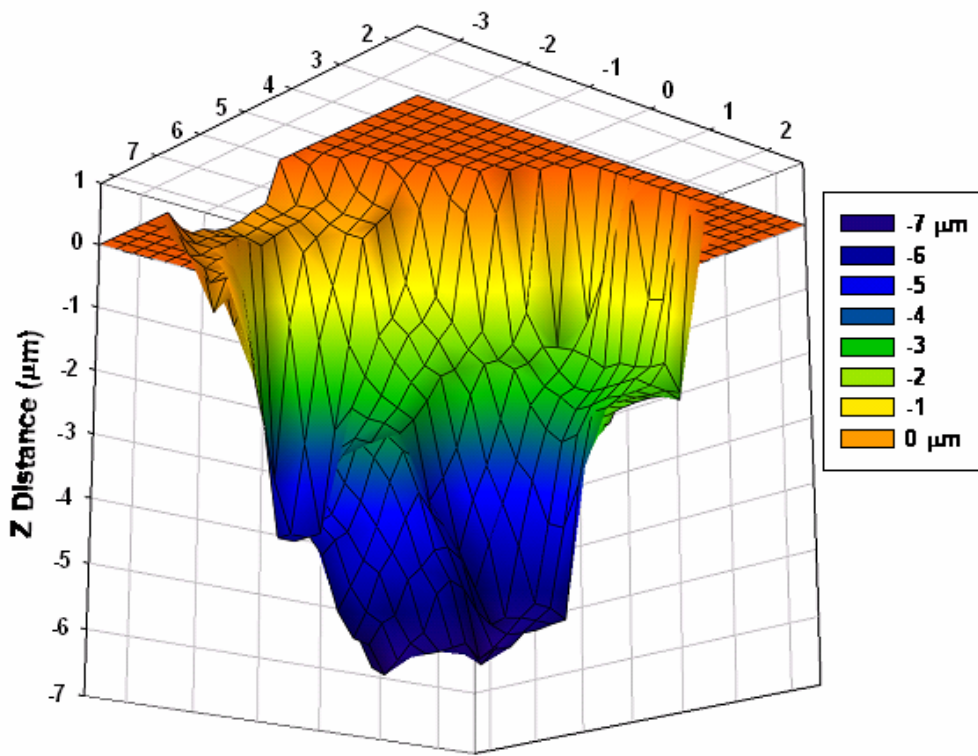


Figure 6.25: 3D Image of a Sintered Tungsten Grain

6.4 Cs-on-Sintered Tungsten: Anneal Cleaned Only

Tungsten exposed to atmospheric contamination does not photoemit after cesiation because the surface dipole layer interacts not with the tungsten substrate, but rather with high-work function oxide layers and other surface impurities. To remove these coatings, two methods are utilized and compared: heat anneal and ion beam cleaning. Annealing the sintered substrate involves rapidly increasing temperature to over 1000°C under high vacuum in order to drive off contaminants. The relative effectiveness of this treatment is reflected in the results below and compared to ion cleaning elsewhere.

6.4.1 QE vs. Coverage

The most relevant photoemission measurement for dispenser cathode studies is the effect of fractional monolayer cesium coverage on the quantum efficiency of sintered tungsten at multiple wavelengths. Data from two separate experiments are shown in Figure 6.26. A heat anneal was performed in each case prior to cesium deposition and the resulting agreement between consecutive data sets demonstrates the high degree of measurement and fabrication repeatability. The wavelength dependent behavior is as expected: shorter wavelengths yield higher QE and exhibit emission at lower cesium coverage than longer wavelengths. The characteristic peak in QE is observed at all wavelengths, and corresponds to a minimum work function caused by optimal surface dipole enhancement. QE increases with coating thickness until reaching a maximum at 67% monolayer coverage, and then decreases to less than half the peak value. This behavior is expected given that excess quantities of

cesium (i.e., more than is required to reach peak QE) lead simply to photoemission from the cesium coating itself.

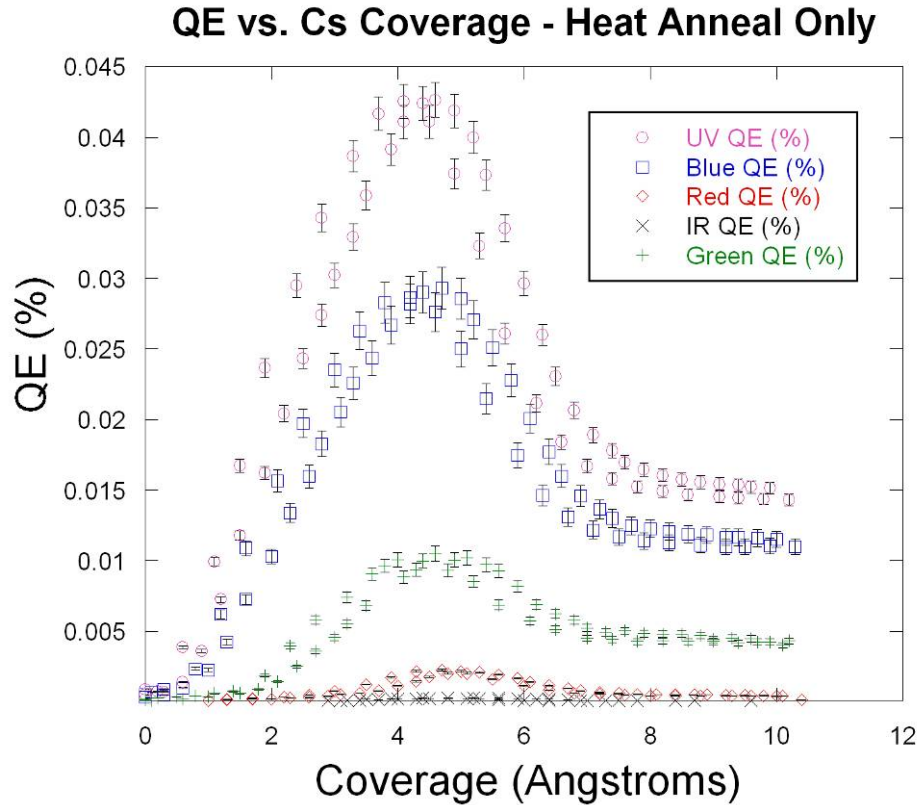


Figure 6.26: Multi- λ QE vs. Coverage for Annealed Sintered Tungsten

Normalizing each wavelength curve in Figure 6.26 to its peak value allows the small-signal IR and red data to be visible along-side other wavelengths, as shown in Figure 6.27. The fact that any photoemission is observed using the 808nm laser suggests that the work function has been lowered to at least 1.53eV. Notice also that the width of each peak broadens (to the left) with increasing photon energy: photoelectrons excited with shorter wavelengths overcome the higher work function barrier associated with less-than-optimum cesium coverage. For this reason, the UV

and blue lasers are used during dispenser cathode activation to monitor photocurrent and signal the onset of cesium delivery to the surface.

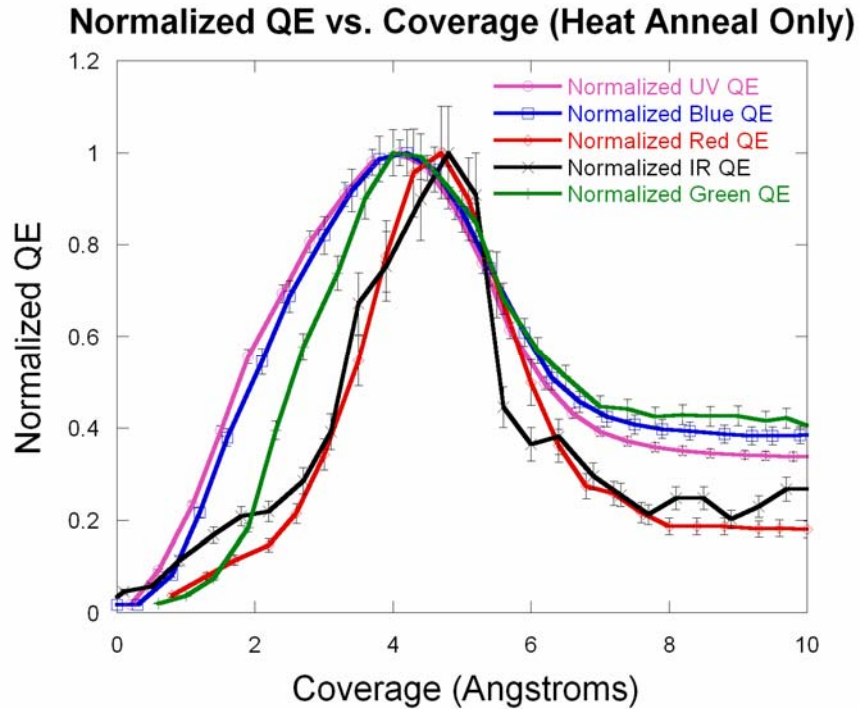


Figure 6.27: Normalized QE vs. Coverage (Heat Anneal Only)

6.4.2 Approximating Work function

The wavelength dependence of QE can be used to estimate the work function of a surface [13]. As discussed in the theory section, QE depends multiplicatively upon:

- 1.) the wavelength-dependent reflectivity $R(\lambda)$ of the photoemitting surface, 2.) the Fowler-Dubridge probability $P_{FD}(\lambda)$ that a photo-electron excited a distance x from the surface has energy greater than the vacuum barrier, and 3.) the electron scattering probability, $f_\lambda < 1$, specifying whether an electron excited a distance x from the

surface will undergo a collision that prevents emission. Using the Richardson approximation described in the previous section and the fact that field and laser intensity are negligible in this experiment, $P_{FD}(\lambda)$ can be expressed as a ratio of simplified Fowler functions $U(x)$:

$$P_{FD}(\lambda) = \frac{U\left[\beta\left(\frac{hc}{\lambda} - \phi\right)\right]}{U[\beta\mu]} \quad (6.5)$$

$$U(x) \approx \frac{1}{2}x^2 + \frac{1}{6}\pi^2 - e^{-x}C$$

where $\beta = 1/(k_B T)$, k_B is Boltzmann's constant, T is temperature, and ϕ is the energy difference between the vacuum barrier and the Fermi energy, μ . The quadratic term dominates because C is a constant known to be less than one and for room temperature $x \gg 1$, so that $QE \propto (E_\lambda - \phi)^2$ with $E_\lambda = \frac{hc}{\lambda}$. This inverse square dependence on wavelength is obvious in the data, as shown in Figure 6.28 and Figure 6.29. Recall from the previous chapter that the final form for QE is given by:

$$QE = f_\lambda (1 - R(\lambda)) \left\{ \frac{U[\beta(E_\lambda - \phi)]}{U[\beta\mu]} \right\} \quad (6.6)$$

Because f_λ is not strongly wavelength dependent, normalization of QE measurements is possible and yields:

$$\frac{QE(\lambda)}{QE_{\max}} = \frac{(1 - R(\lambda))}{(1 - R(\lambda))_{\max}} \left\{ \frac{U[\beta(E_\lambda - \phi)]}{U[\beta(E_{\max} - \phi)]} \right\} \quad (6.7)$$

with

$$\frac{U[\beta(E_\lambda - \phi)]}{U[\beta(E_{\max} - \phi)]} = \frac{3(E_\lambda - \phi)^2 + (\pi k_B T)^2}{3(E_{\max} - \phi)^2 + (\pi k_B T)^2} \quad (6.8)$$

Using this relationship, normalized experimental data can be plotted together with a set of QE vs. E_λ curves corresponding to various work functions. The resulting graph is shown in Figure 6.30 and indicates that with heat annealing, the work function of a monolayer cesium coating on sintered tungsten is approximately 1.65eV.

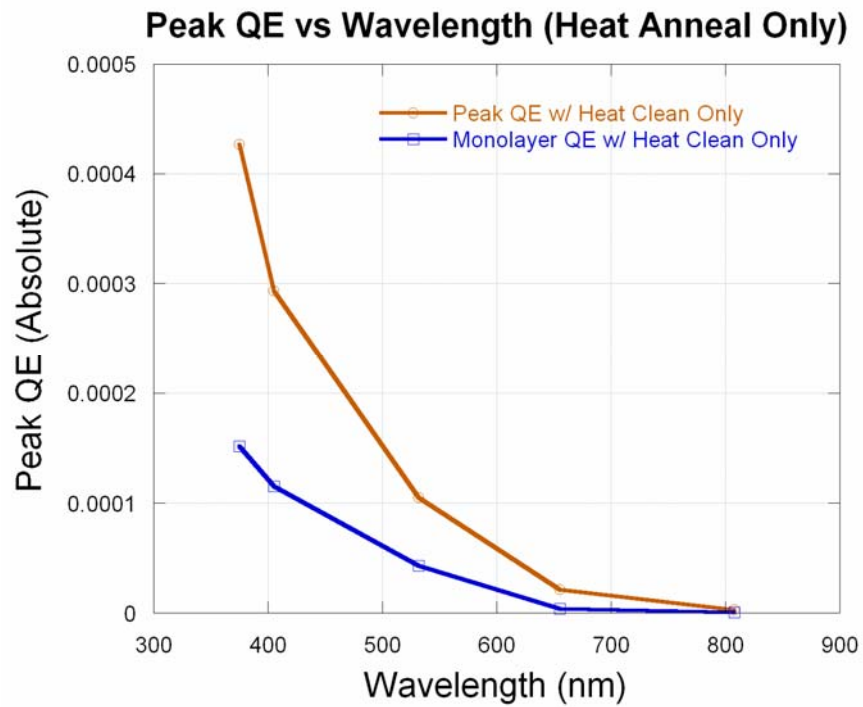


Figure 6.28: Peak QE vs. Wavelength (Heat Anneal Only)

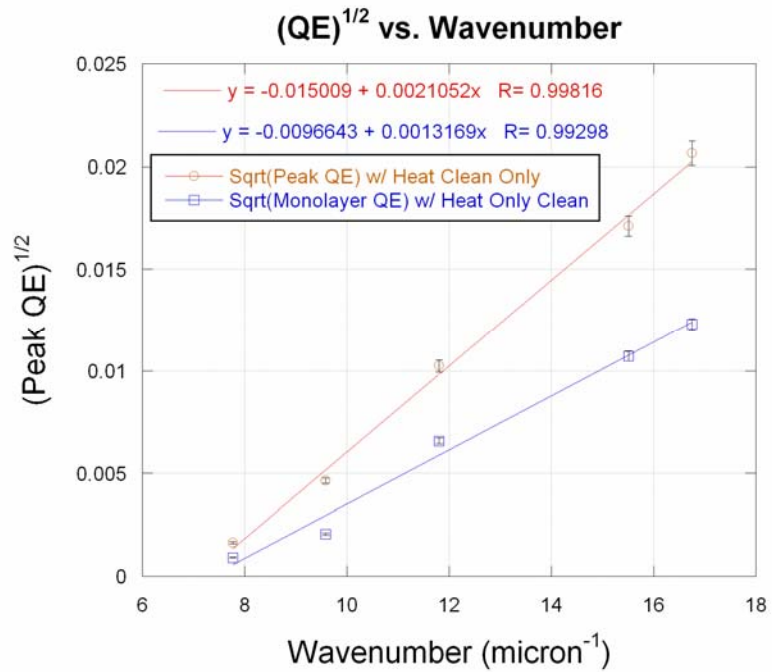


Figure 6.29: Inverse Quadratic Relationship between QE and Wavelength

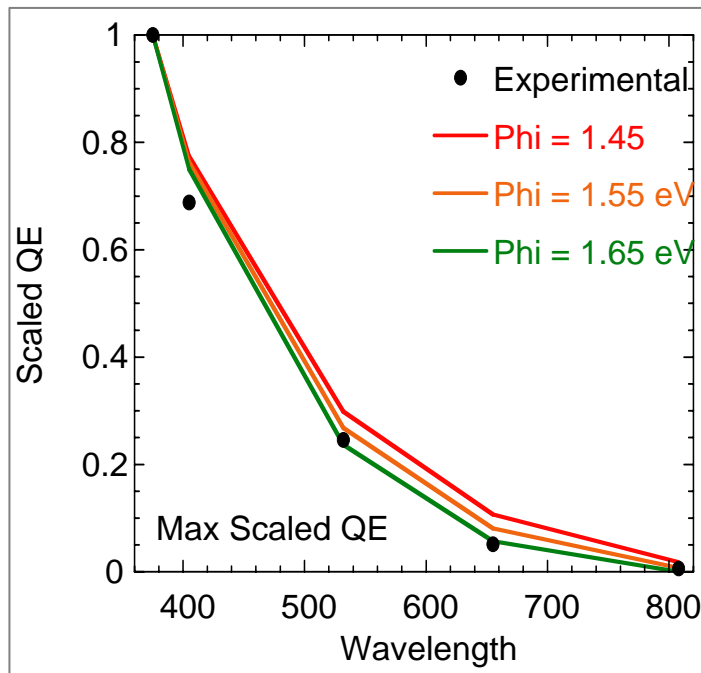


Figure 6.30: Work function of Monolayer Cs on W - Heat Anneal Only

6.4.3 Cathode Lifetime

Because cesium on tungsten has such a low QE ($<0.1\%$) in the visible, it is not considered a particularly good photocathode for present injector designs. It does, however, provide a method for reliably testing the near-room temperature dispenser cathode: delivery of cesium to (and across) the surface can be readily detected and the photosignal, together with QE vs. coverage characteristics, can provide information about surface conditions. The lifetime of most low-work function cathodes, including the dispenser concept, is limited by the loss of cesium from the surface over time. It is important, therefore, to know whether surface preparation techniques (i.e., heat anneal vs. ion beam cleaning) appreciably alter cathode lifetime. To measure this effect, a full monolayer of cesium was deposited to a heat annealed sintered tungsten substrate and the field and lasers were left on continuously as QE was measured. Figure 6.31 shows the behavior of QE over time and is indicative of cathode lifetime. The background gas composition during this measurement consisted mainly of hydrogen, as shown in Figure 6.32, which has no effect on QE. Assuming exponential decay from peak QE, and a constant vacuum environment, a $1/e$ lifetime of about 7 hours is expected. Rigorous lifetime measurement requires monitoring QE for much larger intervals than what is shown below; subsequent measurements mentioned hereafter continued for over 24 hours. Cesium desorption, and the resulting decay in QE, can be accelerated by increasing temperature. The energy E_d required for desorption to occur can be approximated using an Arrhenius fit, as shown in Figure 6.33, and is roughly 0.5eV for cesium on heat-annealed sintered tungsten.

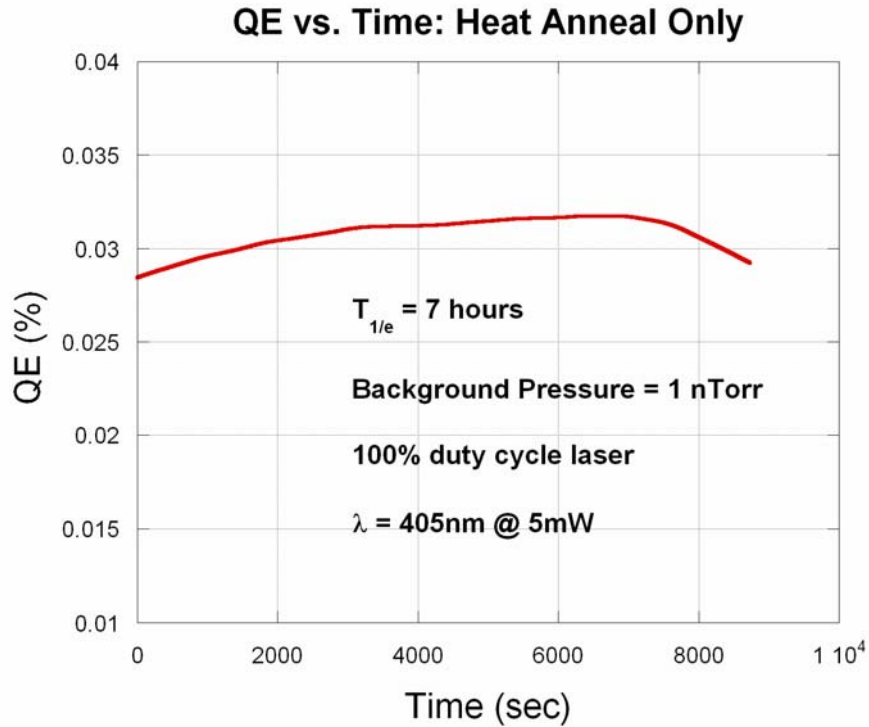


Figure 6.31: Lifetime of Cesium Sintered Tungsten - Heat Anneal Only

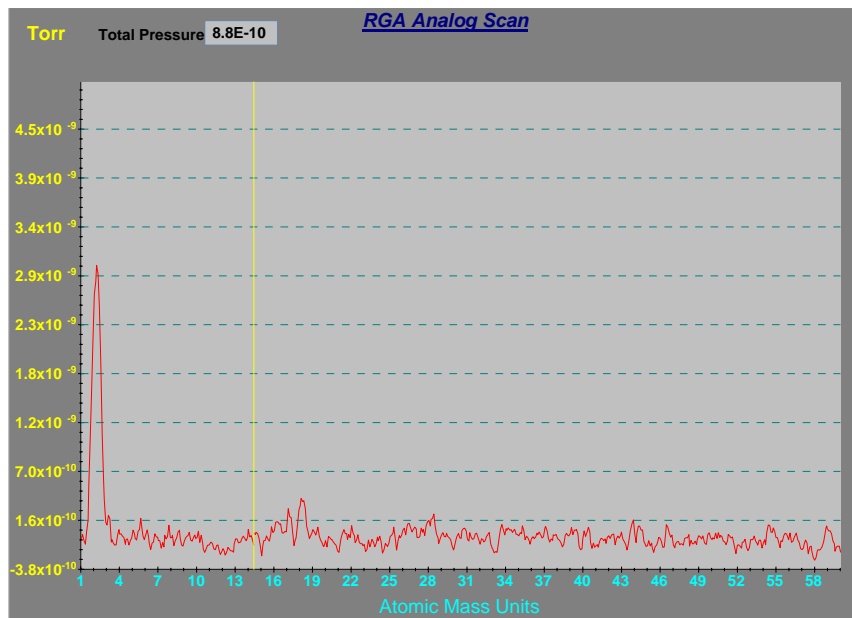


Figure 6.32: Background Gas Composition During Lifetime Measurement

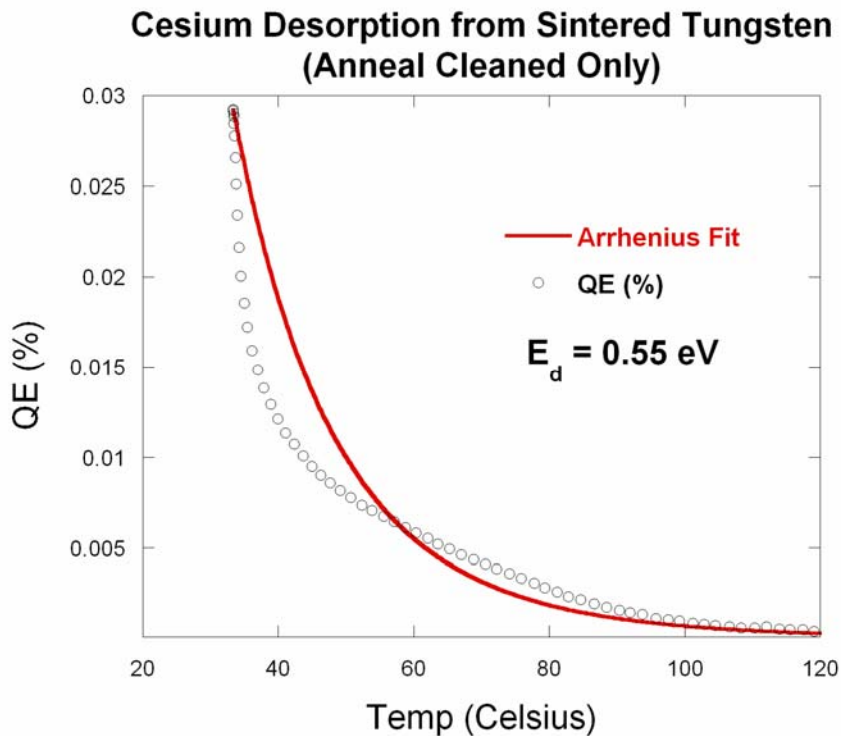


Figure 6.33: Cesium Desorption from Anneal Cleaned Sintered Tungsten

6.4.4 Surface Diffusion of Cesium

As a substrate for a dispenser photocathode, sintered tungsten provides a delivery mechanism of cesium to the surface via pores and grain boundaries. Once at the surface, however, it is necessary for cesium to diffuse 5-10 microns in order to completely cover the surface. A goal of the studies detailed in the next chapter is to determine if this is possible and at what temperature it occurs. In early studies, however, it was observed that desorption of multiple-monolayer coatings of cesium on tungsten produces a higher QE than initial deposition, as shown in Figure 6.34. This QE vs. time graph shows deposition of 2 monolayers of cesium occurring from time $0 < t < 328\text{s}$ and subsequent desorption of this coating for $t > 328\text{s}$ as

temperature is increased to 60°C. In each case, the optimal (67%) coverage is achieved giving peak QE, but the peak observed as cesium is being removed is 10% higher than the peak corresponding to initial deposition.

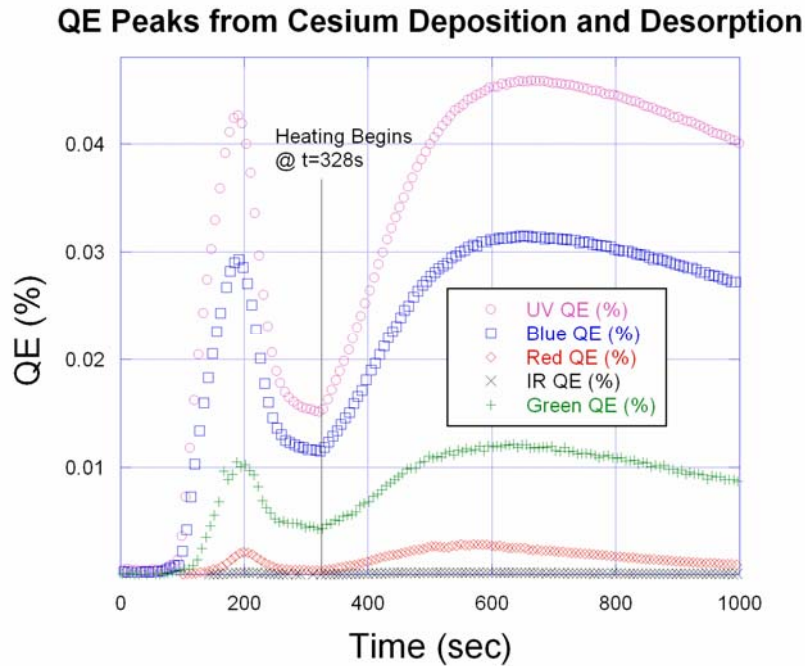


Figure 6.34: QE vs. Time for Deposition Followed By Desorption

This condition indicates that at elevated temperature and during desorption, the coating is changing such that further work function reduction is produced. This behavior is consistent with surface diffusion of cesium: higher temperatures induce cesium mobility and surface atoms assume an energetically favorable spatial distribution that also optimizes the surface dipole enhancement. While this argument is not certain, it is a promising observation in light of subsequent surface diffusion studies with the dispenser cathode.

6.5 Cs-on-Sintered Tungsten: Argon Ion Beam Treated

As will be shown, cathode performance can be significantly improved by subjecting the cathode substrate surface to an energetic ion beam prior to cesiation. The effects of this cleaning were studied for both argon and hydrogen ions, and a standardized cleaning technique was designated and preserved among all trials. Three parameters can be used to control the ion beam's characteristics: accelerating voltage, plasma current, and gas flow. The first two are controlled via the gun's power supply and target values set for each determine which will be the limiting factor in output beam current. Target values of plasma voltage and current were set to 7.5kV and 1.5mA, respectively. The gas flow was selected by opening the attached fine metering valve three complete turns. Thermal equilibrium was reached, as signified by constant beam current, in less than 5 minutes and final adjustment of gas flow was made such that beam current was optimized. These settings resulted in 15 μ A and 40 μ A of beam current impinging upon the cathode for the case of argon and hydrogen, respectively. Each cleaning session referred to in this work lasted 45 minutes, resulting in an ion dose of about 40mC for the case of argon and 100mC for hydrogen. The background pressure during this period was below 1×10^{-4} Torr and its composition was mostly argon, with trace amounts of neon (presumably in the original cylinder mixture). Macroscopically, an effect of the cleaning could be detected on the front face of the anode: the partial area intercepting the ion beam was shinier than the rest of the surrounding surface. Quantitative effects of the cleaning are described below.

6.5.1 QE vs. Coverage

Of the two ion species, argon was tested first and resulted in a two-fold increase in QE (over heat anneal treatment), as shown in Figure 6.35. The cesiation process began when the pressure was below 3×10^{-8} Torr, maintained solely by ion pumping. This higher pressure was permitted during cesiation because the background gas was inert (argon) and did not interfere with cathode fabrication. The goal was to minimize the time between cleaning and cesiation, typically about 10-15 minutes, to preserve substrate cleanliness. To this end, the cesium sources were thoroughly outgassed prior to deposition onto ion-beam cleaned samples. After each cesiation and QE measurement, the cathode surface was ion beam cleaned again, using the parameters outlined above. It is apparent from Figure 6.35 that the substrate surface was substantially altered after ion beam cleaning: the QE vs. coverage curves not only achieve higher values, but become narrower for all wavelengths. This is consistent with the removal of contaminants from the surface: pre-adsorbed contaminants can actually lower the work function of sparsely cesiated metal, but not nearly to the extent shown by 67% cesium coverage. A substrate whose work function is pre-lowered a small amount by contaminants will require less cesium coverage to begin emitting photocurrent at higher photon energies, but will not achieve the maximum QE of a cesiated bare metal. This is the exact behavior shown in the graph: the coverage range over which emission occurs is narrowed after ion beam treatment because the work function reduction is due solely to the presence of cesium, not cesiated contaminants. Notice that the broadening is greatest for UV and

blue wavelengths, again consistent with a slight reduction in high-work function contaminated areas (as they will only photoemit at shorter wavelengths).

Figure 6.36 compares the results of consecutive ion beam cleanings: the QE vs. coverage behavior is nearly identical. These two trials were performed on different days and with different initial surface conditions: the sample was exposed to atmosphere prior to the second ion beam treatment. It is significant that QE remains constant from one cleaning to the next. An increase would indicate that either: 1.) a single cleaning is only partially effective because additional cleaning removes more contaminants; or 2.) cesium from previous coatings is not cleaned off and is building up on the surface. The fact that subsequent cleanings do not improve QE suggests that a single cleaning of 45 minutes is sufficient to achieve atomic cleanliness. Because QE does not *decrease* with consecutive cleanings, the assumption can be made that the substrate surface is not being damaged or appreciably altered.

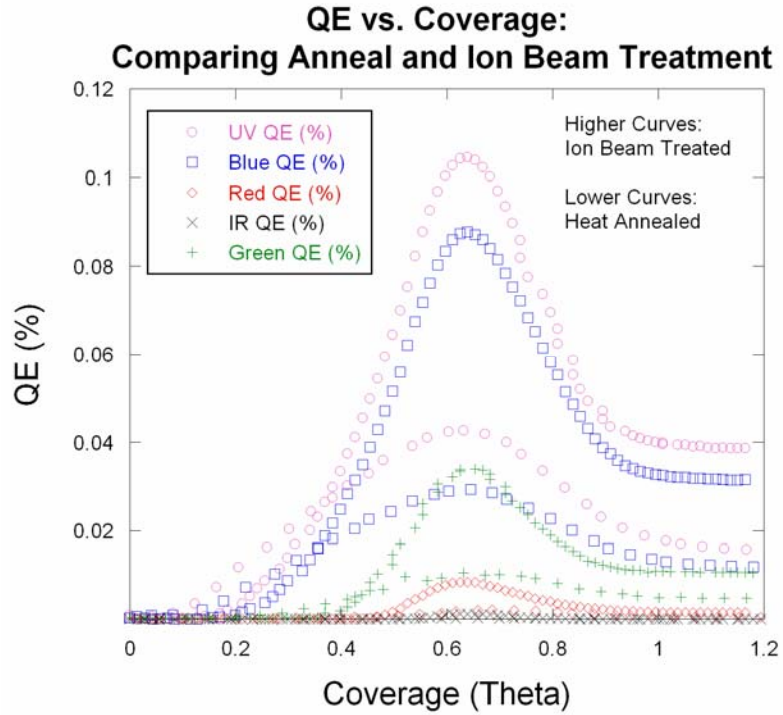


Figure 6.35: Heat Anneal vs. Ion Beam Treatment Using QE Measurements

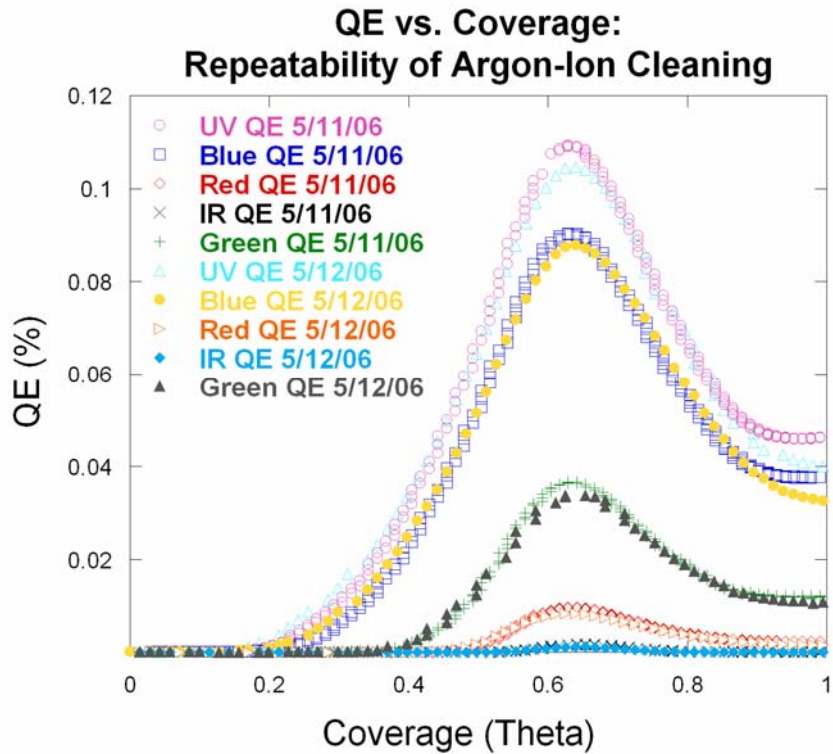


Figure 6.36: Repeatability of Argon Ion Cleaning Process

6.5.2 Approximating Work function

The effect of ion beam cleaning on sub-monolayer work function can be ascertained by the estimation technique outlined in the previous sub-section. Figure 6.37 shows that there is a noticeable barrier reduction of about 0.1eV for peak (67% monolayer) cesium coverage. The fact that work function reduction is not dramatic is consistent with the hypothesis that the two-fold increase in QE is due more to increased emission area than decreased work function. Patches of the cathode that were not emitting at all are able to do so after ion beam treatment, causing a dramatic increase in QE. It is expected, however, that some reduction in work function would be detected because the patchy, non-emitting regions likely hinder the cesium surface dipole enhancement factor of neighboring regions that do photoemit.

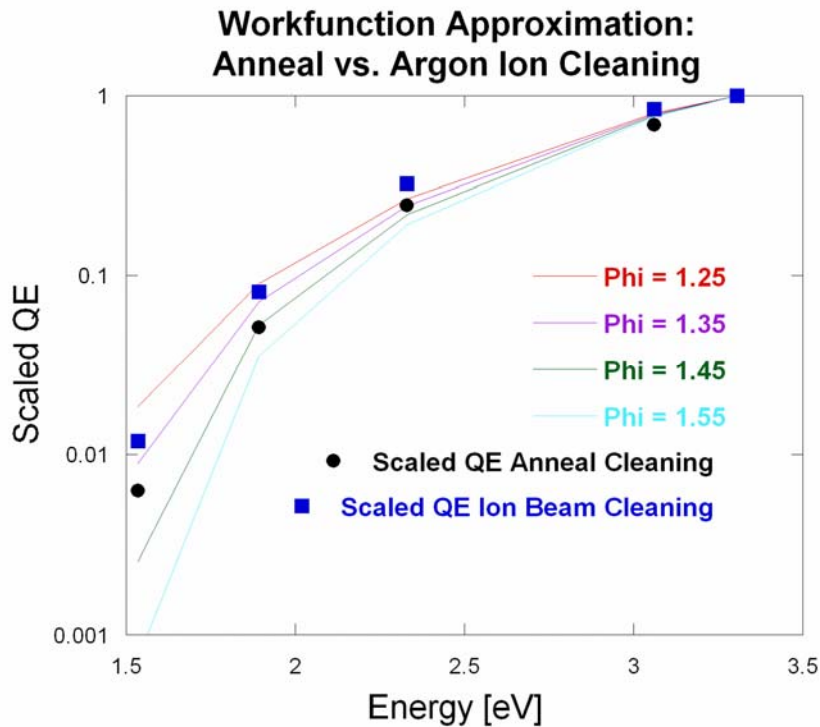


Figure 6.37: Effect of Annealed vs. Ion Beam Treatment on Work function

6.5.3 Cathode Lifetime

Because the desorption rate of cesium depends strongly on substrate composition, it is expected that surface cleaning should have some effect on cathode lifetime. Lifetime is limited by three factors which all conspire to damage the cesium surface layer: ion back-bombardment, vacuum contamination, and natural (room-temperature) desorption. Ion back-bombardment occurs when emitted electrons positively ionize residual gas atoms that accelerate back toward the cathode, damaging the cesium surface layer upon collision. This mechanism, along with contamination, depends strongly on background gas pressure and composition, both of which were tightly controlled for heat annealed and ion beam cleaned cesiated tungsten. Figure 6.38 shows QE vs. time for a cesiated sintered tungsten cathode subjected to a single ion beam treatment of sintered tungsten prior to cesiation: the $1/e$ lifetime was an astounding 9.8 days. This is over 30 times longer than the lifetime of a heat annealed cathode, and includes continuous exposure to the accelerating field and drive lasers for 100 hours. Consider the two-fold increase in QE that is observed with argon ion treatment: if the dominant degradation mechanism were ion back bombardment, the increased QE and electron flux should reduce cathode lifetime since the rate of bombardment degradation increases with emission current. Because cleaning the surface prior to cesiation has a dramatically *opposite* effect, it is reasonable to assume that back bombardment does not play a crucial role in the degradation of cesium-on-tungsten photocathodes operated in the 1×10^{-8} Torr regime. This is especially true because the background chamber pressure during QE measurement of argon-ion cleaned cathodes was higher by an order of magnitude

than during measurement of heat annealed cathodes. A similar argument applies to environmental contamination: if it were a dominant factor, then the increased background pressure for the case of argon-ion cleaned substrates should lead to shorter, not longer, cathode lifetime.

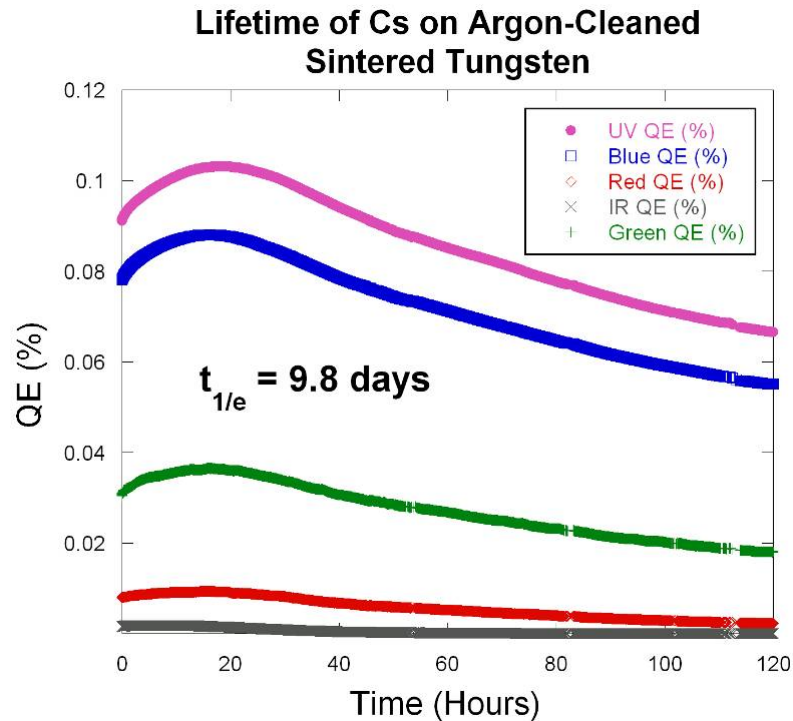


Figure 6.38: Cathode Lifetime for Ar-Ion Cleaned Sintered Substrate

Cesium bonds strongest to metallic substrates because these tend to maximize the electric dipoles which form on the surface and enable its adherence [96]. Thus, a plausible conclusion concerning increased lifetime after ion-beam cleaning is that cesium can better adhere to the substrate because non-metallic contaminants which undermine its dipole attraction are removed. Non-metallic contaminants also have higher work function (i.e. $> 5.5 - 9.9$ eV) and likely constitute the islands of non-emitting surface area that were postulated in the previous section. If these areas are

removed, then cesium can adhere better to the surface and lifetime is extended. The important result is that argon ion cleaning appears to offer comprehensive benefits in terms of work function reduction, increased QE, and lengthened cathode lifetime.

6.5.4 Surface Diffusion of Cesium

Recall from Figure 6.34 that the peak QE during cesium deposition for an annealed sintered substrate is less than its peak QE during desorption. The increase in QE was hypothesized to be the result of cesium mobility: a more optimal arrangement of atoms on the surface is achieved if they have a chance to move. Figure 6.39 shows that for the case of argon-ion beam cleaned cesiated tungsten, the QE peaks for both deposition and desorption are exactly the same.

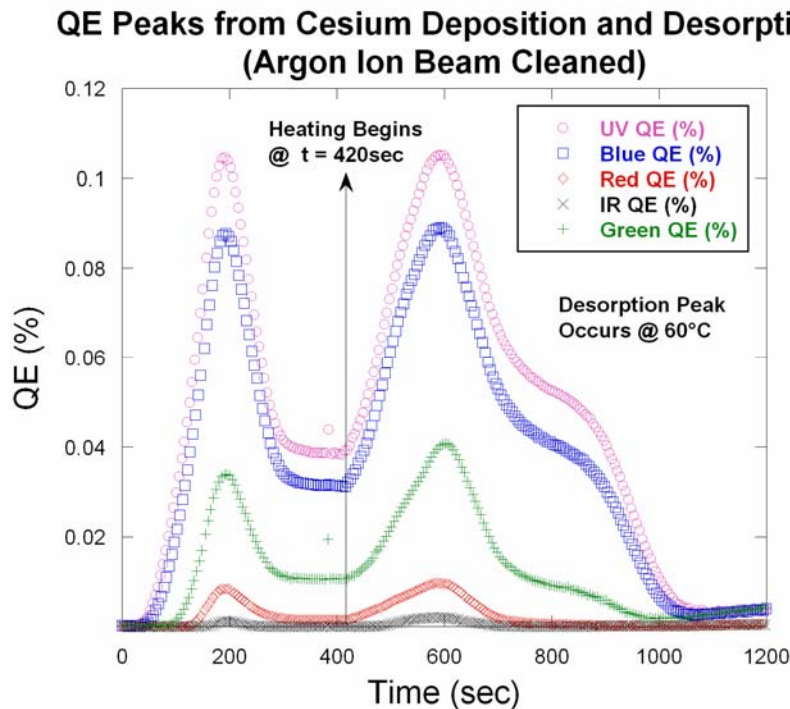


Figure 6.39: QE Peaks from Cesium Deposition and Desorption

Dispenser cathode studies, detailed in the next chapter, decidedly prove that surface diffusion of cesium does indeed occur at the temperatures encountered in a desorption trial ($<160^{\circ}\text{C}$). So given that cesium atoms are mobile at these temperatures, the fact that QE does not increase upon heating can only be due to the fact that the optimal arrangement of cesium on the surface was assumed during the original deposition. If this were not the case, cesium could diffuse across the surface and optimize spatial arrangement, resulting in an increased QE. The unchanging QE peak for deposition and desorption is consistent, therefore, with the assumption that contaminants are removed from the cathode surface during ion beam treatment of the substrate. Consider an irregular and perhaps jagged surface containing random patches of high work function contaminants: it is unlikely that cesium deposition onto such an irregular base would produce an optimal coating. If the coating were heated and allowed to diffuse, cesium atoms would diffuse to locations that maximize their bond strength, i.e. lower work function metallic patches of the substrate. These are the same patches where emission occurs, so increased cesium in these regions could explain the higher peak QE seen during desorption. It has already been shown that argon ion cleaning removes surface contaminants, so it is not surprising that removal of these contaminants would help optimize the initial cesium coating.

6.6 Cesium-on-Tungsten: Theory vs. Experiment

The next two sub-sections evaluate the performance of the theory outlined in chapter five. In anticipation of dispenser cathode studies, the emphasis is on predicting quantum efficiency given the material parameters of the cathode, its coating(s), temperature, and drive laser wavelength. A theoretical model is needed in order to interpret and optimize the performance of the dispenser cathode and the comparisons presented in this chapter serve to validate such a model.

6.6.1 Predicted vs. Measured QE

Figure 6.40 compares theory prediction (solid lines) to measured QE (discrete points) as a function of cesium coverage. The overall agreement is remarkable, given that the effect of the cesium coating on work function and electron emission is evaluated using only a hard sphere model. A sintered substrate (with grains, boundaries, defects, and pores) introduces myriad complexity, so it is expected that a theory using an averaged surface will exhibit some discrepancy. Indeed, the fact that the data is within a factor of 2 or 3 of theory is encouraging, in light of the surface artifacts and irregularities shown in previous micrographs. It is useful, however, to evaluate the discrepancies and their consistency with effects caused by the known complexity of the substrate. While the log scale in Figure 6.40 helps to evaluate overall trends, the linear scale in Figure 6.41 affords a better picture of absolute agreement and experimental uncertainty.

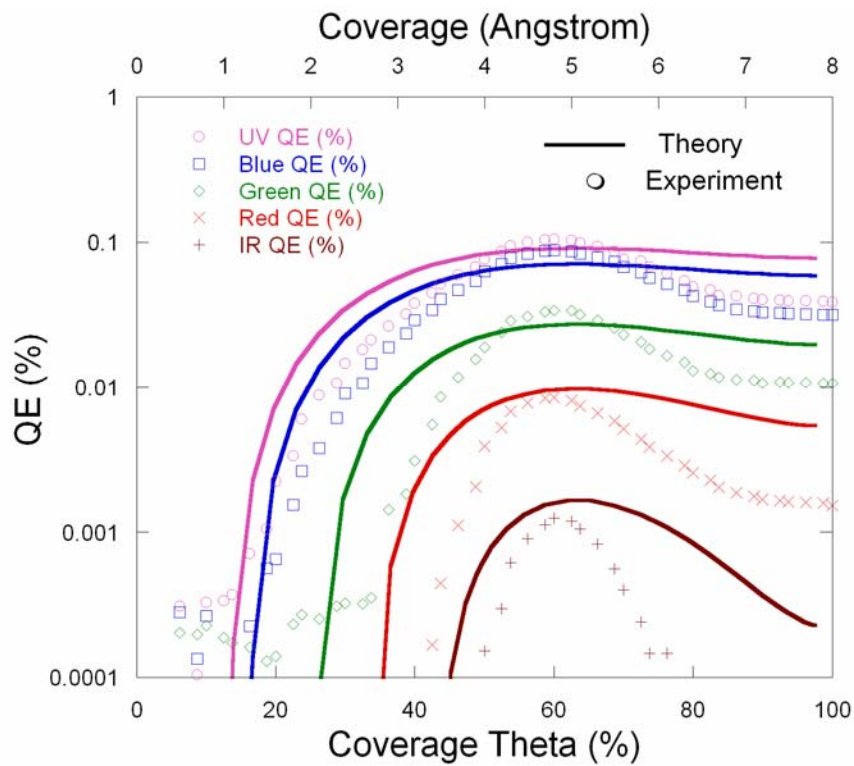


Figure 6.40: QE vs. Coverage - Comparison of Theory to Experiment

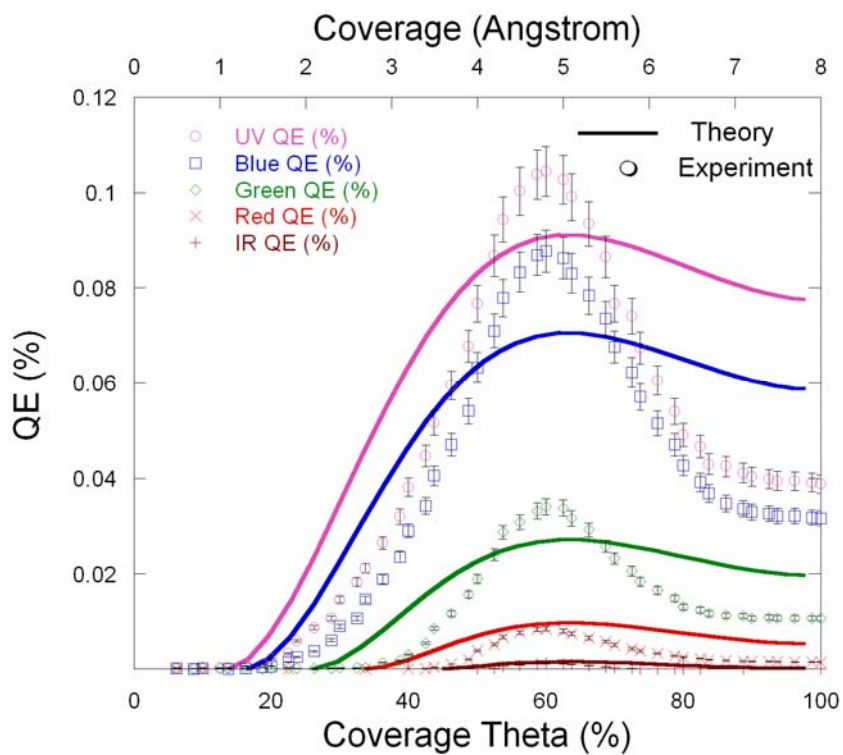


Figure 6.41: QE vs. Coverage - Linear Comparison with Exp Uncertainty

The agreement to the left of the peak is especially good from the perspective that predicted and measured emission begins at about 20% monolayer coverage. This suggests that for very sparse cesium coverage, the effect of the dipole moment on substrate work function approximately follows the hard-sphere model interaction. As coverage increases from 20 to 50%, however, the model predicts for all wavelengths a QE higher than what is observed. This means that the actual dipole enhancement for this coverage range is less than what could be achieved with an ordered arrangement of cesium atoms on single crystal tungsten. Here it is important to remember two things: 1.) cesium packing density depends upon exposed crystal face, and 2.) all crystal faces are randomly present in the polycrystalline distribution of the actual sintered tungsten surface. A detailed treatment of fractional monolayer formation on patchy surfaces has been developed, but is highly parametric and beyond the scope of this program [104]. Furthermore, for the thicker cesium coatings and higher photon energies of interest in dispenser cathode studies, the effects of discrete patches have been shown to be washed out, leaving only a macroscopic average [85]. This average includes the effect of cesium packing density, reflectivity, and single-crystal work function. A plausible explanation for the theory's over-prediction of QE for less-than-peak coverage is that upon increased deposition (i.e. $\geq 20\%$), cesium may not assume a sparsely even distribution but rather aggregates into clumps. If this occurs, as has been observed with alloy substrates [105], then the distribution of cesium over the majority of the surface is actually less than what the theory presumes (leading to higher predicted QE). As more cesium is added, however, the clumping effect

becomes less pronounced and the theory again approximates the surface conditions correctly.

Near the peak QE, the measured efficiency exceeds that predicted for UV, blue, and green, but is less than predicted for red and IR. The differences between predicted and measured peak QE at each of the wavelengths mentioned above are: 15.4%, 23.7%, 27.0%, 16.5%, and 31.7%. As before, there are a host of possibilities that could lead to these discrepancies. One possibility is variation in the number of adsorbate atoms per unit substrate cell. While the value of unity is frequently quoted [30],[27], there is reason to assume it can and does change depending upon specific surface conditions. Studies are underway to better assess the adsorption and diffusion of cesium on controlled surface [106].

This discussion is not definitive, but rather suggests several mechanisms relating to surface complexity that could contribute to the 20-30% discrepancy seen between theory and experiment. It is worth repeating that such qualitative and quantitative agreement is extraordinary given the challenges of modeling a polycrystalline surface containing microscopic features such as grains and pores. The theory is applied later in this chapter to another, different photocathode, and collective performance suggests that it is capable of fulfilling its two stated goals: 1.) predicting performance of existing and future photocathode designs; and 2.) modeling the distribution of electron emission which can be passed along to existing beam simulation codes.

6.6.2 Crystallographic Complications

Because many material parameters depend upon crystal face, the distribution of those represented on the surface substrate is significant. If several faces can be distinguished and occur with equal frequency, for example, then perhaps a realistic average of the surface would include equal contributions from each. Figure 6.42 shows a contrast-enhanced FIB image of sintered tungsten that allows some discernment of the individual crystals. Four specific contrast levels can be distinguished, each presumably corresponding to a different exposed face. Counting the occurrence of various patches of intensity over a $70 \times 100 \mu\text{m}$ region shows severe non-uniformity, as indicated by the histogram in Figure 6.43. Although grain sizes are quite different, one particular crystal orientation is certainly favored and its values for reflectivity, work function, penetration depth, etc., are likely what dominate the average surface characteristics. A separate study is in progress [107] to determine the effects of macroscopic non-uniformities in the crystallographic orientation of cathode substrate materials.

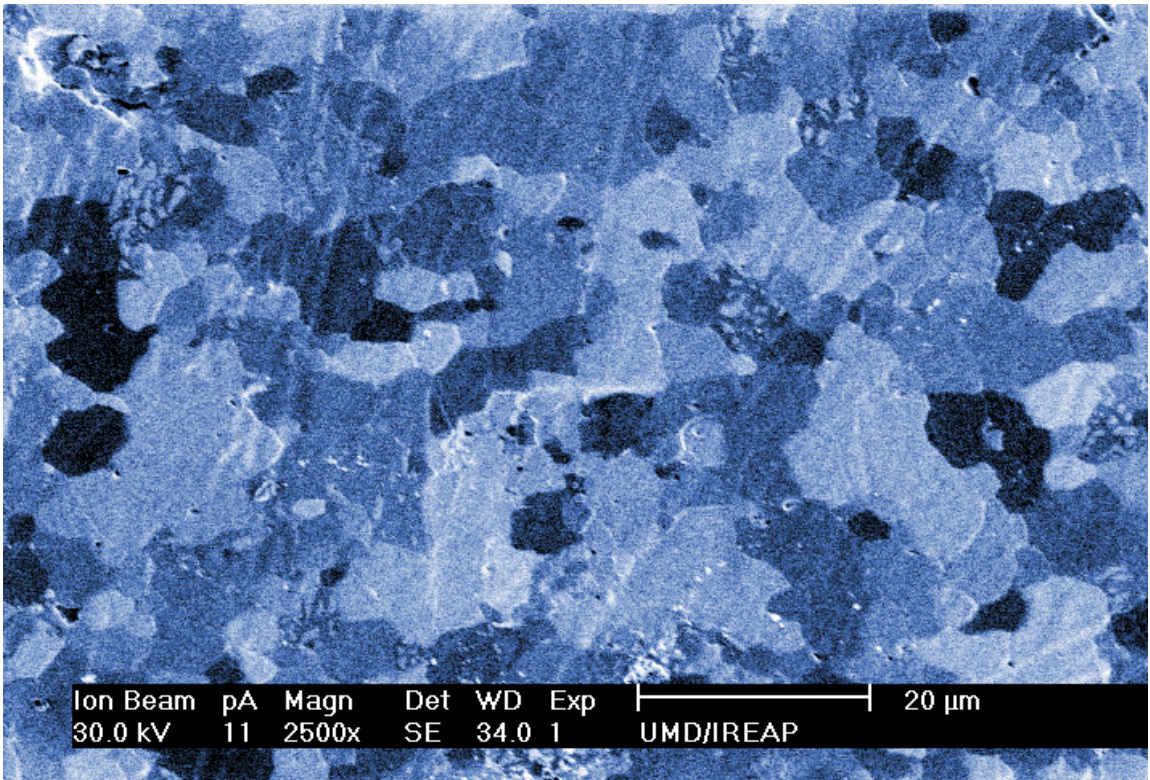


Figure 6.42: Distinguishing Crystal Faces with FIB Image

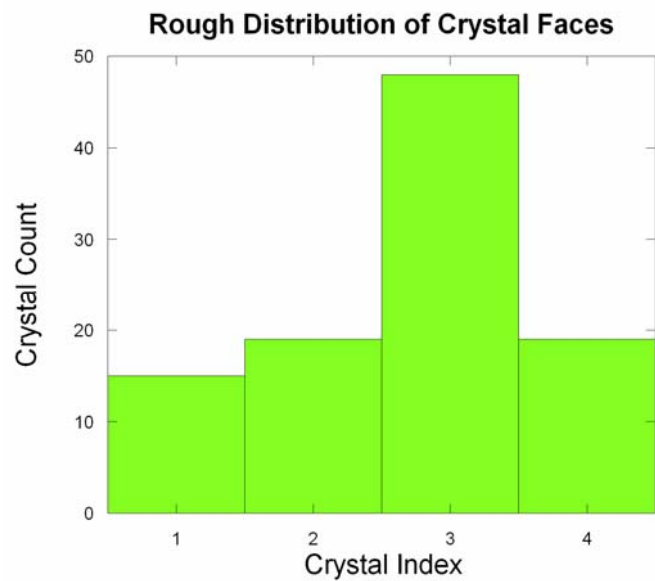


Figure 6.43: Approx. Distribution of Crystal Faces on Sintered Tungsten

6.7 Cesium-on-Silver Photocathode

The previous sub-section demonstrated good agreement between theory and experiment for atomically clean cesiated tungsten. Because the theory is intended to be broadly applicable to various photoemitting surfaces and operating regimes, it is useful to fabricate, model, and measure the behavior of *different* cathodes in an effort to validate the model. The qualitative and quantitative agreement shown in the previous section is noteworthy because it validates the theory for a given cathode composition and an important operating regime. A different photocathode, cesium-on-silver (Cs:Ag), was fabricated by external deposition of cesium onto a polished, annealed silver substrate.

6.7.1 Theory Validation: QE vs. Coverage

With a work function of $\phi_0 = 4.26$ eV, silver was unable to photoemit on its own, but cesiation caused a dramatic decrease in work function ($\phi_{\min} = 1.65$ eV) for the same reasons as outlined for the case of tungsten [19]. Theoretical predictions of QE vs. cesium coverage at various wavelengths were made and then compared to measurement, as shown in Figure 6.44. Note that qualitative agreement is excellent for cesium coverage higher than 40% and the quantitative difference is less than 20%. This sample was tested prior to the installation of the aforementioned ion gun, so its preparatory cleaning included only heat annealing at 650°C. Temperature is reduced because when heated near its melting point (962°C) it began evaporating and coated the chamber's quartz viewports. Because this coating reduced laser power incident on the cathode by an unknown amount, the windows were removed and rehabilitated and

the substrate temperature was henceforth kept below 700°C. The lowered anneal temperature reduced the effectiveness of the cleaning, allowing cesium from previous measurement trials to remain on the surface. This residual coating is likely responsible for the theory-experiment discrepancy at low coverage values: the theory assumes that cesium coverage is zero prior to deposition. Since this is not the case, photoemission begins at a measured coverage less than what theory predicts. Figure 6.45 is an optical micrograph at 500x magnification of the silver cathode substrate revealing tooling marks caused by the polishing process. The topology of the surface, as measured via profilometry, is shown in Figure 6.46. The width of the lines as measured via profilometry are longer than what is visible via the micrograph ($\sim 1\mu\text{m}$) because the diamond-tipped needle was scanned nearly parallel (within 10-15°) to the lines. These illustrations show that the surface is not smooth, certainly introducing some departure from either uniform cesium coverage or optimal dipole formation. Because the theory does not account for either of these effects, the agreement achieved is even more striking. The only differences between theory predictions for cesiated tungsten and cesiated silver were the material parameters of the adsorbate and the substrate (including atomic dimensions, packing density, work function, reflectivity, conductivity, scattering rate, etc.). The agreement achieved simply by changing appropriate constants in response to changes in cathode composition is noteworthy. Together with the results for cesiated tungsten, it signifies that further revision of the theory could potentially be used to optimally select cathode components for further study. Given the large parameter space associated with fabricating and measuring multi-alkali photocathodes, such predictions would be very

valuable in terms of experimental productivity and would represent a distinct departure from the historical progression of photocathode research [22].

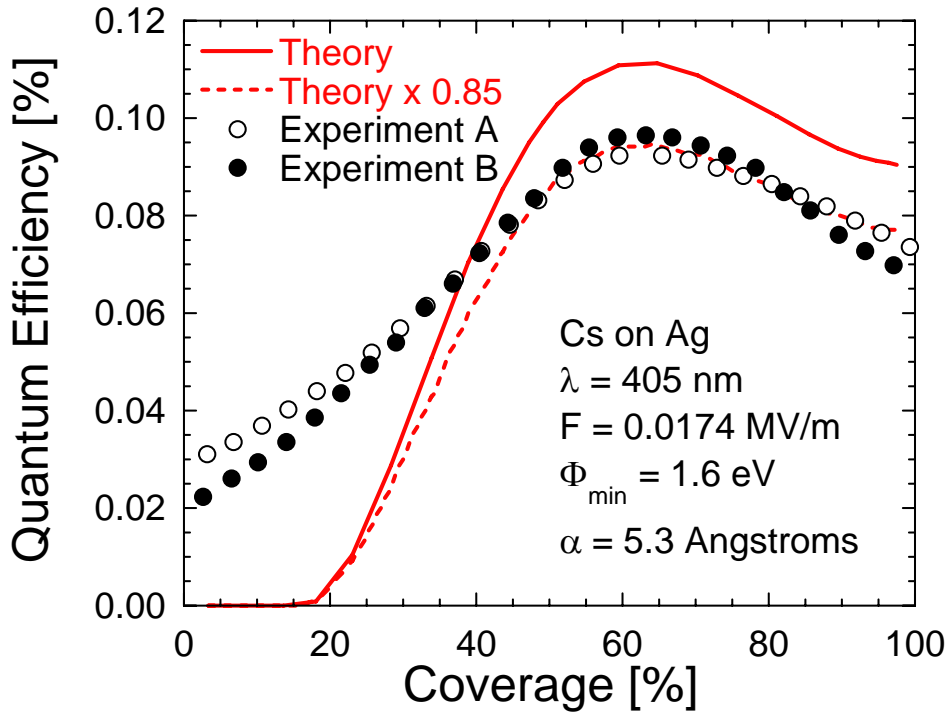


Figure 6.44: Cesium-on-Silver Photocathode: Theory vs. Experiment

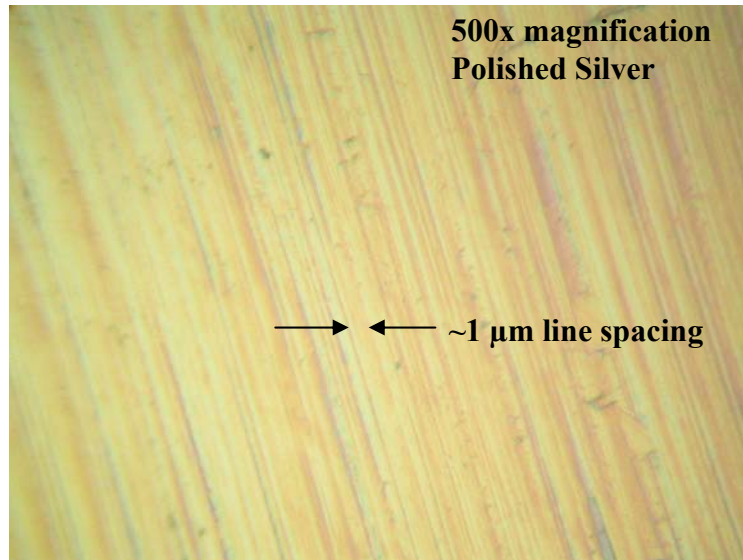


Figure 6.45: Optical Micrograph Showing Roughness of Silver Substrate

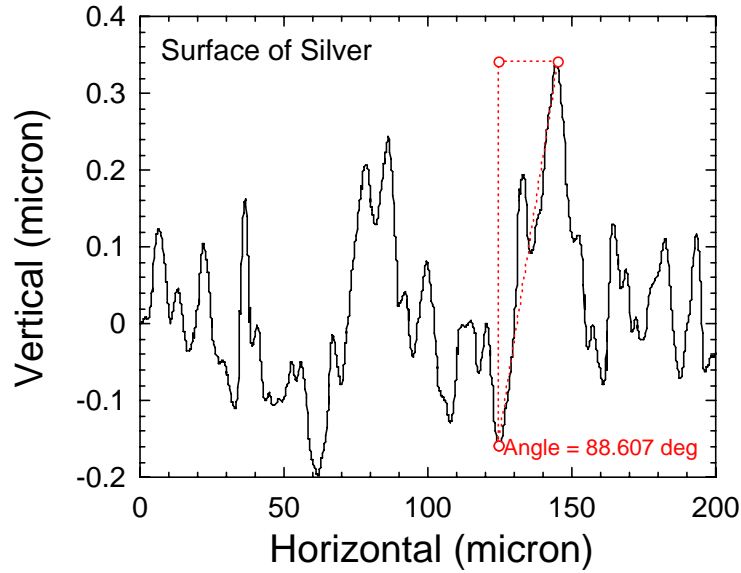


Figure 6.46: Surface Profilometry of Polished Silver Substrate

Compared to a similarly prepared cesiated tungsten photocathode (i.e. heat anneal only), cesiated silver has a rather high peak QE of 0.10% at 405nm. This can be attributed to the fact that silver is the most conductive of all elements, with a resistivity of only $1.6 \text{ m}\Omega\cdot\text{cm}$, compared to tungsten's value of $5 \text{ m}\Omega\cdot\text{cm}$. Resistivity is an important factor for photoemission because it dictates the scattering rate for electrons. Because silver is a better conductor than tungsten, electron scattering occurs less and a greater population of photoexcited electrons can travel to the vacuum boundary without undergoing an emission-terminating collision event. For metals, the dominant scattering mechanism for electrons is collision with other electrons, since the volume number density of carriers is so high ($\sim 5 \times 10^{22} \text{ cm}^{-3}$). Given the large difference in resistivity between tungsten and silver, one might expect an even higher QE upon cesiation of the latter. While photoexcited electrons have a greater escape probability in silver, less are created at a given laser intensity because

reflectivity is 97% and the majority of incoming photons are simply not absorbed. This high value is contrasted by the relatively low reflectivity of tungsten, at 62%. In the case of tungsten substrates, photons are more readily absorbed and create photoexcited electrons, but the high rate of electron-electron scattering limits most of these from escaping the bulk metal.

6.7.2 Cathode Lifetime

Figure 6.47 shows the QE vs. time behavior of a cesiated silver photocathode: its $1/e$ lifetime is roughly 7 days. This is rather extraordinary, considering the limited cleaning procedure applied to the substrate, and suggests that cesium bonds strongly to silver. This hypothesis is substantiated by the fact that high QE is sustained and even enhanced at elevated temperature, as shown in Figure 6.48. Cesium adheres more strongly to silver than tungsten, as evidenced by the fact that a temperature of over 450°C is required to completely eliminate photoemission, compared to only 160°C for annealed tungsten. Notice that QE begins to initially decrease with temperature but then increases to reach a second peak at about 200°C. This is consistent with and suggests that cesium has a very high desorption energy when deposited on silver (or perhaps tarnished silver). Not until 200°C does it begin to diffuse across the surface and achieve a more optimal surface coverage, producing an even higher QE. Then QE decreases monotonically, but still remains significantly high (i.e. greater than that of cesiated tungsten) at temperatures up to 200°C.

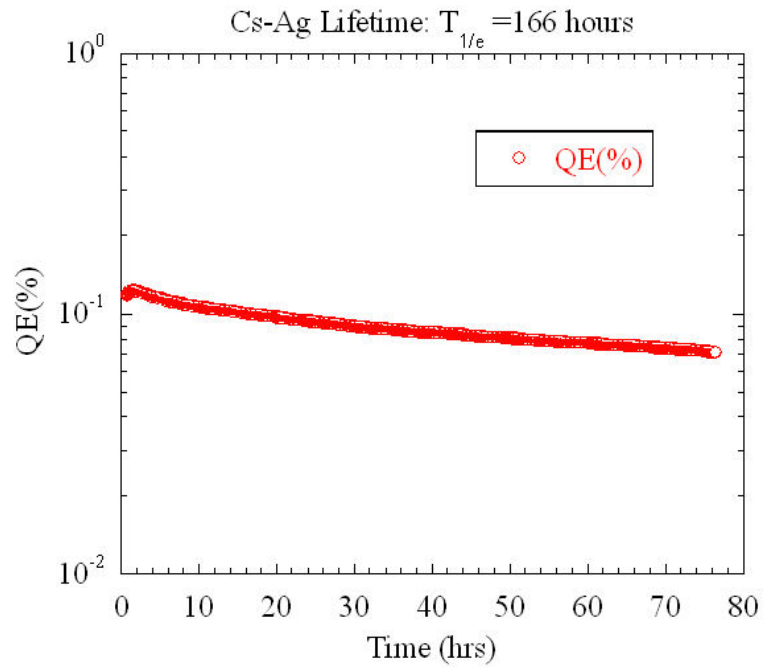


Figure 6.47: Cesium-on-Silver Lifetime

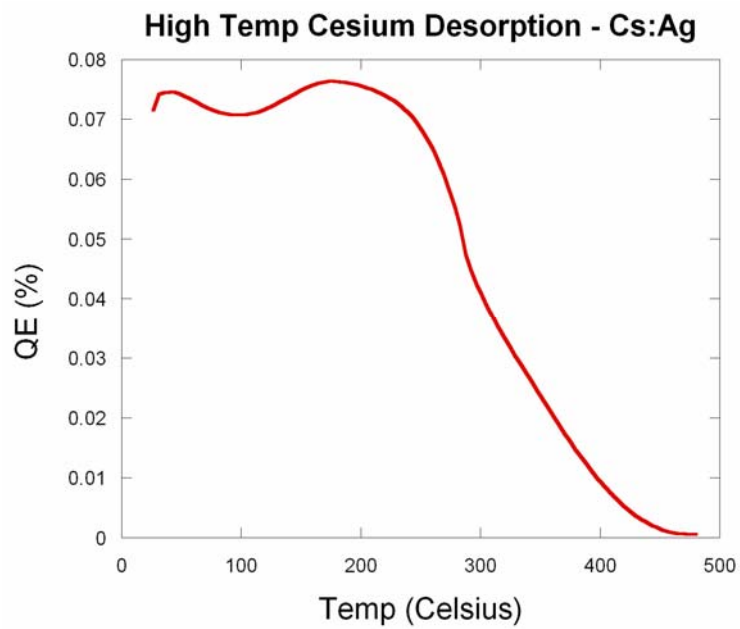


Figure 6.48: Cesium Desorption from Silver at Elevated Temperature

Silver is not very chemically reactive, as evidenced by the fact that it does not react with water or oxygen at room temperature to form an oxide. The typical surface reactant is sulfur, present in atmosphere as hydrogen sulfide, which produces the familiar black tarnish commonly seen on silver tableware. This coating remains on the surface at 600°C, increases the bare metal work function from 4.26 eV to 4.33 eV, and hinders optimal cesium dipole enhancement at the surface [108].

6.8 Discussion of Ion Beam Cleaning

Given the significant effects of argon beam ion treatment on cathode performance, it is useful to draw several conclusions regarding the technique and the cathode surface it produces prior to concluding this chapter.

6.8.1 Summary of Surface Characteristics

Table 18 lists various surface and cathode characteristics for anneal heating and argon ion beam cleaned sintered tungsten substrates. The collective observations concerning ion beam cleaning itself can be summarized as follows:

- 1) Ion beam cleaning produces two-fold increase in peak and monolayer QE
- 2) QE vs. coverage curves become narrower after ion beam cleaning
- 3) Consecutive ion beam cleanings do not further improve QE
- 4) Sintered substrate can be exposed to atmosphere and then optimally cleaned (full QE restored) in one ion beam treatment.
- 5) Work function of cesium monolayer is reduced by 0.1-0.2eV
- 6) Cathode lifetime is extended despite worse background pressure

- 7) Experimentally measured QE is \geq theoretical predictions after ion beam cleaning

This set of observations appear to be self-consistent and for the specific case of cesiated sintered tungsten cathodes, lead to important conclusions concerning surface conditions, effectiveness of ion beam treatment, and the method by which degradation inevitably occurs. Figure 6.49 shows the relationships between the observed effects of ion beam cleaning and the conclusions proposed in this chapter to account for those effects.

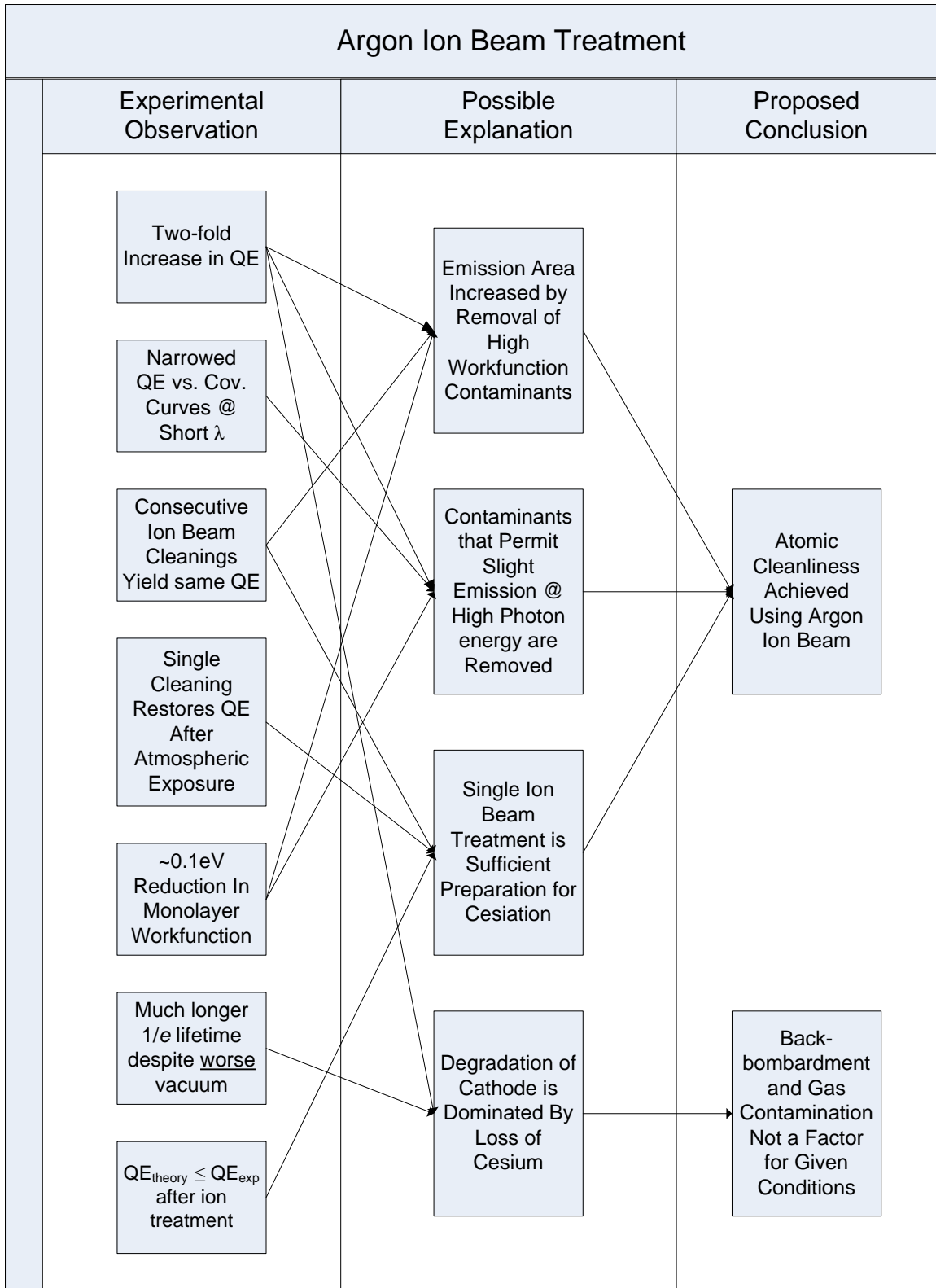


Figure 6.49: Plausible Conclusions from Ion Beam Treatment Data

Parameter	Anneal Heating Only	Ion Beam Treatment Only
Peak QE @ 375nm	4.27×10^{-4}	1.05×10^{-3}
Peak QE @ 655nm	2.19×10^{-5}	8.47×10^{-5}
Monolayer QE @ 375nm	1.56×10^{-4}	3.87×10^{-4}
Monolayer QE @ 655nm (%)	4.87×10^{-6}	1.52×10^{-5}
Approx. work function ϕ	1.65 eV	1.45 eV
1/e lifetime of cathode	7 hours	235.4 hours
1/e desorption temperature	41.1°C	80.5°C
QE vs. Coverage FWHM (UV)	$\Delta\theta_{\text{FWHM}} = 38.3\%$	$\Delta\theta_{\text{FWHM}} = 60.7\%$
Energy of Desorption	0.5 eV	0.55 eV

Table 18: Surface Characteristics of Annealed and Ion Beam Cleaned Substrates

6.8.2 Surface Morphology

It is obvious from the characteristics highlighted in Table 18 that dramatic changes are taking place on the surface. A concern had been that ion beam treatment could damage the sintered surface such that either QE or its ability to deliver and distribute cesium would permanently suffer. Over a period of 16 identical argon ion beam treatments, there was no observable reduction in peak QE or increase in work function. Because of the length of time involved for the measurement, lifetime was not measured after every single cleaning and it is unclear whether it increases or decreases with many repetitious ion beam cleanings. Because peak QE remains the same after consecutive ion beam cleanings, it can be assumed that the photoemissive properties of sintered tungsten are not affected by repeated 40mC doses of 5keV argon ions. This is not to say, however, that the surface remains unchanged. It is well known that the penetration depth of energetic ions depends upon the crystallographic orientation of the exposed face. Indeed, this is the mechanism behind imaging a

surface using the secondary electron emission from ion bombardment. If the incoming beam is sufficiently energetic to remove surface atoms, the rate at which this occurs again depends upon exposed crystal face. To study the possible surface effects of the ion beam cleaning, the sintered tungsten substrate was removed from vacuum after 16 identical cleaning procedures and transferred (in an ethanol bath) to an SEM for analysis. An initial SEM study had been performed on this sample prior to its exposure to any type (anneal or ion beam) type of cleaning. Mill marks were left intentionally on known regions of the cathode so that study of the same area could be done after ion beam treatment. The topmost image in Figure 6.50 shows that prior to argon ion beam treatment, grains adjacent to the mill marker were uniformly smooth. The middle and bottom images show the same grains after exposure to the argon ion beam: certain grains remained smooth while others, including several nearest neighbors, became rough. It is important to remember that the history of the sintered tungsten between these two images included not only ion beam cleaning, but also heat annealing. It is non-physical to assume, however, that simple heating of a substrate can cause preferential roughening of grains based on their crystal orientation. Only surface interactions with the ion beam can account for this type of phenomena. Because not all the grains were roughened, it can be assumed that the energy of the argon ion beam is very near some damage threshold for tungsten. If all were roughened, for example, it could be assumed that the threshold had been crossed.

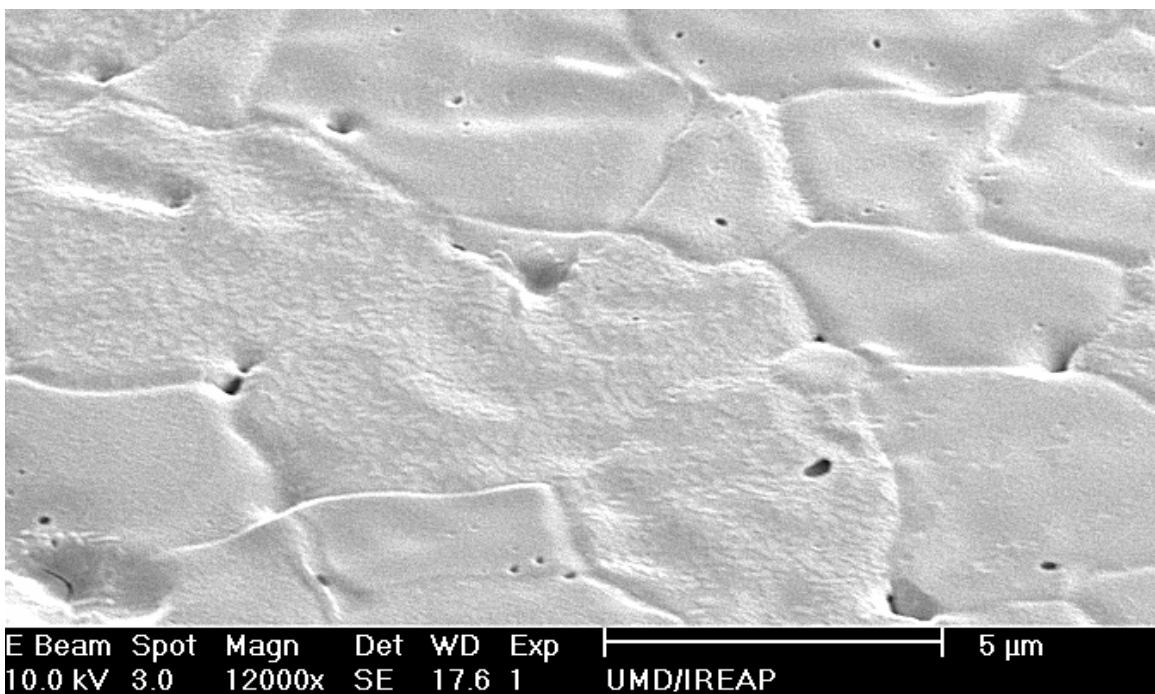
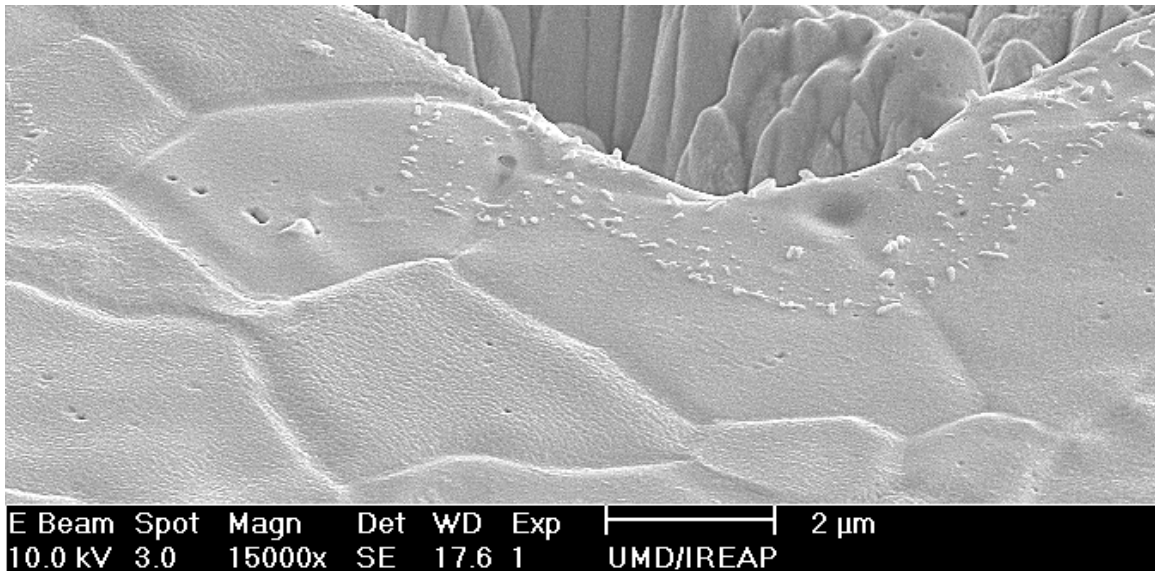
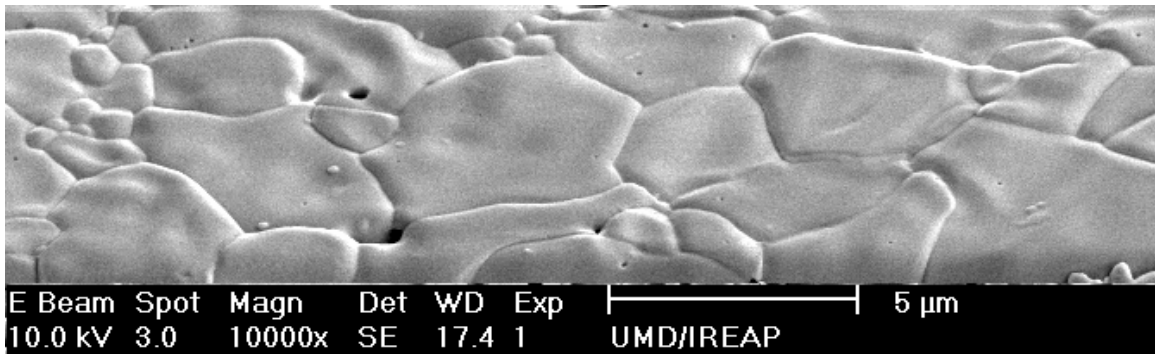


Figure 6.50: Tungsten Before (top) and After (middle, bottom) Ar Beam Cleaning

A useful test would be to progressively increase argon ion energy and observe changes in the grains that had previously remained smooth. These studies were deemed too tedious for the immediate program and were deferred to an ongoing study [107]. Furthermore, simulations using the commercial ion implantation software SRIM[®] suggested that the projected range of a 5keV argon ion was no more than 47 Å in sintered tungsten with a porosity of 40%.

6.8.3 Hydrogen Ion Beam Results

Discussion of ion beam cleaning has thus far been limited to argon, but the apparatus is equipped to use hydrogen as well. The use of hydrogen ions to effectively clean metallic surfaces has been recently established and indeed provided the motivation to utilize a similar technique in this work [59]. Hydrogen ion cleaning using a 1keV beam was shown to increase the QE of copper cathodes by roughly one order of magnitude, with no apparent surface roughness as measured via atomic force microscopy.

Figure 6.51 shows the QE vs. Coverage behavior of a cesiated sintered tungsten photocathode exposed to a 100 mC dose of 5 keV hydrogen ions during fabrication. Comparison to argon ion beam treatment shows that both processes achieved the same peak QE, despite important differences in their interaction with the surface. While energetic argon atoms clean the surface strictly through kinetic impact of the surface, accelerated hydrogen ions clean the surface through chemical reaction. Except for slight differences in the shape of QE vs. coverage curves, hydrogen ion beam cleaning seems to offer no dramatic improvement over that involving argon.

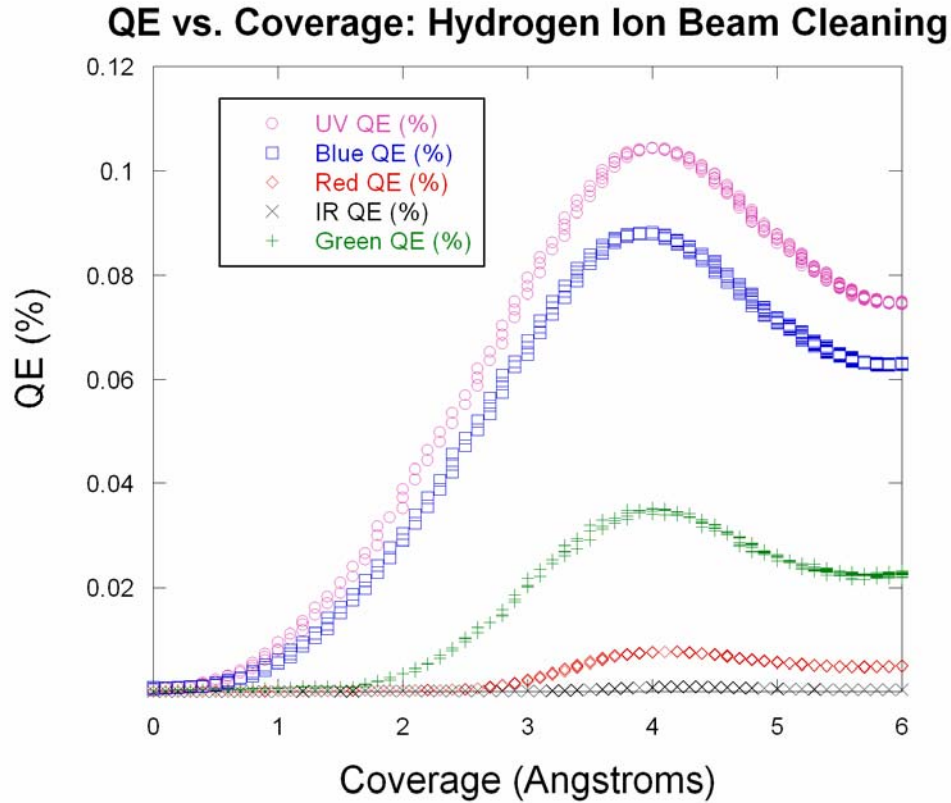


Figure 6.51: QE vs. Cesium Coverage after Hydrogen Ion Beam Cleaning

Cleaning with the hydrogen beam was actually more time consuming than argon because the turbo pump, used during dynamic pumping of the chamber while running the beam, took longer to return the system to approximately 1×10^{-8} Torr. Furthermore, the composition of the hydrogen gas was shown using mass spectroscopy to be less than 99.9% pure, as evidenced by the fact that arcing in the gun occurred after just two consecutive hydrogen cleanings. Arcing in the ion gun occurs when contaminated films build up on the internal insulating surfaces and are then spontaneously released when ohmic loss heats them above a threshold temperature. Not only does this process cause wide fluctuation in the chamber vacuum, but promotes the formation of resistive deposits inside the gun that dissipate

power that would otherwise be transferred to the output beam. The gun was subsequently cleaned using argon plasma discharge and hydrogen was no longer used as part of this research simply because it appeared that argon was sufficient and in many ways preferred.

7. Dispenser Cathode

The work described in the previous three chapters was motivated primarily by the need to design, fabricate, and characterize a cesium-based dispenser photocathode. By providing a sound understanding of photoemission from coated metallic surfaces over a range of temperatures and wavelengths, this precursor effort enables meaningful interpretation of data obtained from subsequent dispenser cathode experiments. This chapter provides a detailed account of the application of this experience to the various stages of dispenser cathode research and is the culminating effort of the dissertation.

7.1 Design and Fabrication

Recall that the dominant degradation mechanism for high QE cesium-based cathodes is the loss of cesium either from a surface monolayer or stoichiometric compound. After a certain amount of permissible degradation, such cathodes must either be replaced or refurbished in some environment other than the electron gun. For a working accelerator system, this frequent repair process is costly and impractical, given the short lifetimes of the highest QE cathodes. The basic concept of a cesium based dispenser photocathode entails *in situ* replenishment of this crucial layer resulting in dramatically extended operational lifetime and simplified overall operations. The dispenser concept pursued in this work is novel because it allows cesium replenishment at near-room temperature. It involves three essential elements: a cesium reservoir, a photoemitting surface, and an interface between the two that controls the rate of cesium arrival. In this design, a small cylinder or cell containing

pellets of a cesium-based compound serve as the reservoir and sintered tungsten serves as both the photoemitting surface and the interface boundary.

7.1.1 Cesium Chromate Pellets

Elemental cesium is unstable in atmosphere and requires some effort to be introduced at high purity in a vacuum system. Some thought was given to incorporating a breakable ampoule of elemental cesium as part of a dispenser design, but a more proven method was ultimately chosen: cesium chromate powder. When heated in the presence of a reducing agent such as titanium, cesium chromate reacts and releases elemental cesium and leaves behind only an inert compound. High purity titanium and cesium chromate powders were mixed in a precise 5:1 ratio and compressed into a small, $\frac{1}{4}'' \times \frac{1}{4}''$ cylindrical pellet that could be conveniently handled and inserted into the cavity of a dispenser cell (discussed in the next sub-section). A 5:1 weight ratio was chosen to guarantee that there would always remain an excess of titanium. The quantity of each powder was measured using a microbalance and their mixture resulted in a total mass of 0.725g. Figure 7.1 shows the powder and pellet, along with the die and press used to apply uniaxial pressure during pellet formation.

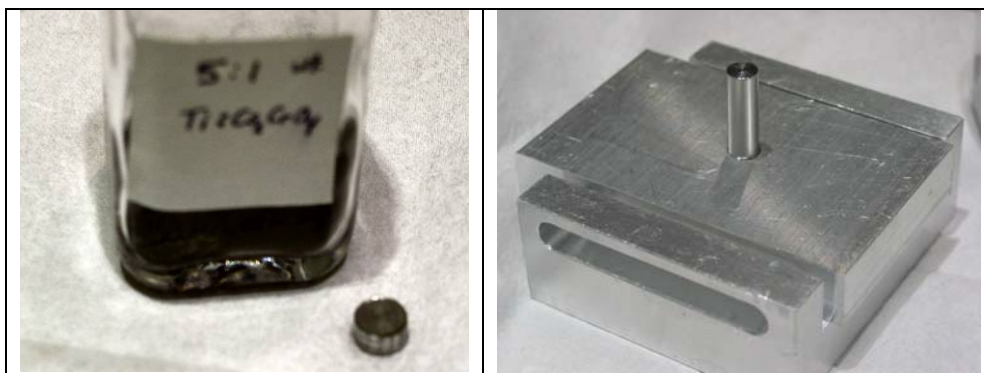


Figure 7.1: Cesium Chromate Powder Pellet, and Fabrication Press

7.1.2 Dispenser Cell

Design of the containment cell for cesium in the dispenser cathode is shown in Figure 7.2. It consists of a cylindrical stainless steel sleeve that is capped at the bottom and into which a single cesium chromate pellet is placed. The wall thickness of the stainless steel sleeve is 0.01” and it is 0.50” in both diameter and height. The top surface serves as the cathode, consisting of a 1mm thick sintered tungsten disk that is carefully brazed to the stainless steel wall, forming a hermetic seal.

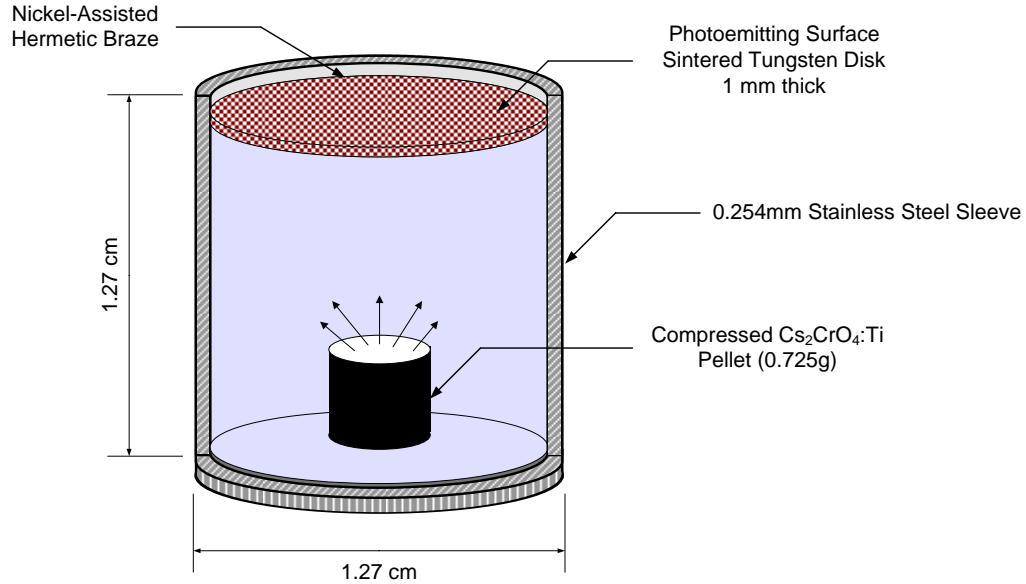


Figure 7.2: Schematic Diagram of the Dispenser Cathode Cell

The entire structure is heated so that the cesium chromate pellet breaks apart and releases elemental cesium, which fills the volume of the dispenser cavity and forms the reservoir discussed earlier. Achieving a hermetic seal between the sintered tungsten disk and the stainless steel sleeve was not trivial. Fabrication of several

prototypes was performed to the author's specifications by B. Vancil of E-Beam, Inc. The porosity of the sintered tungsten proved especially challenging when welding or brazing, because the pores near the weld had to be filled in order to form a hermetic seal. A slurry containing Ruthenium was used to coat the edge of the sintered disk and was fired in a way that minimized over-penetration of the coating into the tungsten [109]. This coated edge is what mates to the stainless steel sleeve. Laser welding was initially chosen, but soon proved problematic because of the mechanical stresses associated with a concentration gradient at the weld. On either side of a weld there exist pure metals, with an alloy in between whose composition varies continuously from one extreme to the other. In the case of tungsten and stainless steel, some concentrations (i.e., alloys) of the constituent metals become brittle and the stresses induced created tiny fractures. These micro-cracks were apparent when the seal was pressure-tested in an acetone bath. An alternative approach was to use a brazing alloy with a known composition and stable inter-metallics. The first challenge was to select an alloy that was not immediately absorbed by porous tungsten. Various tests showed empirically that a composition of 82% gold and 18% nickel was optimal. When brazing was attempted, however, the alloy did not wet the stainless steel and eventually became absorbed into the sintered tungsten.

Stainless steel resists wetting of some metals because of its tenacious surface layer of chrome oxide. Indeed, this tight-packed oxide layer is what gives stainless steel its ability to be "stainless" in the many rugged environments it is typically used in. To overcome the wettability mismatch, the stainless steel was coated first with a layer of nickel, which the aforementioned alloy is known to wet. A subsequent braze

between the sealed edge of the sintered tungsten and the nickel coated stainless steel proved successful. Figure 7.3 shows a brazed cell undergoing a pressure test in an acetone bath: nitrogen gas is forced into the rear of the dispenser and the gas diffuses through the tungsten pores to produce small bubbles. The uniformity of bubbles throughout the surface shows that the brazing process did not clog the pores (with the exception of those adjacent to and beneath the seal). The larger ring surrounding the sintered tungsten is a molybdenum chuck used to apply pressure on the stainless steel sleeve during brazing to prevent high temperature deformation. Also noticeable in the figure below is a region of profuse bubbles caused by a pin hole leak in the seal. This was later repaired, as shown in Figure 7.4.

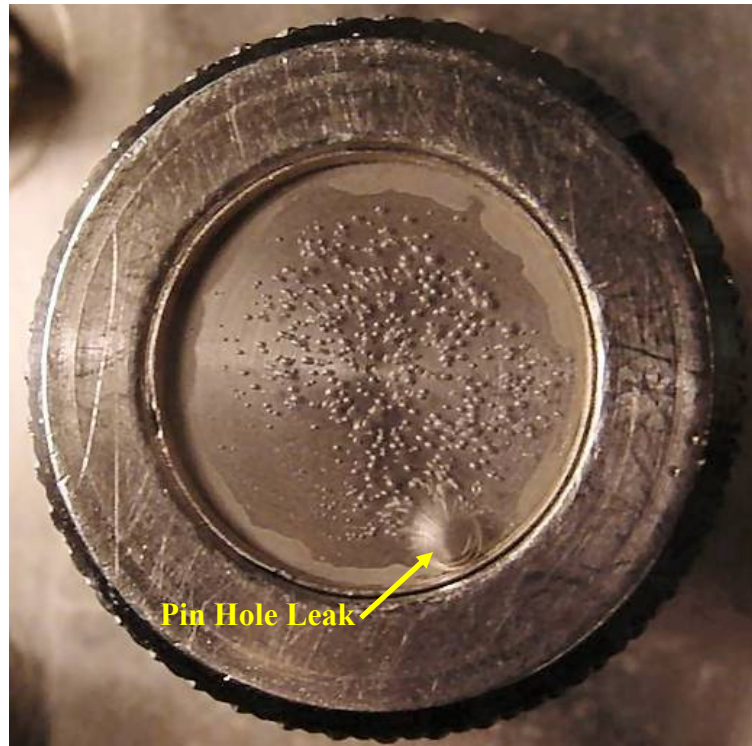


Figure 7.3: Top Surface of Dispenser Cathode Showing Pin Hole Leak



Figure 7.4: Dispenser Hermetic Seal (left); Ready for Vacuum Insertion (right)

7.1.3 Heater Mount

The right-hand side of Figure 7.4 shows the completed prototype dispenser cathode ready for insertion into the vacuum chamber. Because temperature plays a crucial role in the performance of the dispenser, a way must be made for it to be measured and controlled. A custom cathode holder was manufactured using OFHC copper that grips the dispenser cell and is itself mounted to the button heater used in previous experiments. Copper is used to enhance thermal conductivity and assure that the temperature measured by the heater thermocouple is as close as possible to the actual temperature at the cathode. Figure 7.5 shows a dimensioned schematic of the cathode holder while Figure 7.6 shows the dispenser cell inserted into the finished product. Special channels were milled into the back surface of the holder to facilitate gas evacuation during pumpdown, as shown in Figure 7.7.

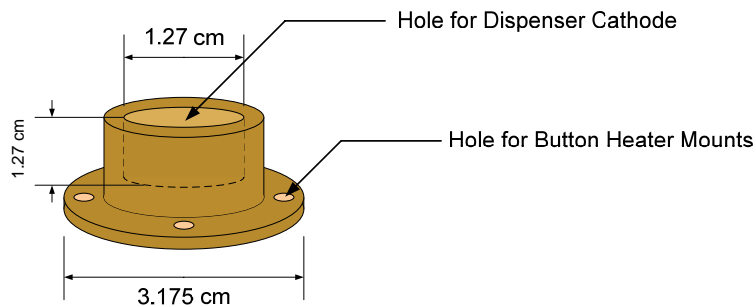
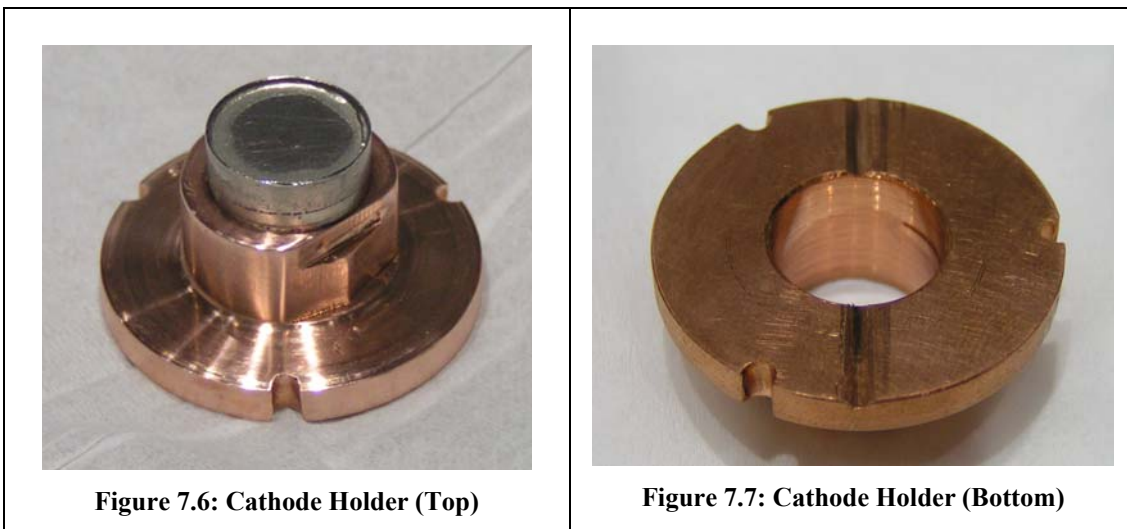


Figure 7.5: Schematic Diagram of Copper Cathode Heater Mount



7.2 Vacuum Insertion

Following the completion of experiments in the previous chapter, the fabrication chamber was brought up to atmospheric pressure using high purity dry nitrogen and the anode-cathode flange was removed so that the new dispenser cell could be installed.

7.2.1 Modified Anode-Cathode Configuration

Prior to vacuum insertion, the dispenser cell was stored in a dry atmosphere and removed only when mounted on the cathode heater. Modification of the anode-cathode configuration was necessary in order to accommodate the larger size of the dispenser cell together with its copper thermal mount. Figure 7.8 shows the pair mounted on the heater using three molybdenum screws. Notice also the clamping feature of the thermal mount: half of the copper sleeve is free to move with respect to the base. As the small compression screw is tightened, this flexible half of the sleeve is drawn inward and grips the dispenser cell, forming a thermally conductive and mechanically strong support. A longer anode mounting bracket was fashioned such that there was a 1cm gap between the top of the dispenser cell and the plane of the anode annulus, as shown in Figure 7.9. The anode is aligned so its center coincides with the axis of the cathode-heater-mount assembly, as shown in Figure 7.10.

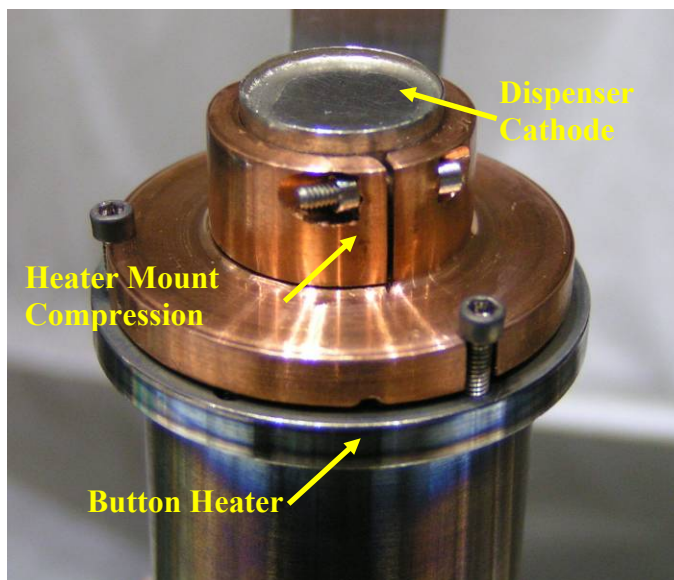


Figure 7.8: Dispenser Cathode Mounted on Button Heater

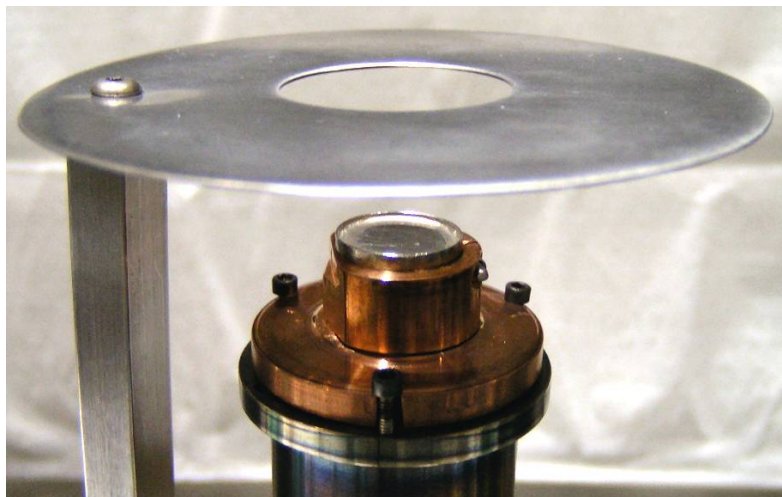


Figure 7.9: Completed Anode-Cathode Assembly



Figure 7.10: Front Face of Anode-Cathode Assembly Showing Mutual Alignment

7.2.2 Pump-down Procedure

Evacuating the fabrication chamber along with the dispenser cathode presents a unique challenge because of the trapped volume of gas inside the cell. If the chamber pressure rapidly drops, as is typical during the startup phase of the roughing pump, then a large pressure gradient forms across the sintered tungsten that has the

potential to fracture or rupture the cell or its hermetic seal. Reduction in pumping speed while in the high pressure regime (10-760 Torr) effectively eliminates this danger and is accomplished by using the fine metering valve already mounted on the system. Its use is somewhat non-standard because gas flow is reversed with respect to its normal direction, but this seemed to have no detrimental effect on the valve. To begin the pump-down process, the main chamber valve was first closed, which allowed the roughing station to pump exclusively on the network of gas lines. The fine metering valve attached to these lines was then slowly opened completely and further pumping speed adjustment was made using the up-stream needle valve. The roughing station was allowed to pump the chamber at a rate of approximately 0.3 Torr-l/s for one hour. This slowly reduced the pressure to approximately 0.1 Torr without damage to the dispenser. At this point, the smaller valves were closed and the main chamber valve was fully opened to allow continued pumping. A problem with this controlled-pumping speed scheme is that it requires the roughing station to experience a relatively high gas load for an extended period of time (1 hour). Its programmed sequence allows the turbo pump to continuously increase its rotational speed, which causes heating of the turbo vanes because of sustained collisions with the abundant gas molecules. An on-board thermocouple registers this temperature increase, which causes the roughing station to automatically shut down. This occurred twice in the process of pumping the dispenser and each time the main valves were closed and the chamber was isolated until the roughing station could be brought back online. Adding additional cooling to the turbo pump was met with some success as it apparently prevented a third shutdown. Following a typical pumpdown schedule, the

chamber was baked after having achieved 1×10^{-6} Torr. During this period, the dispenser cathode was also slowly heated to approximately 225°C (the temperature of the chamber during bakeout) to prevent contaminants leaving the chamber walls from “freezing-out” on the cathode surface. Figure 7.11 shows the background gas composition during dispenser outgassing when its temperature was 160°C . The diverse mix of gasses is not surprising, given the dispenser’s extended exposure to atmosphere. This RGA scan underscores the need for an outgassing process: water and carbon dioxide (cathode poisons) are trapped within what will become the cesium reservoir.

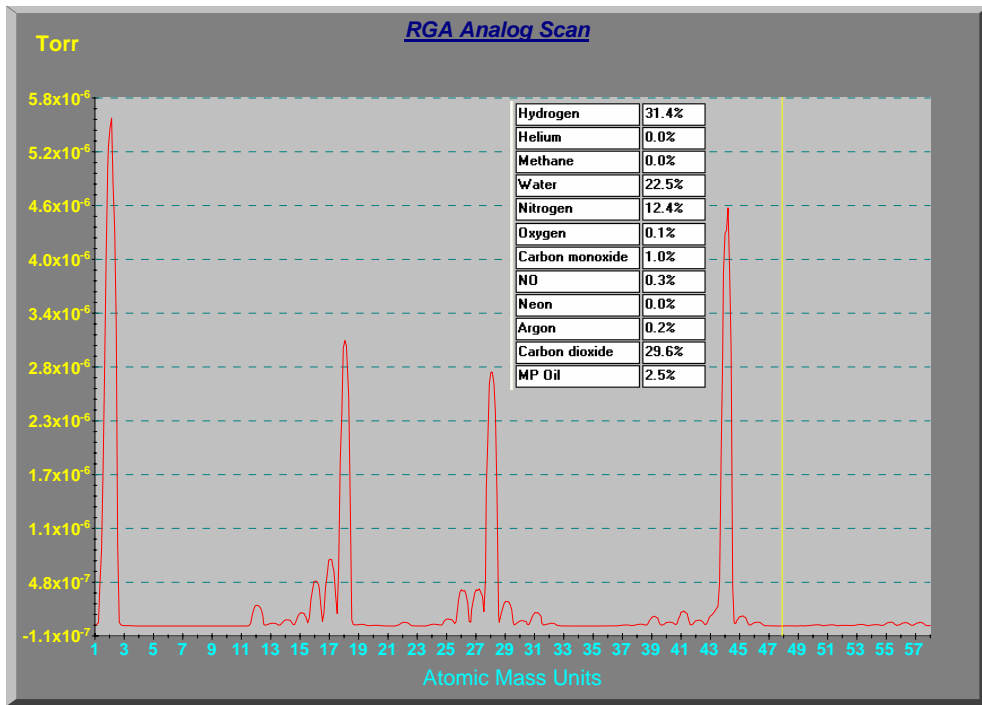


Figure 7.11: Background Gas Composition During Dispenser Outgassing

7.2.3 Argon-Ion Cleaning

Because the first activation procedure is the only opportunity to definitively observe the temperature at which photoemission begins, a clean tungsten surface must be present prior to starting this process. The temperature at which photoemission first begins is roughly the activation temperature, because photoemission signals the presence of cesium on the surface. A contaminated substrate surface would hinder photoemission and mask the presence of cesium on the surface. After the bakeout procedure was completed and base pressure of the roughing pump was achieved, an argon ion beam cleaning treatment was performed following the standard method of the previous chapter. Throughout the cleaning procedure, the temperature of the dispenser cathode was maintained at 225°C in anticipation of the activation procedure to follow.

7.3 Dispenser Activation

A major challenge for this particular dispenser design is the need to reduce the cesium chromate pellet to elemental cesium, a reaction which occurs at about 500°C. Elevated temperature permits not only this reaction, but also the rapid diffusion of newly released cesium through the sintered tungsten. Losing a substantial amount of cesium during the activation process is obviously problematic because of widespread deposition throughout the chamber and a chronic depletion of cesium from the reservoir. It was crucial to precisely determine the temperature at which activation begins, as evidenced by the onset of photoemission, in order to avoid overheating the cathode.

7.3.1 Activation Temperature

Figure 7.12 shows photocurrent and temperature as a function of time during the first activation process of the dispenser cathode. The two traces for current correspond to photoemission from the UV and blue lasers. Two critical temperatures are apparent: $T_A = 425^\circ\text{C}$ at which activation begins, as evidenced by the onset of photoemission, and $T_E \approx 477^\circ\text{C}$ when thermionic emission begins. It is unlikely that much of the cesium chromate pellet had reacted at the lower temperature. Localized heating may have caused a small release of cesium, which was sufficient to cause the first photoemission signal detected.

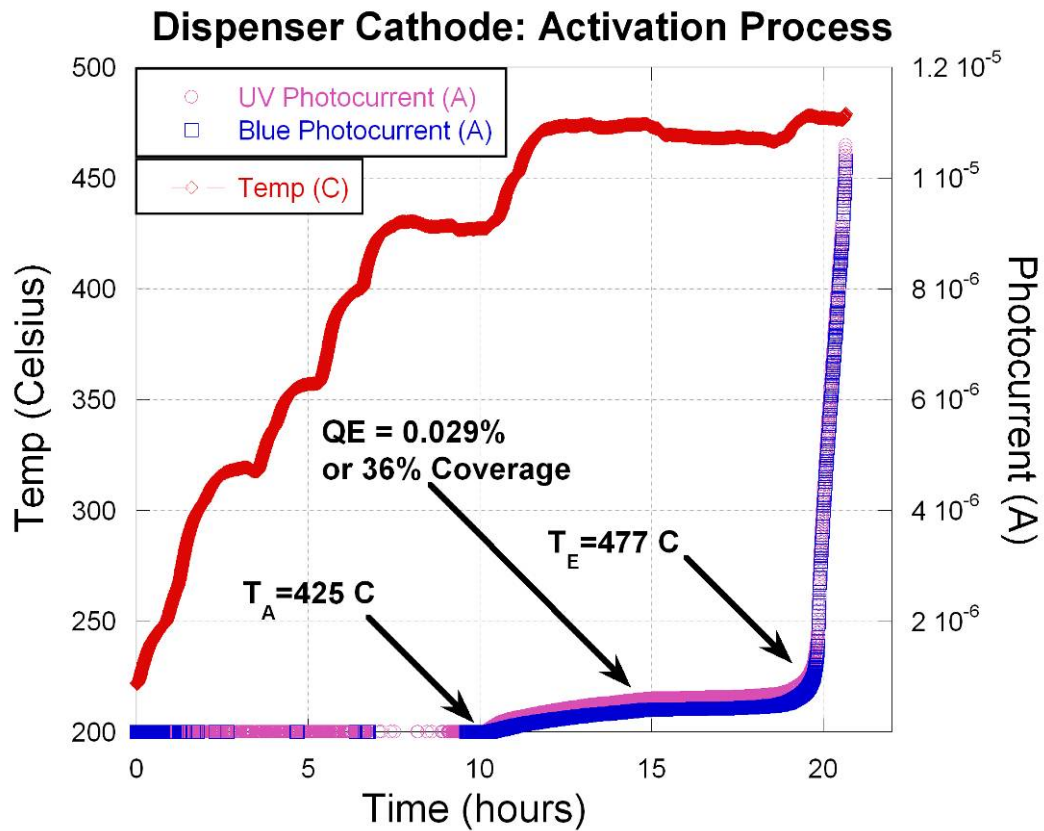


Figure 7.12: Critical Temperatures Observed During Dispenser Activation

As pointed out in the graph, the QE for temperatures less than 477°C is no more than 0.03%. This QE corresponds to much less than a monolayer of cesium coverage (about 36%), suggesting that the rate of cesium delivery to the surface is low. The competing process of high temperature desorption prevents a significant buildup of cesium on the surface. After a sustained period of time (10 hours) at temperatures in excess of 450°C, the pellet apparently crumbled, allowing a large release of cesium and a subsequent spike in thermionic current caused by a reduction in work function at the surface. Fitting this data to the Richardson thermionic emission equation gives a work function of approximately 1.65 eV. If photocurrent is plotted as a function of temperature, the wavelength-dependent behavior of critical temperature becomes apparent, as shown in Figure 7.13. As coverage increases with temperature, photoemission begins first at $T_1 = 425^\circ\text{C}$ with UV and blue light, and later at $T_2 \geq 448^\circ\text{C}$ for all other wavelengths.

7.3.2 Chamber Conditions during Activation

A comprehensive characterization of a dispenser cathode must include its effect on the environment in which it resides. It is expected that in most applications, a dispenser cell will be activated in a chamber separate from the actual photoinjector. A load-lock mechanism would then allow vacuum transfer of an activated cell to the electron gun. Figure 7.14 shows that outgassing persists throughout much of the activation procedure, resulting in pressure spikes (corresponding to increases in temperature) of up to 1.7×10^{-6} Torr. Periodic pressure spikes of this magnitude necessitate the use of the roughing pump throughout the entire activation procedure.

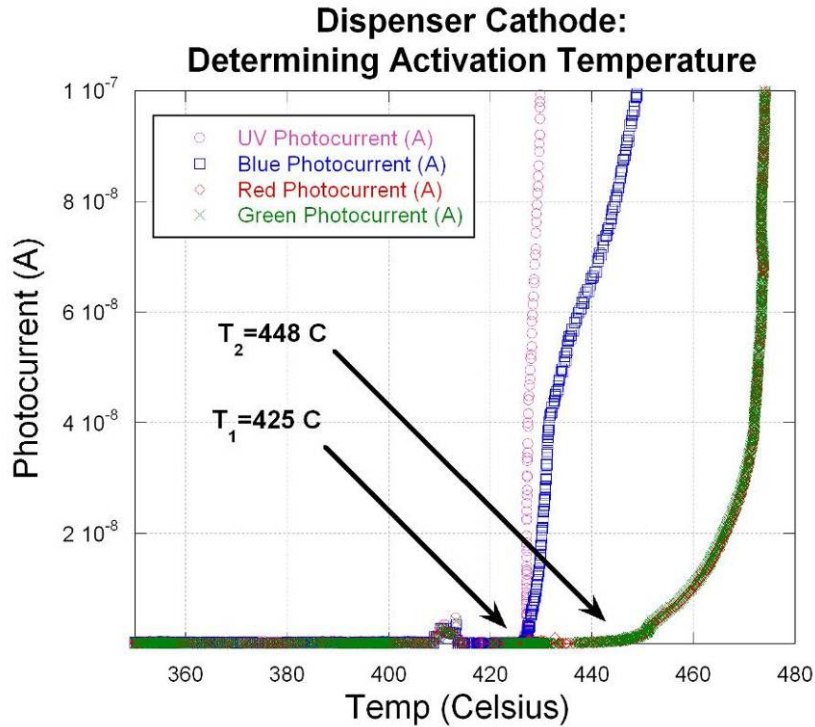


Figure 7.13: Onset of Photoemission for Different Wavelengths

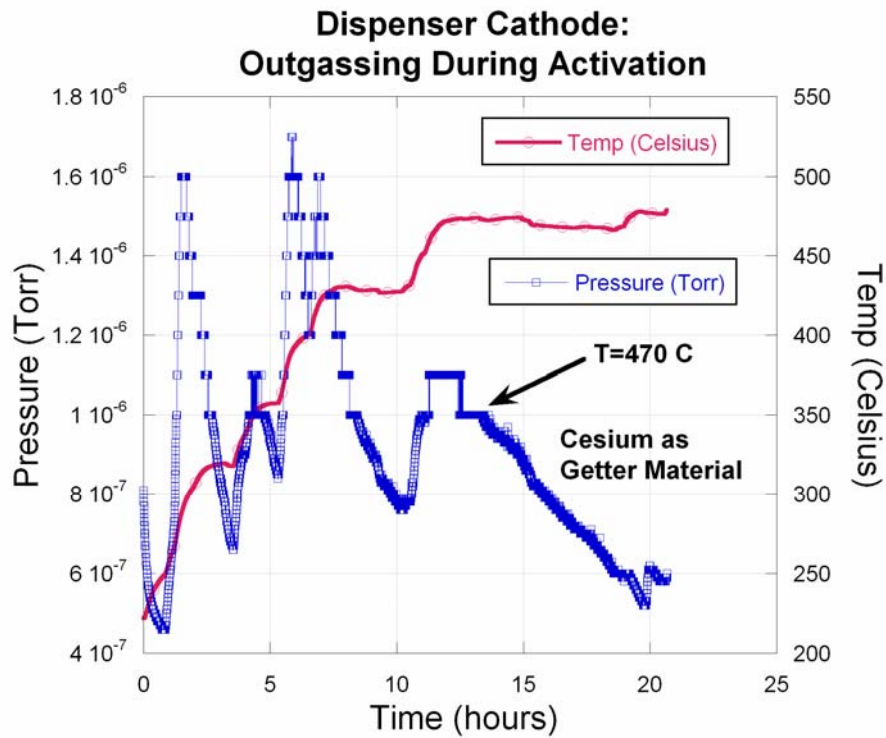


Figure 7.14: Persistent Outgassing During Activation Procedure

Perhaps the most severe environmental effect of the dispenser is its potential to deposit large amounts of cesium throughout the chamber. A very crude method of detecting massive amounts of deposited material is through reduced transmissivity of a quartz viewport. This effect was not observed throughout the activation procedure, but a deposited layer of cesium did register on the quartz crystal monitor (QCM). Notice also that a dramatic reduction in chamber pressure occurs near the activation temperature. This corresponds to the release of cesium and its subsequent reaction with residual background gases (effectively serving as a getter pump on the chamber walls). This observation corroborates the statement made earlier that a temperature higher than 450°C is required to achieve complete activation. Figure 7.15 shows cesium deposition as measured by the quartz crystal monitor. Because the QCM is mounted above the dispenser cathode (i.e., not directly facing it), the coverage measurement it provides approximates the average deposition throughout the chamber. Notice that at approximately 470°C, the chamber coverage increases sharply. This corresponds to the breakup and subsequent reaction of the cesium chromate pellet. It appears that from an operational perspective, it would be best to slowly heat the dispenser to this temperature and then immediately allow it to cool. This would guarantee an abundance of cesium in the dispenser cell and avoid excess deposition throughout the chamber. Using the assumption that the vast majority of cesium leaves the dispenser as ions, the total amount of cesium deposited in any given environment can be ascertained by measuring ion current off the cathode. This effect was indeed observed, but because photocurrent and ion current cannot be measured simultaneously, the former was given priority during data acquisition.

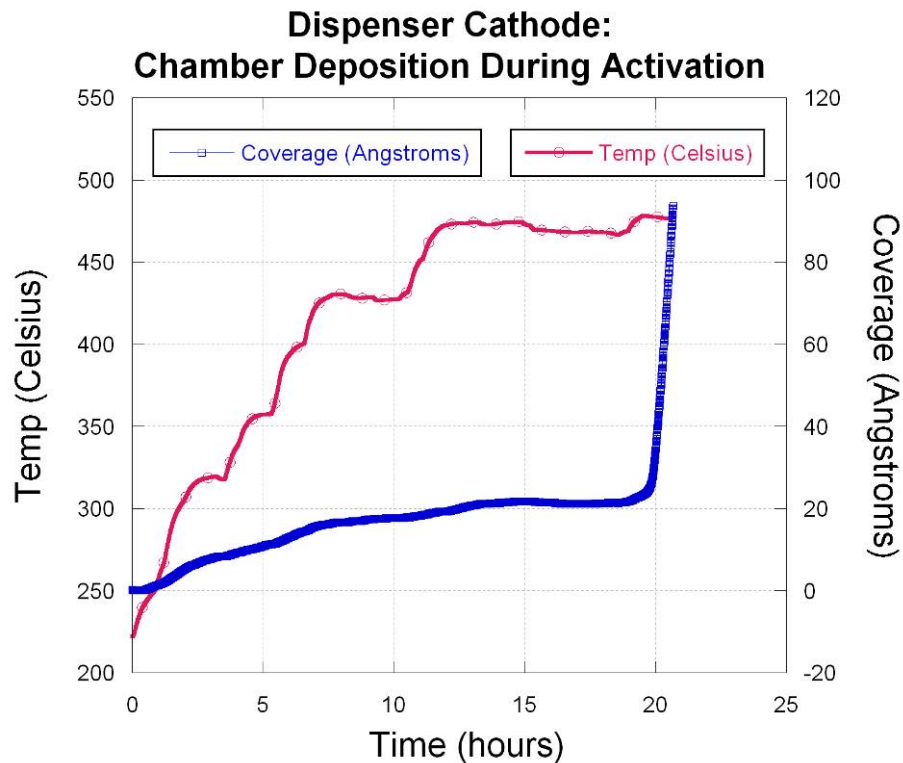


Figure 7.15: Cesium Deposition in Chamber During Dispenser Activation

7.3.3 Post-Activation Performance

After activation temperature was reached, a 45 minute argon ion cleaning procedure was performed in order to remove surface contaminants that may have accumulated during the lengthy activation period. During this period, the cathode was held at activation temperature so that as the surface was cleaned with the argon ion beam, it was immediately coated with cesium. Following the cleaning, the dispenser was allowed to cool while photocurrent, thermionic current and accumulated cesium were measured. Figure 7.16 shows total and thermionic current as the dispenser cathode cools down. Notice that at high temperatures (left-hand side of the graph), the total current is almost entirely thermionic. As temperature falls to about 250°C,

thermionic emission ceases and the total current measured is due entirely to photoemission. This observation places an upper bound on the operating temperature range of the dispenser cathode: photoemission is the only source of electron flux below 250°C. Figure 7.17 shows the output of the deposition monitor as temperature falls from 470°C. Immediately after the heater is shut off, cesium continues to be deposited, but at a much slower rate than what is depicted in Figure 7.15. After some time, the deposition monitor began to register a loss of about 10 Angstroms of cesium from its sensor surface, a relatively small amount given that the initial coating was 128 Angstroms. In any case, it is evident that shortly after the dispenser begins to cool following activation, the deposition of cesium throughout the chamber ceases.

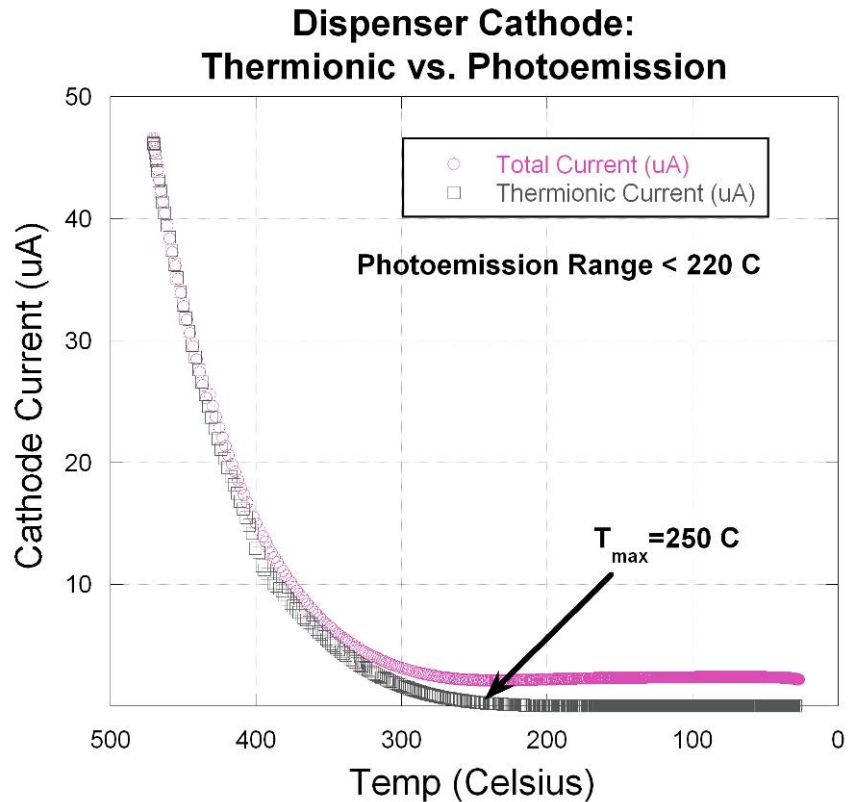


Figure 7.16: Total Cathode Current and Thermionic Current After Activation

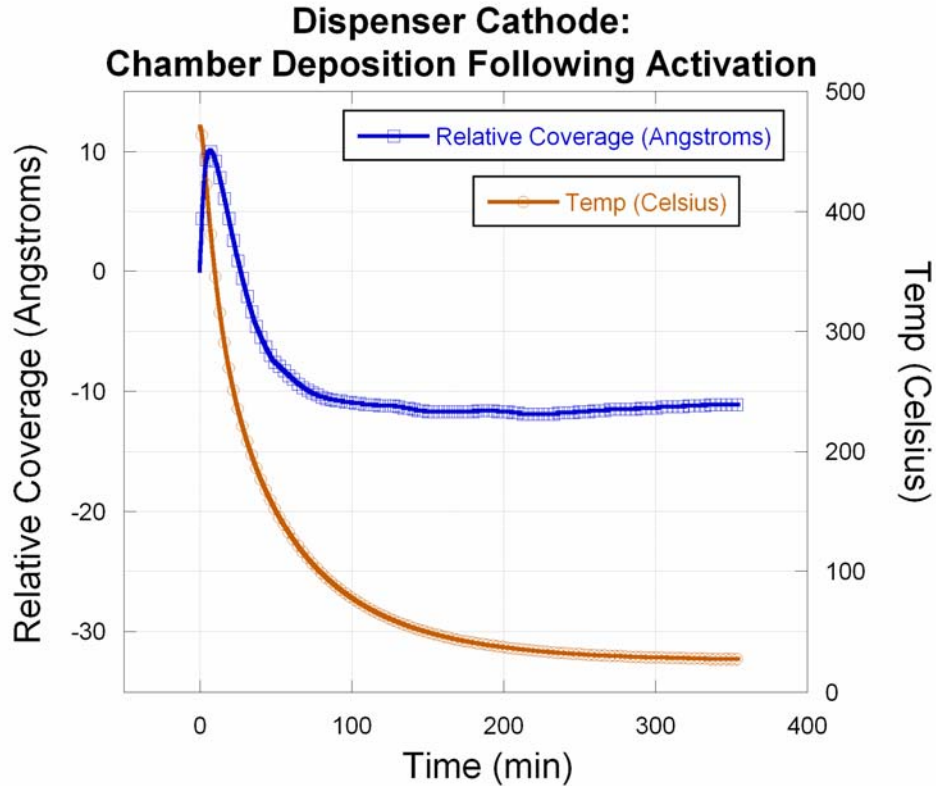


Figure 7.17: Chamber Deposition Immediately Following Dispenser Activation

Having identified an approximate operating temperature range for the dispenser, it is useful to observe its performance (in terms of QE) within this regime. Figure 7.18 shows QE at several wavelengths as the cathode cools from 300°C to room temperature. Notice that at ~250°C, QE begins to increase, reaching a maximum value of 0.11% in the UV. The gradual increase is due to the fact that as the surface cools, cesium is better able to adhere and form an optimal surface coating. Recall from the previous chapter that the peak QE for an *externally* cesiated atomically clean sintered tungsten disk was also 0.11% in the UV. This behavior is very significant because it indicates that the uniformity of cesium coverage achieved via porous diffusion is equivalent to that of direct deposition using an external cesium

source. Let us compare the observed behavior of: 1.) external deposition of cesium on sintered tungsten and 2.) coating the surface by cesium diffusion through (and across) sintered tungsten. If the substrates are identical in composition, and cesium is the only surface layer added to each, then identical QE measurements suggest that the resulting coatings and their effective work functions are identical as well. This is a valid argument because for this experiment, the laser spot sizes and emission areas remained exactly the same. This and subsequent tests are positive evidence that the system of randomly spaced pores throughout the sintered tungsten is sufficient not only to deliver cesium to the surface, but also to facilitate its diffusion into uniform monolayer coverage. This experiment also verifies that the diffusion length of cesium at temperatures in the range of 200-400°C is at least 3-5 μm . This conclusion is reasonably justified on the grounds that average pore-pore separation distance and average grain diameter on the surface of sintered tungsten both share this same characteristic length of 3-4 μm .

Figure 7.19 provides a more comprehensive view of the cooling process by plotting total cathode current for each wavelength instead of QE. Notice that at about 250°C, cathode current begins to decrease briefly and then rise again to reach its aforementioned peak. This apparent decrease is due to the fact that the majority of measured current at elevated temperature is thermionic. As thermionic current decreases to zero, the photocurrent signal remains and increases throughout the cooling period as an optimal cesium coating is formed.

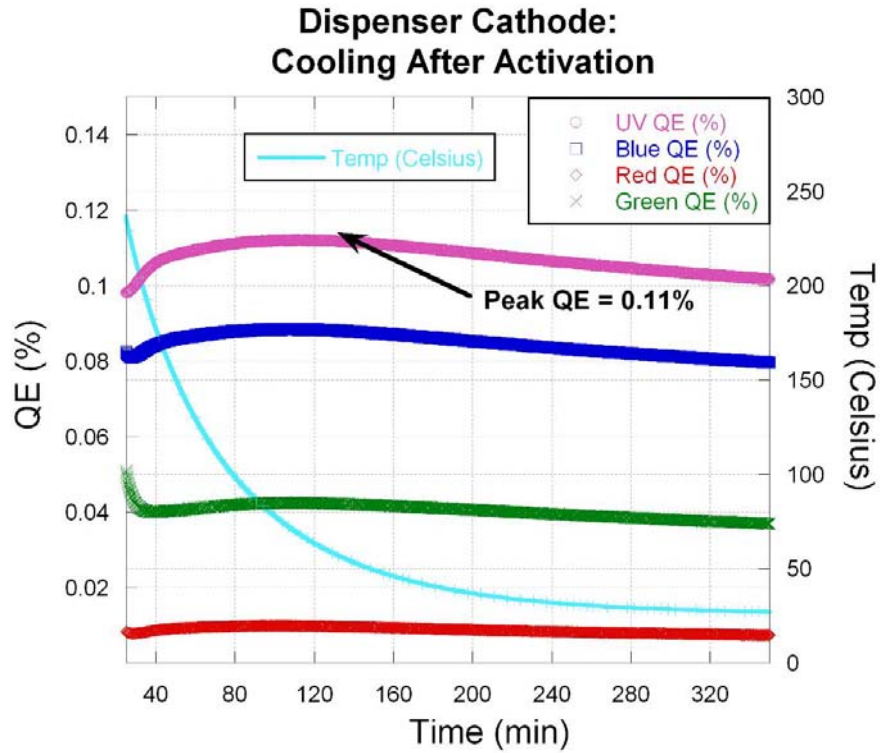


Figure 7.18: QE of Dispenser Cell During Post-Activation Cooling Phase

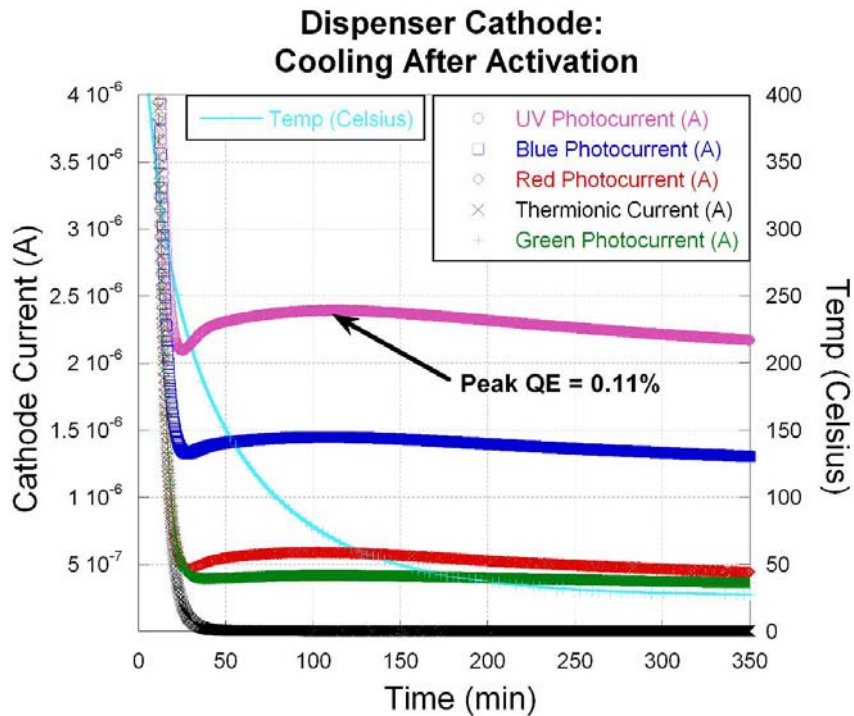


Figure 7.19: Total Cathode Current during Post-Activation Cooling Phase

7.4 Rejuvenation Process

As discussed in the previous chapter, all cesium-based photocathodes exhibit some finite lifetime, after which the cathode must either be replaced or rehabilitated. It has thus far been demonstrated that cesium can be delivered to the surface of the prototype dispenser cathode through an activation procedure whose critical temperatures and behavior has been defined. The goal of this section is to restore the performance of the cathode after its efficiency has been degraded over a long period of time.

7.4.1 QE Recovery

A large quantity (0.725g) of cesium chromate was initially packaged in the dispenser cathode, so it is expected that an excess of cesium was produced after activation at 470°C. Two questions remain at this point: whether enough cesium remained in the reservoir and, if so, can that cesium uniformly recoat the surface to restore peak efficiency. An important observation when considering cathode rejuvenation is that the process will start with some residual cesium already in place. Recall that for the cesiated sintered tungsten experiments of the previous chapter, very little cesium was needed ($<2\text{\AA}$ in most trials) to restore peak sensitivity. To determine whether rejuvenation was possible, photocurrent was extracted from the activated cathode continuously for four days (100% duty cycle) until the QE decayed to half its peak value. The cathode was then slowly warmed and photocurrent and QE was recorded, as shown in Figure 7.20. It is immediately apparent that rejuvenation occurs because QE begins to rise with just a mild 10°C increase in temperature. When QE is plotted as a function of temperature, as in Figure 7.21, it can be seen that at

~140°C, the cathode is completely restored. Notice that the peak QE is again 0.11%. The fact that QE returned to its post-activated value is again very important because it strongly suggests that the optimal cesium layer can be completely reformed following a degradation period of extended use.

It is useful to consider the history of the cathode in light of this return-to-peak behavior: it was cleaned during activation, cooled to room temperature, used continuously for 4 days, and finally reheated and cooled again. The fact that QE returned to the same value after this rigorous use is remarkable and shows that the cathode does not contaminate itself during use or rejuvenation. A concern throughout this program was that if contaminants remaining inside the dispenser cell, they could degrade the cathode surface during extended use or rehabilitation.

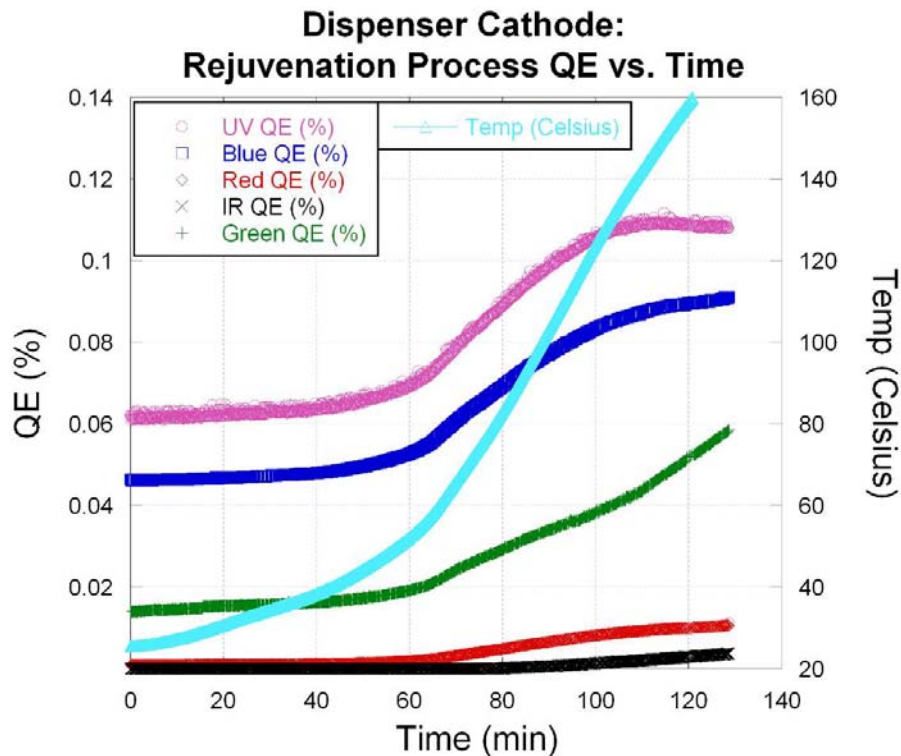


Figure 7.20: Cathode Regeneration Shown By QE Recovery

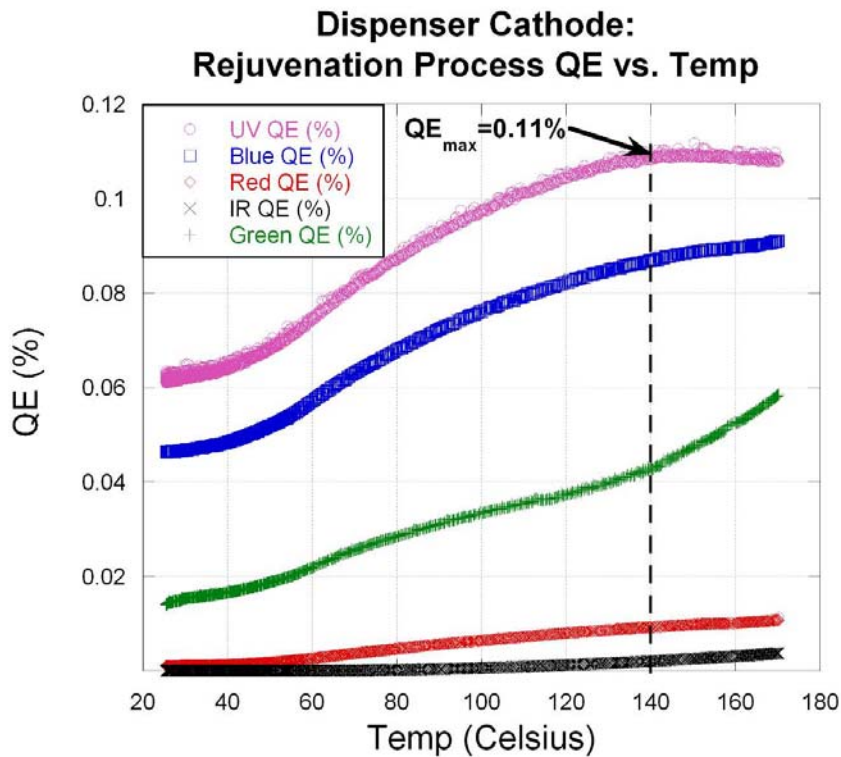


Figure 7.21: Determining Optimal Rejuvenation Temperature

7.4.2 Indirect Coverage Measurement

The direct deposition experiments performed earlier on atomically clean tungsten related QE to cesium coverage and coating thickness. Coverage on the dispenser cathode cannot be directly measured, because the layer is formed as cesium diffuses from within cell. Coverage at the dispenser surface can be measured *indirectly* by using the known relationship between QE and coverage. Figure 7.22 shows cesium coverage as a function of temperature during the rejuvenation process. Notice that at $\sim 140^{\circ}\text{C}$, cesium coverage approaches very close to the 67% value known to produce the lowest possible work function.

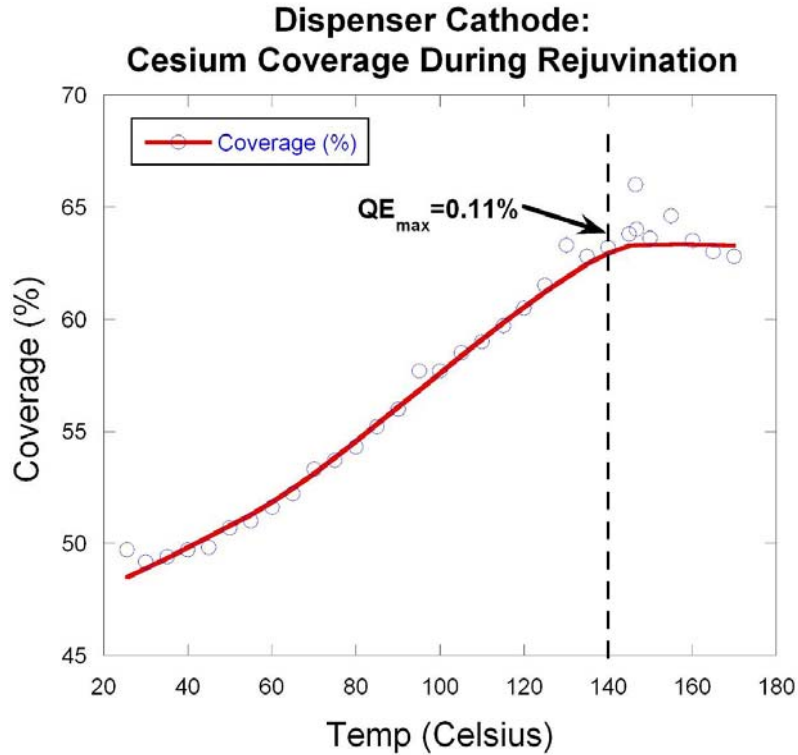


Figure 7.22: Cesium Coverage Measured Indirectly Using QE

7.4.3 Chamber Conditions

As with activation, cesium deposition throughout the chamber remains a concern when the dispenser is held at elevated temperature. It is especially crucial that little or no cesium be released during a rejuvenation process, because this phase will occur *inside* the electron gun. Figure 7.23 shows the minimal effects of the rejuvenation period on chamber pressure and indirect deposition. Pressure remains in the low nano-Torr range, which is noteworthy because despite its larger size, the dispenser cathode during rejuvenation presents less of a gas load than the commercial SAES sources discussed in the previous chapter. Furthermore, only about 2 Angstroms of cesium are detected at the rejuvenation temperature of $\sim 140^{\circ}\text{C}$.

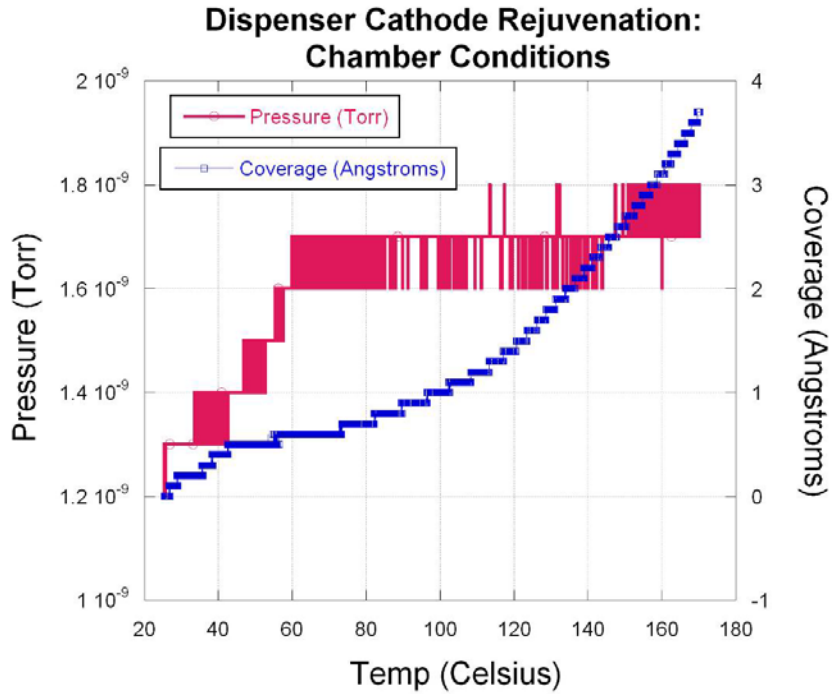


Figure 7.23: Chamber Conditions During Dispenser Rejuvenation Process

7.5 Modes of Operation

This chapter concludes with a discussion of the two basic operating modes of the dispenser cathode: periodic and continuous rejuvenation. It is important to reiterate that cesiated tungsten is a simple test case to evaluate the dispenser cathode's ability to deliver cesium to a photoemitting surface. The prototype design has thus far demonstrated its functionality as a temperature-controlled cesium delivery mechanism upon which many different cesium-based cathodes could be fabricated. In future work, antimony will be evaporated directly onto the porous sintered surface and cesium will be introduced at elevated temperature to create a high QE cathode Cs_3Sb . While this cathode's efficiency is very high (>10%), it must be changed

almost on a daily basis because of its short lifetime [5]. Its QE is very sensitive to deviation in the stoichiometric ratio of cesium to antimony. It is possible that the dispenser platform upon which this cathode would be fabricated could provide a *continuous* source of new cesium to maintain the proper compound on the surface. While the precise details of the dispenser's use would depend upon what type of cathode resides on its surface and the anticipated operating schedule of the gun, it remains clear that for some cathodes, continuous replenishment of cesium would be desirable.

7.5.1 Periodic Rejuvenation

For longer-lived cesium based cathodes, periodic rehabilitation of the photo-sensitive surface may suffice in yielding a long operational lifetime. In comparison to continuous rejuvenation, this mode would seem to better conserve cesium in the reservoir and also has the advantage of allowing room temperature emission. Figure 7.24 shows the QE vs. Time behavior of cesium on atomically-clean sintered tungsten. The $1/e$ lifetime is more than 5 days for continuous current extraction at multiple wavelengths. It was observed that QE does not appreciably change over this length of time (in a clean vacuum system) if the accelerating field and laser remain off. This describes the effective “shelf-life” of the cesiated tungsten cathode. Both lifetimes are linked to the background gas pressure and composition. In all lifetime measurements discussed in this project, the RGA was used to guarantee that nearly the same environment existed in the chamber for all trials. Figure 7.25 shows the typical background gas pressure and composition during lifetime measurements.

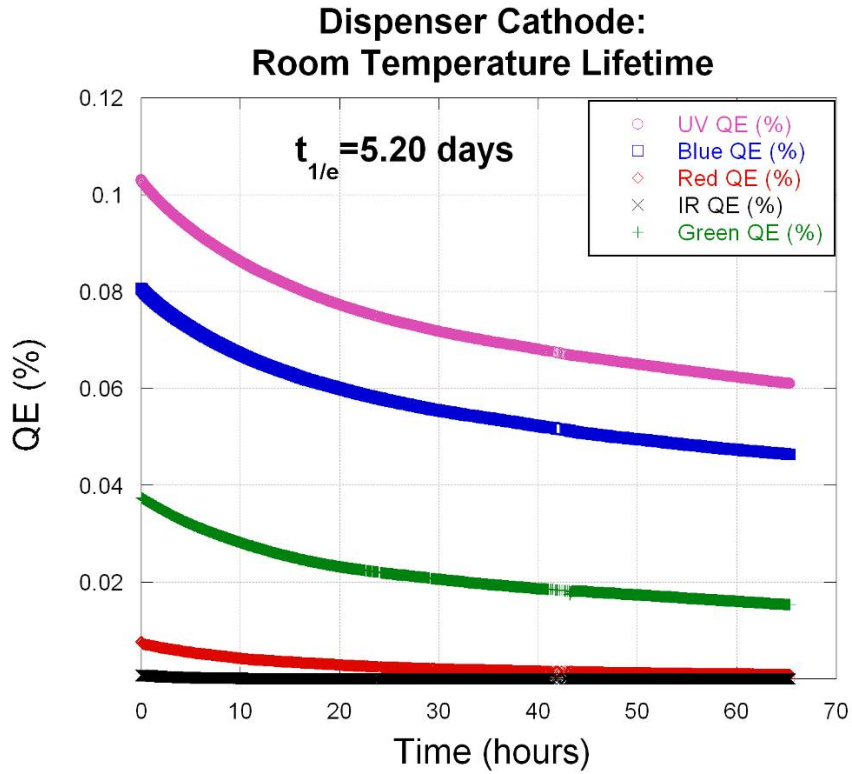


Figure 7.24: Lifetime of Dispenser Cathode at Room Temperature

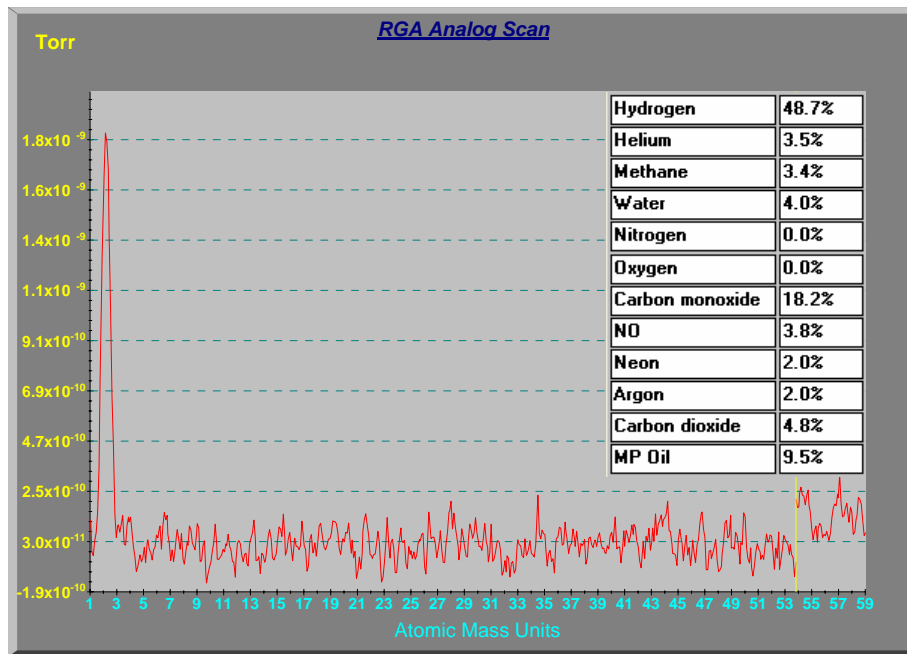


Figure 7.25: Background Gas Composition during Lifetime Test

7.5.2 Continuous Rejuvenation

Perhaps the most impressive test of the dispenser cathode's performance is its effective lifetime in full duty cycle continuous rejuvenation mode. This mode of operation is attained when the cathode is held at an elevated temperature of 160-180°C. Measurement in this mode was made immediately following the room temperature lifetime trial, so the results represent a worst-case scenario since some degradation had already occurred. Figure 7.26 shows an extraordinarily long effective lifetime of 47.2 days exhibited by the dispenser cathode when continuously rejuvenated (after four days of continuous use at room temperature). This result is very encouraging because it clearly demonstrates the dispenser cathode's ability to replenish a cesiated surface for a sustained length of time.

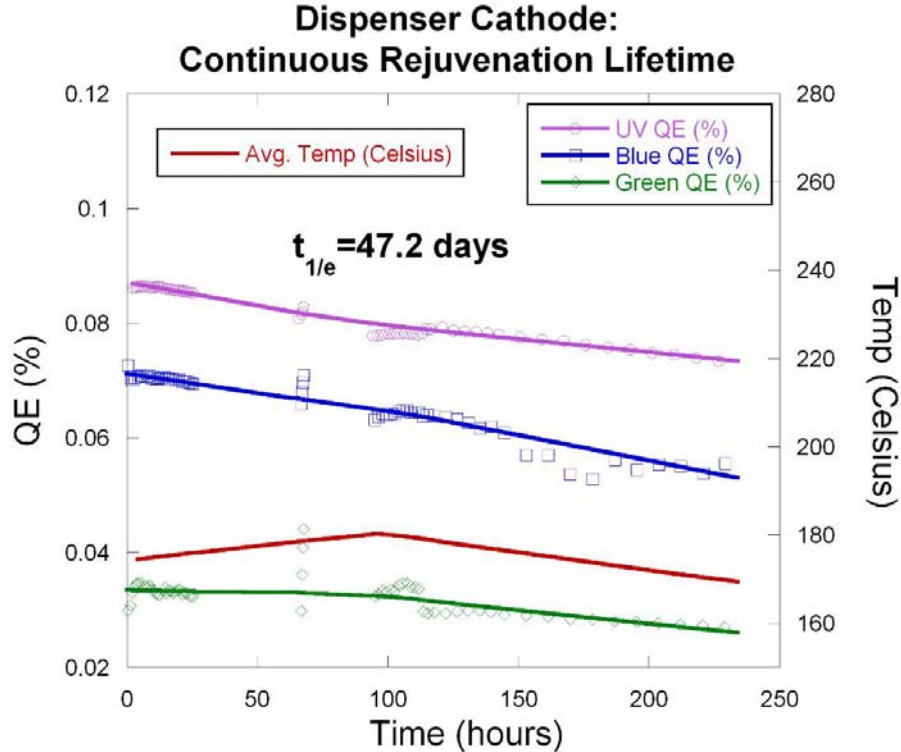


Figure 7.26: Dispenser Cathode Lifetime in Continuous Rejuvenation Mode

8. Conclusion and Discussion

The need for long-lived, high-efficiency photocathodes is motivated primarily by their immediate application in advanced light sources such as the free electron laser (FEL). FELs offer the advantage of very high average output power and dynamic wavelength tunability in regions of the spectrum, including x-ray, THz, and IR, where conventional sources are challenged. The research in this dissertation contributes to the development of photo-switched, high-brightness electron sources in several ways. Most importantly, it demonstrates a potential method for dramatically improving the lifetime of high QE photocathodes which enable the high peak and average beam currents required by FELs and similar applications. It also contributes to the collaborative development of a leading photoemission theory that has already begun to find use in the most popular beam simulation codes [7]. This chapter concludes the dissertation by summarizing the research of previous chapters and outlining future directions for this work in the near and long-term.

8.1 Precursor Studies

An in-depth study of photoemission from coated metallic surfaces was pursued prior to beginning work on a cesium dispenser platform. This phase enabled theory comparisons and provided research experience that shaped the dispenser cathode work that followed.

8.1.2 Coated Metals

A versatile fabrication facility was constructed to accommodate multi-wavelength cathode characterization. The earliest version of the experimental

chamber was an ad-hoc structure whose features were added iteratively when the need for them arose. This approach was profoundly inefficient and was eventually abandoned in favor of model-based design. Using Pro-Engineer design software, a second-generation chamber was modeled and built to accommodate present and future research needs, including increased pumping capacity, a residual gas analyzer, robotic wavelength selection, and an integrated ion gun. Repeatability in fabrication and measurement required not only a properly-equipped fabrication chamber, but also data acquisition and process automation software. National Instruments Labview served as the development platform for these applications due to its ease of use and wide instrument compatibility. Applications were written in modules to automate both routine tasks as well as complete experimental procedures.

8.1.2 Coated Metals

This phase of research determined the effect of partial cesium coverage on the photo-response of tungsten and silver photocathodes. A relationship between quantum efficiency and cesium coverage for atomically cleaned sintered tungsten was established through repeated measurement in preparation for dispenser studies. The behavior of cesiated polycrystalline substrates was shown to be identical to that of sintered substrates, suggesting that the theory's generalized treatment of surface conditions is justified and applicable to surfaces with micron-scale roughness. The work function of a monolayer cesium coating on sintered tungsten was measured and found to be about 1.4eV following ion beam cleaning. Lifetime measurements of cesiated tungsten suggest that the degradation mechanism for this type of cathode is loss of cesium due to surface evaporation.

8.1.3 Surface Metrology

The surface characteristics of sintered tungsten were studied in detail using optical, scanning electron, and focused ion beam microscopy. The porosity and thickness of the sintered disks used in the dispenser cathode were chosen such that extremes in either case were avoided. A 1mm thick disk with 30% porosity was ultimately chosen for its mechanical integrity as a future dispenser cathode. Characteristic length scales of its polished surface were determined, including average pore diameter of 350nm, nearest-neighbor separation distance of 3.1 μ m, and average grain size of 4.8 μ m. The surface area each pore must coat with cesium was found on average to be 33.3 μ m² for uniform monolayer coverage. These lengths are significant because they estimate the surface diffusion length of cesium required to achieve complete coverage. Coverage uniformity is crucial because variation in the cesium surface coating causes similar variation in work function and electron emission, which contribute to beam emittance. Given the success of the prototype dispenser cathode, detailed knowledge of the sintered surface is important not only to replicate these results, but also to design a controlled porosity substrate with similar pore sizes and distribution.

8.1.4 Cleaning Techniques

A standardized cleaning procedure using an ion argon beam was developed and shown to be remarkably effective in cleaning sintered tungsten. When cesium was deposited following the procedure, the effects of the treatment became apparent: a two-fold increase in the QE and a 30-fold increase in cathode lifetime with a peak QE of 0.11% in the UV. A single 45 minute treatment provided a 40mC dose of 6keV

argon ions which was sufficient to produce apparent atomic cleanliness. This claim is justified because increasing the number of consecutive ion treatments and/or the energy of the ion beam did not produce further improvement in QE. Because cesium was deposited uniformly on an atomically clean surface, the QE of 0.11% can be said to be characteristic of a uniform, optimal cesium coating. This cleaning technique dramatically reduces the amount of time required to prepare a cathode for cesium deposition because it eliminates the need for a lengthy high temperature anneal.

8.1.5 Theory Validation

Data describing the effect of surface cesium coverage on the work function and QE of metal photocathodes was compared to theoretical predictions and found on average to be within 22% agreement. The consensus among beam simulation experts is that such agreement serves as validation of the photoemission model for the specific photocathode in question. This experiment enables theory comparison for an important set of operation parameters: low drive laser intensity and low accelerating electric field. These parameters are typically much higher and are usually cited as reasons for drastic discrepancies between theory and experiment (e.g., laser heating, damage to cathode surface, etc.). Comparison between theory and experiment in this regime was accomplished in two ways: initial results for cesiated tungsten were obtained to help refine the theory and subsequent predictions were made for a completely different photocathode – cesiated silver. This cathode was then fabricated and the resulting data was again in close (within 20%) agreement with theory. It is significant to point out that agreement in both cases was not coerced by appealing to specifics of either the cathode surface or the experimental conditions in the

fabrication chamber. The inputs to the theory were simply generalized material parameters that could be widely applied to any number of different photocathodes.

8.2 Dispenser Studies

The motivation of the precursor work was to enable meaningful interpretation of data obtained from the dispenser cathode. Knowledge of cleaning techniques and the effect of surface coatings enabled detailed characterization of the dispenser cathode.

8.2.1 General Remarks

A prototype design for a near-room temperature dispenser cathode was proposed and demonstrated using commonly available components: thin-walled stainless steel and porous sintered tungsten. The overall performance of the dispenser cathode suggests that its design could serve as a temperature-controlled cesium dispensing platform on which a variety of cesium-based photocathodes could be built. It is distinguished from other dispenser-type cathodes by its low operating temperature, which makes it a good candidate technology where cathode thermal management is a concern. A method for conveniently integrating cesium chromate into the dispenser cell was demonstrated by forming the powder into a solid pellet under high pressure. The peak QE of the activated dispenser cathode, following an ion beam cleaning treatment, was 0.11%. This QE value was shown previously to correspond to that of a uniform, optimal cesium coating and suggests that the sintered tungsten interface facilitates uniform cesium coverage. This result shows that the

surface diffusion length of cesium at temperatures ranging from 200-400°C is at least 5 μ m.

8.2.2 Operating Parameters

The two basic procedures for operating the dispenser cathode are activation and rejuvenation. Activation occurs at higher temperatures and initiates a chemical reaction between the powders inside the cell, while rejuvenation occurs at much lower temperature and involves bringing atomic cesium to the surface in a controlled manner. Initial activation prepared the dispenser for use, as seen by the onset of photoemission at 425°C, followed by complete activation at 477°C, which produced a reduction in work function such that a large thermionic current was measured. Because of the elevated temperature, a significant amount of cesium was released throughout the chamber, producing up to a 50Å coating on an adjacent deposition monitor. This release is expected, however, and is not considered problematic because a.) a large quantity of cesium remained within the dispenser following activation, and b.) the activation procedure for a working dispenser cathode would most likely occur in a chamber separate from the actual electron gun (whose contamination with cesium would lead to field breakdown).

Following activation, the dispenser was allowed to cool and its $1/e$ lifetime was measured to be 5.2 days. After 65 hours of continuous operation, its QE decayed from its peak of 0.11% in UV to 0.06%. Complete rejuvenation was demonstrated when QE returned to its previous peak value of 0.11% upon heating to 140°C. Less than 3Å of cesium was deposited during this process, suggesting that *in situ* rehabilitation of the cathode is possible. Coverage at peak QE was indirectly

measured to be about 64% using the relationship to QE established during the precursor study.

Two modes of cathode operation were demonstrated: periodic and continuous rejuvenation. For the continuous mode, temperature is held between 160-180°C, resulting in constant replenishment of the cesium layer. The $1/e$ effective (continuous duty cycle) lifetime in this mode was an astounding 47.2 days. Each mode has advantages depending upon the specific application.

8.2.3 Literature Representation

The novelty of this dispenser approach is evident by the absence of similar concepts in the literature. Thermionic dispenser cathodes (or photo-assisted thermionic cathodes) are well documented and widely used, but these differ significantly in operation and design from the concept presented in this work. Thermionic dispenser cathodes are typically operated at temperatures in excess of 1000°C and are fashioned by impregnating alkali compounds into a sintered matrix. By contrast, the dispenser described herein can be operated at room temperature (with periodic *in situ* rejuvenation) and can accommodate a much larger quantity of cesium.

A cesium ion source was introduced in the 1960's that is conceptually very similar to the dispenser cathode, except that its form factor and intended use are completely different [110],[111]. It uses a smaller, thicker, less-porous sample of sintered tungsten to contain cesium chromate and silicon powders in a confined space. It is then heated to 650-1000°C so that cesium diffuses through the tungsten and immediately leaves the surface as ions. The fact that cesium leaves the surface in

ionic form is advantageous in the case of the dispenser cathode, because the amount of cesium released (as ions) into the chamber can be closely monitored.

8.3 Future Studies

The success of the near-room temperature cesiated tungsten dispenser photocathode motivates continued research in several important directions. This final section of the dissertation suggests and attempts to prioritize additional studies that are required for adapting the dispenser concept to useful applications.

8.3.1 Application to High QE Photocathodes

The dispenser delivery mechanism presented in this work sets the stage for progress toward near-room temperature rejuvenation of high QE photocathodes such as Cs₃Sb and CsK₂Sb. With quantum efficiencies ranging from 4-10% in the visible range, an effectively long lifetime for these emitters would be of great benefit to photocathode and photoinjector technologies. The basic processing steps of a Cs-Sb cathode appear to be compatible with observed performance of the dispenser cell. The two-step process requires evaporation of an antimony film onto the dispenser substrate and then exposure of this film to cesium at temperatures not exceeding 200°C, with an optimal reaction temperature range of 130-150°C [22]. These temperatures align well within the demonstrated operating range of the dispenser cathode. The only requirement would be to both activate and clean the dispenser cell prior to the antimony layer deposition. The cell could then be heated and exposed to cesium (from either the dispenser itself or an external source) to allow formation of Cs₃Sb. It is important to note that the Cs-Sb chemical reaction still proceeds at room

temperature, but the rate is exceedingly slow. The elevated temperature serves not to initiate, but rather to accelerate this reaction. This affords some flexibility in the chosen reaction temperature because lower temperatures simply require longer activation times [22]. In anticipation of these studies, sources of potassium and antimony were custom fabricated and installed in the present version of the fabrication chamber.

8.3.2 Conventional vs. Controlled Porosity

Sintered tungsten was chosen in this work as the interface layer between the cesium reservoir and the photoemitting surface because of its commercial availability and well-documented characteristics. Other substrate materials, such as silicon carbide, could potentially be used in place of sintered tungsten and may allow the operating and activation temperature ranges to be modified to better suit a particular cathode application. In either case, a controlled porosity approach, where pores are arranged in an orderly lattice via laser drilling, could be very beneficial because it would allow precise control of the bulk and surface cesium diffusion rates. The length scales determined in this work for sintered tungsten (pore diameter, separation distance, etc.) could be used as the initial parameters of a controlled porosity surface. A study of cesium coatings using a photoemission electron microscope is ongoing at the Naval Research Laboratory [106]. This work promises to provide a comprehensive understanding of cesium's temperature-dependent surface diffusion and provide more accurate dimensions for a controlled porosity design.

8.3.3 Alternative Forms of Cesium

A disadvantage of the present dispenser cell is that the temperatures of the cathode surface and the cesium reservoir cannot be independently controlled. This is inconvenient because during the required high temperature activation, the hot cathode surface causes cesium atoms to evaporate as soon as they arrive. This results in an unnecessary loss of cesium and coats the walls of the chamber. One solution would be to divide the present reservoir into two separate hermetic enclosures, connected by a low-thermal conductivity tube. Separate heater wire wound around each section would allow independent control of their individual temperatures. Cesium chromate powder could then be reacted at high temperature in one section without heating the cathode surface situated on the opposite section.

Another possible solution is to mount a cesium ampoule inside the reservoir which could be remotely opened either through electromagnetic or electro-mechanical methods (piezoelectric transducer, electromagnetic plunger, bi-metallic expansion strip, etc.). While these methods admittedly introduce a large degree of complexity, they could allow independent control of cathode surface temperature. This would be of immediate benefit to Cs_3Sb cathodes, where a surface reaction must take place at elevated temperature.

8.3.4 Related Studies

Recall that all cathode substrates utilized in this work were polycrystalline in nature, with a significant distribution in work function across the surface. Theory comparison could be further enhanced by measuring the effects of cesium coverage

on the QE of single crystal cathode substrates, whose constant work function would eliminate yet another variable from the theory-experiment comparison.

Cryogenic environments are an as-yet unexplored experimental domain for high QE photocathodes. Theory predictions show that the QE of cesiated tungsten increases by a factor of 3 when it is cooled from 300K to 12K [112]. Cesium evaporation from the surface is also expected to be minimal at cryogenic temperatures, suggesting that longer lifetimes are possible even without the use of a cesium dispenser mechanism. The periodic mode of dispenser rejuvenation discussed earlier could be compatible with superconducting guns because it does not create a thermal load which would interfere with the superconducting cavity walls.

A final area of important study is the effect of various background gases on cathode efficiency and lifetime. Water, carbon-dioxide, and carbon-monoxide are known to “poison” the cathode by reacting with the cesium layer, but the effects of other common gases are not definitively known. Controlled introduction of a known amount of a particular gas could help specify the operating parameters of a given cathode for a given background gas environment.

8.4 Closing Remarks

Photoemission is regarded as an enabling technology for applications requiring high-current, high-brightness electron beams. Photoinjector systems consist of a drive laser producing short bunches of photons and an efficient photocathode, which converts the photon bunches into electron beam pulses. Most high-efficiency photocathodes employ cesium-based surface coatings or compounds to reduce work function and enable efficient electron emission using a visible drive laser. These

surface coatings are delicate and degrade quickly in a practical vacuum environment, leading to very short cathode lifetimes. This dissertation focused primarily on the development and demonstration of a novel dispenser cathode that could extend the useful lifetime of existing and future high efficiency photocathodes. The dispenser consists of a cesium reservoir situated beneath a sintered tungsten substrate upon which a cesium-based photoemitter is built. During an *in situ* rejuvenation process, the reservoir is gently heated such that cesium diffuses through and across this interface to restore the photosensitive layer. A careful study of the photoemissive effects of partial cesium coverage on bare metals was performed to help validate a photoemission model and better understand the behavior of the dispenser photocathode. The prototype dispenser cell was fabricated and its performance showed that uniform surface coverage of cesium could be achieved for two modes of operation: periodic and continuous operation. For a cesium-on-tungsten photoemitter, the dispenser demonstrated a $1/e$ lifetime of more than 47 days. Methods for cleaning and characterizing the surface of the dispenser cathode were developed and employed to optimize cathode performance. As a platform for cesium delivery, the dispenser cathode proposed in this research has demonstrated potential to improve many alkali-based high-efficiency photocathodes and enable their use in practical applications.

Bibliography

- [1] A. H. Sommer and W. E. Spicer, "Photoelectric Emission," Chap. 4 in *Photoelectronic Materials and Devices* (D. Van Nostrand Co., Princeton, 1965).
- [2] P. G. O'Shea, H. P. Freund, *Science* **292**, 1853 (2001)
- [3] D. H. Dowell, S. Z. Bethel, K. D. Friddell, *Nucl. Instr. & Meth. in Phys. Res.*, **A356** 167 (1995).
- [4] P. G. O'Shea, et. al., "Performance of the Photoinjector accelerator for the Los Alamos Free-electron laser," in *Proc. Particle Accel. Conf.*, vol. 5, San Fran., May 6–9, 1991, pp. 2754–2756.
- [5] S. H. Kong, J. Kinross-Wright, D. C. Nguyen, R. L. Sheffield, "Photocathodes for free electron lasers," *Nucl. Instr. & Meth. in Phys. Res.*, **A358** 272 (1995).
- [6] J. S. Fraser, R. L. Sheffield, et. al., *IEEE Trans. Nucl. Sci.*, Vol. **NS-32**, No. 5 (1985).
- [7] K. Jensen, D. Feldman, N. Moody, et. al., "Field-enhanced photoemission from metals and coated materials," *Jour. Vac. Sci. Tech. B* **24**, 2 (2006).
- [8] P. G. O'Shea, "High-Brightness RF Photocathode Guns for Single Pass X-Ray Free-Electron Lasers," *Nucl. Inst. Phys. Res.* **A358**, 36 (1995).
- [9] K. L. Jensen, D. W. Feldman, M. Virgo, P. G. O'Shea, *Phys. Rev. Spec. Top.* **AB6**, 083501 (2003).
- [10] T. Srinivasan-Rao, J. Fisher, T. Tsang, *Jour. Appl. Phys.* **77**, 1275 (1995).

- [11] C. K. Sinclair, *Proceedings of the 1999 Particle Accelerator Conference*, New York, IEEE, Piscataway, NJ, 1999, p. 65.
- [12] L. R. Koller, "Photoelectric emission from thin films of cesium," *Phys. Rev. Lett.*, **36**, no. 11, 1637 (1930).
- [13] K. L. Jensen, D. W. Feldman, N. A. Moody, "A photoemission model for low work function coated metal surfaces and its experimental validation," *Jour. App. Phys.*, **99**, 1 (2006).
- [14] B. Leblond, *Nucl. Inst. Phys. Res.* **A317**, 365 (1992).
- [15] J. S. Faser, "Electron sources for advanced accelerator experiments," in *AIP Conf. Proc.*, 156, 355 (1987).
- [16] M. Reiser, *Theory and Design of Charged Particle Beams* (Wiley-Interscience, New York, 1993).
- [17] C. LeJeune, J. Aubert, "Emittance and Brightness: Definitions and Measurements," in *Applied Charged Particle Optics*, edited by A. Septier (Academic Press, New York, 1980).
- [18] W. E. Spicer, A. Herrera-Gomez, "Modern theory and applications of photocathodes," in *Proc. SPIE*, vol. 2022, San Diego, July 11-16, 1993, pp. 18-33.
- [19] C. N. Berglund, W. E. Spicer, "Photoemission studies of copper and silver: experiment," *Phys. Rev.* **136**, no. 4A, 1044 (1964).
- [20] A. L. Hughes and L. A. DuBridge, *Photoelectronic Phenomena* (McGraw-Hill, New York, 1932).

- [21] H. Frohlich, R. A. Sack, "Light Absorption and selective photo-effect in adsorbed layers," in *Proc. Phys. Soc.*, vol. 59, pp. 30-33, 1947.
- [22] A. H. Sommer, *Photoemissive Materials: Preparation, Properties, and Uses*, (John Wiley & Sons, New York, 1968).
- [23] C. Travier, "RF guns: bright injectors for FEL," *Nucl. Instr. & Meth.*, **A304**, 285 (1991).
- [24] R. H. Fowler, "The analysis of photoelectric sensitivity curves for clean metals at various temperatures," *Phys. Rev.*, **38**, no. 1, 45 (1931).
- [25] L. A. DuBridge, *Phys. Rev.*, **39**, 108 (1932), **43**, 727 (1933).
- [26] P. A. Anderson, "The contact difference of potential between tungsten and barium: the external work function of barium," *Phys. Rev.* **47**, no. 12, 958 (1935).
- [27] K. C. Mishra, R. Garner, P. C. Schmidt, "Model of work function of tungsten cathodes with barium oxide coating," *Jour. Appl. Phys.* **95**, no. 6, 3069 (2004).
- [28] E. P. Gyftopoulos, J. D. Levine, "Work function variation of metals coated by metallic films," *Jour. Appl. Phys.* **33**, no. 1, 67 (1962).
- [29] K. H. Kingdon, I. Langmuir, "The removal of thorium from the surface of a thoriated tungsten filament by positive ion bombardment," *Phys. Rev.* **22**, no. 2, 148 (1923).
- [30] J. B. Taylor, I. Langmuir, "The evaporation of atoms, ions, and electrons from cesium films on tungsten," *Phys. Rev.* **44**, no. 6, 423 (1933).

- [31] J. H. De Boer, *Electron Emission and Adsorption Phenomena* (University Press, Cambridge, 1935).
- [32] A. L. Riemann, *Thermionic Emission*, (Chapman and Hall, London, 1934).
- [33] T. J. Lee, B. H. Lott, B. J. Hopkins, *Brit. Jour. Appl. Phys.* **1**, ser. 2, 1241 (1968).
- [34] W. F. Krolicowski, W. E. Spicer, *Phys. Rev.*, **185**, 882 (1969).
- [35] E. O. Kane, *Phys. Rev.*, **159**, 624 (1967).
- [36] M. Eyckeler, W. Monch, T. U. Kampen, et. al., *Jour. Vac. Sci. Tech.*, B **16**, 2224 (1998).
- [37] D. Heskett, T. M. Wong, A. J. Smith, et. al., *Jour. Vac. Sci. Tech.*, B **7**, 915 (1989).
- [38] C. I. Wu, A. Kahn, *Appl. Phys. Lett.*, **74**, no. 10, 1433 (1999).
- [39] H. Hertz, *Ann. Physik.*, **31**, 983 (1887).
- [40] W. Hallwachs, *Ann. Physik.*, **33**, 301 (1888).
- [41] J. Elster, H. Geitel, *Ann. Physik.*, **38**, 497 (1889).
- [42] P. F. Dahl, *Flash of the Cathode Rays* (Inst. of Physics Publishing, London, 1997).
- [43] N. R. Campbell, "The photoelectric emission of thin films," *Phil. Mag. & Jour. of Sci.*, **12**, no. 173, 1814 (1931).
- [44] A. H. Sommer, in *Proc. SPIE*, vol. 2022, San Diego, July 11-16, 1993, pp. 18-33.
- [45] W. E. Spicer, *Appl. Phys. Lett.*, **12**, 115 (1977).

- [46] J. S. Escher, "NEA Semiconductor Photoemitters," *Semiconductors and Semimetals*, Vol. 15, R. K. Willardson and A. C. Beer (Academic Press, Boston, 1980).
- [47] G. A. Westenskow, J. M. J. Madey, *Laser & Particle Beams* 2, 223 (1984).
- [48] C. H. Lee, et. al., in *Proc. IEEE PAC*, Vancouver, Canada, 1985, IEEE Trans. Nucl. Sci., **NS-32**, no. 5, 3045 (1985).
- [49] R. L. Sheffield, et. al., *Nucl. Instr. & Meth.*, **A272**, 222 (1988).
- [50] P. G. O'Shea, S. C. Bender, et. al., *Nucl. Instr. & Meth.*, **A318**, 52 (1992).
- [51] P. G. O'Shea, S. C. Bender, et. al., *Phys. Rev. Lett.*, **71**, 3661 (1993).
- [52] P. G. O'Shea, Free Electron Laser High Brightness, High Average Current Injector Report, Navy HEL Program Office (PMS-405), 2002.
- [53] B. E. Carlsten, R. L. Sheffield, in *Proc. Linear Accel. Conf.*, Williamsburg, VA, 1988, CEBAF-Report-89-001 (1989) p. 365.
- [54] D. Janssen, V. Volkov, *Nucl. Instr. & Meth.*, **A452**, 34 (2000).
- [55] N. G. Gavrilov, et. al., *Nucl. Instr. & Meth.*, **A359**, 44 (1995), p..
- [56] K. Kui, et. al., *Nucl. Instr. & Meth.*, **A483**, 1 (2002).
- [57] G. R. Neil, et. al., *Phys. Rev. Lett.* **84** 662 (2000).
- [58] P. G. O'Shea, et. al., in *Proc. Linear Accel. Conf.*, Albuquerque, NM, 1990.
- [59] D. H. Dowell, F. K. King, R. E. Kirby, J. F. Schmerge, "In situ cleaning of metal cathodes using a hydrogen ion beam," *Phys. Rev. Spec. Top.*, **AB 9**, 063502 (2006).
- [60] T. Srinivasan-Rao, J. Fischer, T. Tsang, *Jour. Appl. Phys.*, **69** no. 5, 3291 (1991).

- [61] D. H. Dowell, et. al., *Appl. Phys. Lett.*, **63**, 2035 (1993).
- [62] J. Edighoffer, et. al., *Nucl. Instr. & Meth.*, **A358**, 18 (1995).
- [63] C. K. Sinclair, *Nucl. Instr. & Meth.*, **A318**, 410 (1992).
- [64] S. J. Russell, *Nucl. Instr. & Meth.*, **A507**, 304 (2003).
- [65] J. M. Macaulay, I Brodie, C. A. Spindt, C. E. Holland, “Cesium thin-film field-emission microcathode arrays,” *Appl. Phys. Lett.*, **61**, no. 8, 997 (1992).
- [66] A. H. Sommer, “The element of luck in research – photocathodes from 1930 to 1980,” *J. Vac. Sci. Tech.*, **A1** no. 2, 119 (1983).
- [67] M. H. Hablanian, *High Vacuum Technology*, 2nd ed. (Marcel Dekker, New York, 1997).
- [68] *American Institute of Physics Handbook*, 3rd Ed, (McGraw-Hill, New York, 1972).
- [69] M. K. Sullivan, “A method for calculating pressure profiles in vacuum pipes,” Stanford Linear Accelerator Center, Internal Note AP 94-6 (1994).
- [70] P. He, H. C. Hseuh, R. Todd, “Pressure distribution simulation for SNS ring vacuum,” in *Proc. Particle Accel. Conf.*, vol. 2, San Fran., May 12-16, 2003, pp. 791-793.
- [71] W. T. Silfvast, *Laser Fundamentals*, 2nd ed. (Cambridge University Press, Cambridge, 2004).
- [72] S. Nakamura, S. Pearton, G. Fasol, *The Blue Laser Diode*, (Springer, Berlin, 2000).
- [73] Linear Motors, *An Application Guide*, online publication www.aerotech.com
- [74] Private communication with Zaber applications engineer, May, 2005.

- [75] V. Mecea, R. V. Bucur, "The use of RF voltage in quartz crystal microbalance measurements: application to nonmetallic films," *Jour. of Phys. E: Sci. Instr.*, **7**, no. 5, 348 (1974).
- [76] *CRC Handbook of Chemistry and Physics*, 69th ed (CRC Press, Boca Raton, 1988-1989).
- [77] F. Paschen, *Wied. Ann.*, **37**, 69, (1889).
- [78] B. Chapman, *Glow Discharge Processes* (Wiley-Interscience, New York, 1980).
- [79] M. Baylac, P Adderley, J. Clark, et. al, "Effect of atomic hydrogen exposure on electron beam polarization from strained GaAs photocathodes," in *AIP Conference Proceedings*, 2003
- [80] Atomtech Ltd, Microbeam-7, formerly IonTech, LTD.
- [81] G. Herrmann and S. Wagener, *The Oxide-Coated Cathode* (Chapman and Hall, London, 1951).
- [82] H. Bergeret, M. Boussoukaya, R. Chehab, et. al., *Nucl. Instr. Meth. Res.*, **A301**, 389 (1991).
- [83] A. P. Makarov, O. K. Kultashev, *Appl. Surf. Sci.*, **111**, 56 (1997).
- [84] C.-S. Wang, "High photoemission efficiency of submonolayer cesium-covered surfaces," *Jour. Appl. Phys.* **48**, no. 4, 1477 (1977).
- [85] G. A. Haas, R. E. Thomas, in *Techniques of Metals Research*, edited by R. F. Bunshah (Wiley, New York, 1972), Vol. VI, Pt. 1, Chap. 2.
- [86] L. Pauling, *The Nature of the Chemical Bond* (Cornell University Press, Ithaca, New York, 1960), 3rd edition.

- [87] J. Topping, Proc. Roy. Soc. (London) **A114**, 67 (1927).
- [88] E. S. Ritter, J. Chem. Phys. **19**, 1030 (1951)
- [89] K. L. Jensen, D. W. Feldman, P. G. O'Shea, Jour. Vac. Sci. Tech. B **23**, 621 (2005).
- [90] N. A. Papadogiannis, S. D. Moustāzīs, J. P. Girardeau-Montaut, Jour. Phys. D **30**, 2389 (1997).
- [91] N. A. Papadogiannis, S. D. Moustāzīs, Jour. Phys. D **34**, 2389 (2001).
- [92] I. Langmuir, Jour. Chem. Soc. **38**, 2287 (1916).
- [93] L. W. Swanson, R. W. Strayer, Jour. Chem. Phys. **48**, no 6, 2421 (1968).
- [94] S. Zangoie, H. Arwin, Jour. Electrochem. Soc., **148**, no. 6, G297 (2001).
- [95] Private communication with D. I. Moody, May, 2006.
- [96] G. G. Magera, P. R. Davis, Jour. Vac. Sci. Tech, **A11**, no 4, (1993)
- [97] J. Kouptsidis, A. G. Mathewson, *Deutsches Elektronen Synchrotron Notkestrasse Report*, 76/49 (1976).
- [98] H. Hartwig, J. Kouptsidis, IEEE Trans. Nucl. Sci., **24**, no. 3, 1248 (1977).
- [99] N. R. Dean, E. W. Hoyt, M. T. Palrang, B. G. Walker, "Glow discharge processing vs. bakeout for aluminum storage ring vacuum chambers," Jour. of Vac. Sci. Tech., **15**, no. 2, 758 (1978).
- [100] S. Zhang, "Glow discharge cleaning for the Fermi Lab main injector," Fermi-Lab Main Injector Notes, MI-069.
- [101] J. P. Girardeau-Montaut, C. Girardeau-Montaut, "Theory of ultrashort nonlinear multiphoton photoelectric emission from metals," Phys. Rev. B, **51**, no. 19, 13560, (1995).

- [102] C. Tomas, J. P. Girardeau-Montaut, et. al., “Dependence of photoemission efficiency on the pulsed laser cleaning of tungsten photocathodes, part 1: experimental,” *Appl. Phys. A*, **64**, 467 (1997).
- [103] K. L. Jensen, Y. Y. Lau, B. Levush, *IEEE Trans. Plasma Sci.*, **28**, no. 3, 772 (2000).
- [104] N. S. Rasoe, C. Warner, *Jour. Appl. Phys.*, **35**, 9, 2589 (1964).
- [105] T. L. Matskevich, *Soc. Phys. – Tech. Phys.*, **31**, 1481 (1959).
- [106] J. Shaw, J. Yater, et. al., “Surface diffusion measurements by scanning photoelectron microscopy,” 8th Annual DEPS Symposium, Lihue, HI, Nov. 14-18, 2005.
- [107] A. Balter, University of Maryland TREND research program, Summer 2006,
- [108] C. A. Haque, . H. Fritz, “Work function changes on contact materials,” *IEEE Trans. on Parts, Hybrids, and Packing*, **PHP-10**, No. 1, March 1974.
- [109] Personal coorespondence, B. Vancil, EBeam, Inc., 2006.
- [110] D. L. Schaefer, *Rev. Sci. Instr.*, **41**, no. 2, 274 (1970).
- [111] S. Della-Negra, J. Depauw, Y. Le Beyec, in *Proc. of 6th Intl. Conf. on Secondary Ion Mass Spec (SIMS VI)*, Versailles, Paris, 13-18 Sept., 1987.
- [112] K. Jensen, et. al., “Photoemission from cesiated surfaces,” 8th Annual DEPS Symposium, Lihue, HI, Nov. 14-18, 2005.
- [113] K. L. Jensen, et. al., “Time dependent models of field-assisted photoemission,” in *Proc. Intl. Vac. Nano. Conf.*, Cambridge, Mass. July 11-16, 2004.